Doctoral theses at NTNU, 2018:243

Shibo Xu

Seismic data processing in orthorhombic anisotropic media

NTNU
Norwegian University of
Science and Technology

Doctoral thesis

Shibo Xu

ISBN 978-82-326-3276-3 (printed ver.)
ISBN 978-82-326-3277-0 (electronic ver.)
ISSN 1503-8181

NTNU
Norwegian University of Science and Technology
Thesis for the Degree of
Philosophiae Doctor
Faculty of Engineering
Department of Geoscience and Petroleum

Doctoral theses at NTNU, 2018:243

NTNU

Shibo Xu

Seismic data processing in orthorhombic anisotropic media

Thesis for the Degree of Philosophiae Doctor

Trondheim, August 2018

Norwegian University of Science and Technology
Faculty of Engineering
Department of Geoscience and Petroleum

NTNU
Norwegian University of
Science and Technology

NTNU
Norwegian University of Science and Technology

Thesis for the Degree of Philosophiae Doctor

Faculty of Engineering
Department of Geoscience and Petroleum

ISBN 978-82-326-3276-3 (printed ver.)
ISBN 978-82-326-3277-0 (electronic ver.)
ISSN 1503-8181

Doctoral theses at NTNU, 2018:243

Printed by NTNU Grafisk senter

Abstract

Describing the directional dependence of the wave velocity, seismic anisotropy has dramatically been gaining attention from both academic and industry, thanks to advances in the wider offset and azimuthal coverage of 3D surveys in the last two decades. Seismic anisotropy is a very useful and important physical property since it can provide the detailed information regarding both kinematic and dynamic processes. In this thesis, we only discuss the influence of anisotropy on the compressional (P) waves since they represent a majority of data being acquired in oil and gas exploration. The kinematic properties of anisotropic media can be defined in the phase and group domains. In the phase domain, these properties are related to the curvatures of the slowness surface computed at the point where both horizontal projections of the slowness vector are zero. In the group domain, the kinematic properties are related to similar curvatures computed from the traveltime (or group velocity inverse) surface at zero offsets.

The overall aim of this thesis is on the behavior of the seismic waves on an anisotropic model and their applications for seismic data processing (e.g. velocity analysis, parameterization, horizontal resolution, geometrical spreading and the imaging problem etc.). Thomsen type parameters are used to represent the anisotropic model. The models tested in this thesis are including: isotropic (ISO), elliptical isotropic (EI), transverse isotropic model with a vertical symmetry axis (VTI), factorized VTI and orthorhombic (ORT) models with an increase of complexity. The acoustic anisotropy assumption is applied for simplification. For multi-layered anisotropic models, the effective model parameters derived from the Dix-type equations are used for computation.

The traveltime computation is an important tool in seismic data processing that can be applied for velocity analysis, modeling and time migration. The non-hyperbolicity in moveout caused by anisotropy needs to be taken into consideration, as it commonly exists and plays an important role in seismic data processing and interpretation, especially for large offset. My research is mostly about the derivations of traveltime approximation from the parametric traveltime-offset equation computed through the dynamic ray tracing in VTI and ORT media. The traveltime-offset equation can also be utilized to compute the radius of the Fresnel zone through the perturbation-based approach for the study of the horizontal resolution. The analytical form of the relative geometrical spreading can be expressed by the traveltime and its derivatives. We propose the approximations for the relative geometrical spreading defined in the generalized non-hyperbolic moveout (GMA) and anelliptic forms and show their superiority of the accuracy compared with the conventional traveltime-based counterparts in the numerical examples in both VTI and ORT models. The accuracy of these approximations is tested in the numerical examples where the exact (standard) solutions are computed from the parametric equations measured through the dynamic ray tracing.

With the help of seismic anisotropy, a high-quality image of the subsurface is obtained. For the multiparameter stacking, the operator for common reflection surface (CRS) involving the anisotropy parameters is derived for a circular reflector in a homogeneous VTI model. The preserved traveltime smoothing (PTS) technique is extended to an ORT model that can be used to smooth the velocity models for prestack depth migration. We develop the formulas for diving waves in a factorized VTI medium and analyze their behavior. The anisotropy parameters are estimated by semblance analysis of the depth migrated data through the imaging moveout formulation (residual moveout after imaging) to update the velocity model that can be used to provide an initial velocity model for the full waveform inversion (FWI).

Preface

This thesis is submitted to the Norwegian University of Science and Technology (NTNU) to fulfill the requirements for the *Doctor of Philosophy* (Ph.D.). This doctoral research work has been performed at the Department of Geoscience and Petroleum, NTNU, Trondheim, with Professor Alexey Stovas as my main supervisor.

This Ph.D. thesis is written in the type of paper collection. Eight technical papers are involved as following

[1] Xu Shibo and Stovas Alexey, 2015, Curvature and anisotropy estimation through the CRS approximation. *Journal of Geophysics and Engineering*, **12**, 934-945.

[2] Xu Shibo, Stovas Alexey and Alkhalifah Tariq, 2016, Estimation of the anisotropy parameters from imaging moveout of the diving wave in a factorized VTI medium, *Geophysics*, **81**, C139-C150.

[3] Xu Shibo and Stovas Alexey, 2016, Preserved traveltime smoothing in orthorhombic media, *Geophysical Prospecting*, **65**, 1205-1217.

[4] Xu Shibo, Stovas Alexey and Hao Qi, 2016, Perturbation-based moveout approximations in anisotropic media, *Geophysical Prospecting*, **65**, 1218-1230.

[5] Xu Shibo and Stovas Alexey, 2017, 3D generalized nonhyperbolic approximation for relative geometrical spreading, *Geophysical Journal International*, **211**, 1162-1175.

[6] Xu Shibo and Stovas Alexey, 2017, A new parameterization for acoustic orthorhombic media, *Geophysics*, **82**, C229-C240.

[7] Xu Shibo, Stovas Alexey and Sripanich Yanadet, 2018, An anelliptic approximation for geometrical spreading in transversely isotropic and orthorhombic media, *Geophysics*, **83**, C37-C47.

[8] Xu Shibo and Stovas Alexey, 2018, Fresnel zone in vertical transversely isotropic and orthorhombic media, *Geophysical Journal International*, **213**, 181-193.

Acknowledgments

I would like to acknowledge many people who have supported and helped me during my Ph.D. period.

First of all, I would like to thank my supervisor, Professor Alexey Stovas for his great patience and help for my research in the last four years. Without his support and assistance, I would not be possible to complete my study in NTNU. I will never forget the numerous discussions in his office that helping me address my encountered problems and improve my research. He is such an outstanding scholar with a profound knowledge in Exploration Geophysics but always stays low-key and reserved. I can't stop thanking God for such a good supervisor.

We would like to acknowledge China Scholarship Council (CSC) and Rock Seismic Consortium (ROSE) project for financial support. I also thank Statoil publication support for providing me several travel grants.

I am grateful to all my colleagues and friends from NTNU for the help and support. Special thanks to my colleague Yuriy Ivanov in our anisotropic group who has a solid knowledge of Geophysics and creative mind for innovative ideas whom I have benefited a lot by working with. I also acknowledge my colleagues and friends: Professor Tariq Alkhalifah, Professor Dirk Gajewski, Dr Vetle Vinje, Dr Ketil Hokstad and Dr Pavel Golikov from other universities and institutions for their useful discussion and valuable suggestions.

I would like to acknowledge to all reviewers of my papers: Dr Igor Ravve, Dr Nabil Masmoudi, Emanouil Blias, Professor Umair bin Waheed, Yanadet Sripanich, Pavel Golikov, Aslan Gassiyev and these anonymous reviewers for their valuable comments. These comments are very valuable and helpful for revising and improving our papers. Special

gratitude to Dr Igor Ravve for his lasting supports, suggestions and comments that help me improve my research work.

I deeply thank my friends: Hongtao Li, Song Jin, Hailong Jia and the Brothers and Sisters from the Free Church in Trondheim for their love and care. I am particularly grateful to Brother Naiquan Ye and Sister Bordhild Hjelde who take Christ as a model and live a loving and humble life that shows me what kind of person I should become. Special thanks to the Brother Zhenkang Chen who is a man full of wisdom and inspires my mind during the unforgettable discussions in his home.

I would like to show my thanks to my parents for their endless love and support. Particular gratitude is given to my wife Qiqi Deng, who is the helper sent from God, for her considerable care and companionship. How much I love her can't be expressed by words. No matter where I am or what I am going to experience, as long as I'm staying with her, I can feel happy, hope and love.

Finally, all praises are attributed to the almighty God. The more I learned in knowledge, the more I discovered in my ignorance and limitation. If I'm not too stupid, the fact that I am just a negligible dust should be recognized and everything I've got is from the grace of God.

Unless the Lord builds the house, those who build it labor in vain. Unless the Lord watches over the city, the watchman stays awake in vain. ---------- **Psalm 127: 1.**

Contents

Chapter 1 Introduction

This chapter provides a very brief insight about seismic anisotropy, its applications in seismic data processing and the structure of this thesis.

1.1 Seismic anisotropy

Seismic anisotropy can be defined as the dependence of velocity on the direction or upon propagation angle. If the medium's elastic properties with respect to certain parameters change with the direction of a measurement, it is anisotropic; if its properties do not change with direction, it is isotropic. The isotropic assumption for the subsurface has been based on for most history of seismic inversion and processing although a certain degree of anisotropy commonly exists.

Anisotropy dates back to the 19th century following the theory of Elastic wave propagation. The origin of seismic anisotropy is non-unique, a range of phenomena may cause Earth materials to display seismic anisotropy. The anisotropy may be strongly dependent on wavelength if it is due to the average properties of aligned or partially aligned heterogeneity. The notions of heterogeneity and anisotropy are scale dependent and the same medium may behave as heterogeneous for small wavelengths and as anisotropic for large wavelengths (Helbig, 1994). The appreciation of anisotropy increased with the proposition of a new model for the generation of anisotropy in an originally isotropic background and a new exploration concept by Crampin (1987). These split phases propagate with different polarizations and velocities. Crampin (1984) amongst others gives evidence that many rocks are anisotropic for shear wave propagation. Although P wave velocity in anisotropic media can change greatly with respect to the propagation angle, P waves do not split into two modes and their reflection moveout typically is hyperbolic. Shear waves have been observed to split into two or more

fixed polarizations which can propagate in the particular ray direction when entering an anisotropic medium.

The role of anisotropy has dramatically increased over the past two decades due to advances in parameter estimation, the transition from poststack imaging to prestack depth migration, the wider offset and azimuthal coverage of 3D surveys, and acquisition of high-quality multicomponent data (Thomsen, 2001). The breakthrough for the study of seismic anisotropy has taken place after identifying the key parameters in the parameterization of transversely isotropic (TI) models (Thomsen, 1984) and the discovery of the P wave time processing parameter η (Alkhalifah and Tsvankin, 1995) in anisotropic media that greatly simplified the analytical description of seismic signatures, which can help to develop practical methodologies for estimating anisotropy parameters from the seismic data.

In seismic data processing, orthorhombic (ORT) model introduced by Schoenberg and Helbig (1997) is the most realistic anisotropic velocity model to describe fractured reservoirs and explains well the azimuthal dependency in surface seismic data. Tsvankin (1997, 2012) defined nine elastic model parameters for ORT model that can be reduced to six parameters in an acoustic approximation (Alkhalifah, 2003). In group domain, we call the first order curvatures the normal moveout (NMO) velocity ellipses (Grechka and Tsvankin, 1999a, 1999b) and the second order curvatures the anellipticities as they represent the anelliptic behavior for slowness or traveltime surface. Recently, more research works have been done for the parameterization of the acoustic ORT model (Vasconcelos and Tsvankin, 2006; Stovas, 2015; Xu and Stovas, 2017). For 2D cases, two main type of anisotropy are commonly used in seismic data processing: transverse isotropy medium with a vertical axis (VTI) and transverse isotropy medium with a horizontal axis (HTI), where VTI model is associated with layering and shale; HTI model is associated with cracks and fractures.

1.2 Stiffness matrix

The wave equation for seismic wave's propagation is based on two important laws: Newton's First Law of Motion and Hooke's Law of Elasticity.

Newton's First Law of Motion is written for a constant density medium by

$$\rho \frac{\partial^2 u_i}{\partial t^2} = \frac{\partial \tau_{ij}}{\partial x_j}, \tag{1.1}$$

where u_i are the components of the displacement vector u, τ_{ij} are the components of the stress tensor τ, x_j are the components of the coordinate position x, ρ is density and t is time.

The Hooke's Law is given by

$$\tau_{ij} = C_{ijkl} \varepsilon_{kl}, \tag{1.2}$$

where ε_{ij} are components of the strain tensor ε and C_{ijkl} are components of the fourth-rank elasticity tensor (stiffness tensor) C.

The wave equation is obtained by inserting equation (1.2) into (1.1) with the locally homogeneous assumption

$$\frac{\partial^2 u_i}{\partial t^2} = \frac{C_{ijkl}}{\rho} \frac{\partial^2 u_k}{\partial x_j \partial x_l}, \tag{1.3}$$

The stiffness tensor C is responsible for the anisotropic properties of the medium.

Generally, the stiffness tensor has four indices, two corresponding to the indices of stress and two to the indices of strain with $3 \times 3 \times 3 \times 3 = 81$ components. Since both stress and strain are symmetric, the number of independent elastic moduli can be reduced to 21 shown in equation (1.4)

$$C = \begin{pmatrix} C_{11} & C_{12} & C_{13} & C_{14} & C_{15} & C_{16} \\ C_{12} & C_{22} & C_{23} & C_{24} & C_{25} & C_{26} \\ C_{13} & C_{23} & C_{33} & C_{34} & C_{35} & C_{36} \\ C_{14} & C_{24} & C_{34} & C_{44} & C_{45} & C_{46} \\ C_{15} & C_{25} & C_{35} & C_{45} & C_{55} & C_{56} \\ C_{16} & C_{26} & C_{36} & C_{46} & C_{56} & C_{66} \end{pmatrix}. \tag{1.4}$$

The medium with 21 independent stiffness coefficients is the most complicated case and general kind of anisotropy (triclinic) for seismic wave propagation. However, it is almost impossible to measure all of these coefficients in any geophysical field survey. Thanks to the symmetric behaviors of the geological objects, we have a chance to describe the model with simpler symmetries (less independent stiffness coefficients).

The simplest one is the isotropic (ISO) model that using only two independent stiffness coefficients given by

$$C_{ISO} = \begin{pmatrix} M & \lambda & \lambda & & & \\ \lambda & M & \lambda & & & \\ \lambda & \lambda & M & & & \\ & & & \mu & & \\ & & & & \mu & \\ & & & & & \mu \end{pmatrix}, \tag{1.5}$$

where $M = \lambda + 2\mu$, λ and μ are Lamé parameters, the element in the matrix does not show is zero.

If the elastic properties do not change in any direction perpendicular to an axis of symmetry, the medium is transversely isotropic. There are special cases of transverse isotropy: the transversely isotropic medium with the vertical axis (VTI) and horizontal axis (HTI). For VTI model, the velocities do not vary from one lateral direction to another but vary from one direction to another on a vertical plane that coincides with a given lateral direction. For HTI

model, known as azimuthal anisotropy, for which velocities vary from on lateral direction to another.

The stiffness matrices for VTI and HTI media have five independent parameters given in equation (1.6) and (1.7), respectively.

The stiffness matrix of VTI media is given by

$$C_{VTI} = \begin{pmatrix} C_{11} & C_{11}-2C_{66} & C_{13} & & & \\ C_{11}-2C_{66} & C_{11} & C_{13} & & & \\ C_{13} & C_{13} & C_{33} & & & \\ & & & C_{55} & & \\ & & & & C_{55} & \\ & & & & & C_{66} \end{pmatrix}. \tag{1.6}$$

The stiffness matrix of HTI media is given by

$$C_{HTI} = \begin{pmatrix} C_{11} & C_{13} & C_{13} & & & \\ C_{13} & C_{33} & C_{33}-2C_{44} & & & \\ C_{13} & C_{33}-2C_{44} & C_{33} & & & \\ & & & C_{44} & & \\ & & & & C_{55} & \\ & & & & & C_{55} \end{pmatrix}. \tag{1.7}$$

Both VTI and HTI media can be treated as special cases of the more complex orthorhombic (ORT) model.

Orthorhombic model is characterized by three mutually orthogonal symmetry planes. In the coordinate system associated with the symmetry planes, orthorhombic media have nine independent stiffness coefficients given by

$$C_{ORT} = \begin{pmatrix} C_{11} & C_{12} & C_{13} & & & \\ C_{12} & C_{22} & C_{23} & & & \\ C_{13} & C_{23} & C_{33} & & & \\ & & & C_{44} & & \\ & & & & C_{55} & \\ & & & & & C_{66} \end{pmatrix}. \tag{1.8}$$

Orthorhombic anisotropy in sedimentary basins is a combination of parallel vertical fractures with vertical transverse isotropy in the background medium. ORT symmetry can be caused by two or three mutually orthogonal fracture systems or two identical systems of fractures making an arbitrary angle with each other. Therefore, orthorhombic anisotropy can be treated as the most realistic symmetry for many geophysical problems that can describe fractured reservoirs and explains well the azimuthal dependency in surface seismic data.

1.3 Anisotropy parameters

Based on the propagation and polarization direction, three types of the wave mode are defined for the body wave: P wave and S waves (SH and SV wave). We can compute the corresponding phase velocities for a given medium by solving the Christoffel equation

$$\left(G_{ik} - \rho V^2 \delta_{ik}\right) U_k = 0, \tag{1.9}$$

where $G_{ik} = C_{ijkl} n_j n_l$ are elements of the Christoffel matrix, n_j is the components of the directional unit vector, V is the phase velocity, δ_{ik} is the Kronecker's delta and U_k is amplitude for different wave modes.

In the isotropic case, two solutions in equation (1.9) are coupled; two waves P and S with velocities are defined by

$$V_P = \sqrt{\frac{\lambda + 2\mu}{\rho}},$$
$$V_S = \sqrt{\frac{\mu}{\rho}}. \tag{1.10}$$

These velocities do not depend on the propagation direction.

In the case of the VTI medium, solving the Christoffel equation gives three different solutions. For SH wave, which is always polarized orthogonal to the propagation plane, and for qP and qSV waves (q for “quazi”), which are polarized orthogonal to each other and also orthogonal to the SH wave polarization.

With the pioneering paper of Leon Thomsen (1986), anisotropy becomes a commonly accepted tool for analyzing seismic data. Instead of using the stiffness coefficients (C_{ij}), he innovatively used the simpler and understandable parameters to represent the VTI model referred as the Thomsen parameters.

The Thomsen parameters (Thomsen, 1986) are given by

$$V_{P0} = \sqrt{\frac{C_{33}}{\rho}},$$
$$V_{S0} = \sqrt{\frac{C_{44}}{\rho}},$$
$$\varepsilon = \frac{C_{11} - C_{33}}{2C_{33}}, \tag{1.11}$$
$$\delta = \frac{(C_{13} + C_{44})^2 - (C_{33} - C_{44})^2}{2C_{33}(C_{33} - C_{44})},$$
$$\gamma = \frac{C_{66} - C_{44}}{2C_{44}},$$

where V_{P0} and V_{S0} are vertical P and S wave velocities, respectively, ρ is density, δ, ε and γ are the dimensionless anisotropic parameters.

For the ORT model, Tsvankin (1997) defined the similar type of the anisotropy parameters in the model parameterization for three symmetry $[X,Z]$, $[Y,Z]$ and $[X,Y]$ planes shown in the slowness surface in Figure 1.1.

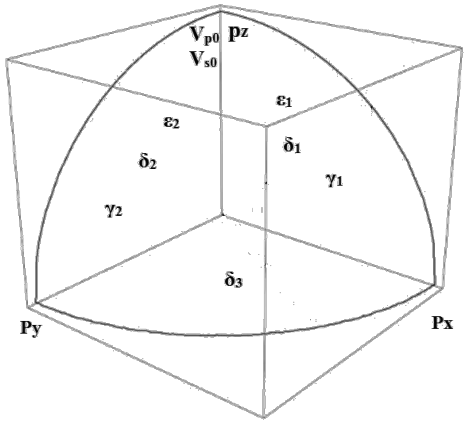

Figure 1.1. The anisotropy parameters defined in the ORT model.

Note that the definition in this thesis is slightly different with Tsvankin (1997) that we define the anisotropy parameters δ_1, ε_1 and γ_1 in $[X,Z]$ plane and δ_2, ε_2 and γ_2 in $[Y,Z]$ plane, which is opposite with the definition in Tsvankin (1997).

The anisotropy parameters normalized by density in ORT model are given by

$$
\begin{aligned}
V_{P0} &= \sqrt{C_{33}}, \\
V_{S0} &= \sqrt{C_{44}}, \\
\varepsilon_1 &= \frac{C_{11} - C_{33}}{2C_{33}}, \\
\delta_1 &= \frac{(C_{13} + C_{44})^2 - (C_{33} - C_{44})^2}{2C_{33}(C_{33} - C_{44})}, \\
\gamma_1 &= \frac{C_{66} - C_{44}}{2C_{44}}, \\
\varepsilon_2 &= \frac{C_{22} - C_{33}}{2C_{33}}, \\
\delta_2 &= \frac{(C_{23} + C_{44})^2 - (C_{33} - C_{44})^2}{2C_{33}(C_{33} - C_{44})}, \\
\gamma_2 &= \frac{C_{66} - C_{55}}{2C_{55}}, \\
\delta_3 &= \frac{(C_{12} + C_{66})^2 - (C_{11} - C_{66})^2}{2C_{11}(C_{11} - C_{66})}.
\end{aligned}
\tag{1.12}
$$

The inverse transformation can be given as

$$
\begin{aligned}
C_{33} &= V_{p0}^2, \\
C_{55} &= V_{s0}^2, \\
C_{11} &= (1 + 2\varepsilon_1)V_{p0}^2, \\
C_{22} &= (1 + 2\varepsilon_2)V_{p0}^2, \\
C_{13} &= \sqrt{(V_{p0}^2 - V_{s0}^2)((1 + 2\delta_1)V_{p0}^2 - V_{s0}^2)} - V_{s0}^2, \\
C_{12} &= \sqrt{((1 + 2\varepsilon_1)V_{p0}^2 - (1 + 2\gamma_2)V_{s0}^2)((1 + 2\varepsilon_1)(1 + 2\delta_3)V_{p0}^2 - (1 + 2\gamma_2)V_{s0}^2)} - (1 + 2\gamma_2)V_{s0}^2, \\
C_{23} &= \sqrt{\left(V_{p0}^2 - \left(\frac{1 + 2\gamma_2}{1 + 2\gamma_1}\right)V_{s0}^2\right)\left((1 + 2\delta_2)V_{p0}^2 - \left(\frac{1 + 2\gamma_2}{1 + 2\gamma_1}\right)V_{s0}^2\right)} - \left(\frac{1 + 2\gamma_2}{1 + 2\gamma_1}\right)V_{s0}^2, \\
C_{44} &= \left(\frac{1 + 2\gamma_2}{1 + 2\gamma_1}\right)V_{s0}^2, \\
C_{66} &= (1 + 2\gamma_2)V_{s0}^2.
\end{aligned}
\tag{1.13}
$$

1.4 Acoustic anisotropy

Acoustic approximation for processing in VTI model is obtained by setting the vertical S wave velocity into zero (Alkhalifah, 1998). The VTI model can be characterized by three

parameters: V_{P0}, δ and ε. The complexity of the wave equation is reduced greatly. The difference in P wave by using the acoustic assumption is negligible for most cases. The acoustic equations are much simpler and more compact than the elastic ones and can be expected to increase the efficiency of the processes when used in seismic processing.

We introduce a homogeneous VTI model with the parameters: ($V_{P0} = 2km/s$, $\delta = 0.1$, $\varepsilon = 0.22$ and $\gamma = 0.1$) and plot the relative error in the vertical slowness q ($(q - q_0) \times 100/q$) versus horizontal slowness p by using the acoustic approximation q_0 in Figure 1.2. One can see from the plot that the relative error in the vertical slowness is very small.

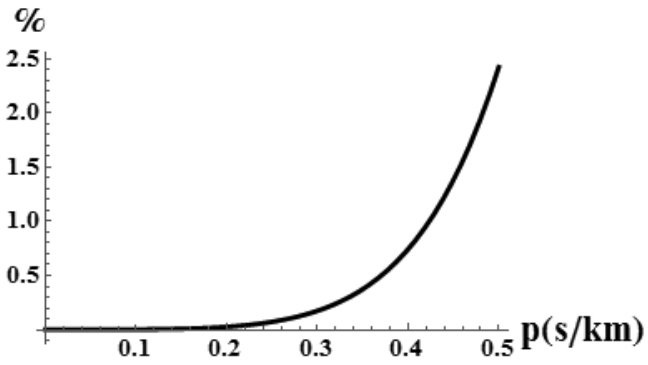

Figure 1.2. The relative error in the vertical slowness q ($(q - q_0) \times 100/q$) for a VTI model versus horizontal slowness p.

The parametric offset-traveltime equation in VTI model is computed from the derivative of the vertical slowness given by

$$\begin{aligned} x &= -z\frac{\partial q}{\partial p}, \\ t &= zq + xp, \end{aligned} \tag{1.14}$$

where z is the depth is the reflector.

We show the relative error in traveltime versus offset using the acoustic assumption in the introduced VTI model above in Figure 1.3. We can see from the plot that the error is negligibly small.

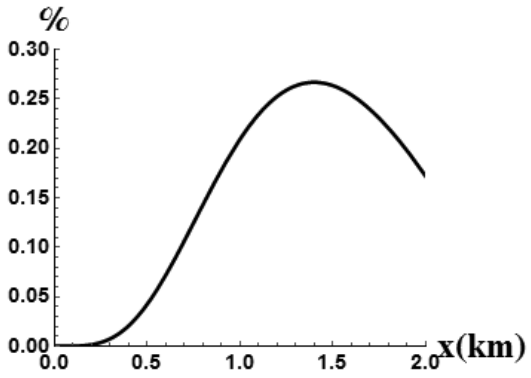

Figure 1.3. The relative error in the traveltime versus offset using the acoustic approximation in the VTI model with the parameters: $V_{P0} = 2km/s$, $\delta = 0.1$, $\varepsilon = 0.22$ and $\gamma = 0.1$.

A similar strategy is applied to ORT model (Alkhalifah, 2003) to compute the kinematic properties of P wave. The model parameters used for characterizing the acoustic ORT model are: V_{P0}, V_{nmo1}, η_1, V_{nmo2}, η_2 and η_3 (Vasconcelos and Tsvankin, 2006), where V_{nmo1} and V_{nmo2} are the normal moveout (NMO) velocities defined in $[X,Z]$ and $[Y,Z]$ planes, respectively, given by

$$\begin{aligned} V_{nmo1} &= V_{P0}\sqrt{1+2\delta_1}, \\ V_{nmo2} &= V_{P0}\sqrt{1+2\delta_2}. \end{aligned} \tag{1.15}$$

Anisotropy parameters η_1, η_2 and η_3 are the anellipticity parameters defined in $[X,Z]$, $[Y,Z]$ and $[X,Y]$ planes, respectively, given by

$$\eta_1 = \frac{\varepsilon_1 - \delta_1}{1 + 2\delta_1},$$
$$\eta_2 = \frac{\varepsilon_2 - \delta_2}{1 + 2\delta_2}, \tag{1.16}$$
$$\eta_3 = \frac{\varepsilon_2 - \varepsilon_1 - \delta_3(1 + 2\varepsilon_1)}{(1 + 2\delta_3)(1 + 2\varepsilon_1)}.$$

Stovas (2015) developed azimuthally dependent properties of the acoustic ORT model using the parameters: V_{P0}, V_{n1}, V_{n2}, η_1, η_2 and η_{xy}. The cross-term anellipticity parameter is defined by

$$\eta_{xy} = \sqrt{\frac{(1+2\eta_1)(1+2\eta_2)}{(1+2\eta_3)}} - 1. \tag{1.17}$$

More details about the parameterization in acoustic ORT model can be found in Chapter 5.

1.5 Thesis structure

There are eight Chapters and two Appendices in this thesis. Six Chapters (From Chapter 2 to 7) and two Appendices can be treated as independent papers with their own structure and presented exactly in the publication form.

In Chapter 2, the analytical expression for the common-reflection-surface (CRS) operator that involving the anisotropy parameters for a circular reflector in the acoustic VTI model is derived. We start with the isotropic CRS approximation, then we take anisotropy into consideration, and finally, we evaluate the structural and anisotropic parameters. We propose a new approach to investigate the effects of anisotropy and vertical heterogeneity on the P-wave CRS attributes and their inversion into the model parameters. The proposed result can be used for the multiparameter stacking to get a high-quality time image of the subsurface. The results of this Chapter were presented at the Workshop Meeting Active and Passive Seismic in Laterally Inhomogeneous Media (APSLIM), June, 2015, Prague, Czech Republic; and the paper was published in *Journal of Geophysics and Engineering* in October 2015.

In Chapter 3, we use the analytical formulas to describe the behavior of diving waves in a factorized anisotropic medium and approximate the imaging moveout formulation (residual moveout after imaging) to update the velocity model when the wrong model parameters (isotropic assumption) are used for imaging. We then utilize these analytical representations of the image moveout to establish a semblance analysis framework to search for the optimal anisotropic parameters. We have also discussed different parameterizations of the factorized medium to find the one that gave the best accuracy in anisotropy parameters estimation. These inverted models can provide an initial velocity model used for the update of the full waveform inversion (FWI). The results of this Chapter were presented at the 78th EAGE Conference and Exhibition, June, 2016, Vienna, Austria and the paper was published in *Geophysics* in July 2016.

In Chapter 4, we extend the preserved traveltime smoothing (PTS) method (Vinje et al., 2012) to an acoustic ORT model for two cases: with and without azimuthal variation between the layers. In case of azimuthal variations in the symmetry axis between the layers, the least squares approximation is adopted to estimate the effective anellipticity parameters from this layered medium to preserve the complexity of the model when doing smoothing. The PTS technique is proposed to address the drawback of the shifting problem in the conventional smoothing in the prestack migration process. The results of this Chapter were presented at the 78th EAGE Conference and Exhibition, June, 2016, Vienna, Austria and the paper was published in *Geophysical Prospecting* in November 2016.

In Chapter 5, a group of new parameterizations for P wave in acoustic ORT media are defined. The corresponding perturbation based approximations for traveltime in ORT model are developed using the newly defined parameterizations. The sensitivity of the group velocity inverse to anellipticity parameters is also analyzed for different parameterizations and different range of offsets. Different parameterization results in different accuracy in the

perturbation based traveltime approximation, which impacts the seismic data processing such as velocity analysis, modeling, and time migration. The results of this Chapter were presented at the 87th SEG Conference and Exhibition in September, 2017, Houston, USA and the paper was published in *Geophysics* in October 2017.

In Chapter 6, we have developed an anelliptic approximation for the relative geometric spreading of P-wave in a homogeneous VTI and an ORT medium under the acoustic anisotropy assumption. The coefficients in our approximation are only defined within the symmetry planes and computed from fitting with the exact parametric expression. Due to the symmetric behavior in different symmetry planes by using the acoustic anisotropy assumption, the computation for the coefficients in ORT model becomes easier by applying the corresponding changes in the forms of the coefficients that are obtained in one symmetry plane. The analytical form of the relative geometrical spreading can be used for the seismic data processing methods that require true amplitude processing. The results of this Chapter were presented at the 87th SEG Conference and Exhibition in September, 2017, Houston, USA and the paper was published in *Geophysics* in November 2017.

In Chapter 7, we derive an analytic expression for the radius of the Fresnel zone in the time domain in a homogeneous VTI and ORT models using the perturbation method from the parametric offset-traveltime equation. We show that the size of the Fresnel zone is proportional to the corresponding traveltime, depth and the frequency. From the numerical examples, we can see that the Shanks transform approximations for Fresnel zone are very accurate for both VTI and ORT media. This perturbation based method for the Fresnel zone in the anisotropic model can be extended for the model with a dipping reflector. The results of this Chapter were presented at the 80th EAGE Conference and Exhibition in June, 2018, Copenhagen, Denmark and the paper was published in *Geophysical Journal International* in December 2017.

In Appendix A, we propose a new set of moveout approximations based on a perturbation series in terms of anellipticity parameters using the alternative elliptical background model defined by vertical and horizontal velocities. The contents of this Appendix can be treated as a special case shown in Chapter 5 (new parameterization for ORT model). The results of this Appendix were presented at the 86th SEG Conference and Exhibition in October, 2016, Dallas, USA and the paper was published in *Geophysical Prospecting* in December 2016.

In Appendix B, we investigate another form of the approximation for the relative geometrical spreading. Since the anelliptic form approximation is presented in Chapter 6, we place this 3D GMA form approximation in the Appendix part. We develop a 3D GMA-type approximation for the relative geometrical spreading in a homogeneous ORT medium. Two type of GMA form approximations is defined by the different selection of reference rays: two reference rays with finite offsets and two horizontal reference rays in two corresponding vertical symmetry planes. One horizontal ray in between the vertical symmetry planes is selected to compute the cross-term coefficient in the approximation. The result of this Appendix is published in *Geophysical Journal International* in August 2017.

Chapter 2 Curvature and anisotropy estimation through the CRS approximation

Shibo Xu and Alexey Stovas

Norwegian University of Science and Technology, Trondheim, Norway

Abstract. Multiparameter stacking is a crucial tool to get the high-quality time image of the subsurface, which can provide a basis for many important applications. We analyze the CRS approximation for a circular reflector embedded into effective anisotropic media. In this case, the CRS attributes depend on both reflector curvature and anisotropy parameters. We consider the effective anisotropic model from two anisotropic cases: elliptical isotropic and transversely isotropic with vertical symmetry axis and one vertically heterogeneous isotropic case, i.e. two layer model. By performing the sensitivity analysis, we show how the estimates depend on anisotropy parameters. We convert the CRS attributes into parameters for isotropic model and analyze these estimates behavior along the seismic line. From this behavior, we estimate both structure and anisotropy parameters.

Presented at the Workshop Meeting Active and Passive Seismic in Laterally Inhomogeneous Media (APSLIM), June, 2015, Prague, Czech Republic; Published in Journal of Geophysics and Engineering in October 2015.

2.1 Introduction

Stacking plays an important role in seismic data processing, which is treated as one of the fundamental operations in seismic data analysis (Yilmaz, 2000). The signal-to-noise ratio can be improved considerably by adopt the multiparameter stacking operator as the information of the same subsurface region are carried from the neighboring CMP gathers. A number of multiparameter stacking operators have been proposed during the last years. The common-reflection-surface (CRS) method is developed (Jäger et al, 2001) as an extension of the classical stacking operation, stacks data from multiple CMP locations. The traveltime surface of CRS method can be described by a hyperbolic approximation from a Taylor series expansion of the squared traveltime around a reference ray. By introducing the concepts of the normal (N) and normal-incident-point (NIP) waves by Hubral (1983), the series coefficients can be formulated in terms of three kinematic attributes (Jäger et al, 2001, Tygel and Santos, 2007), these attributes have a clear physical interpretation that can be used for structural interpretation, velocity model estimation for depth migration (Duveneck, 2004), and prestack seismic data interpolation (Baykulov and Gajewski, 2009). The implicit expression for the reflection traveltime on a spherical reflector derived by Taylor expansion with a fourth-order expansion is presented in (Höcht et al, 1999). The multifocusing (MF), originally developed by Gelchinsky et al (1999a,b), is a double square root based approximation parameterized with the same attributes as the CRS operator in addition to the conventional stacking velocity. The extended approach is modified by Landa et al (2010) to provide the analytical solution to the spherical reflector problem and take heterogeneity into consideration. A non-hyperbolic CRS (NCRS) approximation has been proposed to improve the accuracy at offset and midpoint coordinates with the same set of parameters (Fomel and Kazinnik, 2013). A new implicit CRS approach (i-CRS) by combining the high sensitivity to curvature of the MF with the robustness of CRS with respect to inhomogeneity on circular interface is introduced by

Schwarz et al (2014). The extend work for i-CRS by taking weak-anisotropy into account is done by Vanelle et al (2012).

In this paper, we start with the isotropic CRS approximation then take anisotropy into consideration, and evaluate the structural and anisotropic parameters in the end. We propose a new approach to investigate the effect of anisotropy and vertical heterogeneity on the P-wave CRS attributes and their inversion into the model parameters. In order to distinguish between the reflector curvature, anisotropy and heterogeneity, we consider a simple circular anisotropic and layered isotropic background models. To describe all these models in the same framework of effective anisotropic medium, we use the generalized moveout approximation (GMA) proposed by Fomel and Stovas (2010) to define the group velocity as a function of group angle. In order to simplify our method, we assume that the difference between incidence and reflection phase and group angles is negligibly small.

The comparison of CRS attributes and inverted model parameters exhibit different behaviour depending on background model. Considering the estimated model parameters $\hat{R}$ and $\hat{z}_0$ from different midpoint positions, we estimate the effective anisotropy parameters. The CRS attributes being inverted into the model parameters under the isotropic model assumption exhibit the dependence on position of the midpoint. From these dependences, we can evaluate the parameters of reflector and anisotropy parameters.

2.2 CRS approximation for a circular reflector

In order to introduce the effect of reflector curvature, we start with the simplest (circular) reflector embedded in a homogeneous isotropic medium with velocity V. In this case, the traveltime surface can be described by the parametric relations (Höcht et al, 1999). The model is shown in Figure 2.1 (left). The reflector is given by a circle with a radius R and the centre located at the $(0, z_0)$. For isotropic model, the model parameters are R, V and z_0. The source

and receiver lateral coordinates are x_s and x_r, respectively. For a given x_s and x_r, the reflection point is specified by the dip angle α and reflection angle θ (Figure 2.1, left).

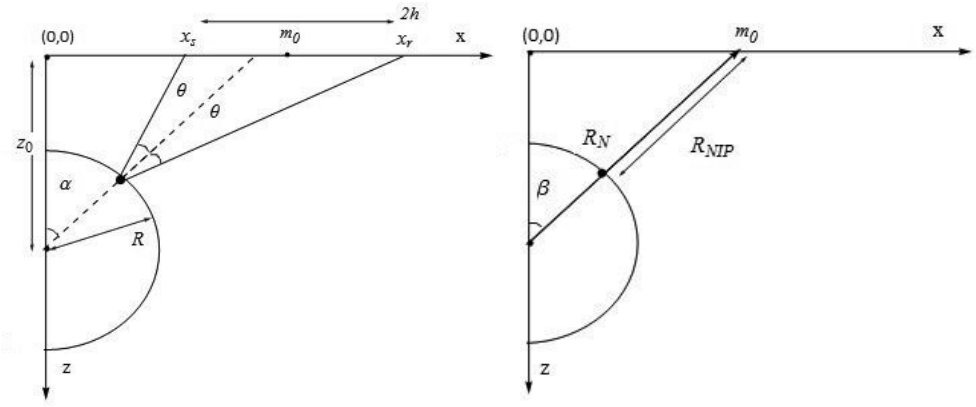

Figure 2.1. (left) is the reflection from a circular reflector in a homogeneous medium, (right) is the illustration of the three CRS attributes β, R_{NIP} and R_N, where β is the emergence angle of the reflector, R_{NIP} is the distance from the reflection point to the surface, and R_N is the distance from the centre of the reflector to the surface.

The coordinates x_s and x_r are given by the geometrical relations as

$$\begin{aligned} x_s &= R\sin\alpha + (z_0 - R\cos\alpha)\tan(\alpha-\theta), \\ x_r &= R\sin\alpha + (z_0 - R\cos\alpha)\tan(\alpha+\theta). \end{aligned} \tag{2.1}$$

The midpoint, half-offset and the reflection traveltime function can be expressed as

$$\begin{aligned} m &= \frac{x_r + x_s}{2} = R\sin\alpha + (z_0 - R\cos\alpha)\frac{\sin\alpha\cos\alpha}{\cos^2\alpha - \sin^2\theta}, \\ h &= \frac{x_r - x_s}{2} = (z_0 - R\cos\alpha)\frac{\sin\theta\cos\theta}{\cos^2\alpha - \sin^2\theta}, \end{aligned} \tag{2.2}$$

$$T = \frac{(z_0 - R\cos\alpha)}{V\cos(\alpha-\theta)} + \frac{(z_0 - R\cos\alpha)}{V\cos(\alpha+\theta)} = 2\frac{(z_0 - R\cos\alpha)}{V}\frac{\cos\alpha\cos\theta}{\cos^2\alpha - \sin^2\theta}. \tag{2.3}$$

The parametric equations (2.2)-(2.3) define the reflection traveltime surface $T(m,h)$. We select a certain midpoint position m_0 and expand the traveltime squared in series for $\Delta m = m - m_0$ and half offset h (Figure 2.2). By expanding the traveltime squared in Taylor

series for Δm and h, we obtain the second order CRS approximation in a form (Jäger et al, 2001),

$$T_{CRS}^2(\Delta m, h) = A_0 + A_1 \Delta m + A_2 \Delta m^2 + B_2 h^2. \qquad (2.4)$$

The series coefficients A_0, A_1, A_2 and B_2 are computed for a given m_0 and depend on the model parameters R, V and z_0.

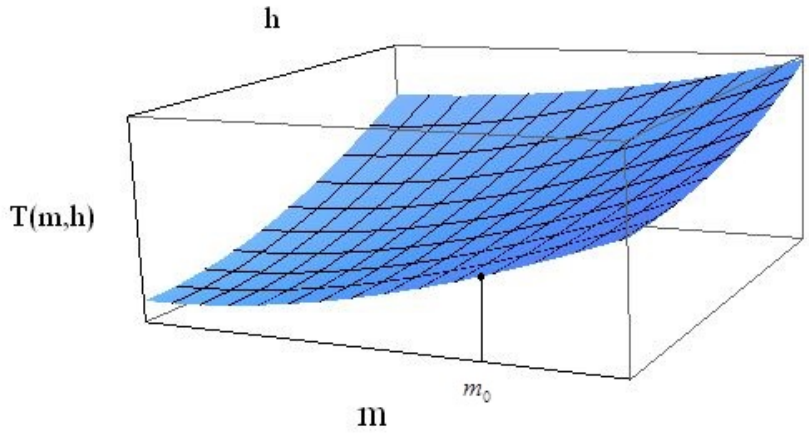

Figure 2.2. Traveltime surface $T(m,h)$ from a circular reflector and the reference point ($m = m_0$) for Taylor series expansion (equation 2.4).

2.3 Inversion of CRS attributes and estimated model parameters

The CRS operator in simulated zero-offset (ZO) section can be represented in terms of three kinematic wavefield attributes. The parameters R_{NIP} and R_N are the radius of the normal incidence and normal waves (Jäger et al, 2001) and the emergence angle is denoted by β. The meaning of the attributes is illustrated in Figure 2.1 (right). According to the concept of R_{NIP}, R_N and β, the series coefficients in equation (2.4) can be expressed through these CRS attributes.

$$A_0 = \frac{4R_{NIP}^2}{V_0^{\,2}},\ A_1 = \frac{8R_{NIP}\sin\beta}{V_0^{\,2}},\ A_2 = \frac{4(R_{NIP}\cos^2\beta + R_N\sin^2\beta)}{V_0^{\,2}R_N},\ B_2 = \frac{4\cos^2\beta}{V_0^{\,2}}. \tag{2.5}$$

The CRS attributes can be represented in terms of the model parameters for isotropic model.

$$R_{NIP} = z_0\sec\alpha_0 - R,\ R_N = z_0\sec\alpha_0,\ \beta = \alpha_0, \tag{2.6}$$

where α_0 is the incidence angle for a given m_0.

The CRS attributes can be, consequently, given in terms of A_0, A_1, A_2 and B_2.

$$\hat{R}_{NIP} = \frac{2A_0}{\sqrt{4A_0B_2 + A_1^2}},\ \hat{R}_N = \frac{8A_0^2B_2}{(4A_0A_2 - A_1^2)\sqrt{4A_0B_2 + A_1^2}},\ \sin\hat{\beta} = \frac{A_1}{\sqrt{4A_0B_2 + A_1^2}}, \tag{2.7}$$

and the isotropic model parameters can be defined as

$$\hat{R} = \frac{2A_0(A_1^2 + 4A_0B_2 - 4A_0A_2)}{(4A_0A_2 - A_1^2)\sqrt{4A_0B_2 + A_1^2}},\ \hat{V} = \sqrt{\frac{16A_0}{A_1^2 + 4A_0B_2}},\ \hat{z}_0 = \frac{16A_0^2B_2\sqrt{A_0B_2}}{(4A_0A_2 - A_1^2)(A_1^2 + 4A_0B_2)}. \tag{2.8}$$

All the expressions above are derived for isotropic case. Therefore, in case of isotropic model, the equations (2.8) result in exact values for the R, V and z_0.

2.4 Application of the CRS method for effective anisotropic models

In order to compute the CRS attributes for a circular reflector embedded into effective anisotropic medium, we use the GMA approximation (Fomel and Stovas, 2010) to define the group velocity as a function of group angle. This velocity can lately be used in equation (2.3) replacing the constant velocity V.

$$\frac{1}{V(\phi)^2} = \frac{\cos^2\phi}{V_0^2} + \frac{\sin^2\phi}{V_N^2} + \frac{A\sin^2\phi\tan^2\phi}{V_N^4\left(\frac{1}{V_0^2} + \frac{B\tan^2\phi}{V_N^2} + \sqrt{\frac{1}{V_0^4} + \frac{2B\tan^2\phi}{V_0^2V_N^2} + \frac{C\tan^4\phi}{V_N^4}}\right)}, \tag{2.9}$$

where V_0 is the vertical velocity, V_N is the NMO velocity, the parameters A, B and C are model dependent, and ϕ is the ray propagation angle. The CRS operators related with anisotropy can be obtained by adopting the GMA velocity in anisotropic media.

If the model above the reflector shown in Figure 2.1 (left) is anisotropic, the group velocities for incoming ray and outcoming ray are different, and the incidence and reflection phase (or group) angles are also different due to the Snell's law. We show that the difference between the incidence and reflection group angles is negligibly small see Appendix A, and the geometrical equations (2.1) and (2.2) are still valid for further computation.

Therefore, by adopting the group velocity equation from equation (2.9), the traveltime equation (2.3) takes the form

$$T = \frac{(z_0 - R\cos\alpha)}{\cos(\alpha-\theta)}\frac{1}{V(\alpha-\theta)} + \frac{(z_0 - R\cos\alpha)}{\cos(\alpha+\theta)}\frac{1}{V(\alpha+\theta)}. \tag{2.10}$$

Equation (2.10) with velocity defined in equation (2.9) is more complicated comparing with equation (2.3) defined for isotropic model. When using equation (2.9), we have additional parameters (V_N, A, B, C) that affect the solution. In order to compute the CRS series coefficients A_0, A_1, A_2 and B_2 for effective anisotropic case in equation (2.4), we use equations (2.9)-(2.10). We adopt new traveltime equation (2.10) using the anisotropic group velocity defined by GMA equation (2.9) with the same geometry form given in equation (2.2). The new CRS attributes are obtained by equating the coefficients with equation (2.4).

We introduce three velocity models: elliptical isotropic (EI) case with Thomsen parameters $\delta = \varepsilon$ (Thomsen, 1986), transversely isotropic case with vertical symmetry axis (VTI) and two-layer isotropic model (2LI).

For the EI case, by setting $A = 0$, the group velocity equation (2.9) takes the form

$$\frac{1}{V^2(\phi)} = \frac{\cos(\phi)^2}{V_0^2} + \frac{\sin(\phi)^2}{V_N^2}. \tag{2.11}$$

For the VTI case, the parameters A, B and C in equation (2.9) given in terms of anelliptic parameter $\eta = (\varepsilon - \delta)/(1+2\delta)$ (Alkhalifah, 1998) take the form (Fomel and Stovas, 2010)

$$A = -4\eta, \quad B = \frac{1+8\eta+8\eta^2}{1+2\eta}, \quad C = \frac{1}{(1+2\eta)^2}. \tag{2.12}$$

For the 2LI case, we introduce two layers with velocities V_1 and V_2. The first layer is specified from the surface to the top of circular reflector. The second layer is beneath the first one (Figure 2.3, top). The kinematical properties of this model depend on the depth for reflection point. Therefore, for each reflection point, we define the parameters V_0, V_N, A, B and C. It means that the velocity model given in equation (2.9) will be different for different reflection point (Figure 2.3, bottom).

For 2LI model, the GMA parameters take the form (see Appendix B for details):

$$\begin{aligned}
V_0 &= V_1 \frac{1+\lambda}{1+\frac{\lambda}{\gamma}}, \\
V_N &= V_1 \sqrt{\frac{1+\lambda\gamma}{1+\frac{\lambda}{\gamma}}}, \\
A &= -\frac{\lambda(\gamma^2-1)^2}{2\gamma(1+\lambda\gamma)^2}, \\
B &= \frac{(\gamma^2-1)(1+\frac{\lambda}{\gamma})}{2(1+\lambda\gamma)^2}, \\
C &= 0.
\end{aligned} \tag{2.13}$$

The parameters λ and γ are defined by the ratios, $\lambda = \frac{z_2}{z_1}$, $\gamma = \frac{V_2}{V_1}$, and the parameter λ is related to the model parameters as

$$\lambda = \frac{R(1-\cos\alpha)}{z_0 - R}, \tag{2.14}$$

which is controlled by the midpoint position m_0. If the medium is not a homogeneous isotropic one, equations (2.8) and (2.7) result in estimates represented by hats that are dependent on the position m_0, where the series coefficients A_0, A_1, A_2 and B_2 are computed. To illustrate the different velocity models introduced above, we show the group velocity from EI, VTI and two 2LI models. In Figure 2.4, the group velocities are shown as the function of group angle. The velocity model parameters are $R = 1\,\text{km}$, $z_0 = 2\,\text{km}$, $V_0 = 2\,\text{km/s}$, $V_N = V_0\sqrt{1+2\delta}$, $\delta = 0.1$, $\eta = 0.2$. For 2LI model, we select $V_1 = 2\,\text{km/s}$, $V_2 = 2.5\,\text{km/s}$ and two m_0 positions: $m_0 = 2\,\text{km}$ and $m_0 = 4\,\text{km}$, that give $\lambda_1 \approx 0.29$, $\lambda_2 \approx 0.55$ and $\gamma = 1.25$.One can see that the 2LI models result in significantly different behaviour of the group velocity.

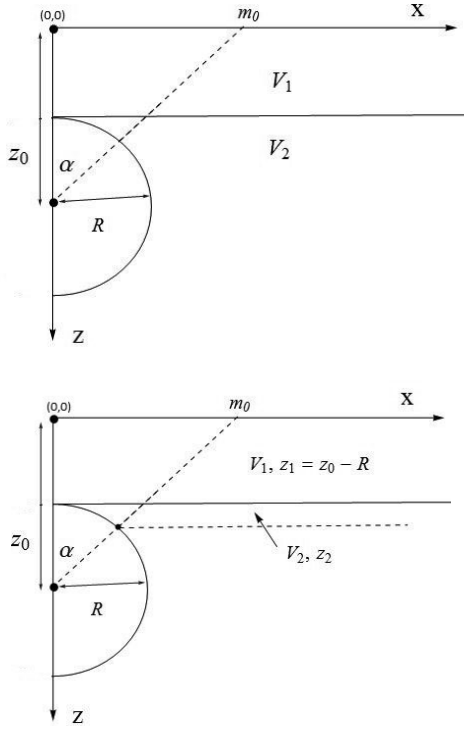

Figure 2.3. Reflector in the layered isotropic medium (top) and two effective layers (bottom).

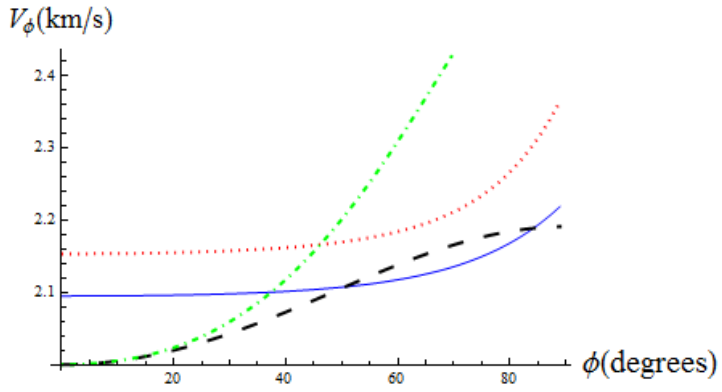

Figure 2.4. The plot of GMA group velocity of different models versus group angle ϕ. The 2LI ($m_0 = 2$), 2LI ($m_0 = 4$), EI and VTI cases are shown by solid, dotted, dashed and dot-dashed lines, respectively.

2.5 Influence of effective anisotropy

In order to test our approach and investigate the effect of the anisotropy and inhomogeneity on the CRS attributes and estimated model parameters, we select the circular reflector with parameters $R = 1\,\text{km}$, $z_0 = 2\,\text{km}$ and four velocity models. The first velocity model is isotropic (ISO) with velocity $V_0 = 2\,\text{km/s}$. The EI model has two parameters $V_0 = 2\,\text{km/s}$ and $\delta = 0.1$, the VTI model has the same parameters as EI model plus anisotropy parameter $\eta = 0.2$ and the parameters for 2LI model are $V_1 = 2\,\text{km/s}$ and $V_2 = 2.5\,\text{km/s}$.

First, we compute the coefficients A_0, A_1, A_2 & B_2 for all the models mentioned above. Then, we compute the CRS attributes (equation (2.7)) and the "isotropic" model parameters (equation (2.8)). As stacking is not considered in this paper, the analytical expressions of CRS coefficients A_0, A_1, A_2 and B_2 in effective anisotropic media are not computed here.

In Figure 2.5, we show the series coefficients A_0, A_1, A_2 and B_2 from equations (2.5) plotted versus m_0 for all the models mentioned above (note that $m_0 = 0$ is the circle centre position). The tendency of coefficients A_0 and A_1 are similar for all the models, but the behaviour of

coefficients A_2 and B_2 for VTI model is quite different. For all m_0, the largest and the smallest values for series coefficients are obtained from ISO and VTI models, respectively. The corresponding CRS attributes computed from equations (2.7) are plotted versus m_0 in Figure 2.6. The tendency for ISO and EI case is very similar for all attributes, while, the VTI and 2LI model result in different attributes behaviour.

The CRS attributes obtained from all the models are converted into the isotropic model parameters by using equations (2.8). The results are shown in Figure 2.7. One can see that the inversion from isotropic model produces the estimates that equal to model parameters and do not depend on m_0. All other models result in estimates that depend on m_0. From the plots in Figure 2.7, we can see the estimated reflector radius, in the presence of anisotropy, is underestimated above the circle and overestimated when the midpoint is far away from lateral position of the circle centre. In our computation, we use the limit $m_0 \to \infty$. However, in practice, one can use the value when estimate exhibits asymptotic behaviour. $\hat{z}_0$ is slightly underestimated for small midpoint and overestimated for large m_0. For 2LI model, $\hat{R}$ and $\hat{z}_0$ are overestimated for all m_0. The estimated velocity is larger than the model velocity for all the models.

We also reconstruct the reflection surface by computing the position for each reflection point, $\hat{x} = m_0 - \hat{R}_{NIP} \sin\hat{\beta}$ and $\hat{z} = \hat{R}_{NIP} \cos\hat{\beta}$. The shape of the surface obtained from the estimates computed from the different models is shown in Figure 2.8. To reconstruct all these surfaces, we use the range of $m_0 \in (0,\ 5\,km)$. The most dramatic difference in the shape of reflector comparing with the circle is obtained for the VTI case. The EI model results in a shape that is very similar to the circle with another radius. The 2LI model gives the shape which is very similar to the circle but slightly deviates for larger emergence angles.

The diffraction plays an important role in seismic processing and interpretation. In order to investigate the effect of diffraction in our approach, we set $R = 0$ (point diffractor) and perform similar analysis as above (see Appendix C).

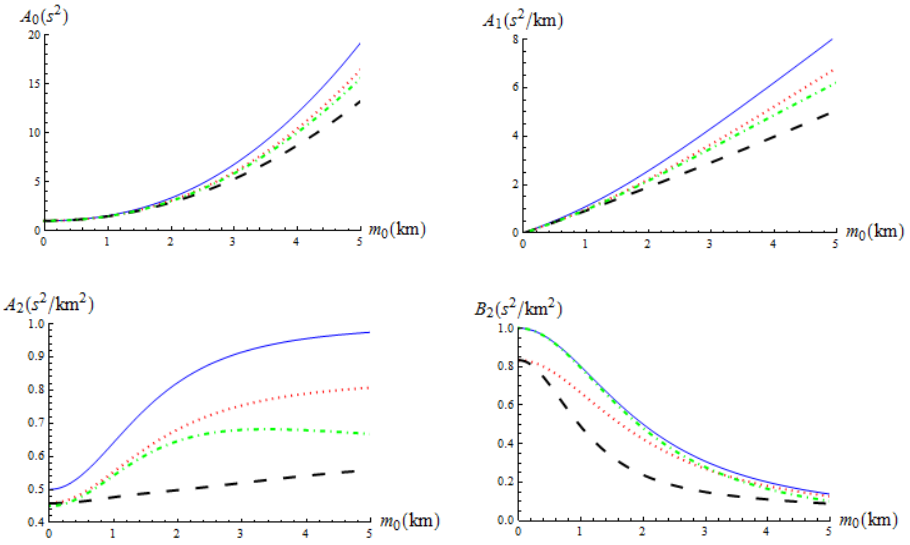

Figure 2.5. The series coefficients in equations (2.4) plotted versus m_0. The ISO, EI, VTI and 2LI cases are shown by solid, dotted, dashed and dot-dashed lines, respectively.

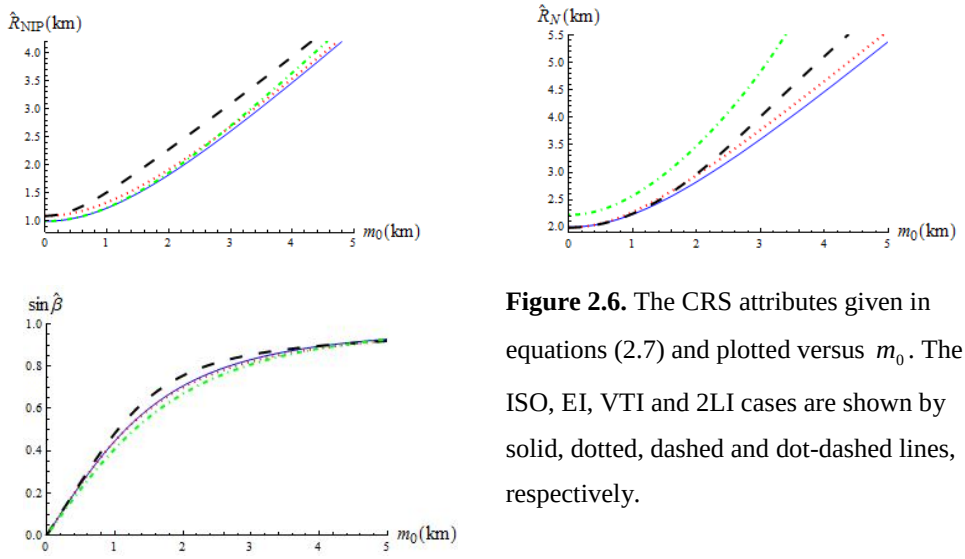

Figure 2.6. The CRS attributes given in equations (2.7) and plotted versus m_0. The ISO, EI, VTI and 2LI cases are shown by solid, dotted, dashed and dot-dashed lines, respectively.

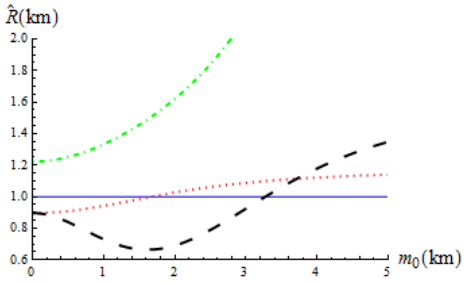

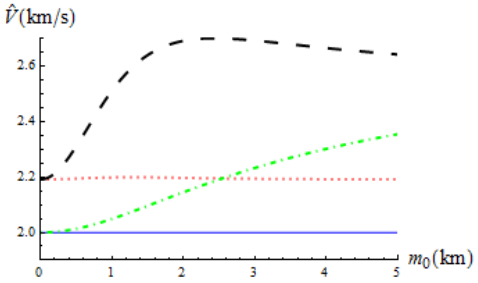

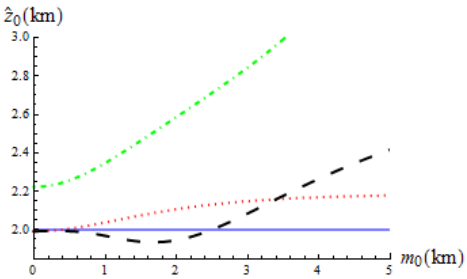

Figure 2.7. The estimates in isotropic model parameters in equations (2.8) plotted versus m_0. The ISO, EI, VTI and 2LI cases are shown by solid, dotted, dashed and dot-dashed lines, respectively.

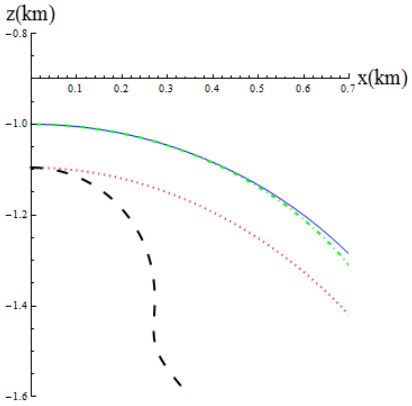

Figure 2.8. The reconstructed shape of reflector based on estimations of $\hat{R}_{NIP}(m_0)$ and $\sin\hat{\beta}(m_0)$ for different models. The ISO, EI, VTI and 2LI cases are shown by solid, dotted, dashed and dot-dashed lines, respectively.

2.6 Curvature and anisotropy estimation

For a VTI model, we can linearize the CRS attributes and estimated model parameters in terms of anisotropy parameters δ and η. These results are shown in Appendix D.

The behaviour of estimated parameters $\hat{R}$, $\hat{V}$ and $\hat{z}_0$ is controlled by anisotropy parameters δ and η. Shown in Figure 2.9, the estimated radius and depth for EI and VTI model approach to an asymptotic value when m_0 goes to infinity. When m_0 equals zero, these values are the same since the anelliptic parameter η does not affect the vertical wave propagation. It allows us to estimate $\hat{R}$ and $\hat{z}_0$ along with the anisotropy parameters.

The results of $\hat{R}$ and $\hat{z}_0$ in zero and infinite limit are specified by $\hat{R}^{(0)} = \hat{R}(m_0 = 0)$, $\hat{R}^{(\infty)} = \hat{R}(m_0 \to \infty)$, $\hat{z}_0^{(0)} = \hat{z}_0(m_0 = 0)$ and $\hat{z}_0^{(\infty)} = \hat{z}_0(m_0 \to \infty)$.

For EI model, in the weak-anisotropy approximation (small δ), the estimated $\hat{R}$ is varying from $R(1-\delta)$ at m_0=0 to $R(1+2\delta)$ at $m_0 \to \infty$. Therefore, the anisotropy parameter δ and radius R can be evaluated from the variation of $\hat{R}$ with m_0. The expressions of $\hat{R}^{(0)}$ and $\hat{R}^{(\infty)}$ are given by

$$\hat{R}^{(0)} = \lim_{m_0 \to 0} \hat{R} = R\left(\frac{z_0 + 2R\delta - 2z_0\delta}{z_0 + 2R\delta}\right)\sqrt{1+2\delta} \approx R(1-\delta), \tag{2.15}$$

$$\hat{R}^{(\infty)} = \lim_{m_0 \to \infty} \hat{R} = R\frac{1+4\delta}{1+2\delta} \approx R(1+2\delta). \tag{2.16}$$

The estimation for curvature and anisotropy parameter can be obtained from the inversion of equation (2.15) and (2.16).

$$\tilde{R} = \frac{2\hat{R}^{(0)} + \hat{R}^{(\infty)}}{3}, \quad \tilde{\delta} = \frac{\hat{R}^{(\infty)} - \hat{R}^{(0)}}{2\hat{R}^{(0)} + \hat{R}^{(\infty)}}. \tag{2.17}$$

For VTI case, the results of $\hat{R}$ and $\hat{z}_0$ in zero and infinite limit are given as follows

$$\hat{R}^{(0)} = \lim_{m_0 \to 0} \hat{R} = R(\frac{z_0 + 2R\delta - 2z_0\delta}{z_0 + 2R\delta})\sqrt{1+2\delta} \approx R(1-\delta), \tag{2.18}$$

$$\hat{R}^{(\infty)} = \lim_{m_0 \to \infty} \hat{R} = R(2 - \frac{1}{(1+2\delta)(1+2\eta)^2}) \approx R(1+2\delta+4\eta), \tag{2.19}$$

$$\hat{z}_0^{(0)} = \lim_{m_0 \to 0} \hat{z}_0 = \frac{z_0^2\sqrt{1+2\delta}}{z_0 + 2R\delta} \approx z_0(1+\delta) - 2R\delta, \tag{2.20}$$

$$\hat{z}_0^{(\infty)} = \lim_{m_0 \to \infty} \hat{z}_0 = z_0\sqrt{1+2\delta}(1+2\eta) \approx z_0(1+\delta+2\eta). \tag{2.21}$$

The anisotropy parameters δ, η, radius, and depth can be inversed from equation (2.18) to (2.21).

For the real data, we do not have measurements taken at infinite midpoint position. Instead of it, we are going to use the data from $m_0 = 5\,\text{km}$. From the estimates, we obtained from a VTI model, $\hat{R}^{(0)} = 0.896\,\text{km}$, $\hat{R}^{(\infty)} = 1.348\,\text{km}$, $\hat{z}_0^{(0)} = 1.992\,\text{km}$ and $\hat{z}_0^{(\infty)} = 2.417\,\text{km}$. Using these estimates in equations (2.18)-(2.21) results in $R = 0.941\,\text{km}$, $z_0 = 1.987\,\text{km}$, $\delta = 0.048$ and $\eta = 0.084$ (see comparison in Table 2.1). The circular reflector parameters are estimated very well, but the anisotropy parameters are underestimated. The reason for that is the original anisotropy parameters are very large for using weak-anisotropy approximation equations (2.18)-(2.21). For real data, one can use the optimization searching for the CRS attributes by fitting the operators, then using this inversion method to estimate geophysical information (curvature, depth and anisotropy parameters).

	R (km)	z_0 (km)	δ	η
VTI model parameters	1.0	2.0	0.1	0.2
Estimates	0.941	1.987	0.048	0.084

Table 2.1. The comparison of structural and anisotropy parameters made between VTI model parameters and the estimates.

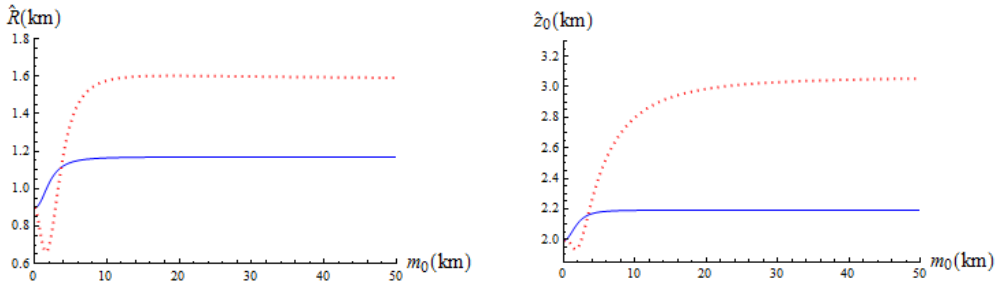

Figure 2.9. The plot of the estimated radius (left) and depth for the centre of a circular reflector (right) plotted versus m_0. The EI and VTI cases are shown by solid, dotted lines, respectively.

2.7 Conclusions

Based on the CRS approximation, we propose a new method to evaluate the anisotropy parameters and the circular reflector parameters from the behaviour of estimates with the midpoint position m_0 for a circular reflector. We consider two anisotropic models and a two layered isotropic model, which we treat in the same framework of effective anisotropic media by using the GMA for group velocity.

In the presence of anisotropy, the estimated reflector curvature is overestimated from the midpoints just above the circle and underestimated when midpoints are far away from the circle. The estimated depth for the centre of the circular reflector is underestimated above the reflector and overestimated for far away midpoints. Both of the estimated depth and radius are overestimated for 2LI model. By analysing the variations in estimated model parameters computed for anisotropic media versus midpoint positon, we can evaluate both structural and anisotropic parameters. Despite of we do not know the lateral position of the circular object, we can estimate and plot the estimated attributes (computed in vicinity of each m_0) as a function of m_0. From these functions, the lateral position of the object can be clearly seen.

2.8 Acknowledgements

We would like to acknowledge the ROSE project and the China Scholarship Council (CSC) for financial support.

2.9 Appendix A. Incidence and reflection group angle

In the case of a circular reflector in a homogeneous anisotropic velocity model (Figure 2.10), the velocity varies with the wave propagation direction. For EI case ($\delta = \varepsilon$), the phase velocity for P-wave is given by (Alkhalifah and Tsvankin, 1995)

$$V_P(\theta) = V_{P0}\sqrt{1+2\delta\sin^2\theta}, \tag{2.A.1}$$

where V_{P0} is the vertical velocity, θ is the phase angle, δ is the Thomsen (1986) anisotropy parameter. The expression for group velocity is

$$\frac{1}{V_P^2(\phi)} = \frac{\cos^2\phi}{V_{P0}^2} + \frac{\sin^2\phi}{V_N^2}, \tag{2.A.2}$$

ϕ is the ray/group angle, V_N is the NMO velocity being $V_N = V_{P0}\sqrt{1+2\delta}$.

The Snell's law is derived from the plane wave propagation and valid in the phase domain. The form for Snell's law is the following,

$$\frac{\sin\theta_1}{\sin\theta_2} = \frac{V_P(\theta_1)}{V_P(\theta_2)}, \tag{2.A.3}$$

with θ_1 and θ_2 being the incidence and reflection phase angle.

The relation for incidence and reflection group angle in EI model can be obtained after a tedious computation from equation (2.A.1) - (2.A.3) and takes the form

$$\tan\phi_2 = \frac{\tan\phi_1(1+2\delta)(\delta\cos 2\alpha - \delta - 1)}{2\delta^2\cos 2\alpha + 2\tan\phi_1\delta\sin 2\alpha + \delta\cos 2\alpha - 2\delta^2 - 3\delta - 1}, \qquad (2.A.4)$$

where ϕ_1 is the incidence group angle, ϕ_2 is the reflection group angle, α is the dip angle.

From equation (2.A.4), one can see that the behaviour of difference group angle $\Delta\phi$ is controlled by ϕ_1, α and δ.

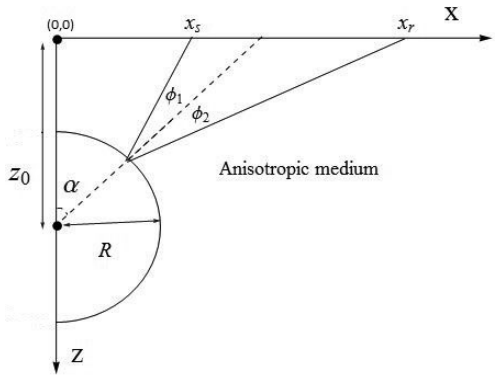

Figure 2.10. The reflection from a circular reflector in a homogeneous anisotropic medium.

The difference between reflection and incidence group angles $\Delta\phi = \phi_2 - \phi_1$ is shown versus incidence group angle ϕ_1 and reflector dip angle α in Figure 2.11 for δ=0.1 (top) and δ=0.2 (bottom). One can see that for moderate incidence angles, the difference is small, and we neglect that in our derivations.

2.10 Appendix B. CRS approximation in 2LI model

In order to analyse the effect of heterogeneity, we introduce a two layer model, with the first layer being adjusted to the top of circular reflector (Figure 2.3, top). We introduce an effective artificial layer with the thickness from the reflection point to the top of the circular reflector. The offset and moveout of 2LI model can be represented in terms of horizontal slowness,

$$x(p) = \frac{2z_1 pV_1}{\sqrt{1-p^2V_1^2}} + \frac{2z_2 pV_2}{\sqrt{1-p^2V_2^2}}, \tag{2.B.1}$$

$$t(p) = \frac{2z_1}{V_1\sqrt{1-p^2V_1^2}} + \frac{2z_2}{V_2\sqrt{1-p^2V_2^2}}. \tag{2.B.2}$$

From equations (2.B.1) and (2.B.2), we can compute all the parameters of GMA approximation in equation (2.9).

If is convenient to express the GMA parameters in terms of the thickness and velocity ratios for $\lambda = \frac{z_2}{z_1}$ and $\gamma = \frac{V_2}{V_1}$ as follows

$$V_0 = V_1\frac{1+\lambda}{1+\frac{\lambda}{\gamma}},\ V_N = V_1\sqrt{\frac{1+\lambda\gamma}{1+\frac{\lambda}{\gamma}}},\ A = -\frac{\lambda(\gamma^2-1)^2}{2\gamma(1+\lambda\gamma)^2}. \tag{2.B.3}$$

The other parameters are defined from a horizontal ray in layer one. It gives

$$B = \frac{t_0^2(1-V_N^2p_\infty^2)}{t_0^2-T_\infty^2} - \frac{A}{1-V_N^2p_\infty^2} = \frac{(\gamma^2-1)(1+\frac{\lambda}{\gamma})}{2(1+\lambda\gamma)^2},$$
$$C = (\frac{t_0^2(1-V_N^2p_\infty^2)}{t_0^2-T_\infty^2})^2 = 0. \tag{2.B.4}$$

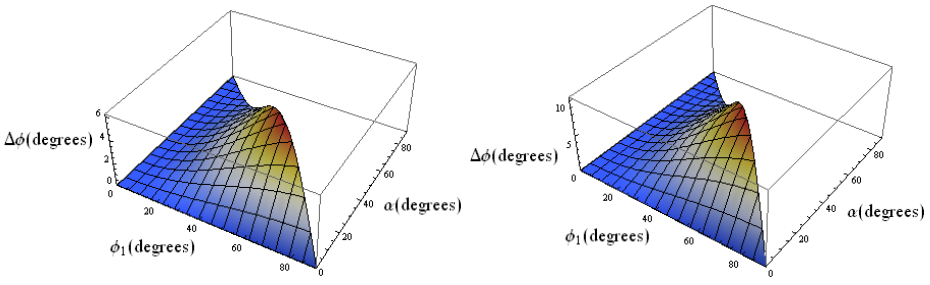

Figure 2.11. The difference between reflection and incidence group angle in EI model plotted versus ϕ_1 and α ($\delta = 0.1$ top, $\delta = 0.2$ bottom), $\phi_1 + \alpha \le \frac{\pi}{2}$.

2.11 Appendix C. Diffraction case

The diffraction case can be considered as a special case of the circular reflector by setting $R = 0$ (Figure 2.12). In terms of CRS attributes, it gives $R_N = R_{NIP}$.

By setting $R = 0$ in equation (2.2) and (2.3), we obtain the double square root (DSR) equation,

$$T = \frac{1}{V}\sqrt{z_0^2 + (m+h)^2} + \sqrt{z_0^2 + (m-h)^2}. \qquad (2.C.1)$$

If the point diffractor is embedded into anisotropic model, the equation (C.1) becomes

$$T = \frac{\sqrt{z_0^2 + (m-h)^2}}{V_1} + \frac{\sqrt{z_0^2 + (m+h)^2}}{V_2}, \qquad (2.C.2)$$

$V_1 = V(\phi = \tan^{-1}(\frac{m_0 - h}{z_0}))$ and $V_2 = V(\phi = \tan^{-1}(\frac{m_0 + h}{z_0}))$, where $V(\phi)$ is defined in equation (2.9).

When applying the inversion equation (2.8) for anisotropic velocity models, we observe that $\hat{R} = 0$ regardless to anisotropic parameters. It means that the presence of anisotropy does not result in smearing of the point diffractor.

The CRS attributes computed from equation (2.C.2) are shown in Figure 2.13. The plot for $\sin\hat{\beta}$ is very similar for all three cases. The estimated $\hat{R}_N$ ($\hat{R}_{NIP}$) in VTI case is larger than the one estimated from other cases.

In Figure 2.14, we show the estimated model parameters $\hat{V}$ and $\hat{z}_0$ for the point diffractor plotted versus m_0. The value for estimated velocity and depth in EI case does not depend on m_0. For a VTI case, the estimated velocity and depth exhibit strong variation with m_0.

The estimated $\hat{z}_0$ for point diffractor in a VTI model is varying from $z_0\sqrt{1+2\delta}$ at $m_0 = 0$ to $z_0\sqrt{1+2\delta}(1+2\eta)$ at $m_0 \to \infty$. This variation can be used as an indicator for anelliptic parameter η.

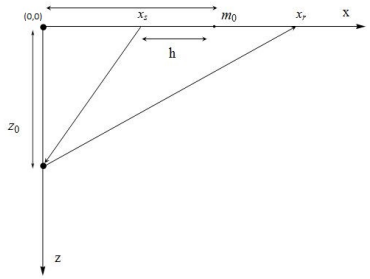

Figure 2.12. The point diffractor in a homogeneous medium.

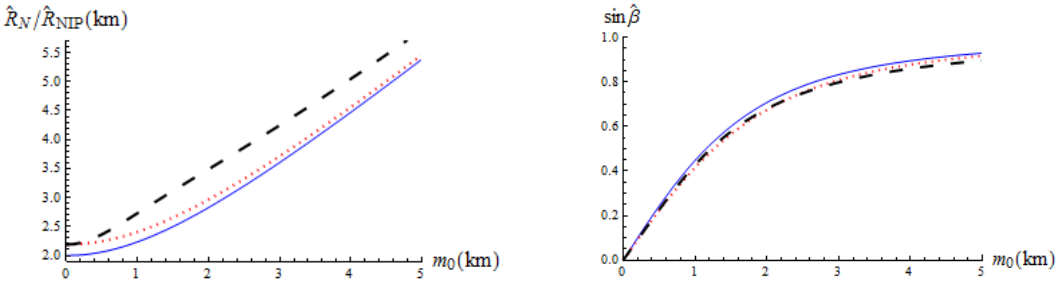

Figure 2.13. The CRS attributes for a point diffractor plotted versus m_0. The ISO, EI and VTI cases are shown by solid, dotted and dashed lines, respectively.

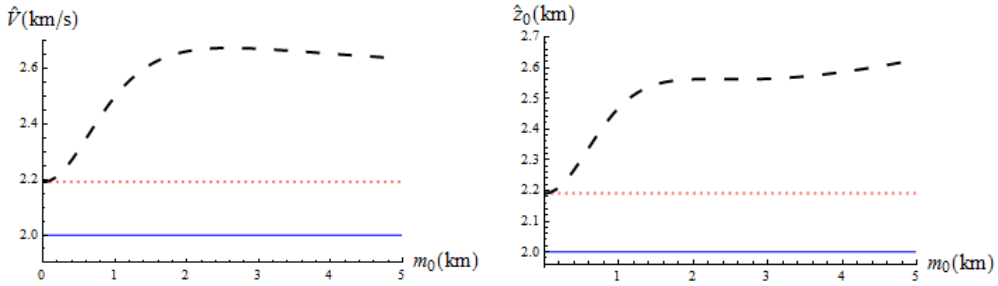

Figure 2.14. The estimated model parameters for a point diffractor plotted versus m_0. The ISO, EI and VTI cases are shown by solid, dotted and dashed lines, respectively.

2.12 Appendix D. Sensitivity analysis

In the case of a circular reflector embedded into anisotropic velocity model, the CRS attributes and estimated model parameters depend on anisotropy parameters.

In order to perform the sensitivity analysis, we linearize $\hat{R}_{NIP}$, $\hat{R}_N$, $\sin\hat{\beta}$ and $\hat{R}$, $\hat{V}$, $\hat{z}_0$ in terms of anisotropy parameters δ and η.

The expressions for the CRS attributes take the form,

$$\hat{R}_{NIP} = (\sqrt{m_0^2 + z_0^2} - R)(1 + \frac{z_0^2}{m_0^2 + z_0^2}\delta + \frac{2m_0^2 z_0^2 (m_0^2 + 3z_0^2)}{(m_0^2 + z_0^2)^3}\eta), \tag{2.D.1}$$

$$\hat{R}_N = \sqrt{m_0^2 + z_0^2}(1 + \frac{z_0^2(\sqrt{m_0^2 + z_0^2} - 2R) + 2m_0^2 R}{(m_0^2 + z_0^2)^{3/2}}\delta + \frac{6m_0^2 z_0^2 (z_0^2 - 2R\sqrt{m_0^2 + z_0^2}) + 2m_0^4 (z_0^2 + 2R\sqrt{m_0^2 + z_0^2})}{(m_0^2 + z_0^2)^3}\eta), \tag{2.D.2}$$

$$\sin\hat{\beta} = \frac{m_0}{\sqrt{m_0^2 + z_0^2}}(1 - \frac{z_0^2(\sqrt{m_0^2 + z_0^2} - 2R)}{(m_0^2 + z_0^2)^{3/2}}\delta + \frac{2m_0^2 z_0^2 (z_0^2 - m_0^2 + 2R\sqrt{m_0^2 + z_0^2})}{(m_0^2 + z_0^2)^3}\eta). \tag{2.D.3}$$

For estimated model parameters, the analytical expressions are given in the form

$$\hat{R} = R(1 + \frac{2m_0^2 - z_0^2}{m_0^2 + z_0^2}\delta + \frac{2m_0^2 (2m_0^4 - 3m_0^2 z_0^2 - 3z_0^4)}{(m_0^2 + z_0^2)^3}\eta), \tag{2.D.4}$$

$$\hat{V} = V_0(1 + \delta + \frac{m_0^2 (m_0^4 + 3m_0^2 z_0^2 + 6z_0^4)}{(m_0^2 + z_0^2)^3}\eta), \tag{2.D.5}$$

$$\hat{z}_0 = z_0(1 + \frac{(m_0^2 + z_0^2)^2 - 2z_0^2 R\sqrt{m_0^2 + z_0^2}}{(m_0^2 + z_0^2)^2}\delta + \frac{2m_0^2 (m_0^4 + 3z_0^4 - 6Rz_0^2\sqrt{m_0^2 + z_0^2})}{(m_0^2 + z_0^2)^3}\eta). \tag{2.D.6}$$

The sensitivity coefficients for anisotropy parameters δ and η computed for the CRS attributes and estimated model parameters are plotted versus m_0 in Figure 2.15 and 2.16, respectively.

From Figure 2.15, we can see that the effect of parameter δ is predominant over the effect of parameter η for $\hat{R}_{NIP}$ and $\hat{R}_N$ when m_0 is small (the lateral CMP position is closed to position of the centre of a circular reflector). The presence of anisotropy results in overestimating of CRS parameters $\hat{R}_{NIP}$ and $\hat{R}_N$. The parameter δ results in underestimation of $\sin\hat{\beta}$ for moderate values of m_0.

From Figure 2.16, we can see that for small m_0, $\hat{R}$ is underestimated due to presence of anisotropy, while $\hat{V}$ is overestimated. The contribution of parameter δ into $\hat{V}$ does not depend on m_0 see equation (2.D.5). For large m_0, the presence of anisotropy results in overestimation of $\hat{z}_0$. For all estimations, the effect of anellipticity parameter η is very small for small value of m_0.

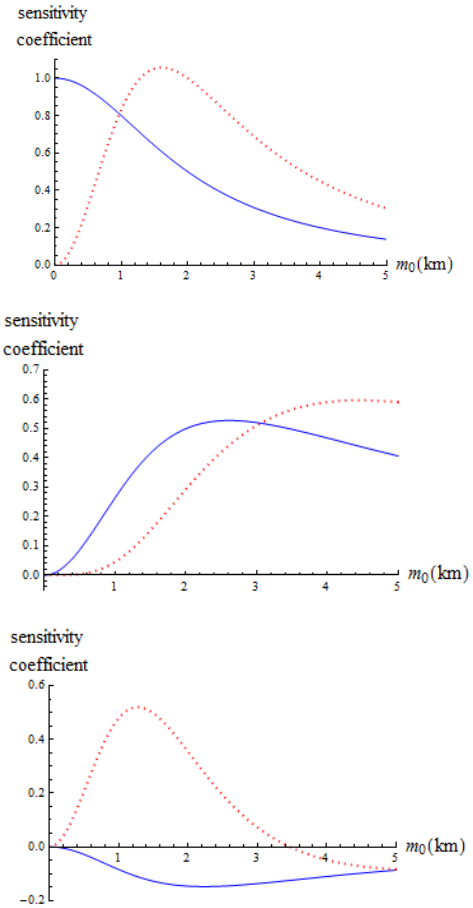

Figure 2.15. The sensitivity coefficients for anisotropy parameters δ and η, shown by solid, dotted lines, respectively, and plotted versus m_0. The corresponding CRS attributes are $\hat{R}_{NIP}$ (top), $\hat{R}_N$ (middle) and $\sin\hat{\beta}$ (bottom).

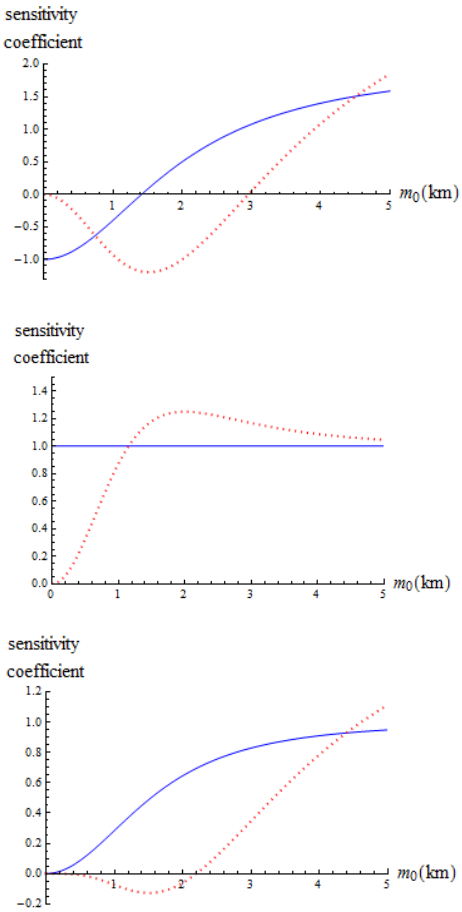

Figure 2.16. The sensitivity coefficients for anisotropy parameters δ and η, shown by solid, dotted lines, respectively, and plotted versus m_0. The corresponding estimates for isotropic model parameters are $\hat{R}$ (top), $\hat{V}$ (middle) and $\hat{z}_0$ (bottom).

Chapter 3 Estimation of the anisotropy parameters from imaging moveout of diving wave in a factorized VTI medium

Shibo Xu[1], Alexey Stovas[1] and Tariq Alkhalifah[2]

[1]Norwegian University of Science and Technology, Trondheim, Norway

[2]King Abdullah University of Science and Technology, Thuwal, Saudi Arabia.

Abstract. The importance of diving waves is being realized since they provide long wavelength model information, which can be utilized to help invert for the reflection information in full waveform inversion (FWI). The factorized model is defined here as a combination of vertical heterogeneity and constant anisotropy and it admits closed form description of the traveltime. We use these resulting analytical formulas to describe the behavior of diving waves in a factorized anisotropic medium and utilize an approximate imaging moveout formulation (residual moveout after imaging) to update the velocity model when the wrong model parameters (isotropic assumption) are used for imaging. We then use these analytical representations of the image moveout to establish a semblance analysis framework to search for the optimal anisotropic parameters. We also discuss different parameterizations of the factorized medium to find the one that gives the best accuracy in anisotropy parameters estimation.

Presented at the 78th EAGE Conference and Exhibition, June, 2016, Vienna, Austria; Published in Geophysics in July 2016.

3.1 Introduction

Recently, direct arrivals and specifically diving waves are experiencing a new lease on life as they can work as one of the major sources of the information for the long wavelength component of the velocity model (Virieux and Operto, 2009). These inverted models, which are based on diving waves, can provide an initial velocity model that is sufficiently close to the true model within the full waveform inversion (FWI) requirements. In a general FWI, we update the velocity model by using the information from both reflected and diving waves. Recently, many have suggested that we focus initially on the diving (transmission) waves and try to isolate them (Tang et al, 2013) since they provide long wavelength update for updating the velocity model (Sirgue and Pratt, 2004). A sensitivity analysis to assess the contribution of refracted, reflected and diving waves for the reconstructed velocity perturbation is studied by Kazei et al (2013). The moveout behavior and the focusing of the imaging process for reflected waves have been studied for years, and we have obtained considerable analytical insights of such behavior. Compared with the reflected waves, the imaging of diving waves has lagged behind and studies in this matter are rare. With the emergence of FWI, the importance of diving waves is now being realized. In fact, the acquisition of large offsets capable of acquiring diving waves is becoming highly desirable because they penetrate at large depths. One of the earliest analysis of the diving waves acquisition and traveltime can be found in Levin (1996). An approach to measure the defocusing in imaging of diving waves in the subsurface due to velocity errors was analyzed by Shen (2013). In this paper, the update kernel is essentially similar to that experienced for FWI of diving waves. Therefore, this defocusing (residual image moveout) can be utilized to update the velocity model. Stovas and Alkhalifah (2014) proposed to use analytical approximations of image moveout of diving waves in a constant-gradient isotropic velocity model to gain better understanding of the role of diving waves and the update of the velocity model from the defocusing in imaging. We

extend this approach to factorized anisotropic models. The factorized model, assuming vertical heterogeneity and a constant anisotropy parameters, is useful in seismic data processing and modeling (Alkhalifah, 1995, Sarkar and Tsvankin, 2003). Ray-tracing problem in factorized models with elliptic anisotropy is discussed extensively in Rogister and Slawinski (2005). The equations for offset, traveltime and relative geometrical spreading for an analytically described factorized model that combines vertical inhomogeneity with a constant transversely isotropic model with vertical symmetry axis (VTI) are derived by Stovas (2010). In this paper, we develop such formulas for diving waves in a factorized VTI medium and analyze their behavior. We define the imaging moveout formulation resulting from using the wrong velocity (isotropic assumption). The explicit equations for imaging moveout are obtained by considering various approximations. We test the accuracy of these approximations for different values of velocity gradients. Synthetic seismic data are used to illustrate this approach. We evaluate the anisotropy parameters by semblance analysis of the depth migrated data. The parameterization is very important for multi-parameter FWI (Alkhalifah and Plessix, 2014). Finally, we discuss the estimation results by adopting different parameterizations.

3.2 Diving waves in a factorized VTI medium

The factorized model (Stovas 2010, Sarkar and Tsvankin, 2003) involves both anisotropy and vertical heterogeneity. In our case, the factorized medium is defined as a transversely isotropic model with a vertical symmetry axis (VTI) under the acoustic approximation (Alkhalifah, 1998). The vertical P-wave velocity is linearly changing with depth while the anisotropy parameters (Thomsen, 1986) remain constant. The vertical velocity in this factorized model is given by

$$V_z = V_0 + Gz, \tag{3.1}$$

Where V_0 is the P wave vertical velocity on the surface and G is the gradient of velocity.

For this model, we focus on the diving wave propagation. The fact that the diving wave propagates mostly horizontally points us to a specific choice of parameters to represent the VTI medium. Specifically, we would like to preserve the horizontal wave propagation properties rather than vertical. Therefore, we parameterize the VTI part of the model with the parameters V_0, ε, and η. In the following, we analyze other parameterizations and their effect on the anisotropy parameters estimation.

Based on the parameterization introduced above, the VTI slowness surface can be given by

$$q(p) = \frac{1}{V_0}\sqrt{\frac{1-(1+2\varepsilon)p^2V_z^2}{1-\frac{2\eta}{1+2\eta}(1+2\varepsilon)p^2V_z^2}}, \tag{3.2}$$

where q and p are vertical and horizontal slownesses, respectively.

Because of the anisotropy, the ray trajectory of the diving wave in a factorized VTI medium is different from the isotropic case and is shown in Figure 3.1. The shape of the ray is given by an arc of quasi-ellipse. The ray trajectories are affected by V_0, G and the anisotropy parameters. The changes in ray trajectory due to the changes in V_0, G, ε and η are shown in Figure 3.2. The model parameters are $V_0 = 2\,km/s$, $G = 0.5\,s^{-1}$, $\varepsilon = 0.2$ and $\eta = 0.2$ with considered perturbations: $\Delta V_0 = \pm 0.2\,km/s$, $\Delta G = \pm 0.1\,s^{-1}$, $\Delta\varepsilon = \pm 0.1$ and $\Delta\eta = \pm 0.1$. Compared with the change in the anisotropy parameter η, the influence of a change in the anisotropy ε is much more pronounced on the ray geometry. The position of the turning point

(x_0, z_0) (Figure 3.3) in a factorized VTI medium can be obtained by setting the vertical slowness to zero, and defined as

$$\begin{aligned} x_0(p) &= \frac{1}{Gp}\sqrt{\frac{R_1}{R_2}}, \\ z_0(p) &= \frac{1-\sqrt{1+2\varepsilon}\,pV_0}{\sqrt{1+2\varepsilon}Gp}, \end{aligned} \tag{3.3}$$

where

$$\begin{aligned} R_1 &= 1-(1+2\varepsilon)p^2V_0^2, \\ R_2 &= 1-\frac{2\eta}{1+2\eta}(1+2\varepsilon)p^2V_0^2. \end{aligned} \tag{3.4}$$

The traveltime from the source position $(0,0)$ to the turning point (x_0, z_0) takes the form (Stovas, 2010)

$$T_0(p) = \frac{1}{G}(A_1 + A_2 + A_3), \tag{3.5}$$

where A_1 and A_2 are given by

$$\begin{aligned} A_1 &= \sqrt{\frac{R_1}{R_2}}, \\ A_2 &= \ln\left(\sqrt{1+2\eta}\,\frac{\sqrt{R_1}+\sqrt{R_2}}{\sqrt{1+2\varepsilon}\,pV_0}\right), \end{aligned} \tag{3.6}$$

and the expression for A_3 depends on the sign of η,

$$A_3 = \begin{cases} \frac{1}{2}\sqrt{\frac{1+2\eta}{2\eta}}\ln\left(1+4\eta R_1 - 2\sqrt{2\eta(1+2\eta)R_1R_2}\right), & \eta > 0, \\ \frac{1}{2}\sqrt{\frac{1+2\eta}{-2\eta}}\arctan\left(\frac{2\sqrt{-2\eta(1+2\eta)R_1R_2}}{1+4R_1\eta}\right), & \eta < 0. \end{cases} \tag{3.7}$$

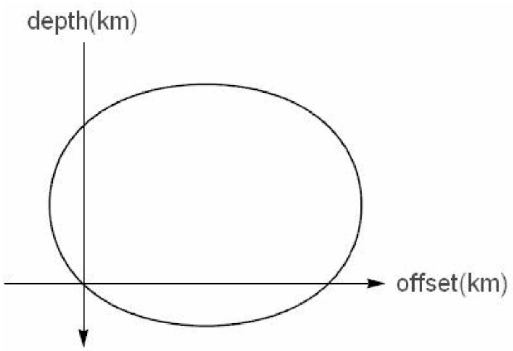

Figure 3.1. Ray trajectory of diving wave in a factorized VTI medium.

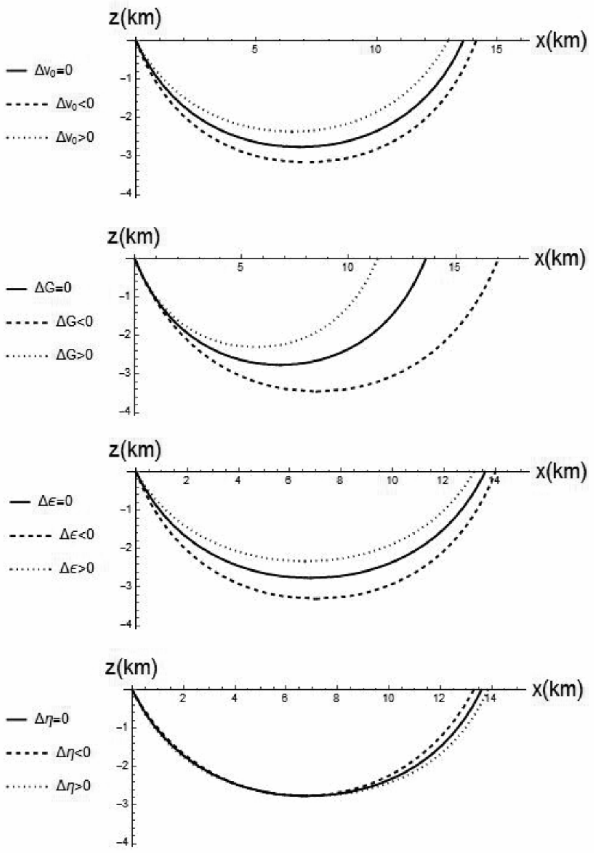

Figure 3.2. Change in ray trajectory due to perturbations in V_0, G, ε and η, respectively. The model parameters are $V_0 = 2\,km/s$, $G = 0.5\,s^{-1}$, $\varepsilon = 0.2$ and $\eta = 0.2$ with perturbations of $\Delta V_0 = \pm 0.2\,km/s$, $\Delta G = \pm 0.1\,s^{-1}$, $\Delta\varepsilon = \pm 0.1$ and $\Delta\eta = \pm 0.1$.

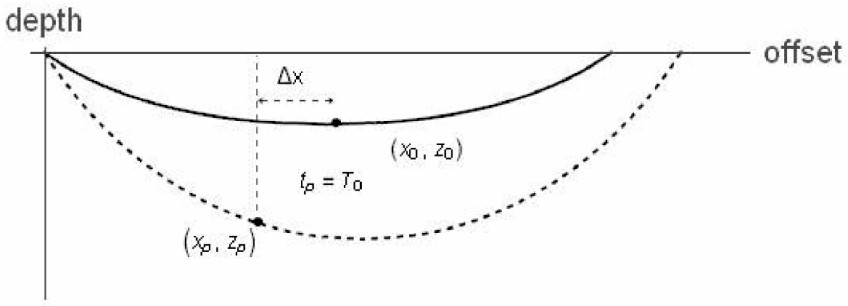

Figure 3.3. Diving-wave imaging moveout. (imaging point shift from the turning point). The ray trajectories in factorized VTI and isotropic media are shown by solid and dashed lines, respectively.

3.3 Diving wave imaging moveout

The definition of diving wave imaging moveout is illustrated in Figure 3.3. The imaging point of the diving wave, when using the accurate velocity model, will be focused in the turning point position with the coordinates given in equation (3.3) after applying the imaging condition (Shen, 2013). If the parameters in the velocity model are not accurate, this point will shift and is given by a different ray trajectory defined by the same traveltime and horizontal slowness. This image point dispersal (residual image moveout) can be used to extract information to update the velocity model.

The behavior of diving waves for a constant-gradient velocity model in an isotropic medium has been described analytically by Stovas and Alkhalifah (2014). The traveltime from source $(0,0)$ to a point (x_p, z_p) is defined by the relation

$$t_p = \frac{1}{G}\log\left(\frac{V_0 + Gz_p}{V_0}\frac{1+\sqrt{1-p^2V_0^2}}{1+\sqrt{1-p^2(V_0+Gz_p)^2}}\right), \tag{3.8}$$

where z_p is the corresponding depth of the focusing point with wrong velocity model (isotropic assumption).

We can get the expression of the depth z_p by solving the equation $t_p = T_0$ from equations (3.5) and (3.8),

$$
\begin{aligned}
\mathrm{z}_p &= \frac{V_0(-b_0 + b_1 e^{GT_0} + b_2 e^{2GT_0} + b_3 e^{3GT_0} + b_4 e^{4GT_0})}{G(b_0 - b_2 e^{2GT_0} - b_4 e^{4GT_0})}, \\
b_0 &= p^2 V_0^2, \\
b_1 &= 2(1 - \sqrt{1 - p^2 V_0^2}), \\
b_2 &= 2(p^2 V_0^2 - 2), \\
b_3 &= 2(1 + \sqrt{1 - p^2 V_0^2}), \\
b_4 &= -p^2 V_0^2.
\end{aligned}
\tag{3.9}
$$

where T_0 is defined in equation (3.5)-(3.7). The relation between x_p and z_p in an isotropic medium with a linearly increasing velocity is given in Stovas and Alkhalifah (2014)

$$
x_p = \frac{1}{Gp}(\sqrt{1 - p^2 V_0^2} - \sqrt{1 - p^2 (V_0 + G z_p)^2}). \tag{3.10}
$$

We can get a similar approximate expression for VTI media by substituting equation (3.9) into equation (3.10).

The difference in the lateral position of the imaging point, $\Delta x_p = x_0 - x_p$, where x_0 is defined in equations (3.3) and (3.4), can be represented as a function of the vertical depth z_p, which is the so called diving wave imaging moveout. Both Δx_p and z_p are parametric equations represented in terms of the horizontal slowness p.

As it is shown in Figure 3.4, one can see the exact imaging moveout with the perturbations in V_0, G, ε and η with the parameters: $V_0 = 2\ km/s$, $G = 0.5\ s^{-1}$, $\varepsilon = 0.3$ and $\eta = 0.15$, and the perturbations: $\Delta V_0 = \pm 0.5\ km/s$, $\Delta G = \pm 0.2\ s^{-1}$, $\Delta\varepsilon = \pm 0.1$ and $\Delta\eta = \pm 0.1$. We can see from the plots that Δx_p increases with vertical velocity V_0 and anisotropy parameter ε, while

decreases with gradient G and anisotropy parameter η. From the plots in Figure 3.4, we observe that the imaging moveout is very insensitive to the changes in anisotropy parameter η under the parameterization: V_0, ε, η.

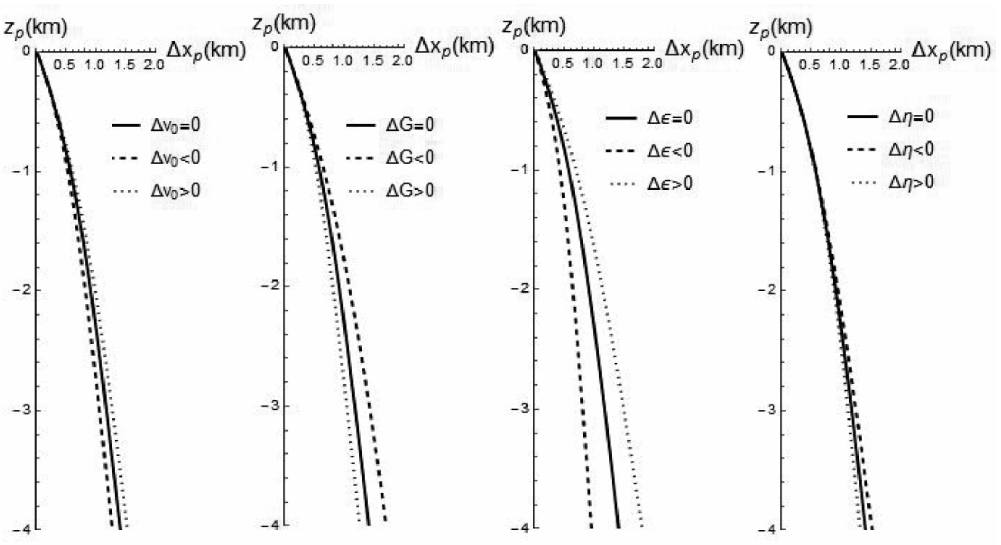

Figure 3.4. Exact imaging moveout with the perturbations in V_0 and G and anisotropy parameters ε and η. The parameters are $V_0 = 2\ km/s$, $G = 0.5\ s^{-1}$, $\varepsilon = 0.3$ and $\eta = 0.15$, and with the perturbations are $\Delta V_0 = \pm 0.5\ km/s$, $\Delta G = \pm 0.2\ s^{-1}$, $\Delta\varepsilon = \pm 0.1$ and $\Delta\eta = \pm 0.1$.

3.4 Imaging moveout approximations

In order to choose the best approximation for the imaging moveout, we analyze three types of approximations for $\Delta x_p(z_p)$: the fourth order Taylor series, the Padé approximation and the rational approximation.

First, we obtain the analytical Taylor series expansion in depth z_p, which takes the form (see Appendix A)

$$\Delta x_p = a_1 z_p + a_2 z_p^2 + a_3 z_p^3 + a_4 z_p^4, \tag{3.11}$$

with the series coefficients

$$
\begin{aligned}
a_1 &= \sqrt{2}\sqrt{\varepsilon}, \\
a_2 &= -\frac{(1+2\varepsilon)G}{2\sqrt{2}\sqrt{\varepsilon}V_0}, \\
a_3 &= \frac{(1+2\varepsilon)(-\eta+\varepsilon(3+4\eta))G^2}{6\sqrt{2}\varepsilon^{3/2}V_0^2(1+2\eta)}, \\
a_4 &= \frac{(1+2\varepsilon)(1-2\eta-16\varepsilon^2(1+\eta)+\varepsilon(2+4\eta))G^3}{32\sqrt{2}\varepsilon^{5/2}V_0^3(1+2\eta)}.
\end{aligned}
\tag{3.12}
$$

The first two coefficients in equation (3.12) do not depend on the anisotropy parameter η. It confirms our observation on the weak dependency of the imaging moveout on this parameter. In order to provide an accurate approximation, the Padé approximation is adopted to stabilize the series in equation (3.11). We define a Padé approximation $P[i, j]$ to be the rational function given by

$$
P[i, j] = \frac{M_i(z_p)}{N_j(z_p)} = \frac{m_1 z_p + m_2 z_p^2 + \cdots m_i z_p^i}{1 + n_1 z_p + n_2 z_p^2 + \cdots n_j z_p^j}. \tag{3.13}
$$

The series coefficients in the Padé approximation are associated with the Taylor series in equation (3.11) for $A(z) = \Delta x_p = \sum_{j=1}^{4} a_j z_p^j$, and the series coefficients in equation (3.13) can be calculated by $A(z) - P[i, j] = O(z^{i+j})$. If $i + j > 4$ the corresponding coefficient of z^{i+j} in the Taylor series will be zero, $a^{i+j} = 0$ (Baker et al., 1961).

We analyze three types of Padé approximations i.e. $P[2,2]$, $P[2,3]$, and $P[3,3]$ for the diving wave imaging moveout $\Delta x_p(z_p)$.

To define a more stable and accurate approximation, we compute the infinite depth limit,

$$
a_\infty = \lim_{z_p \to \infty} \left(\frac{\Delta x_p}{z_p}\right). \tag{3.14}
$$

Then, we define two types of rational approximation in the following forms

$$R_1 = \frac{p_1 z_p + p_2 z_p^2}{1 + q_1 z_p}, \tag{3.15}$$

$$R_2 = \frac{P_1 z_p + P_2 z_p^2 + P_3 z_p^3}{1 + Q_1 z_p + Q_2 z_p^2}, \tag{3.16}$$

where the coefficients $p_1, p_2, q_1, P_1, P_2, P_3, Q_1$ and Q_2 are represented in terms of the Taylor series coefficients in equation (3.12) and the infinite limit term a_∞ (Appendix B).

3.5 Numerical examples

To test the accuracy of different approximations, we choose a factorized model with the parameters: $V_0 = 2\,km/s$, $G = 1.5\,s^{-1}$, $\varepsilon = 0.22$ and $\eta = 0.1$.

First, we test the accuracy of Taylor series approximation with different terms and their errors S in Figure 3.5. The error function is the difference between exact imaging moveout $\Delta x_{\mathbf{exact}}(z_p)$ and the approximation one $\Delta x_{\mathbf{app}}(z_p)$ with $S = \Delta x_{\mathbf{exact}}(z_p) - \Delta x_{\mathbf{app}}(z_p)$. From the plots in Figure 3.5, we can see that in the presence of anisotropy, the third-order Taylor series approximation has a higher accuracy.

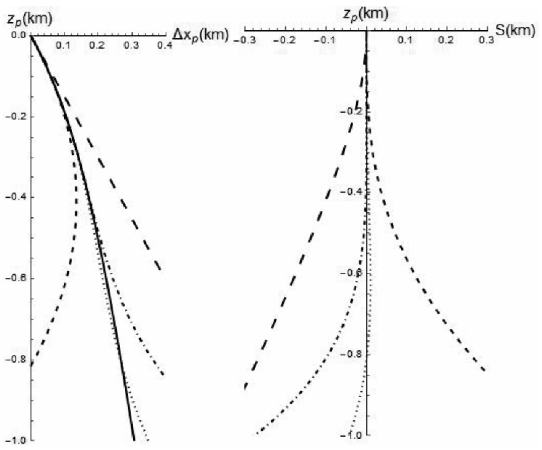

Figure 3.5. The limited Taylor series approximations from equation (3.11) (left) and their errors (right). The one-, two-, three- and four-term approximations are shown by large dashed, tiny dashed, dotted and dash-dotted lines, respectively. The exact imaging moveout curve is shown by solid line. The parameters are $V_0 = 2\ km/s$, $G = 1.5\ s^{-1}$, $\varepsilon = 0.22$ and $\eta = 0.1$. The error in imaging moveout is $S = \Delta x_{\mathbf{exact}}(z_p) - \Delta x_{\mathbf{app}}(z_p)$.

In Figure 3.6, we show three types of Padé approximation $P[2,2]$, $P[2,3]$, $P[3,3]$ and their error plots. From the plots in Figure 3.6, one can see that the Padé approximation $P[2,2]$ is more accurate than the other two, while $P[2,3]$ is unstable (Figure 3.6) since the denominator can vanish at a certain depth.

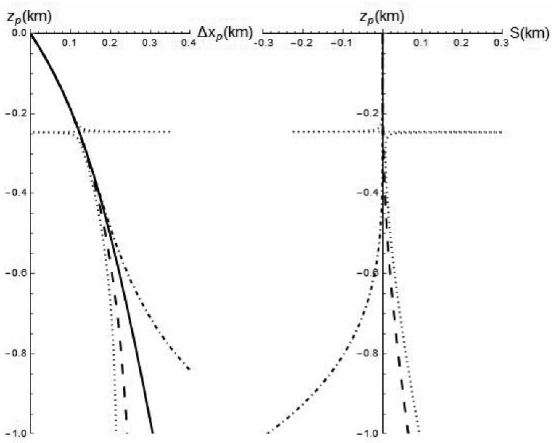

Figure 3.6. The imaging moveout of three types of Padé approximation $P[2,2]$, $P[2,3]$, $P[3,3]$ (left) and their errors (right) are shown by dashed, dotted and dash-dotted lines, respectively. The exact imaging moveout curve is shown by solid line.

The imaging moveout of two rational approximations in equations (3.15) and (3.16) are shown in Figure 3.7. From the error plots in Figure 3.7, one can see that the rational approximation R_2 is very accurate. It is almost as accurate as the exact solution up to a depth of 0.6 km. We select the rational approximation R_2 as our approximation for the upcoming examples.

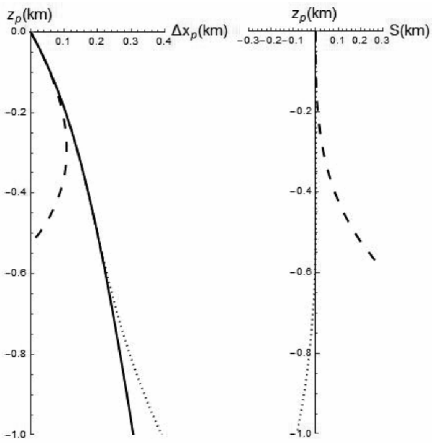

Figure 3.7. The imaging moveout of two rational approximations in equations (3.15) and (3.16) and their errors are shown in dashed and dotted lines, respectively. The exact imaging moveout curve is shown by solid line.

3.6 Semblance analysis

First, we test the accuracy on two common-shot synthetic gathers corresponding to different values of the gradient (Figure 3.8) $G_1 = 1.5\, s^{-1}$ (model a) and $G_2 = 2\, s^{-1}$ (model b). The remaining parameters are $V_0 = 2\, km/s$, $\varepsilon = 0.22$ and $\eta = 0.1$. The source is located at the surface at lateral position 4 km, with receivers spanning the whole surface. Imaging the shot gather using reverse time migration (RTM) with a space lag imaging condition allows us to obtain the common image gathers. Figure 3.9 shows the common image gathers from applying the RTM with the accurate parameters. There is no residual imaging moveout when the exact velocity model is used. In Figure 3.10, we show the residual imaging moveout when applying RTM under the isotropic assumption on the data shown in Figure 3.8. For the isotropic model, we keep the same V_0 and gradients as that of the anisotropic models and set ε and η to zero. The use of wrong anisotropy parameters cause the residual imaging moveout we see in Figure 3.10. We overlay the numerically computed imaging moveout with the curves corresponding to our analytical second-order rational approximation R_2 given in

equation (3.16). We represent the numerically computed imaging moveout in Figure 3.10 with a yellow color. Although this equation is approximate, it can accurately predict the residual curve of the imaging moveout for both models. For a larger gradient, the matching between the analytical approximation and RTM is not as accurate with increasing difference at large depths (Figure 3.10 (b)). As the typical velocity gradients lie between $0.5-1.0\,s^{-1}$, so our results are acceptable.

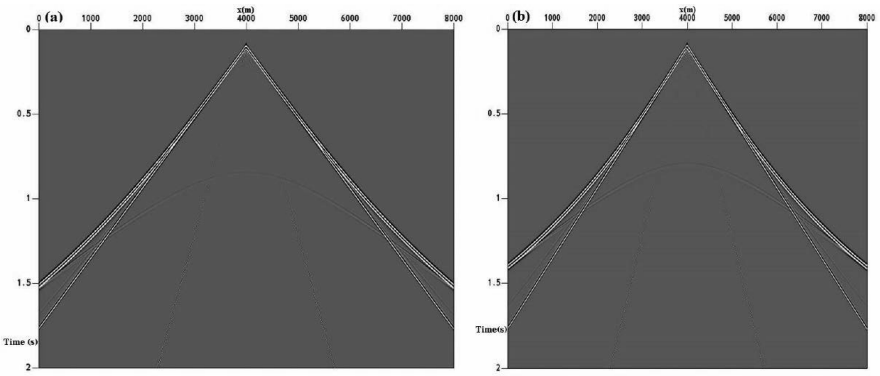

Figure 3.8. (a) The common shot gather for the diving wave from the synthetic data with the parameters $V_0 = 2\,km/s$, $G_1 = 1.5\,s^{-1}$, $\varepsilon = 0.22$ and $\eta = 0.1$. (b) The common shot gather for the diving wave from the synthetic data with the parameters $V_0 = 2\,km/s$, $G_2 = 2\,s^{-1}$, $\varepsilon = 0.22$ and $\eta = 0.1$.

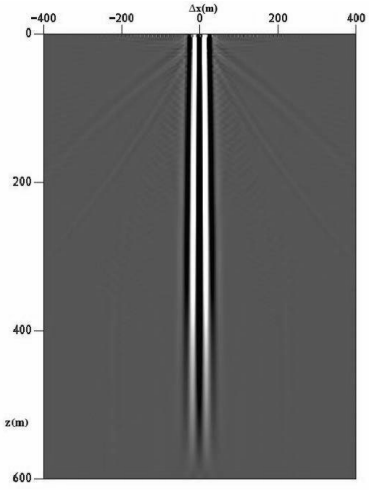

Figure 3.9. The common image gather for the diving wave when applying the anisotropic RTM with the accurate parameters.

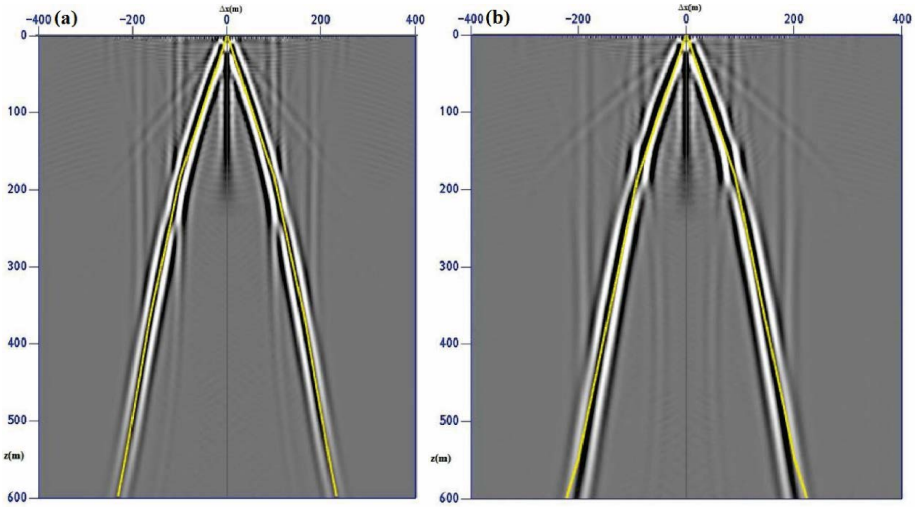

Figure 3.10. (a) The common image gather when using the isotropic RTM with parameters $V_0 = 2\ km/s$, $G_1 = 1.5\ s^{-1}$, $\varepsilon = 0.22$ and $\eta = 0.1$. (b) The common image gather when using the isotropic RTM with parameters $V_0 = 2\ km/s$, $G_2 = 2\ s^{-1}$, $\varepsilon = 0.22$ and $\eta = 0.1$. We overlay the residual curve predicted by the imaging moveout from rational approximation R_2 in equation (3.16).

We apply the semblance analysis on the RTM result based on the analytical prediction corresponding to the rational approximation R_2. The equation for the semblance coherency function is given by

$$SB = \frac{\sum_{j}^{nz} A_{i(j),j}^2}{(\sum_{j}^{nz} A_{i(j),j})^2}, \tag{3.17}$$

where SB is the semblance value, $A_{i,j}$ is the amplitude of the RTM data, $i(j)$ is the discretized representation of $x_p(z_p)$ and j is the discretized representation of z_p in the rational approximation R_2 given by equation (3.16). In order to analyze the influence of VTI medium parameterization, we test a range of anisotropy combinations and show the errors in estimation of anisotropy parameters $\Delta\varepsilon$ and $\Delta\eta$ for gradient G_1 in Table 3.1 (see Appendix

C). From this table, we can see that the estimates from all the examples are reasonably accurate and the differences between them are very small. Then, we apply the same analysis for the larger gradient G_2 and show the results in Table 3.2. The anisotropy estimates for this model are less accurate because the approximation in equation (3.16) deviates from the RTM result at larger depths as shown in Figure 3.10 (b). However, the results are still sufficiently accurate for use as a potential initial model for FWI. Based on the accuracy of estimation of $\tilde{\varepsilon}$ and $\tilde{\eta}$, we select the four best parameterizations: (V_N, ε, η), $(V_N, \varepsilon, \delta)$, (V_0, ε, V_H) and (V_N, ε, V_H) for semblance plots.

In Figure 3.11, the semblance plots computed for the depth range of $0-600\,m$ for these four types of parameterizations, where V_0, V_N and V_H are the vertical, NMO and horizontal velocities on the top for gradient G_1, demonstrate the variations with different parameterizations. The anisotropy parameters can be evaluated from the coordinates by picking the maximal value of the semblance plots.

The semblance plots for a larger gradient G_2 are shown in Figure 3.12. Comparing with the semblance plots in Figure 3.11, we observe that the semblance anomalies are more focused while the estimation results are less accurate. The trade-off between anisotropy parameters also decreases.

G1=1.5s^{-1}			
One velocity + two anisotropy parameters			
1	V_0, ε, η	$\Delta\varepsilon \approx 0.002$	$\Delta\eta \approx -0.004$
2	V_0, δ, η	$\Delta\varepsilon \approx 0.0015$	$\Delta\eta \approx -0.0055$
3	V_0, δ, ε	$\Delta\varepsilon \approx 0.002$	$\Delta\eta \approx -0.0035$
4	V_N, ε, η	$\Delta\varepsilon \approx 0.0025$	$\Delta\eta \approx -0.005$
5	V_N, δ, η	$\Delta\varepsilon \approx 0.002$	$\Delta\eta \approx 0.008$
6	V_N, δ, ε	$\Delta\varepsilon \approx 0.0025$	$\Delta\eta \approx -0.0045$
7	V_H, ε, η	$\Delta\varepsilon \approx 0.002$	$\Delta\eta \approx -0.0045$
8	V_H, δ, η	$\Delta\varepsilon \approx 0.0015$	$\Delta\eta \approx -0.006$
9	V_H, δ, ε	$\Delta\varepsilon \approx 0.002$	$\Delta\eta \approx -0.0045$
Two velocities + one anisotropy parameter			
10	V_0, ε, V_N	$\Delta\varepsilon \approx 0.002$	$\Delta\eta \approx -0.00355$
11	V_0, η, V_N	$\Delta\varepsilon \approx 0.0016$	$\Delta\eta \approx -0.0045$
12	V_0, δ, V_H	$\Delta\varepsilon \approx 0.0018$	$\Delta\eta \approx -0.0047$
13	V_0, η, V_H	$\Delta\varepsilon \approx 0.0018$	$\Delta\eta \approx -0.005$
14	V_N, δ, V_H	$\Delta\varepsilon \approx 0.002$	$\Delta\eta \approx -0.006$
15	V_N, ε, V_H	$\Delta\varepsilon \approx 0.0025$	$\Delta\eta \approx -0.005$
16	V_H, δ, V_N	$\Delta\varepsilon \approx 0.0016$	$\Delta\eta \approx -0.0044$
17	V_H, ε, V_N	$\Delta\varepsilon \approx 0.002$	$\Delta\eta \approx -0.0044$
Three velocities			
18	V_0, V_N, V_H	$\Delta\varepsilon \approx 0.0018$	$\Delta\eta \approx -0.0048$

Table 3.1. The anisotropy estimation errors for gradient G_1 for all parameterizations. We fix the first value of each parameterization and evaluate the other two through semblance analysis, then convert them into the estimation for anisotropy parameters $\tilde{\varepsilon}$ and $\tilde{\eta}$.

G2=2s^{-1}			
One velocity + two anisotropy parameters			
1	V_0, ε, η	$\Delta\varepsilon \approx 0.0075$	$\Delta\eta \approx 0.0385$
2	V_0, δ, η	$\Delta\varepsilon \approx 0.0080$	$\Delta\eta \approx 0.0385$
3	V_0, δ, ε	$\Delta\varepsilon \approx 0.0075$	$\Delta\eta \approx 0.045$
4	V_N, ε, η	$\Delta\varepsilon \approx 0.0045$	$\Delta\eta \approx 0.0370$
5	V_N, δ, η	$\Delta\varepsilon \approx 0.0060$	$\Delta\eta \approx 0.0380$
6	V_N, δ, ε	$\Delta\varepsilon \approx 0.0045$	$\Delta\eta \approx -0.0355$
7	V_H, ε, η	$\Delta\varepsilon \approx 0.0080$	$\Delta\eta \approx 0.0385$
8	V_H, δ, η	$\Delta\varepsilon \approx 0.0085$	$\Delta\eta \approx 0.0380$
9	V_H, δ, ε	$\Delta\varepsilon \approx 0.0080$	$\Delta\eta \approx -0.0215$
Two velocities + one anisotropy parameter			
10	V_0, ε, V_N	$\Delta\varepsilon \approx 0.0075$	$\Delta\eta \approx 0.0377$
11	V_0, η, V_N	$\Delta\varepsilon \approx 0.0083$	$\Delta\eta \approx 0.0385$
12	V_0, δ, V_H	$\Delta\varepsilon \approx 0.0072$	$\Delta\eta \approx 0.0367$
13	V_0, η, V_H	$\Delta\varepsilon \approx 0.0072$	$\Delta\eta \approx 0.0375$
14	V_N, δ, V_H	$\Delta\varepsilon \approx 0.0060$	$\Delta\eta \approx 0.0380$
15	V_N, ε, V_H	$\Delta\varepsilon \approx 0.0045$	$\Delta\eta \approx 0.0370$
16	V_H, δ, V_N	$\Delta\varepsilon \approx 0.0082855$	$\Delta\eta \approx 0.0377855$
17	V_H, ε, V_N	$\Delta\varepsilon \approx 0.0080$	$\Delta\eta \approx 0.0383862$
Three velocities			
18	V_0, V_N, V_H	$\Delta\varepsilon \approx 0.007218$	$\Delta\eta \approx 0.036906$

Table 3.2. The anisotropy estimation errors for gradient G_2 for all parameterizations. We fix the first value of each parameterization and evaluate the other two through semblance analysis, then convert them into the estimation for anisotropy parameters $\tilde{\varepsilon}$ and $\tilde{\eta}$.

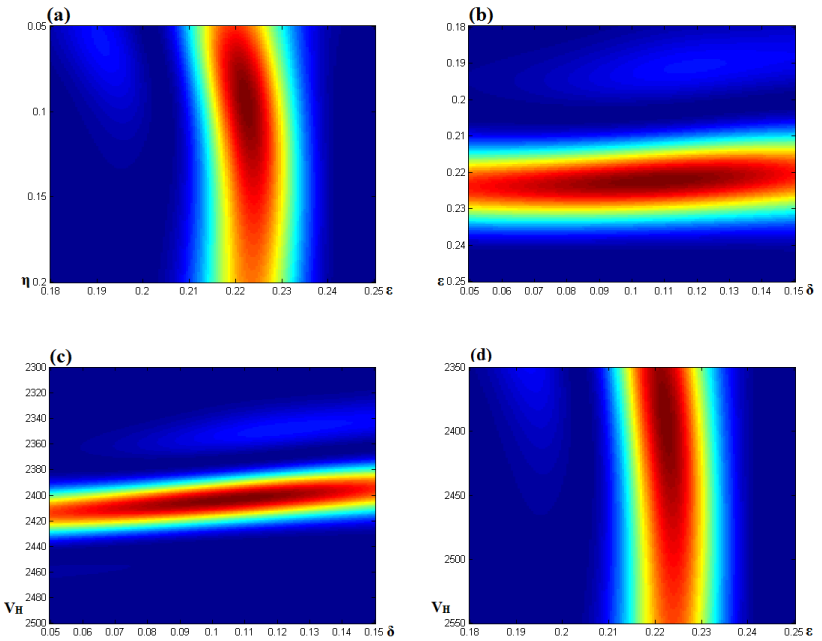

Figure 3.11. The semblance plots for different parameterizations computed for factorized model with $G_1 = 1.5s^{-1}$ (a) V_N-fixed, ε,η; (b) V_N-fixed, ε,δ; (c) V_0-fixed, δ,V_H; (d) V_N-fixed, ε,V_H. The anisotropy parameters can be evaluated from the coordinates of the maximal value of the semblance plot.

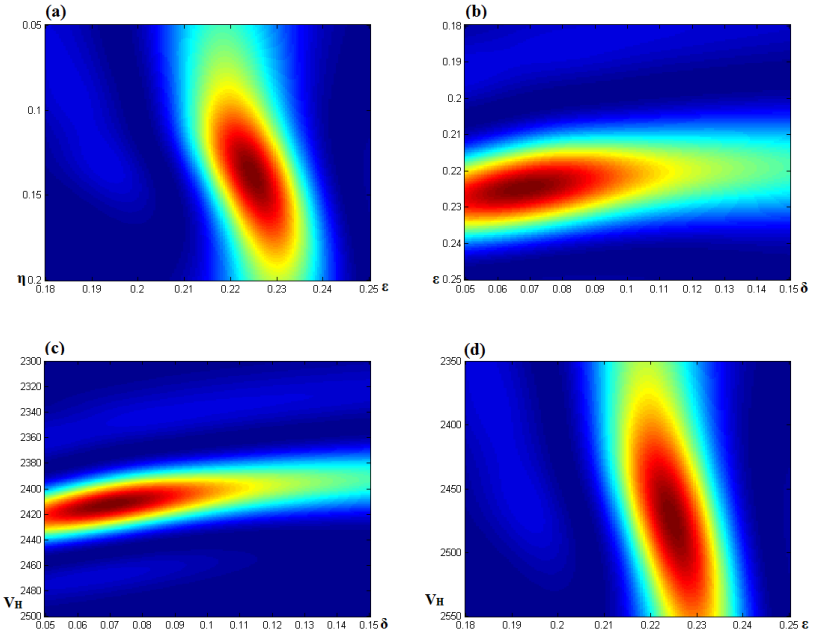

Figure 3.12. The semblance plots for different parameterizations computed for factorized model with $G_1 = 2s^{-1}$ (a) V_N-fixed, ε,η; (b) V_N-fixed, ε,δ; (c) V_0-fixed, δ,V_H; (d) V_N-fixed, ε,V_H. The anisotropy parameters can be evaluated from the coordinates of the maximal value of the semblance plot.

3.7 Discussions

Despite the fact that the linear velocity model used for our analysis is an approximation to the real case, it can be used as a part of a factorized model for many real situations. Like in the moveout approximations for reflections where the medium is assumed to be homogeneous to yield such approximations, for diving waves vertical increase of velocity is a necessary ingredient for recording such waves. As a result, we develop the analytical approximations based on a constant gradient assumption, which will allow for closed form solutions. In the same way as Dix-type approximations are used to describe the reflection moveout in a $V(z)$

medium, similar formulas can be derived for the diving wave moveout, where the gradient is varying with depth. Such studies can be a topic of future investigations.

Despite that diving waves admit low frequency long wavelength energy over the whole wavepath when imaging, it is stationary near the turning point, so the contributions from many source and receivers at the end allows the turning point part to provide the major contribution and at the high frequency asymptotic limit, we end up with the turning ray contribution. We definitely do not get energy focused only at the turning point, as the classic image for turning waves from a source to a receiver is has a banana shape. However, we are focusing our analysis at the center which includes the turning point, as it represents the deepest level in which a diving wave travels shown in Figure 3.13. Using different intervals, we sum all sources and receivers that covering the surface, the turning point represents the major stationary contribution to the image. The subsurface offset gathers from left and right parts of the model are shown in Figures 3.14 (a) and (b), respectively, using the correct velocity in migration. They need to be compared with Figure 3.9. We can see that they all focused at the center of corresponding gather. The basic idea is that the increased focusing of image in subsurface offset is induced by the increased degree of similarity between the migration velocity and the true velocity. This is equivalent to what we see in extending the image with an offset lag as we demonstrate in Figures 3.9 and 3.10 similar to Shen (2013). So the image point dispersal is equivalent to the non-focusing to zero offset we obtain when we look at extended images. In FWI for diving waves, such dispersal depending on the frequency suggests to us the depth in which the gradient can be trusted, and thus, provides wrong direction updates when the dispersal exceeds a half of the wavelength.

Using the rational approximation, we ended up with relatively small errors under the assumptions made. However, as expected, we observe trade-off between the anisotropy parameters in the estimation (Figures 3.11 and 3.12). The trade-off is an ongoing challenge in

analyzing multi parameter problems like those in anisotropy. However, with analytical formulas the computation of the Hessian becomes straightforward, which provides for another opportunity to benefit from these approximations.

The semblance analysis exercise was mainly meant to analyze the role of parameterization in reducing the tradeoff, but it also provides a valid tool for extracting effective anisotropic parameters corresponding to the depth covered by the diving waves. These effective values can serve as potential initial values for tomographic inversion or FWI.

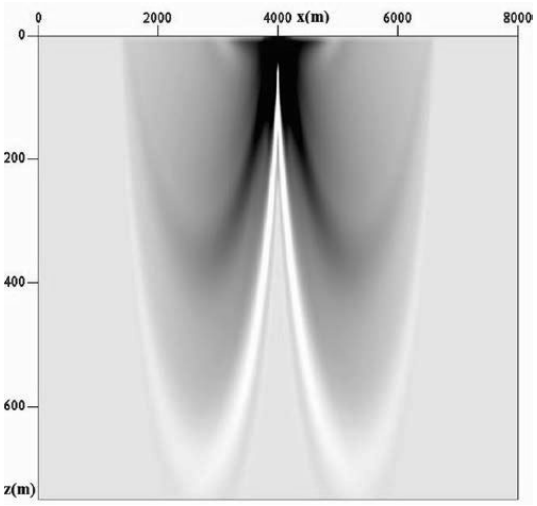

Figure 3.13. The ray trajectory of the diving waves.

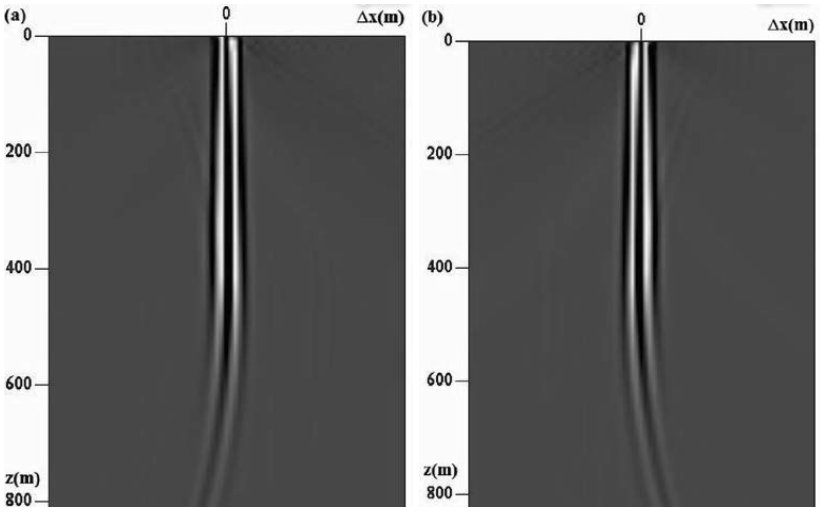

Figure 3.14. Subsurface image gathers in offset pulled from left (a) (4400m) and right (b) (4600m) of the model migrated with the correct velocity.

3.8 Conclusions

We develop a method to estimate the anisotropy parameters from the residual moveout of diving waves in a factorized velocity model. We analyze different approximations for the imaging moveout, and find that the second order rational approximation R_2 is the most accurate one. By testing it with different anisotropy parameterizations, we select (V_N, ε, η), $(V_N, \varepsilon, \delta)$, (V_0, ε, V_H) and (V_N, ε, V_H) as potentially the best combinations for this problem as they provide the best results even for large values of velocity gradients. We estimate the anisotropy parameters from the semblance analysis on residual moveout in the RTM image gathers. From the semblance plots, we observe that an increase in velocity gradient results in a decrease in the trade-off between anisotropy parameters. However, for the larger gradient the accuracy of our moveout equation reduces. Nevertheless, the anisotropy estimation using semblance analysis for all parameterizations is reasonably accurate even for large values of velocity gradients.

3.9 Acknowledgments

We would like to thank Wiktor Weibull for providing the modeling and RTM codes and Chenlong Wang from Tongji University for his useful discussions. We also acknowledge the China Scholarship Council (CSC) and the ROSE project for financial support. We also thank KAUST for its support.

3.10 Appendix A

Taylor series for residual imaging moveout

In order to simplify the expression, we substitute the horizontal slowness by the following variable s using,

$$p = \frac{1-s}{V_0\sqrt{1+2\varepsilon}}. \tag{3.A1}$$

Then the parametric expressions of $z_p(s)$ and $\Delta x_p(s)$ can be expanded in a series,

$$\begin{aligned} z_p(s) &= n_1\sqrt{s} + n_2 s + n_3 s^{3/2} + n_4 s^2 + \cdots \\ \Delta x_p(s) &= m_1\sqrt{s} + m_2 s + m_3 s^{3/2} + m_4 s^2 + \cdots, \end{aligned} \tag{3.A2}$$

where $n_j, m_j,\ j = 1,\ldots,4$ are the series coefficients.

From series (3.A2), we define the series for $\Delta x_p(z_p)$ in the form,

$$\Delta x_p(z_p) = a_1 z_p + a_2 z_p^2 + a_3 z_p^3 + a_4 z_p^4. \tag{3.A3}$$

The coefficients in series (3.A3) are given in terms of coefficients in series (3.A2) and (3.A3) as follows

$$
\begin{aligned}
a_1 &= \frac{m_1}{n_1}, \\
a_2 &= \frac{m_2 n_1 - m_1 n_2}{n_1^3}, \\
a_3 &= \frac{m_3 n_1^2 + 2 m_1 n_2^2 - m_1 n_1 n_3 - 2 n_1 n_2 m_2}{n_1^5}, \\
a_4 &= \frac{m_4 n_1^3 - 3 m_3 n_1^2 n_2 + 5 m_2 n_1 n_2^2 - 5 m_1 n_2^3 - 2 m_2 n_1^2 n_3 + 5 m_1 n_1 n_2 n_3 - m_1 n_1^2 n_4}{n_1^7}.
\end{aligned}
\tag{3.A4}
$$

Finally, these coefficients take the form,

$$
\begin{aligned}
a_1 &= \sqrt{2}\sqrt{\varepsilon}, \\
a_2 &= -\frac{(1+2\varepsilon)G}{2\sqrt{2}\sqrt{\varepsilon}V_0}, \\
a_3 &= \frac{(1+2\varepsilon)(-\eta + \varepsilon(3+4\eta))G^2}{6\sqrt{2}\varepsilon^{3/2}V_0^2(1+2\eta)}, \\
a_4 &= \frac{(1+2\varepsilon)(1-2\eta-16\varepsilon^2(1+\eta)+\varepsilon(2+4\eta))G^3}{32\sqrt{2}\varepsilon^{5/2}V_0^3(1+2\eta)}.
\end{aligned}
\tag{3.A5}
$$

Note that the lower order coefficients a_1 and a_2 do not depend on the anisotropy parameter η.

3.11 Appendix B

Rational approximation

We define two types of rational approximations with the following forms

$$
\begin{aligned}
R_1 &= \frac{p_1 z_p + p_2 z_p^2}{1 + q_1 z_p}, \\
R_2 &= \frac{P_1 z_p + P_2 z_p^2 + P_3 z_p^3}{1 + Q_1 z_p + Q_2 z_p^2},
\end{aligned}
\tag{3.B1}
$$

where $p_1, p_2, q_1, P_1, P_2, P_3, Q_1$ and Q_2 are the series coefficients. In order to compute these coefficients, we define the infinite depth limit,

$$a_\infty = \lim_{z_p \to \infty} \left(\frac{\Delta x_p}{z_p}\right). \tag{3.B2}$$

The coefficients in the rational approximation R_1 can be represented by

$$\begin{aligned} p_1 &= a_1, \\ p_2 &= \frac{a_2 a_\infty}{a_\infty - a_1}, \\ q_1 &= \frac{a_2}{a_\infty - a_1}, \end{aligned} \tag{3.B3}$$

where the coefficients a_j are given in equation (3.A5).

The coefficients in rational approximation R_2 can be given by

$$\begin{aligned} P_1 &= a_1, \\ P_2 &= \frac{a_2^3 - 2a_1 a_2 a_3 + a_1^2 a_4 + a_2 a_3 a_\infty - a_1 a_4 a_\infty}{a_2^2 - a_1 a_3 + a_3 a_\infty}, \\ P_3 &= \frac{(a_3^2 - a_2 a_4) a_\infty}{a_2^2 - a_1 a_3 + a_3 a_\infty}, \\ Q_1 &= \frac{a_1 a_4 - a_2 a_3 - a_4 a_\infty}{a_2^2 - a_1 a_3 + a_3 a_\infty}, \\ Q_2 &= \frac{a_2 a_4 - a_3^2}{a_1 a_3 - a_2^2 - a_3 a_\infty}. \end{aligned} \tag{3.B4}$$

where the coefficients a_j are given in equation (3.A5).

3.12 Appendix C

Different parameterizations

In order to analyse the impact of the different parameterizations on our analysis, we use three types of parameterizations: one velocity plus two anisotropy parameters, two velocities plus one anisotropy parameter, and three velocities. Different anisotropy parameters can be transferred by the following relations

$$\begin{aligned} \eta &= \frac{\varepsilon - \delta}{1+2\delta}, \\ V_N &= V_0\sqrt{1+2\delta}, \\ V_H &= V_0\sqrt{1+2\delta}\sqrt{1+2\eta}, \end{aligned} \tag{3.C1}$$

where V_0 is the P wave vertical velocity on the surface, V_N is the NMO velocity on the surface, V_H is the horizontal velocity on the surface. The value of the anisotropy parameters are set to $V_0 = 2\,km/s$, $G_1 = 1.5\,\mathbf{s}^{-1}$, $\varepsilon = 0.22$ and $\eta = 0.1$.

Type one: One velocity + two anisotropy parameters

The parameterizations given by type one are (V_0, ε, η), (V_0, δ, η), $(V_0, \delta, \varepsilon)$, (V_N, ε, η), (V_N, δ, η), $(V_N, \delta, \varepsilon)$, (V_H, ε, η), (V_H, δ, η) and $(V_H, \delta, \varepsilon)$. We fix the first value of the velocity and evaluate the other two-anisotropy parameters through semblance analysis. Then we convert the estimation errors into the same form $\Delta\tilde{\varepsilon}$ and $\Delta\tilde{\eta}$ to analyze the accuracy of different parameterizations by the relation $\Delta\tilde{\varepsilon} \approx \Delta\tilde{\delta} + \Delta\tilde{\eta}$.

Type two: Two velocities + one anisotropy parameter

The parameterizations in type two are (V_0, ε, V_N), (V_0, η, V_N), (V_0, δ, V_H), (V_0, η, V_H), (V_N, δ, V_H), (V_N, ε, V_H), (V_H, δ, V_N), and (V_H, ε, V_N). We fix the first parameter of the velocity and evaluate the velocity and the anisotropy parameter through semblance analysis. Then we convert the estimation errors into the same form $\Delta\tilde{\varepsilon}$ and $\Delta\tilde{\eta}$ to analyze the accuracy of different parameterizations using the following relations

$$
\begin{aligned}
\tilde{\delta} &= \frac{(\frac{\tilde{V}_N}{V_0})^2 - 1}{2}, \\
\tilde{\varepsilon} &= \frac{(\frac{\tilde{V}_H}{V_0})^2 - 1}{2}, \\
\tilde{\eta} &= \frac{(\frac{\tilde{V}_H}{V_N})^2 - 1}{2} = \frac{(\frac{V_H}{\tilde{V}_N})^2 - 1}{2}, \\
\Delta\tilde{\varepsilon} &\approx \Delta\tilde{\delta} + \Delta\tilde{\eta}.
\end{aligned}
\tag{3.C2}
$$

Type three: Three velocities

The parameterization in type three is (V_0, V_N, V_H). We fix the first value of the velocity and evaluate the other two velocities through semblance analysis. Then we again convert the estimation errors into the same form $\Delta\tilde{\varepsilon}$ and $\Delta\tilde{\eta}$ to analyze the accuracy of different parameterizations by the relations shown in equation (3.C2).

The errors in anisotropy estimations $\Delta\tilde{\varepsilon}$ and $\Delta\tilde{\eta}$ for eighteen parameterizations are shown in Table 3.1. From this table, one can see that the estimations from all parameterizations are reasonably accurate and the differences between them are very small.

Chapter 4 Preserved traveltime smoothing in orthorhombic media

Shibo Xu and Alexey Stovas

Norwegian University of Science and Technology, Trondheim, Norway

Abstract. Certain degree of smoothness of velocity model is required for most ray based migration and tomography. Applying the conventional smoothing in model parameters results in the offset-dependent traveltime errors for reflected events, which can be large even for small contrasts in model parameters between the layers. This causes the shift in both the depth and residual moveout (RMO) of the migrated images. To overcome this problem in transversely isotropic medium with a vertical symmetry axis (VTI), the preserved traveltime smoothing (PTS) method was proposed earlier. We extend this method for orthorhombic media with and without azimuthal variation between the layers. We illustrate this method for a single interface between two orthorhombic layers and show that the smoothing driven errors in traveltime are very small for practical application.

Presented at the 78th EAGE Conference and Exhibition, June, 2016, Vienna, Austria;

Published in Geophysical Prospecting in November 2016.

4.1 Introduction

The velocity models for prestack depth migration (PSDM) are commonly built by layer-stripping with velocity discontinuities across the horizons. The ray tracing (Červený, 2001) used in Kirchhoff or beam migration requires certain smoothness of the depth velocity model. Current industrial practice for smoothing is to perform a bell-shaped filter (Gonzalez and Woods, 2008) to the step of model parameters. The drawback of the conventional smoothing is that the migrated events will shift to higher velocity layer at the discontinuities compared with results from the unsmoothed model. The shift is offset-dependent, and the errors in depth and the residual moveout (RMO) for the migrated images are induced by the smoothing process, which will cause errors in velocity analysis. Several approaches are proposed for this problem like adding the horizons in the ray-tracing process (Vinje et al, 1996) and combing the unsmoothed and smoothed models (Baina et al, 2006). The Preserved traveltime smoothing (PTS) (Vinje et al, 2012) is proposed to solve this problem based on the kinematically equivalent media (Stovas, 2008) and the traveltime filter. It is designed to smooth the depth models accompanied by preserving the traveltime parameters at the velocity discontinuities.

The orthorhombic (ORT) medium is introduced by Schoenborg and Helbig (1997) to describe the fractured earth and has become a new standard to define model parameters to cover the azimuthal dependence of the traveltime surface. Tsvankin (1997, 2012) defines the elastic ORT model with nine parameters that can be reduced to six parameters in an acoustic approximation (Alkhalifah, 2003). These parameters are: vertical velocity V_0, two local NMO velocities defined in vertical symmetry planes and three local anelliptic parameters. The anelliptic parameters can be defined in all symmetry planes (Grechka and Tsvankin, 1999) or can be defined in terms of azimuthally dependent anellipticity (Stovas, 2015). In addition to

that, we might have one extra parameter responsible for azimuthal orientation of the symmetry planes.

In this paper, we extend the Preserved traveltime smoothing (PTS) method to ORT model based on the azimuthal dependence of kinematic properties defined for an acoustic ORT medium (Stovas, 2015) to preserve the traveltime parameters for smoothed ORT model. In case of azimuthal variations in the symmetry axis between the layers, the least-squares approximation is adopted to estimate the effective anellipticity parameters from this layered medium to preserve the complexity of the model when doing smoothing (ORT both input and output). The traveltime parameters are preserved for the azimuthally dependent ORT model, and the resulting error in traveltime is sufficiently small from the numerical examples. In our paper, we focus on defining the composite parameters only and use very simple Gaussian filter instead of the complicated smoothing operator as proposed in Vinje et al (2012).

4.2 Velocity moments and composite parameters for VTI media

In order to preserve traveltime when smoothing the velocity model, Vinje et al. (2012) defines the depth dependent composite parameterization of a transversely istropic model with a vertical symmetry axis (VTI) medium under the acoustic approximation (Alkhalifah, 1998) represented by kinematic parameters (Stovas, 2008),

$$\begin{aligned} m_1(\xi) &= \frac{1}{V_0(\xi)}, \\ m_2(\xi) &= \frac{V_{nmo}^2(\xi)}{V_0(\xi)}, \\ m_3(\xi) &= \frac{V_{nmo}^4(\xi)(1+8\eta(\xi))}{V_0(\xi)}, \end{aligned} \tag{4.1}$$

where m_1, m_2 and m_3 are the unsmoothed composite parameters, V_0 is the vertical P-wave velocity, V_{nmo} is the normal moveout velocity defined by $V_{nmo} = V_0\sqrt{1+2\delta}$, $\eta = (\varepsilon - \delta)/(1+2\delta)$, where δ and ε are the anisotropy parameters (Thomsen, 1986).

The composite parameters m_1, m_2 and m_3 are smoothed by Gaussian filter so that the velocity moments are preserved at the velocity discontinuities. It means that the integral for composite parameter m_j (before and after smoothing) remains the same,

$$\int_0^z m_j(\xi)d\xi = \int_0^z \tilde{m}_j(\xi)d\xi,\ j = 1,2,3. \tag{4.2}$$

The model is studied in 1 D (vertical direction), therefore, the smoothing for the composite parameters is also computed in 1D, consequently.

The smoothed composite parameter $\tilde{m}_j$ can be obtained by using a conventional Gaussian filter,

$$\tilde{m}_j(z) = \frac{\int_{z-\Delta z/2}^{z+\Delta z/2} w(\xi)m_j(\xi)d\xi}{\int_{z-\Delta z/2}^{z+\Delta z/2} w(\xi)d\xi}, \tag{4.3}$$

where $\tilde{m}_j$ and m_j are smoothed and unsmoothed composite parameter, respectively, and w is the Gaussian function and Δz is the length of the filter. Vinje et al. (2012) designed the special filter used for smoothing, but, in this paper, we use the simple Gaussian filter for simplicity.

The smoothed composite parameter $\tilde{m}_j$ is shown in Figure 4.1 (left). In order to preserve the traveltime parameters, compensation function needs to be added before and after the step (Figure 4.1, right).

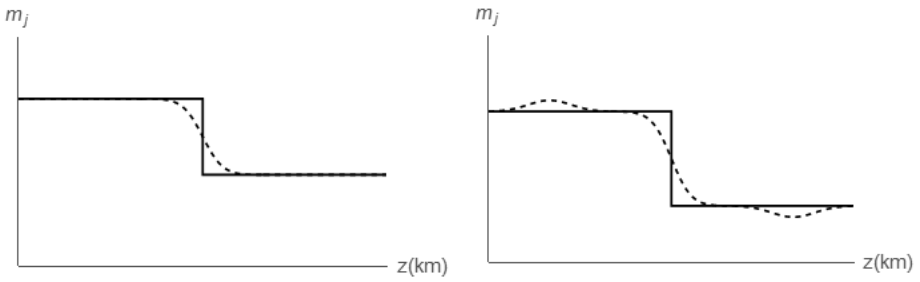

Figure 4.1. The unsmoothed and smoothed composite parameters (left). The same composite parameter with compensation functions (right). The unsmoothed and smoothed parameters are shown by solid and dashed lines, respectively.

The smoothed composite parameters $\tilde{m}_1$, $\tilde{m}_2$ and $\tilde{m}_3$ can be converted into the model parameters by following equations (Vinje et al, 2012),

$$\begin{aligned}
\tilde{V}_0(\xi) &= \frac{1}{\tilde{m}_1(\xi)}, \\
\tilde{V}_{nmo}(\xi) &= \sqrt{\frac{\tilde{m}_2(\xi)}{\tilde{m}_1(\xi)}}, \\
\tilde{\eta}(\xi) &= \frac{1}{8}\left(\frac{\tilde{m}_3(\xi)\tilde{m}_1(\xi)}{\tilde{m}_2^2(\xi)} - 1\right).
\end{aligned} \tag{4.4}$$

To illustrate the smoothing procedure and the accuracy of the method, we select a two-layer VTI model. The parameters of upper layer are: $V_0 = 1.5\,\text{km/s}$, $V_{nmo} = 2\,\text{km/s}$, $\eta = 0.1$ and parameters of lower layer are: $V_0 = 2.5\,\text{km/s}$, $V_{nmo} = 3.2\,\text{km/s}$, $\eta = 0.12$ and the thickness for both layers is 3 km. Unsmoothed and smoothed composite parameters $m_j\,(j = 1..3)$ computed for model specified above are shown in Figure 4.2. One can see that the smoothing operator in equation (4.3) performs very similarly for all composite parameters.

The corresponding smoothed model parameters computed in equations (4.4) are shown in Figure 4.3. From these plots, one can see that the shape of the smoothed anellipticity parameter η is very different from other kinematic parameters at the interface.

If the unsmoothed velocity model is isotropic ($\delta = \varepsilon = 0$), the PTS results in the smoothing induced anisotropy illustrated in Figure 4.4. The behavior of the smoothed V_{nmo} is similar to behavior of the smoothed V_0 (Figure 4.3). However, the smoothing induced anellipticity parameter is different from the one obtained for VTI model. We can decompose kinematic parameters shown in Figure 4.4 into anisotropic parameters δ and ε (Figure 4.5). The smoothed anisotropic parameters δ and ε have similar shape. The induced anellipticity from elliptic isotropic (EI) and isotropic (ISO) cases are shown in Figure 4.6. From this plot, one can see that the induced anellipticity from ISO model is larger than the one obtained from EI model.

In order to illustrate the accuracy of the proposed method, we compute the depth dependent offset-traveltime by the integrals (Fomel and Stovas, 2010),

$$\begin{aligned} X(p) &= \int_0^z \frac{pV_{NMO}^2(\xi)}{V_0(\xi)(1-2\eta(\xi)p^2V_{NMO}^2(\xi))^{3/2}\sqrt{1-(1+2\eta(\xi))p^2V_{NMO}^2(\xi)}}d\xi, \\ T(p) &= \int_0^z \frac{(1-2\eta(\xi)p^2V_{NMO}^2(\xi))^2+2\eta(\xi)p^4V_{NMO}^4(\xi)}{V_0(\xi)(1-2\eta(\xi)p^2V_{NMO}^2(\xi))^{3/2}\sqrt{1-(1+2\eta(\xi))p^2V_{NMO}^2(\xi)}}d\xi, \end{aligned} \tag{4.5}$$

where $X(p)$ and $T(p)$ are the parametric offset and traveltime that represented by horizontal slowness p. The relative traveltime error between unsmoothed and smoothed VTI, EI and ISO models with parameters mentioned above is shown in Figure 4.7. From the plot, one can see that the travletime error increases with offset, and the error is very small even for large offset. Notice that the PTS method applied for VTI and EI models results in smaller traveltime error comparing with ISO model.

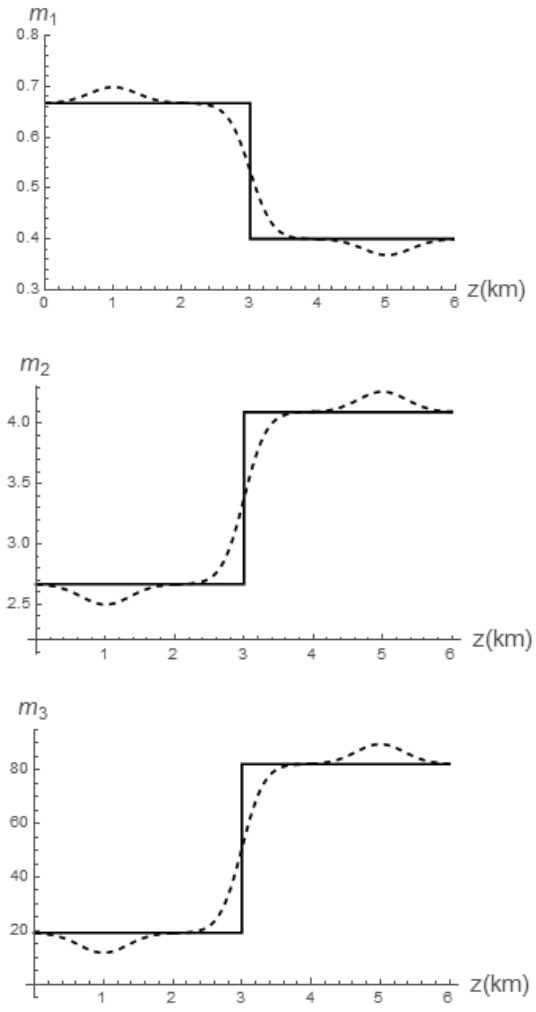

Figure 4.2. The composite parameters m_1 (top), m_2 (middle) and m_3 (bottom) before and after smoothing for VTI model. The unsmoothed and smoothed parameters are shown by solid and dashed lines, respectively.

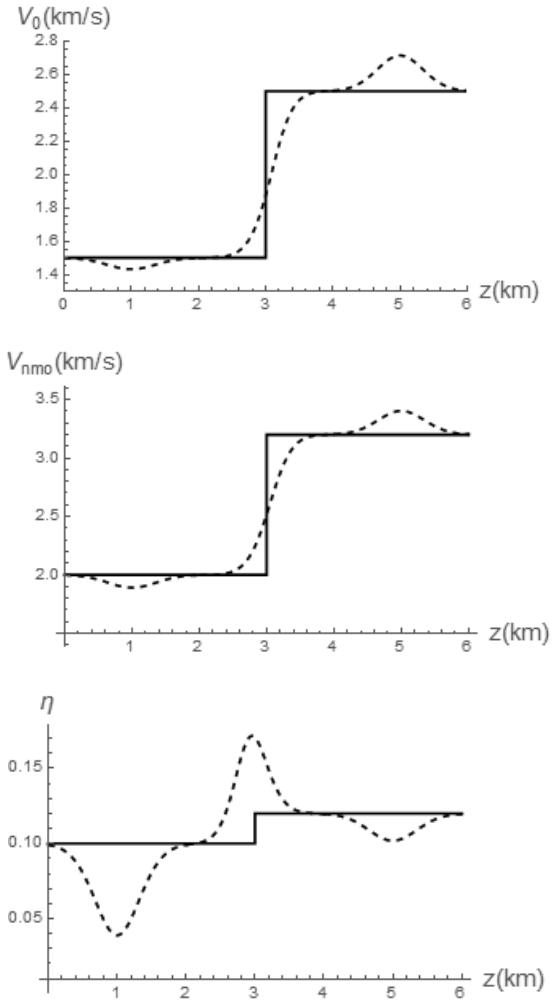

Figure 4.3. The model parameters V_0 (top), V_{nmo} (middle) and η (bottom) before and after smoothing for VTI model. The unsmoothed and smoothed parameters are shown by solid and dashed lines, respectively.

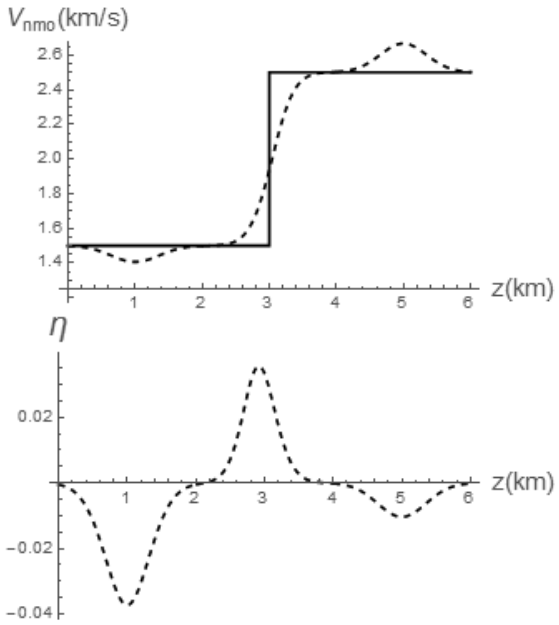

Figure 4.4. The kinematic parameters V_{nmo} (top) and η (bottom) computed for isotropic model.

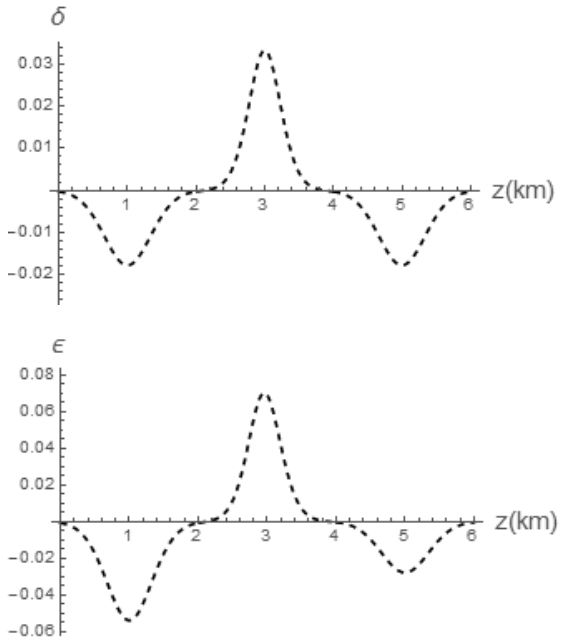

Figure 4.5. The smoothing induced anisotropy parameters δ (top) and ε (bottom) computed for isotropic model.

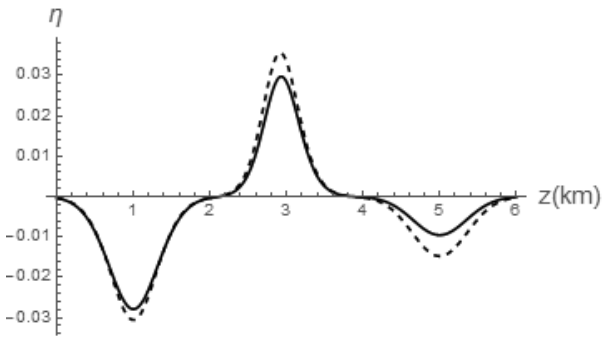

Figure 4.6. The induced anellipticity from EI (solid line) and ISO (dashed line) models.

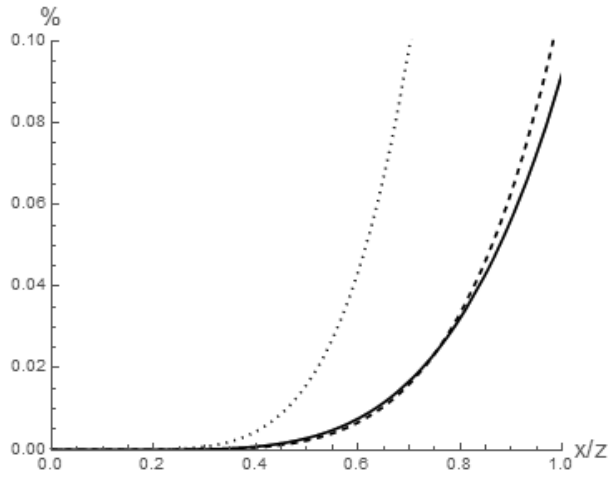

Figure 4.7. The traveltime error between two models-smoothed and unsmoothed for VTI, elliptical isotropic (EI) and the isotropic (ISO) cases shown by solid, dashed and dotted lines, respectively.

4.3 Preserved traveltime smoothing in orthorhombic media without azimuth variation between the layers

The kinematic properties in ORT model without azimuth variation can be defined following Stovas (2015). The limited series for vertical slowness in ORT medium is given by

$$q(p_x, p_y) = \frac{1}{V_0} - \frac{p_x^2 V_{nmo1}^2}{2V_0} - \frac{p_y^2 V_{nmo2}^2}{2V_0} - \frac{(1+8\eta_1) p_x^4 V_{nmo1}^4}{8V_0} - \frac{(1+8\eta_2) p_y^4 V_{nmo2}^4}{8V_0} - \frac{(1+4\eta_{xy}) p_x^2 p_y^2 V_{nmo1}^2 V_{nmo2}^2}{4V_0} + ..., \tag{4.6}$$

where q, p_x and p_y denote the vertical and two horizontal projections of the slowness vector. The ORT medium parameters are vertical P wave velocity V_0, the NMO velocities V_{nmo1}, and V_{nmo2} are defined in the $[x,z]$ and $[y,z]$ symmetry planes, respectively. The cross-term parameter η_{xy} is defined in Stovas (2015),

$$\eta_{xy} = \sqrt{\frac{(1+2\eta_1)(1+2\eta_2)}{1+2\eta_3}} - 1, \tag{4.7}$$

where η_1, η_2 and η_3 are the anellipticity parameters defined in symmetry planes $[x,z]$, $[y,z]$, and $[x,y]$, respectively.

For ORT model with no azimuthal variation between the layers, we define the depth dependent composite parameters $\boldsymbol{n_j (j = 1..6)}$ are based on series coefficients in equation (4.6),

$$\begin{aligned} n_1(\xi) &= \frac{1}{V_0(\xi)}, \; n_2(\xi) = \frac{V_{nmo1}^2(\xi)}{V_0(\xi)}, \\ n_3(\xi) &= \frac{V_{nmo2}^2(\xi)}{V_0(\xi)}, \; n_4(\xi) = \frac{V_{nmo1}^4(\xi)(1+8\eta_1(\xi))}{V_0(\xi)}, \\ n_5(\xi) &= \frac{V_{nmo2}^4(\xi)(1+8\eta_2(\xi))}{V_0(\xi)}, \; n_6(\xi) = \frac{V_{nmo1}^2(\xi) V_{nmo2}^2(\xi)(1+4\eta_{xy}(\xi))}{V_0(\xi)}. \end{aligned} \tag{4.8}$$

Three parameters in equations (4.8) are low-order (two coefficients related to slowness squared and one constant term) while three others are high-order (related to slowness to power four).

The first five composite parameters in equations (4.8) are similar to the ones defined for a VTI model, and only parameter n_6 is different. To illustrate the smoothing, we define a two-

layer ORT model. The parameters for upper layer are $V_0 = 1.5km/s$, $V_{nmo1} = 2km/s$, $V_{nmo2} = 1.8km/s$, $\eta_1 = 0.1$, $\eta_2 = 0.15$ and $\eta_{xy} = 0.22$, and for lower layer are $V_0 = 2.5km/s$, $V_{nmo1} = 3.2km/s$, $V_{nmo2} = 2.8km/s$, $\eta_1 = 0.12$, $\eta_2 = 0.2$ and $\eta_{xy} = 0.2$. The thickness for both layers is 3 km. We show the smoothed composite parameters from equations (4.8) in Figure 4.8. From these plots, we can see that smoothing curves for composite parameters are very similar with the ones obtained in VTI case.

We convert the smoothed composite parameters into the model parameters by

$$\begin{aligned}
&\tilde{V}_0(\xi) = \frac{1}{\tilde{n}_1(\xi)},\ \tilde{V}_{nmo1}(\xi) = \sqrt{\frac{\tilde{n}_2(\xi)}{\tilde{n}_1(\xi)}},\ \tilde{V}_{nmo2}(\xi) = \sqrt{\frac{\tilde{n}_3(\xi)}{\tilde{n}_1(\xi)}},\\
&\tilde{\eta}_1(\xi) = \frac{\tilde{n}_4(\xi)\tilde{n}_1(\xi) - \tilde{n}_2^2(\xi)}{8\tilde{n}_2^2(\xi)},\ \tilde{\eta}_2(\xi) = \frac{\tilde{n}_5(\xi)\tilde{n}_1(\xi) - \tilde{n}_3^2(\xi)}{8\tilde{n}_3^2(\xi)},\\
&\tilde{\eta}_{xy}(\xi) = \frac{\tilde{n}_1(\xi)\tilde{n}_6(\xi) - \tilde{n}_2(\xi)\tilde{n}_3(\xi)}{4\tilde{n}_2(\xi)\tilde{n}_3(\xi)}.
\end{aligned} \tag{4.9}$$

The smoothed anellipicity parameter $\tilde{\eta}_3$ can be obtained from equation (4.7) by

$$\tilde{\eta}_3 = \frac{(1+2\tilde{\eta}_1)(1+2\tilde{\eta}_2) - (1+\tilde{\eta}_{xy})^2}{2(1+\tilde{\eta}_{xy})^2}. \tag{4.10}$$

We show the smoothing for three effective velocities V_0, V_{nmo1} and V_{nmo2} in Figure 4.9. From the plots, we can see that the smoothing curves are quite similar for these three effective velocities $\tilde{V}_0$, $\tilde{V}_{nmo1}$ and $\tilde{V}_{nmo2}$. The smoothing for anellipticity parameters including effective parameter computed from equation (4.10) is illustrated in Figure 4.10. One can see that the smoothing curves are very similar for parameters $\tilde{\eta}_1$, $\tilde{\eta}_2$ and $\tilde{\eta}_{xy}$, while slightly different for $\tilde{\eta}_3$.

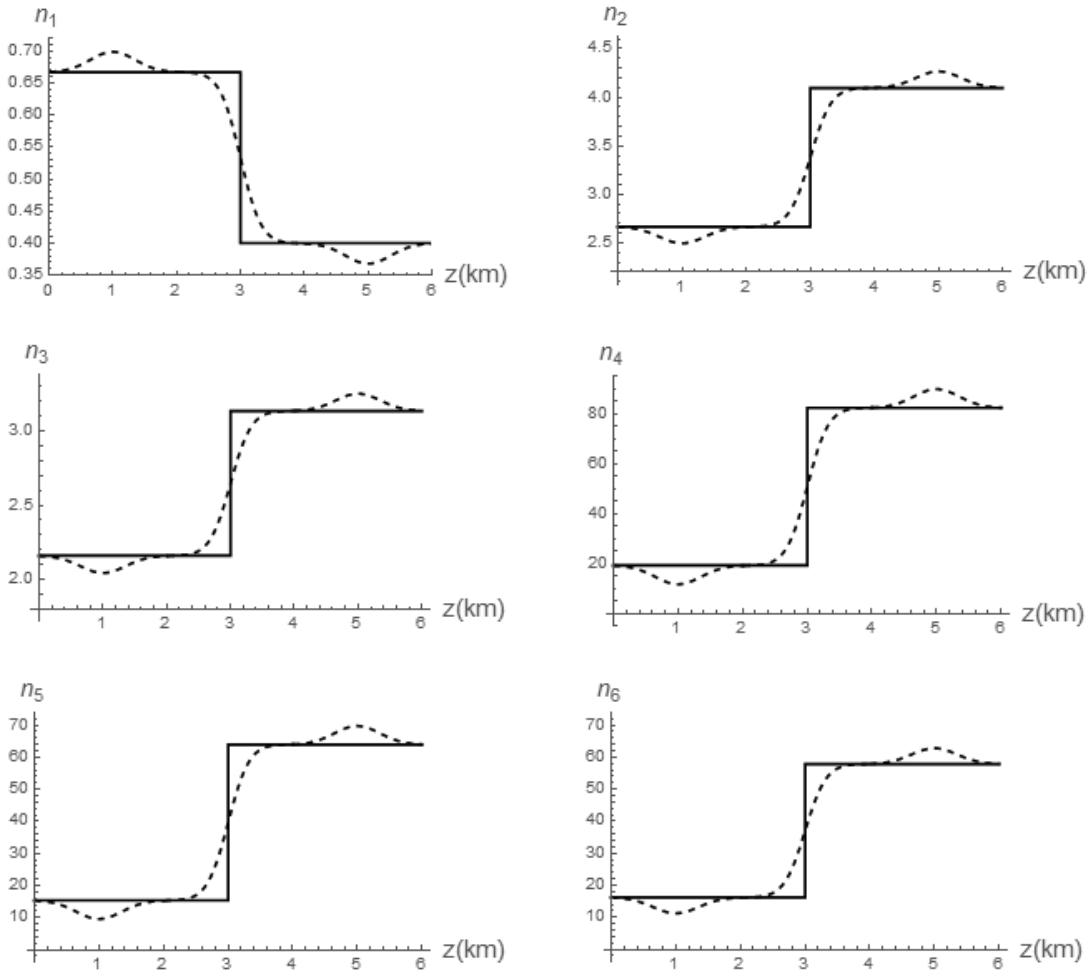

Figure 4.8. The composite parameters before and after smoothing for ORT model. The unsmoothed and smoothed parameters are shown by solid and dashed lines, respectively.

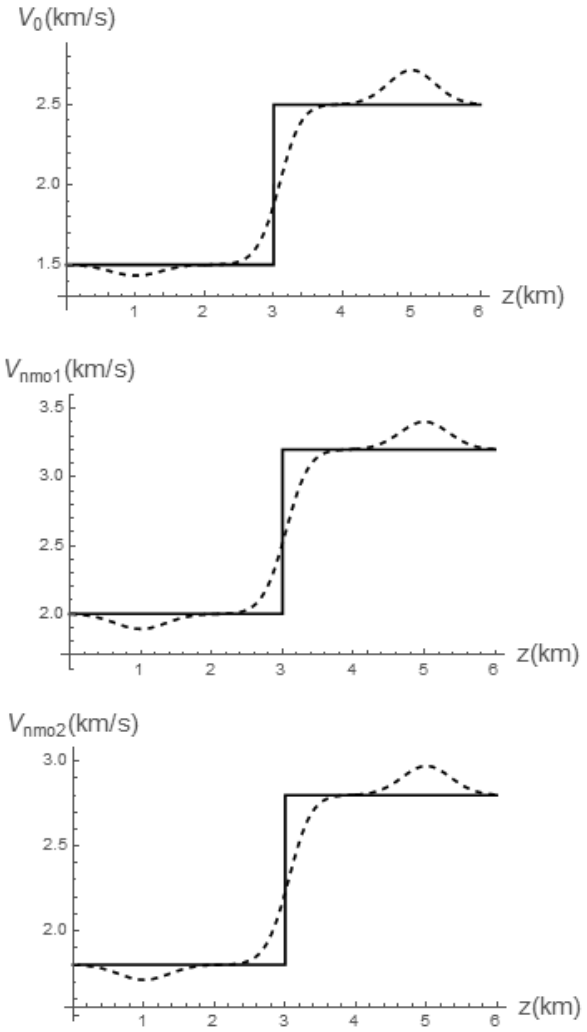

Figure 4.9. The model parameters V_0 (top), V_{nmo1} (middle) and V_{nmo2} (bottom) before and after smoothing for ORT model. The unsmoothed and smoothed parameters are shown by solid and dashed lines, respectively.

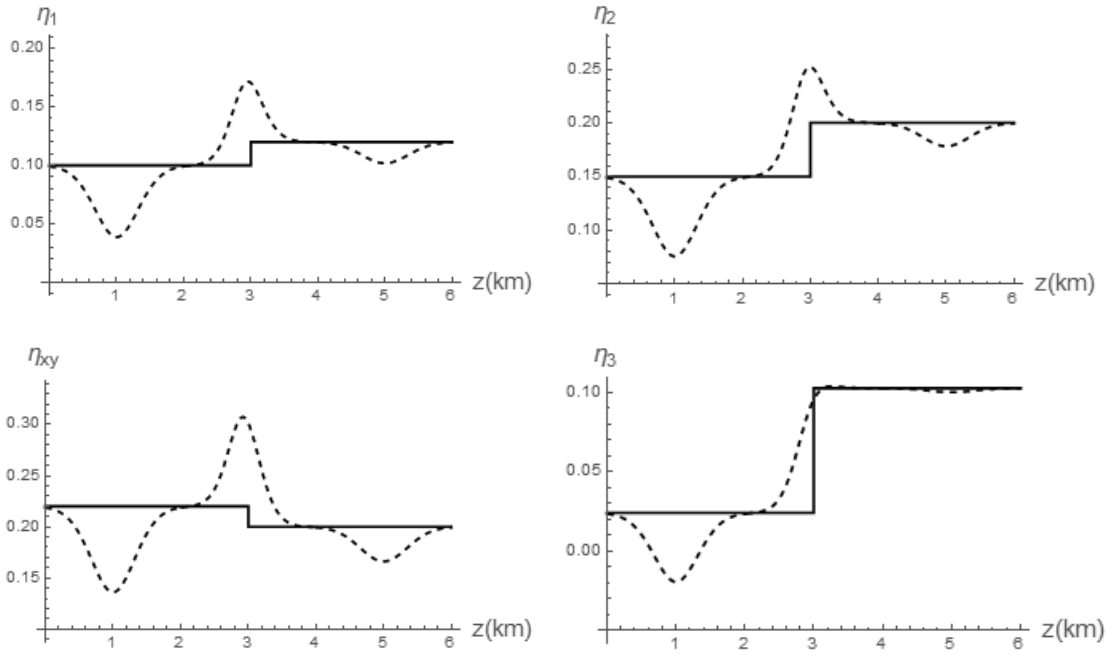

Figure 4.10. Four anellipticity parameters before and after smoothing for ORT model. The unsmoothed and smoothed parameters are shown by solid and dashed lines, respectively.

4.4 Preserved traveltime smoothing in orthorhombic media with azimuth variation between the layers

In case of azimuthal variation between ORT layers, we have to apply the rotation operator in X-Y plane by $\begin{pmatrix} \cos\phi & \sin\phi \\ -\sin\phi & \cos\phi \end{pmatrix}$ to equation (4.6) to specify the clockwise rotation azimuth.

The effective kinematic properties of the ORT model with the azimuth variation between layers can be found in Stovas (2015). The series for vertical slowness takes the form

$$
\begin{aligned}
q(p_x, p_y) = & \frac{1}{V_0} - \frac{1}{2V_0}(V_{nmo1}^2 \cos^2\phi + V_{nmo2}^2 \sin^2\phi) p_x^2 - \frac{1}{2V_0}(V_{nmo1}^2 \sin^2\phi + V_{nmo2}^2 \cos^2\phi) p_y^2 - \frac{1}{2V_0}(V_{nmo1}^2 - V_{nmo2}^2) \sin 2\phi \, p_x p_y \\
& - \frac{1}{8V_0}[(1+8\eta_1)V_{nmo1}^4 \cos^4\phi + (1+8\eta_2)V_{nmo2}^4 \sin^4\phi + \frac{1}{2}(1+4\eta_{xy})V_{nmo1}^2 V_{nmo2}^2 \sin^2 2\phi] p_x^4 \\
& - \frac{1}{4V_0}[(1+8\eta_1)V_{nmo1}^4 \cos^2\phi - (1+8\eta_2)V_{nmo2}^4 \sin^2\phi - (1+4\eta_{xy})V_{nmo1}^2 V_{nmo2}^2 \cos 2\phi] \sin 2\phi \, p_x^3 p_y \\
& - \frac{1}{16V_0}[3(1+8\eta_1)V_{nmo1}^4 \sin^2 2\phi + 3(1+8\eta_2)V_{nmo2}^4 \sin^2 2\phi + (1+4\eta_{xy})V_{nmo1}^2 V_{nmo2}^2 (1+3\cos 4\phi)] p_x^2 p_y^2 \\
& - \frac{1}{4V_0}[(1+8\eta_1)V_{nmo1}^4 \sin^2\phi - (1+8\eta_2)V_{nmo2}^4 \cos^2\phi + (1+4\eta_{xy})V_{nmo1}^2 V_{nmo2}^2 \cos 2\phi] \sin 2\phi \, p_x p_y^3 \\
& - \frac{1}{8V_0}[(1+8\eta_1)V_{nmo1}^4 \sin^4\phi + (1+8\eta_2)V_{nmo2}^4 \cos^4\phi + \frac{1}{2}(1+4\eta_{xy})V_{nmo1}^2 V_{nmo2}^2 \sin^2 2\phi] p_y^4 + ..,
\end{aligned}
\tag{4.11}
$$

where ϕ is specified as the azimuthal orientation of the vertical symmetry plane $[x, z]$ with respect to the global coordinate system.

In order to get the effective model parameters in this case, we smooth the composite parameters that are the series coefficients in equation (4.11). To convert the smoothed composite parameters into the models, we use two steps.

The equations for first four composite parameters from equation (4.11) are

$$
\begin{aligned}
& k_1 = \frac{1}{V_0}, \; k_2 = \frac{1}{V_0}(V_{nmo1}^2 \cos^2\phi + V_{nmo2}^2 \sin^2\phi), \\
& k_3 = \frac{1}{V_0}(V_{nmo1}^2 \sin^2\phi + V_{nmo2}^2 \cos^2\phi), \; k_4 = \frac{1}{V_0}(V_{nmo1}^2 - V_{nmo2}^2) \sin 2\phi,
\end{aligned}
\tag{4.12}
$$

These $k_j (j = 1..4)$ are smoothed into $\tilde{k}_j (j = 1..4)$ and can be converted into three smoothed velocities and effective azimuth Φ by following equations

$$
\begin{aligned}
& \tilde{V}_0 = \frac{1}{\tilde{k}_1}, \; \tilde{V}_{nmo1} = \sqrt{\frac{\tilde{k}_2 + \tilde{k}_3 + \sqrt{(\tilde{k}_2 - \tilde{k}_3)^2 + \tilde{k}_4^2}}{2\tilde{k}_1}}, \\
& \tilde{V}_{nmo2} = \sqrt{\frac{\tilde{k}_2 + \tilde{k}_3 - \sqrt{(\tilde{k}_2 - \tilde{k}_3)^2 + \tilde{k}_4^2}}{2\tilde{k}_1}}, \; \Phi = \frac{1}{2}\tan^{-1}(\frac{\tilde{k}_4}{\tilde{k}_2 - \tilde{k}_3}),
\end{aligned}
\tag{4.13}
$$

where $\tilde{V}_0$ is the effective P-wave vertical velocity, $\tilde{V}_{nmo1}$ and $\tilde{V}_{nmo2}$ are the effective NMO velocities in symmetry planes. A similar technique is discussed by Grechka and Tsvankin (1999a, 1999b). Φ stands for the effective azimuthal orientation.

To illustrate the first step, we define an azimuth dependent ORT model ORT_ϕ by using the same two layer ORT model as above with zero azimuth $\phi = 0^\circ$ in upper layer and $\phi = 30^\circ$ in lower layer. The composite parameters $k_j\,(j = 1,4)$ before and after smoothing are shown in Figure 4.11. We can see that the curves are very similar with the ones before. The effective velocities $\tilde{V}_0$, $\tilde{V}_{nmo1}$, $\tilde{V}_{nmo2}$ and azimuth Φ are shown in Figure 4.12. From comparison of Figures 4.9 and 4.12, one can see that the presence of azimuth variation between the layers does not significantly affect the smoothed NMO velocities $\tilde{V}_{nmo1}$ and $\tilde{V}_{nmo2}$. However, there is a difference in V_{nmo1} and V_{nmo2} between two cases of about 20 m/s with and without the azimuth variation between the layers. This difference for V_{nmo1} and V_{nmo2} has opposite sign.

In the second step, we solve the overdetermined system of the linear equations when estimating the effective anellipticity parameters. We apply the least-squares method (Stovas 2015) to evaluate the effective parameters $\tilde{\eta}_1$, $\tilde{\eta}_2$ and $\tilde{\eta}_{xy}$. First, we define the effective anellipticity vector $\mathrm{N} = (\tilde{\eta}_1, \tilde{\eta}_2, \tilde{\eta}_{xy})^T$. The linear system of equations can be written in matrix form,

$$\mathbf{UN} = \mathbf{DS}, \tag{4.14}$$

where the effective NMO slowness vector is defined as

$$\mathbf{S} = \left(\frac{1}{\tilde{V}_{nmo1}^4}, \frac{1}{\tilde{V}_{nmo2}^4}, \frac{1}{\tilde{V}_{nmo1}^2 \tilde{V}_{nmo2}^2}\right)^T, \tag{4.15}$$

and the azimuthal matrix $\mathbf{U(\Phi)}$ is given by

$$\mathbf{U} = \begin{pmatrix} 2\cos^4\Phi & 2\sin^4\Phi & 2\sin^2\Phi\cos^2\Phi \\ 2\sin 2\Phi\cos^2\Phi & -2\sin 2\Phi\sin^2\Phi & -\cos 2\Phi\sin 2\Phi \\ 6\sin^2 2\Phi & 6\sin^2 2\Phi & 1+3\cos 4\Phi \\ 2\sin 2\Phi\sin^2\Phi & -2\sin 2\Phi\cos^2\Phi & \cos 2\Phi\sin 2\Phi \\ 2\sin^4\Phi & 2\cos^4\Phi & 2\sin^2\Phi\cos^2\Phi \end{pmatrix}. \tag{4.16}$$

Note that the effective smoothed NMO velocities $\tilde{V}_{nmo1}$ and $\tilde{V}_{nmo2}$ and the effective azimuth Φ are precomputed in equations (4.13).

The least squares method gives the solution of equation (14) as follows

$$\begin{aligned} &\mathbf{N} = \mathbf{GS}, \\ &\mathbf{G} = \mathbf{FD}, \\ &\mathbf{F} = (\mathbf{U}^T\,\mathbf{U})^{-1}\,\mathbf{U}^T, \end{aligned} \tag{4.17}$$

where **F** is 3×5 matrix and **D**=(d_{ij}) is 5×3 matrix. The elements of matrix **D** are defined in Appendix A.

If there is no azimuth variation between the layers $(\phi = 0^\circ)$ or there is 90° azimuth variation $(\phi = \pi/2)$, matrix **F** has only three nonzero elements. The solution for effective anellipticity vector $\mathbf{N}$ reduced to the one defined in equations (4.9).

In order to smooth the parameters in this case, we need to define the matrix elements d_{ij}, $(i = 1..5; j = 1..3)$ (Appendix A) and smooth each of these parameters by using the PTS method described above. The effective velocities and effective azimuth are substituted from the computation in step one. The smoothed effective anellipticity parameters are computed from equations (4.17).

The effective anellipticity parameters in ORT_ϕ model are shown in Figure 4.13. Being compared with the results from ORT model, the smoothing curves for parameters $\tilde{\eta}_1$, $\tilde{\eta}_2$ and

$\tilde{\eta}_{xy}$ in ORT_{ϕ} model are similar but with different amplitudes, larger for $\tilde{\eta}_1$ and $\tilde{\eta}_{xy}$, but smaller for $\tilde{\eta}_2$. The smoothed parameter $\tilde{\eta}_3$ is very different for models ORT and ORT_{ϕ}.

Note that the application of PTS method in ORT and ORT_{ϕ} models results in smoothing induced anellipticity. We illustrate that by using two models with $(\eta_1 = \eta_2 = \eta_{xy} = 0)$ without (EI) and with (EI_{ϕ}) azimuth variations. The smoothing induced anelliptic parameters for EI and EI_{ϕ} models are shown in Figure 4.14. We can see that the magnitude anelliptic parameters η_1 and η_2 is different for these models, while for parameter η_{xy} is very similar. The biggest anomaly for smoothing induced anelliptic parameters is always located at the interface depth.

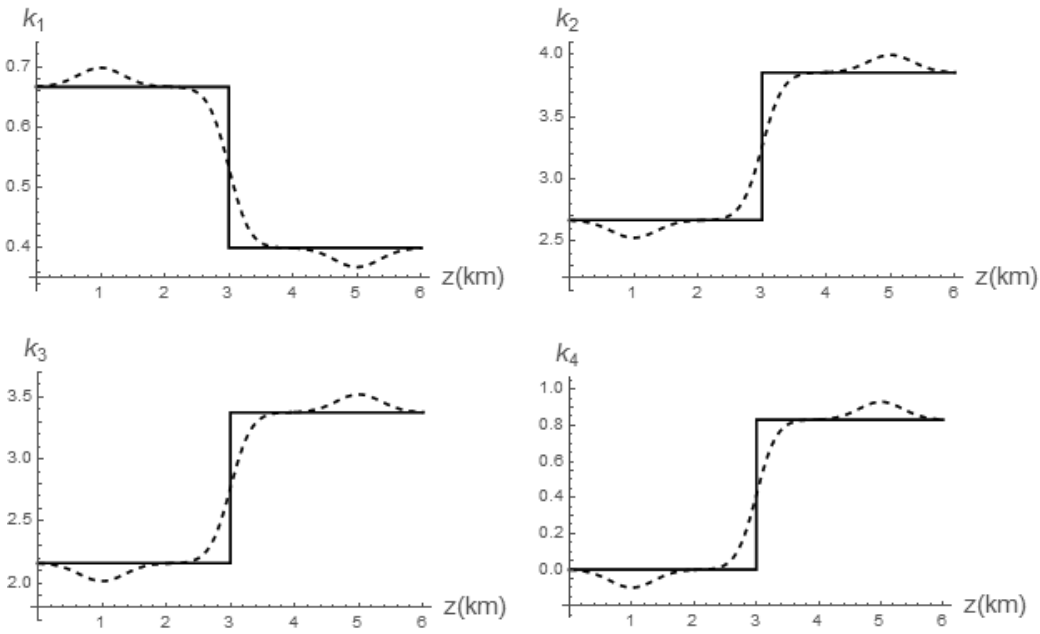

Figure 4.11. The composite parameters before and after smoothing for ORT_{ϕ} model. The unsmoothed and smoothed parameters are shown by solid and dashed lines, respectively.

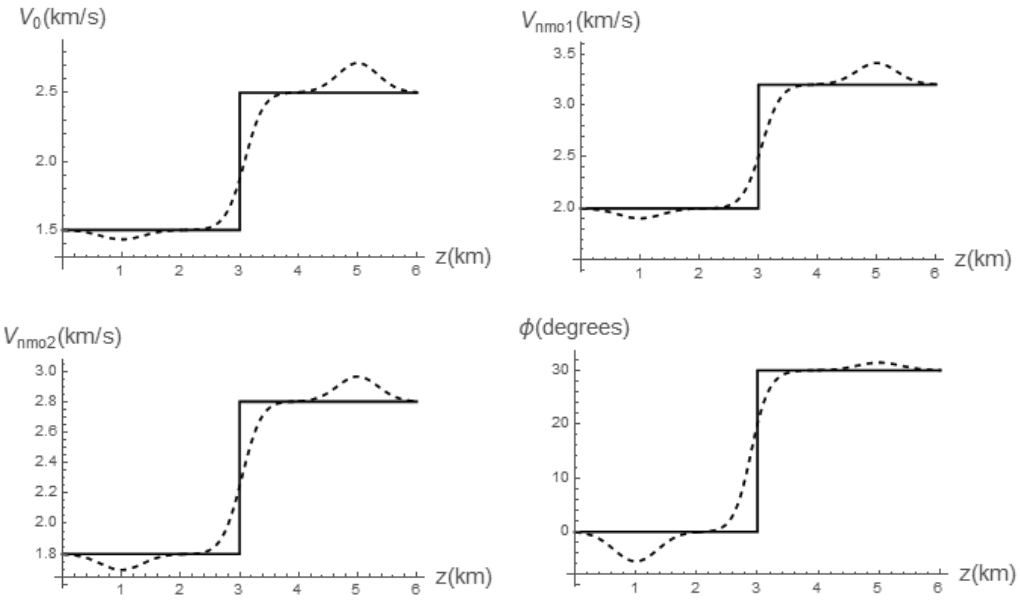

Figure 4.12. The effective velocities and effective azimuth before and after smoothing for ORT_{ϕ} model. The unsmoothed and smoothed parameters are shown by solid and dashed lines, respectively.

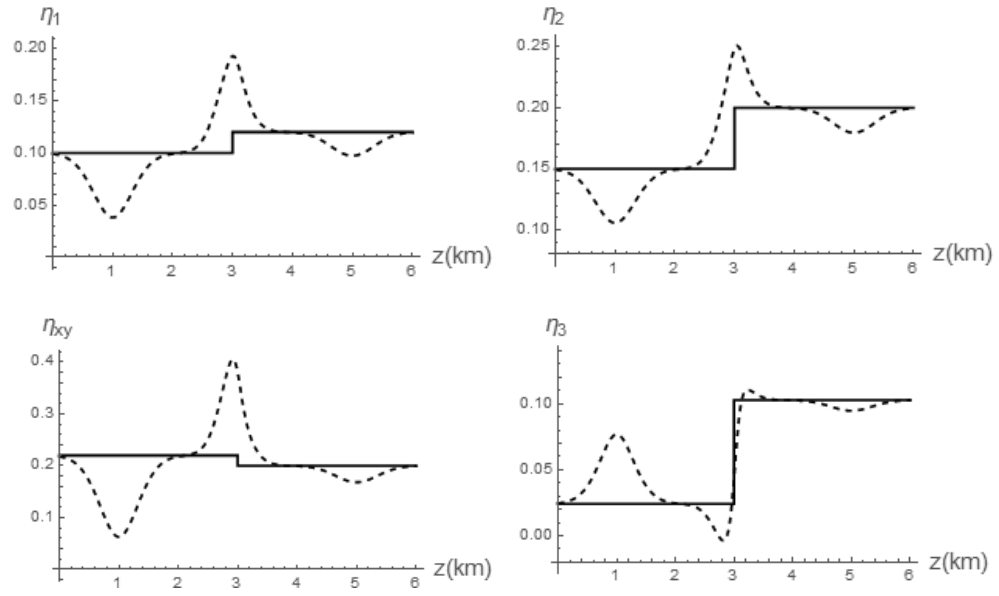

Figure 4. 13. Four anellipticity parameters before and after smoothing for ORT_{ϕ} model. The unsmoothed and smoothed parameters are shown by solid and dashed lines, respectively.

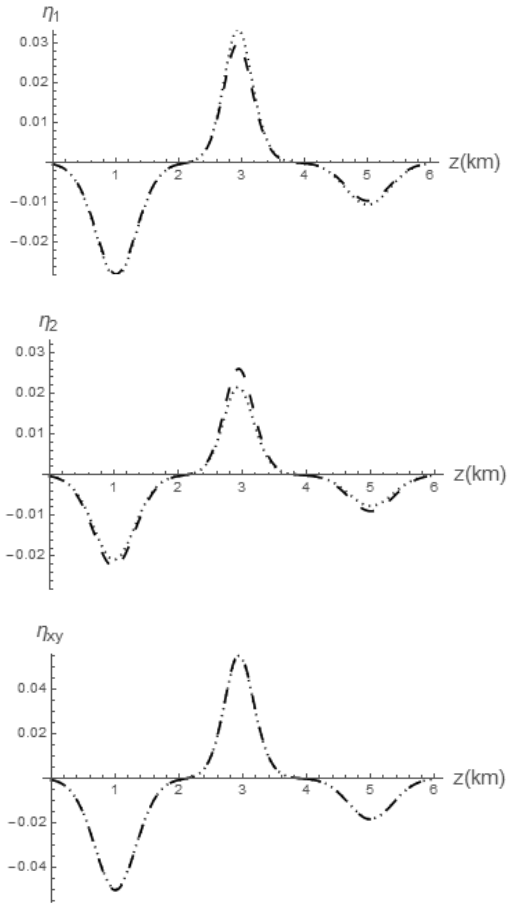

Figure 4.14. The PTS results in smoothing induced anellipticity, η_1 (top), η_2 (middle) and η_{xy} (bottom). The anellipticity from the ORT model and ORT_ϕ model are shown in dashed and dotted lines, respectively.

4.5 The accuracy in traveltime

To illustrate the accuracy by the PTS method for ORT model, we use the parametric offset-traveltime equations (Stovas, 2015):

$$
\begin{aligned}
X(p_x,p_y) &= p_x\int_0^z \frac{V_{nmo1}^2}{f_1^{1/2}f_2^{3/2}V_0}F_2 d\xi,\\
Y(p_x,p_y) &= p_y\int_0^z \frac{V_{nmo2}^2}{f_1^{1/2}f_2^{3/2}V_0}F_1 d\xi,\\
T(p_x,p_y) &= \int_0^z \frac{F_1 p_y^2 V_{nmo2}^2 + F_2 p_x^2 V_{nmo1}^2 + f_1 f_2}{f_1^{1/2}f_2^{3/2}V_0} d\xi,
\end{aligned}
\tag{4.18}
$$

where X and Y are corresponding offset projections, and

$$
\begin{aligned}
F_1(\xi) &= \left(p_x^2 V_{nmo1}^2(\xi)(2\eta_1(\xi)-\eta_{xy}(\xi))-1\right)^2,\\
F_2(\xi) &= \left(p_y^2 V_{nmo2}^2(\xi)(2\eta_2(\xi)-\eta_{xy}(\xi))-1\right)^2,\\
f_1(\xi) &= 1-(1+2\eta_1(\xi))p_x^2 V_{nmo1}^2(\xi)-(1+2\eta_2(\xi))p_y^2 V_{nmo2}^2(\xi)\\
&\quad +((1+2\eta_1(\xi))(1+2\eta_2(\xi))-(1+\eta_{xy}(\xi))^2)p_x^2 p_y^2 V_{nmo1}^2(\xi)V_{nmo2}^2(\xi),\\
f_2(\xi) &= 1-2\eta_1(\xi)p_x^2 V_{nmo1}^2(\xi)-2\eta_2 p_y^2 V_{nmo2}^2(\xi)+(4\eta_1(\xi)\eta_2(\xi)-\eta_{xy}^2(\xi))p_x^2 p_y^2 V_{nmo1}^2(\xi)V_{nmo2}^2(\xi).
\end{aligned}
\tag{4.19}
$$

We compute the relative traveltime error due to smoothing for ORT and EI (Figure 4.15) and ORT_ϕ and EI_ϕ (Figure 4.16) models. From comparison of the error plots, one can see that the error for ORT_ϕ and EI_ϕ models are similar with the one from ORT and EI models. The traveltime error for EI is larger than the error for ORT model, and the error for EI_ϕ model is also larger than the one for ORT_ϕ model. For all the models, the maximal traveltime error is very small.

In order to make a comparison, we also plot the traveltime errors by using the conventional smoothing for ORT and EI (Figure 4.17) models and ORT_ϕ and EI_ϕ (Figure 4.18) models. Different from the PTS, the model parameters ($1/V_0, \delta_1, \delta_2, \varepsilon_1, \varepsilon_2$ and δ_3) are smoothed directly in conventional smoothing using the same smoothing operator in equation (4.3), δ_i and ε_i ($i=1,2$) are the Thomsen parameters in the corresponding symmetry planes. δ_3 is the anisotropy parameter defined by Vasconcelos and Tsvankin (2006),

$$\delta_3 = \frac{\varepsilon_2 - \varepsilon_1 - \eta_3 - 2\varepsilon_1\eta_3}{(1+2\varepsilon_1)(1+2\eta_3)}. \tag{4.20}$$

Compared with the errors in PTS, the conventional smoothing results in larger error for long offset for all these four models.

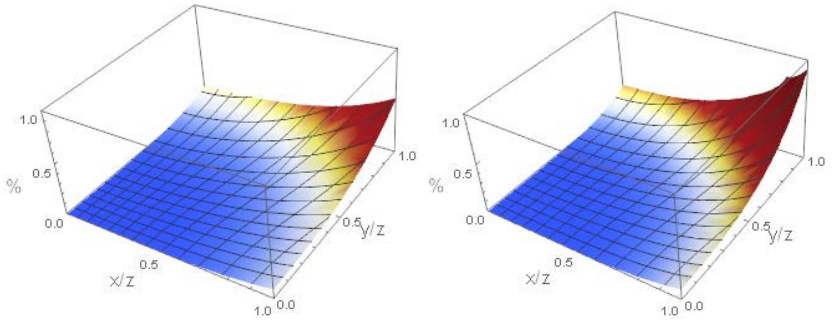

Figure 4.15. The traveltime error surface for ORT model (left) and EI model (right).

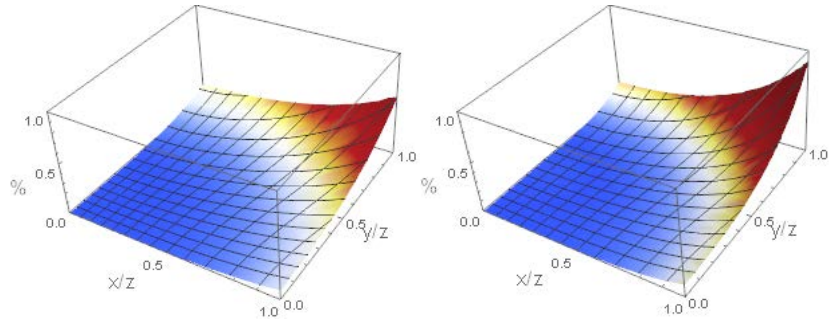

Figure 4.16. The traveltime error surface for ORT_ϕ model (top) and EI_ϕ model (bottom).

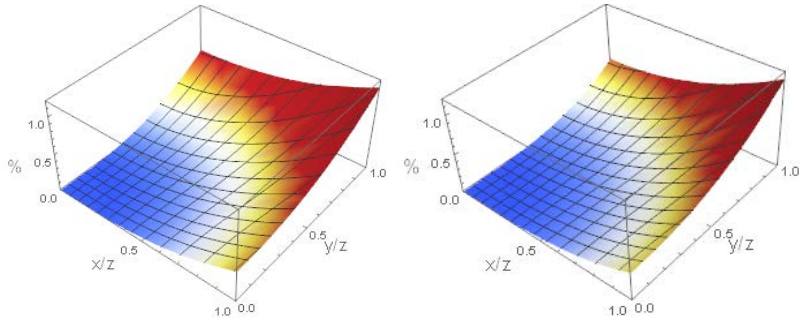

Figure 4.17. The traveltime error surface using conventional smoothing for ORT model (top) and EI model (bottom).

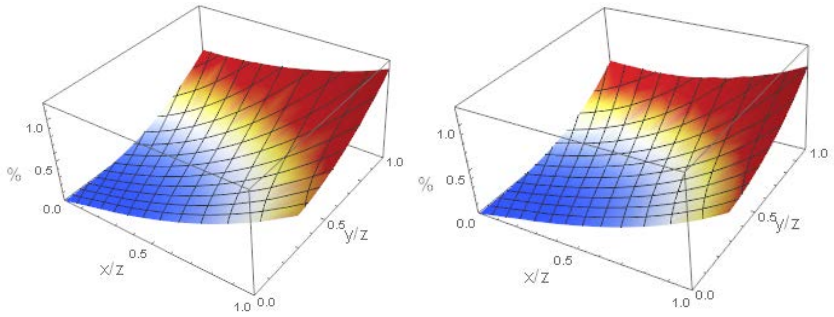

Figure 4.18. The traveltime error surface using conventional smoothing for ORT_{ϕ} model (top) and EI_{ϕ} model (bottom).

4.6 Conclusions

We develop the preserved traveltime smoothing method (PTS) for ORT velocity model without and with azimuthal variation between the layers. Smoothing is performed for composite parameters that are different for ORT and ORT_{ϕ} models. In computation of anelliptic parameters for ORT_{ϕ} model, the least squares method is used. We show that PTS results in smoothing induced anellipticity and illustrate that for EI and EI_{ϕ} models. The traveltime errors due to smoothing are sufficiently small for all the models.

4.7 Acknowledgments

We would like to acknowledge China Scholarship Council (CSC) and ROSE project for financial support.

4.8 Appendix A

In order to smooth the model parameters by PTS method, we need to define the elements of matrix **D**, which represent the composite parameters for ORT_{ϕ} model (Stovas, 2015)

$$
\begin{aligned}
d_{11} &= \frac{1}{V_0(\xi)}(1+8\eta_1(\xi))V_{nmo1}^4(\xi)\cos^4\phi, \\
d_{12} &= \frac{1}{V_0(\xi)}(1+8\eta_2(\xi))V_{nmo2}^4(\xi)\sin^4\phi, \\
d_{13} &= \frac{1}{V_0(\xi)}(1+4\eta_{xy}(\xi))V_{nmo1}^2(\xi)V_{nmo2}^2(\xi)\sin^2\phi\cos^2\phi, \\
d_{21} &= \frac{1}{V_0(\xi)}(1+8\eta_1(\xi))V_{nmo1}^4(\xi)\cos^2\phi\sin 2\phi, \\
d_{22} &= \frac{1}{V_0(\xi)}(1+8\eta_2(\xi))V_{nmo2}^4(\xi)\sin^2\phi\sin 2\phi, \\
d_{23} &= \frac{1}{V_0(\xi)}(1+4\eta_{xy}(\xi))V_{nmo1}^2(\xi)V_{nmo2}^2(\xi)\cos 2\phi\sin 2\phi, \\
d_{31} &= \frac{1}{V_0(\xi)}(1+8\eta_1(\xi))V_{nmo1}^4(\xi)\sin^2 2\phi, \\
d_{32} &= \frac{1}{V_0(\xi)}(1+8\eta_2(\xi))V_{nmo2}^4(\xi)\sin^2 2\phi, \\
d_{33} &= \frac{1}{V_0(\xi)}(1+4\eta_{xy}(\xi))V_{nmo1}^2(\xi)V_{nmo2}^2(\xi)(1+3\cos 4\phi), \\
d_{41} &= \frac{1}{V_0(\xi)}(1+8\eta_1(\xi))V_{nmo1}^4(\xi)\sin^2\phi\sin 2\phi, \\
d_{42} &= \frac{1}{V_0(\xi)}(1+8\eta_2(\xi))V_{nmo2}^4(\xi)\cos^2\phi\sin 2\phi, \\
d_{43} &= \frac{1}{V_0(\xi)}(1+4\eta_{xy}(\xi))V_{nmo1}^2(\xi)V_{nmo2}^2(\xi)\cos 2\phi\sin 2\phi, \\
d_{51} &= \frac{1}{V_0(\xi)}(1+8\eta_1(\xi))V_{nmo1}^4(\xi)\sin^4\phi, \\
d_{52} &= \frac{1}{V_0(\xi)}(1+8\eta_2(\xi))V_{nmo2}^4(\xi)\cos^4\phi, \\
d_{53} &= \frac{1}{V_0(\xi)}(1+4\eta_{xy}(\xi))V_{nmo1}^2(\xi)V_{nmo2}^2(\xi)\sin^2\phi\cos^2\phi,
\end{aligned}
\tag{4.A1}
$$

where V_0 is the P-wave vertical velocity, the NMO velocities V_{nmo1}, and V_{nmo2} are defined in the $[x,z]$and $[y,z]$symmetry planes, respectively. The cross-term parameter η_{xy} is defined in equation (4.7). Azimuth angle ϕ is specified as the azimuthal orientation of the vertical symmetry plane $[x,z]$ with respect to the global coordinate system.

We smooth the composite parameters shown in equation (4.A1) and substitute the results into the elements of matrix $\mathbf{D}$ as follows,

$$
\begin{aligned}
D_{11} &= \frac{1}{4}(\tilde{V}_0\tilde{d}_{11} - \tilde{V}_{nmo1}^4\cos^4\Phi),\\
D_{12} &= \frac{1}{4}(\tilde{V}_0\tilde{d}_{12} - \tilde{V}_{nmo2}^4\sin^4\Phi),\\
D_{13} &= \frac{1}{2}(\tilde{V}_0\tilde{d}_{13} - \tilde{V}_{nmo1}^2\tilde{V}_{nmo2}^2\sin^2\Phi\cos^2\Phi),\\
D_{21} &= \frac{1}{4}(\tilde{V}_0\tilde{d}_{21} - \tilde{V}_{nmo1}^4\cos^2\Phi\sin 2\Phi),\\
D_{22} &= \frac{1}{4}(-\tilde{V}_0\tilde{d}_{22} + \tilde{V}_{nmo2}^4\sin^2\Phi\sin 2\Phi),\\
D_{23} &= \frac{1}{4}(-\tilde{V}_0\tilde{d}_{23} + \tilde{V}_{nmo1}^2\tilde{V}_{nmo2}^2\cos 2\Phi\sin 2\Phi),\\
D_{31} &= \frac{3}{4}(\tilde{V}_0\tilde{d}_{31} - \tilde{V}_{nmo1}^4\sin^2 2\Phi),\\
D_{32} &= \frac{3}{4}(\tilde{V}_0\tilde{d}_{32} - \tilde{V}_{nmo2}^4\sin^2 2\Phi),\\
D_{33} &= \frac{1}{4}(\tilde{V}_0\tilde{d}_{33} - \tilde{V}_{nmo1}^2\tilde{V}_{nmo2}^2(1+3\cos 4\Phi)),\\
D_{41} &= \frac{1}{4}(\tilde{V}_0\tilde{d}_{41} - \tilde{V}_{nmo1}^4\sin^2\Phi\sin 2\Phi),\\
D_{42} &= \frac{1}{4}(-\tilde{V}_0\tilde{d}_{42} + \tilde{V}_{nmo2}^4\cos^2\Phi\sin 2\Phi),\\
D_{43} &= \frac{1}{4}(\tilde{V}_0\tilde{d}_{43} - \tilde{V}_{nmo1}^2\tilde{V}_{nmo2}^2\cos 2\Phi\sin 2\Phi),\\
D_{51} &= \frac{1}{4}(\tilde{V}_0\tilde{d}_{51} - \tilde{V}_{nmo1}^4\sin^4\Phi),\\
D_{52} &= \frac{1}{4}(\tilde{V}_0 d_{52} - \tilde{V}_{nmo2}^4\cos^4\Phi),\\
D_{53} &= \frac{1}{2}(\tilde{V}_0 d_{53} - \tilde{V}_{nmo1}^2\tilde{V}_{nmo2}^2\sin^2\Phi\cos^2\Phi).
\end{aligned}
\tag{4.A2}
$$

where the effective velocities $\tilde{V}_0$, $\tilde{V}_{nmo1}$, $\tilde{V}_{nmo2}$ and the effective azimuth Φ are already computed in equation (4.13).

Chapter 5 A new parameterization for acoustic orthorhombic media

Shibo Xu and Alexey Stovas

Norwegian University of Science and Technology, Trondheim, Norway

Abstract. We define a group of new parameterizations for P-wave in acoustic orthorhombic (ORT) media with three cross-term normal moveout (NMO) velocities and three cross-term anellipticity parameters. The corresponding perturbation-based approximations for traveltime in ORT model are developed using the new parameterizations. The perturbation coefficients are computed by solving the eikonal equation in corresponding parameterization. Eight types of parameterization are defined based on different elliptical background model and selection of anellipticity parameters. As the traveltime can be converted from the group velocity inverse, the sensitivity of the group velocity inverse to anellipticity parameters is analyzed for different parameterizations and different range of offsets. To stabilize the perturbation series and improve the accuracy, the Shanks transform is applied. From the comparison of traveltime after the Shanks transform using different parameterizations, we conclude that the parameterization with vertical, two horizontal velocities, and three cross-term anellipticity parameters results in the best accuracy of traveltime function for P-wave in acoustic ORT medium.

Presented at the 87th SEG Conference and Exhibition, September, 2017, Houston, USA; Published in Geophysics in October 2017.

5.1 Introduction

The traveltime approximations are commonly used in seismic data processing such as velocity analysis, modeling and time migration (Yilmaz, 2001; Červený, 2001). The estimation for model parameters in velocity analysis depends on the accuracy of the traveltime approximation. For time domain migration, the accuracy of the result is also depend on the traveltime approximation used in modeling part. In homogeneous isotropic or elliptical isotropic media, the moveout function has a hyperbolic form. We need to take non-hyperbolicity (driven by anellipticity parameters) into consideration, as it commonly exists and plays an important role in seismic data processing and interpretation, especially for large offsets. The moveout function has a non-hyperbolic form in anisotropic media. Non-hyperbolic (long-spread) moveout is often used in velocity analysis of P-waves in transversely isotropic media with a vertical symmetry axis (VTI). The P-wave time domain signature in VTI model depends on two interval parameters: normal moveout (NMO) velocity from a horizontal reflector and the anellipticity coefficient η (Alkhalifah and Tsvankin, 1995; Tsvankin, 2005). Different nonhyperbolic moveout approximations for a homogeneous VTI are listed and discussed in Fowler (2003), Fomel (2004) and Golikov and Stovas (2012). Fomel and Stovas (2010) derived a generalized nonhyperbolic moveout approximation (GMA) for the traveltime approximation defined from zero-offset and one nonzero-offset ray computation. Alkhalifah (2011) proposed the traveltime expression with series in terms of anelliptic parameter η by solving the eikonal equation for acoustic VTI medium and by applying the Shanks transform to obtain the higher accuracy.

The orthorhombic (ORT) model is introduced by Schoenberg and Helbig (1997) to describe fractured reservoirs and explains well the azimuthal dependency in surface seismic data. Tsvankin (1997, 2012) defined nine elastic model parameters for ORT model that can be reduced to six parameters in an acoustic approximation (Alkhalifah, 2003). The first order

curvatures are defined by the normal moveout (NMO) velocity ellipse (Grechka and Tsvankin, 1999a, 1999b), and the second order curvatures are defined by the azimuth-dependent anellipticity. Vasconcelos and Tsvankin (2006) derived the nonhyperbolic moveout of P-wave in orthorhombic media using the NMO velocities V_{n1} and V_{n2} defined in vertical symmetry planes, and the anellipticity parameters η_1, η_2 and η_3 defined in all three symmetry planes. Note that η_1 are η_2 the anellipticity parameters (Tsvankin, 1997) defined in $[XOZ]$ and $[YOZ]$ symmetry planes, η_3 is the anellipticity parameter defined in $[XOY]$ plane (Vasconcelos and Tsvankin, 2006). Stovas (2015) derived the azimuthally dependent kinematic properties of the orthorhombic media and introduced new anellipticity parameter η_{xy}. Sripanich and Fomel (2015) modified the anelliptic functional form of Fomel (2004) and extended it to ORT model to approximate P-wave phase and group velocities. Alkhalifah (2013) and Masmoudi and Alkhalifah (2014) develop this concept to approximate traveltime in horizontal transversely isotropic (HTI) media with arbitrary symmetry-axis azimuth ϕ and estimate the anisotropy parameter η and the azimuthal angle ϕ. The perturbation based moveout approximation with a traditional elliptic background for ORT media is discussed by Stovas et al (2016). The traveltime approximation for the orthorhombic model using perturbation theory by other anellipticity parameters in inhomogeneous background medium is developed by Masmoudi and Alkhalifah (2016). Xu et al. (2016) proposed a new set of moveout approximations based on the perturbation series in anellipticity parameter using the alternative elliptical background model defined by vertical and horizontal velocities in a homogeneous ORT media. A horizontally layered ORT medium with parameters compouted for the fourth-order moveout is studies in (Ravve and Koren, 2017; Koren and Ravve, 2017). Different parameterization impacts the accuracy of the traveltime approximation due to different proportion in perturbation parameters (anellipticity parameters) and the anisotropy estimation in velocity analysis depends on the accuracy of the traveltime approximation. The

subsurface parameterization also plays an important role in sensitivity and trade-off analysis for full waveform inversion (FWI) in acoustic anisotropic medium (Alkhalifah and Plessix, 2014) and (Gholami et al, 2013).

In this paper, we define new parameterizations for acoustic ORT medium with different combinations of elliptical background and anellipticity coefficients. The list of parameterization including eight different ones is split into symmetric and non-symmetric groups. The sensitivity analysis to anellipticity parameters at near-, mid- and far-offset is performed for the group velocity inverse. The parameterization with vertical and two horizontal velocities and three cross-term anellipticity parameters results in the most accurate approximation based on Shanks transform as it shown in the numerical example.

5.2 A new parameterization for an acoustic ORT model

The symmetry behavior of the orthorhombic (ORT) model is commonly used to describe the fractured formation. ORT media have three mutually orthogonal symmetry planes: two vertical and one horizontal. Six model parameters are defined for acoustic ORT model (Alkhalifah, 2003). Vasconcelos and Tsvankin (2006) represent the ORT model by the vertical velocity V_0, two NMO velocities V_{n1} and V_{n2} that defined in corresponding $[XOZ]$ and $[YOZ]$ symmetry planes and three anellipticity parameters η_1, η_2 and η_3 defined in $[XOZ]$, $[YOZ]$ and $[XOY]$ symmetry planes, respectively. Stovas (2015) developed azimuthally dependent properties of the acoustic ORT model using the parameters V_0, V_{n1}, V_{n2}, η_1, η_2 and η_{xy}.

In this paper, we define three cross-term anellipticity parameters η_{xy}, η_{xz} and η_{yz} (Figure 5.1, left) by

$$\eta_{xy} = \sqrt{\frac{(1+2\eta_1)(1+2\eta_2)}{(1+2\eta_3)}} - 1,$$
$$\eta_{xz} = \sqrt{\frac{(1+2\eta_1)(1+2\eta_3)}{(1+2\eta_2)}} - 1, \tag{5.1}$$
$$\eta_{yz} = \sqrt{\frac{(1+2\eta_2)(1+2\eta_3)}{(1+2\eta_1)}} - 1.$$

Note that the cross term η_{xy} is defined by Stovas (2015). Each cross-term anellipticity parameter is represented by all three anellipticity parameters (η_1, η_2 and η_3) from corresponding symmetry plane. The inverse transformations of anellipticity parameters are given by

$$\eta_1 = \frac{(1+\eta_{xy})(1+\eta_{xz})-1}{2},$$
$$\eta_2 = \frac{(1+\eta_{xy})(1+\eta_{yz})-1}{2}, \tag{5.2}$$
$$\eta_3 = \frac{(1+\eta_{xz})(1+\eta_{yz})-1}{2}.$$

The NMO velocities in ORT model (Figure 5.1, right) are defined by the curvatures in corresponding symmetry planes

$$V_{n01}^2 = \frac{V_{h1}^2}{1+2\eta_1}, V_{n02}^2 = \frac{V_{h2}^2}{1+2\eta_2}, V_{n10}^2 = \frac{V_0^2}{1+2\eta_1},$$
$$V_{n12}^2 = \frac{V_{h2}^2}{1+2\eta_3}, V_{n20}^2 = \frac{V_0^2}{1+2\eta_2}, V_{n21}^2 = \frac{V_{h1}^2}{1+2\eta_3}. \tag{5.3}$$

Note that here $V_{n01} = V_{n1}$ and $V_{n02} = V_{n2}$. We define new NMO velocities by the geometrical averaging of corresponding NMO velocities from equation 5.3,

$$V_{12}^2 = V_{n01}V_{n02} = \frac{V_{h1}V_{h2}}{\sqrt{(1+2\eta_1)(1+2\eta_2)}},$$
$$V_{13}^2 = V_{n10}V_{n12} = \frac{V_0 V_{h2}}{\sqrt{(1+2\eta_1)(1+2\eta_3)}}, \tag{5.4}$$
$$V_{23}^2 = V_{n20}V_{n21} = \frac{V_0 V_{h1}}{\sqrt{(1+2\eta_2)(1+2\eta_3)}}.$$

The definition of the indices is slightly different for NMO velocities. For the NMO velocities V_{nij}, i and j are corresponding to the axis since we use V_0 for vertical velocity, V_1 and V_2 for two horizontal velocities, respectively. The indices for cross-term NMO velocity V_{ij} is defined corresponding to the symmetry plane, where $1, 2$ and 3 represent for $[XOZ]$, $[YOZ]$ and $[XOY]$ symmetry planes, respectively.

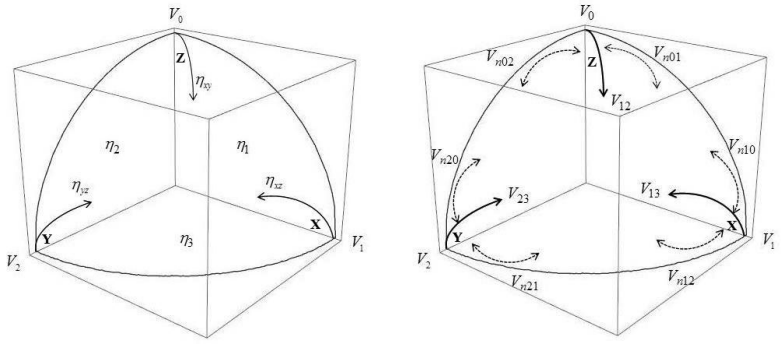

Figure 5.1. Sketch for cross-term anellipticity parameters: η_{xy}, η_{xz} and η_{yz} (left) and cross-term NMO velocities: V_{12}, V_{13} and V_{23} (right) in ORT model.

The inverse transformations for vertical velocity V_0 and horizontal velocities V_{h1} and V_{h2} are given by

$$
\begin{aligned}
V_0^2 &= \frac{V_{13}^2 V_{23}^2}{V_{12}^2}\left(1+2\eta_3\right) = \frac{V_{13}^2 V_{23}^2}{V_{12}^2}\left(1+\eta_{xz}\right)\left(1+\eta_{yz}\right), \\
V_{h1}^2 &= \frac{V_{12}^2 V_{23}^2}{V_{13}^2}\left(1+2\eta_2\right) = \frac{V_{12}^2 V_{23}^2}{V_{13}^2}\left(1+\eta_{xy}\right)\left(1+\eta_{yz}\right), \\
V_{h2}^2 &= \frac{V_{12}^2 V_{13}^2}{V_{23}^2}\left(1+2\eta_1\right) = \frac{V_{12}^2 V_{13}^2}{V_{23}^2}\left(1+\eta_{xy}\right)\left(1+\eta_{xz}\right).
\end{aligned}
\tag{5.5}
$$

Eight types of parameterization for acoustic ORT model based on different elliptical background model and anellipticity parameters are listed in Table 5.1. Based on the symmetric behavior, these parameterizations are divided into two groups: symmetrical (Cases A-D) and non-symmetrical (Cases E-H). We illustrate two groups of parameterization in Figure 5.2 and 5.3, respectively. In order to perform the sensitivity analysis, we select the parameterization with V_0, V_{h1}, V_{h2}, η_{xy}, η_{xz} and η_{yz} (Case H) as an example for the following analysis.

Parameterization	Elliptical background	Anellipticity parameters
Non-symmetric parameterizations		
Case A	V_0, V_{n1}, V_{n2}	η_1, η_2, η_3
Case B	V_0, V_{n1}, V_{n2}	$\eta_1, \eta_2, \eta_{xy}$
Case C	V_0, V_{n1}, V_{n2}	$\eta_{xy}, \eta_{xz}, \eta_{yz}$
Case D	V_0, V_{h1}, V_{h2}	$\eta_1, \eta_2, \eta_{xy}$
Symmetric parameterizations		
Case E	V_{12}, V_{13}, V_{23}	η_1, η_2, η_3
Case F	V_{12}, V_{13}, V_{23}	$\eta_{xy}, \eta_{xz}, \eta_{yz}$
Case G	V_0, V_{h1}, V_{h2}	η_1, η_2, η_3
Case H	V_0, V_{h1}, V_{h2}	$\eta_{xy}, \eta_{xz}, \eta_{yz}$

Table 5.1. Eight types of parameterizations with different background model and different set of anellipticity parameters.

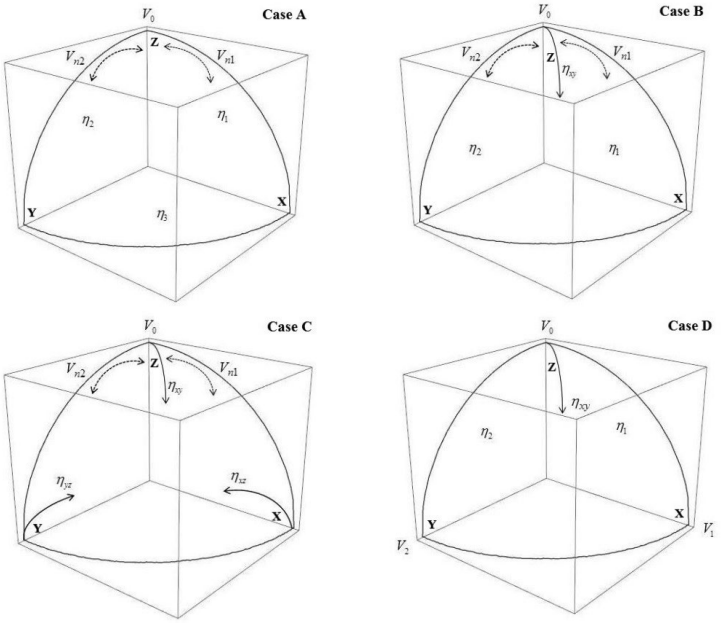

Figure 5.2. Sketch for non-symmetric parameterizations for acoustic ORT model defined by Cases A-D.

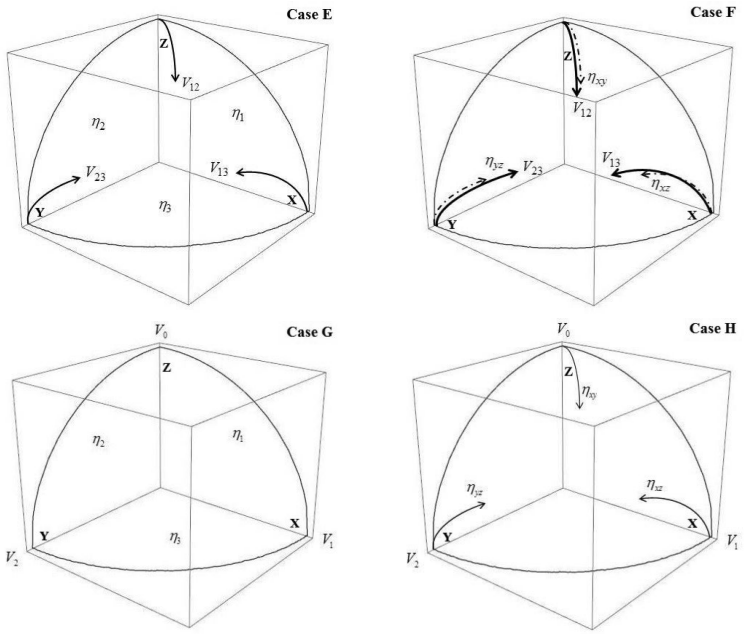

Figure 5.3. Sketch for symmetric parameterizations for acoustic ORT model defined by Cases E-H.

5.3 Perturbation-based traveltime approximation using a new parameterization

The perturbation series for traveltime (Stovas et al., 2016) in terms of new cross-term anellipticity parameters is defined up to the second order by

$$\tau = \tau_0 + \sum_i a_i \eta_i + \sum_{i,j} b_{ij} \eta_i \eta_j, \ (i, j = 1,2,3), \tag{5.6}$$

where the index $1 \equiv xy$, $2 \equiv xz$ and $3 \equiv yz$. The elliptical background model is given by

$$\tau_0 = \sqrt{t_0^2 + \frac{x^2}{V_{h1}^2} + \frac{y^2}{V_{h2}^2}}, \tag{5.7}$$

where t_0 is the vertical traveltime with $t_0 = z/V_0$.

The ORT eikonal equation (Alkhalifah, 2003) with the new parameterization takes the form

$$\begin{aligned} &V_0^2\left(\frac{\partial \tau}{\partial z}\right)^2 + V_{h1}^2\left(\frac{\partial \tau}{\partial x}\right)^2 + V_{h2}^2\left(\frac{\partial \tau}{\partial y}\right)^2 - \left(\frac{(1+\eta_{xy})(1+\eta_{xz})-1}{(1+\eta_{xy})(1+\eta_{xz})}\right) V_{h1}^2 V_0^2 \left(\frac{\partial \tau}{\partial x}\right)^2 \left(\frac{\partial \tau}{\partial z}\right)^2 \\ &- \left(\frac{(1+\eta_{xy})(1+\eta_{yz})-1}{(1+\eta_{xy})(1+\eta_{yz})}\right) V_{h2}^2 V_0^2 \left(\frac{\partial \tau}{\partial y}\right)^2 \left(\frac{\partial \tau}{\partial z}\right)^2 - \left(\frac{(1+\eta_{xz})(1+\eta_{yz})-1}{(1+\eta_{xz})(1+\eta_{yz})}\right) V_{h1}^2 V_{h2}^2 \left(\frac{\partial \tau}{\partial x}\right)^2 \left(\frac{\partial \tau}{\partial y}\right)^2 \\ &+ \left(\frac{\eta_{xz}\eta_{yz} + \eta_{xy}\left((1+\eta_{xz})(1+\eta_{yz})-1\right)}{(1+\eta_{xy})(1+\eta_{xz})(1+\eta_{yz})}\right) V_{h1}^2 V_{h2}^2 V_0^2 \left(\frac{\partial \tau}{\partial x}\right)^2 \left(\frac{\partial \tau}{\partial y}\right)^2 \left(\frac{\partial \tau}{\partial z}\right)^2 = 1. \end{aligned} \tag{5.8}$$

Solving the eikonal equation 5.8 with the corresponding perturbation series in equation 5.6, we obtain the series coefficients a_i and b_{ij}, $(i, j = 1,2,3)$ that are given in Appendix A.

In order to obtain a higher accuracy, the Shanks transform (Bender and Orszag, 1978) is applied by the form

$$\tau_3 = \tau_0 + \frac{\tau_1^2}{\tau_1 - \tau_2}, \tag{5.9}$$

where τ_0 is defined in equation 5.7, $\tau_1 = \sum_i a_i \eta_i$ and $\tau_2 = \sum_{ij} b_{ij} \eta_i \eta_j$ are the first- and second- order terms in equation 5.6.

In order to test the sensitivity of the perturbation coefficients a_i and b_{ij}, we select the ORT model with the parameters: $V_0 = 2km/s$, $V_{h1} = 2.4km/s$, $V_{h2} = 2.6km/s$, $\eta_1 = 0.15$, $\eta_2 = 0.18$ and $\eta_3 = 0.1$. The perturbation coefficients a_i and b_{ij}, $(i, j = 1,2,3)$ from our proposed parameterization (V_0, V_{h1}, V_{h2}, η_{xy}, η_{xz} and η_{yz}, Case H) are plotted in Figure 5.4, 5.5 and 5.6, respectively, One can see that the shape of the first-order coefficients a_2 and a_3 is very similar and the magnitude of them is larger than the coefficient a_1. For quadratic coefficients, similarly, the coefficient b_{22} and b_{33} is larger than b_{11} in magnitude. Note that the magnitude of first- and second-order coefficients a_1 and b_{11} are changing dramatically at near offsets. The magnitude of three cross-term coefficients is quite similar while the shape of cross-term b_{23} is very complicated.

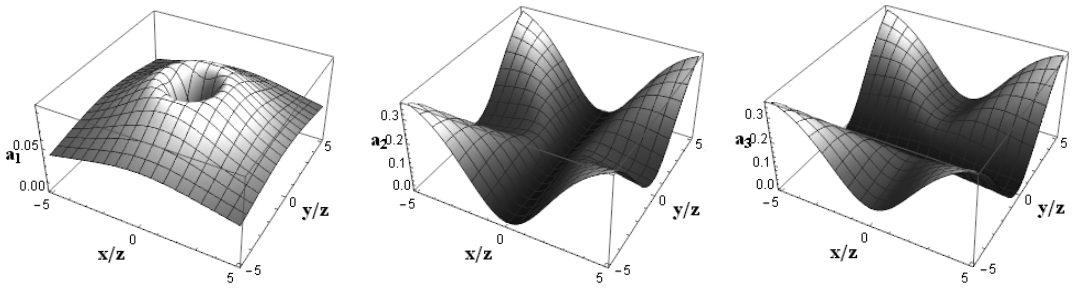

Figure 5.4. The first order perturbation coefficients a_i (Case H). Coefficients a_1, a_2 and a_3 are shown in left, middle and right, respectively.

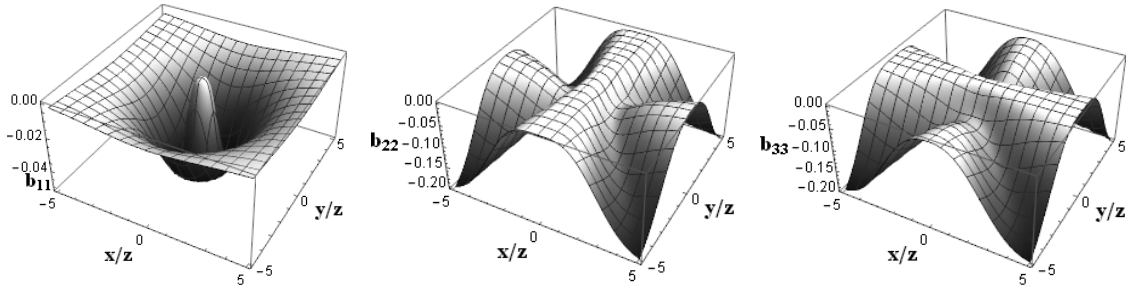

Figure 5.5. The quadratic perturbation coefficients b_{ii} (Case H). Coefficients b_{11}, b_{22} and b_{33} are shown in left, middle and right, respectively.

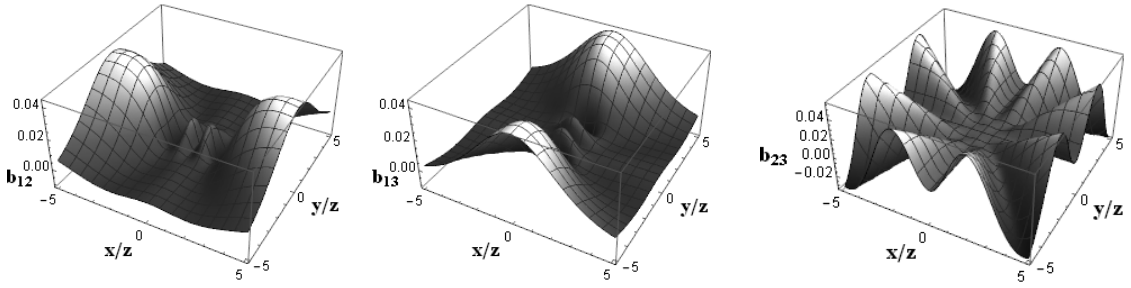

Figure 5.6. The cross-term perturbation coefficients $b_{ij}, (i \neq j)$ (Case H). Coefficients b_{12}, b_{13} and b_{23} are shown in left, middle and right, respectively.

5.4 The sensitivity of traveltime to anellipticity parameters

In order to analyze the sensitivity of traveltime to anellipticity parameters, we define the group velocity inverse related coefficients $\tilde{a}_i$ and $\tilde{b}_{ij}$ by

$$\frac{1}{V(\theta,\phi)} = \frac{1}{\tilde{V}_0(\theta,\phi)} + \sum_i \tilde{a}_i(\theta,\phi)\eta_i + \sum_{i,j} \tilde{b}_{ij}(\theta,\phi)\eta_i\eta_j, \tag{5.10}$$

where

$$
\begin{aligned}
&\frac{1}{\tilde{V}_0(\theta,\phi)} = \frac{\tau_0 \cos\theta}{z}\left(x = z\tan\theta\cos\phi, y = z\tan\theta\sin\phi\right),\\
&\tilde{a}_i(\theta,\phi) = \frac{a_i \cos\theta}{z}\left(x = z\tan\theta\cos\phi, y = z\tan\theta\sin\phi\right),\\
&\tilde{b}_{ij}(\theta,\phi) = \frac{b_{ij} \cos\theta}{z}\left(x = z\tan\theta\cos\phi, y = z\tan\theta\sin\phi\right),
\end{aligned}
\tag{5.11}
$$

where τ_0 is defined in equation 5.7, coefficients a_i and b_{ij} are given in Appendix A, θ is the dip angle to the vertical and the azimuth ϕ is the azimuth defined from the x axis. To analyze the sensitivity at different offset range, we compute the integral from coefficients $\tilde{a}_i$ and $\tilde{b}_{ij}$ with respect to different range of dip angle θ ($\theta \in (0,30^\circ), (30^\circ,60^\circ)$ and $(60^\circ,90^\circ)$) that corresponding to near-, mid- and far-offset,

$$
\begin{aligned}
&\hat{a}_i(\phi) = \frac{1}{\theta_2 - \theta_1}\int_{\theta_1}^{\theta_2} \tilde{a}_i(\theta,\phi)d\theta,\\
&\hat{b}_{ij}(\phi) = \frac{1}{\theta_2 - \theta_1}\int_{\theta_1}^{\theta_2} \tilde{b}_{ij}(\theta,\phi)d\theta.
\end{aligned}
\tag{5.12}
$$

The polar plots for the sensitivity coefficients $\hat{a}_i$ and $\hat{b}_{ij}$ versus azimuth ϕ for model with parameterization (Case H) for near- (left), mid- (middle) and far (right) offset are shown in Figures 5.7, 5.8 and 5.9, respectively. One can see that the first and quadratic order coefficients have similar sensitivity plots. The sensitivity in anellipticity parameter η_{xy} has an elliptic shape in $[XOY]$ plane regardless of the range of offsets. The sensitivities to anellipticity parameters η_{xz} and η_{yz} reach the maximum values for 0 and $\pi/2$ azimuth angle, respectively. This is valid for near- and mid-offset. The reason for that is that the impact of anellipticity parameter η_3 is not dominating for near- and mid-offset range. For large offset, the effect of η_3 starts to dominate in both $\hat{a}_2$ and $\hat{a}_3$ resulting in pronounced anomaly at about 45° azimuth angle. The azimuthal behavior of cross-term coefficients $b_{ij}, (i \neq j)$ is more complicated (Figure 5.9). One can see that coefficient $\hat{b}_{12}$ and $\hat{b}_{13}$ are

symmetric, while the magnitude of $\hat{b}_{23}$ increases with increase in offset. There is almost no impact from $\hat{b}_{23}$ ($\eta_{xz}\eta_{yz}$) at near offset since the cross-talk between η_{xz} and η_{yz} is very small. With increase in offset, the cross-talk is getting more pronounced, and the magnitude of coefficient $\hat{b}_{23}$ increasing at far offset. The cross-term coefficients $\hat{b}_{12}$ ($\eta_{xy}\eta_{xz}$) and $\hat{b}_{13}$ ($\eta_{xy}\eta_{yz}$) become equal at about 45° azimuth at any offset range while mostly focused along the x and y axes, respectively.

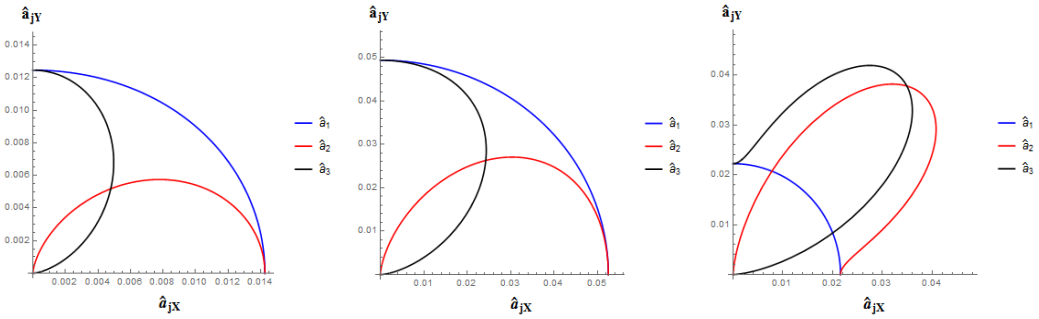

Figure 5.7. The first order sensitivity coefficients $\hat{a}_i$ in Case H for short offset (left) ($\theta \in (0,30^\circ)$), intermediate offset (middle) ($\theta \in (30^\circ,60^\circ)$), and far offset (right) ($\theta \in (60^\circ,90^\circ)$). The coefficients a_1, a_2 and a_3 are shown by blue, red and black colors, respectively.

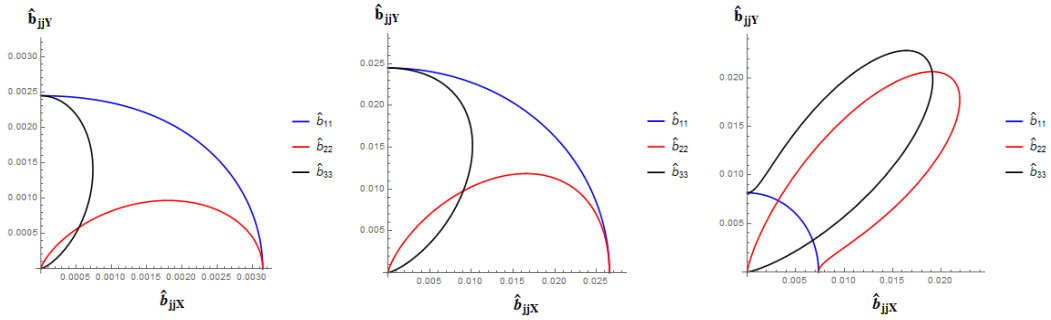

Figure 5.8. The quadratic sensitivity coefficients $\hat{b}_{ii}$ in Case H for short offset (left) ($\theta \in (0,30^\circ)$), intermediate offset (middle) ($\theta \in (30^\circ,60^\circ)$), and far offset (right) ($\theta \in (60^\circ,90^\circ)$). The coefficients b_{11}, b_{22} and b_{33} are shown by blue, red and black colors, respectively.

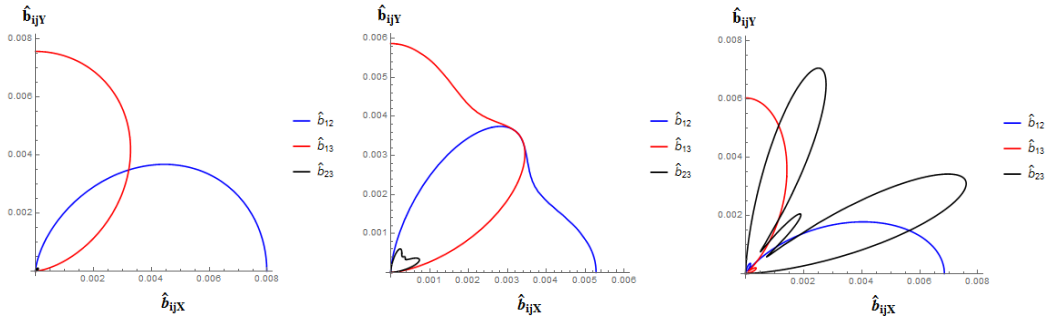

Figure 5.9. The cross-term sensitivity coefficients $b_{ij}, (i \neq j)$ in Case H for short offset (left) ($\theta \in (0,30^\circ)$), intermediate offset (middle) ($\theta \in (30^\circ,60^\circ)$), and far offset (right) ($\theta \in (60^\circ,90^\circ)$). The coefficients b_{12}, b_{13} and b_{23} are shown by blue, red and black colors, respectively.

The overall sensitivity coefficients $\hat{A}_i$ and $\hat{B}_{ij}$ can be computed in a similar way as the ones given in equations 5.12 but with double integrals over the entire angle range,

$$\begin{aligned} \hat{A}_i &= \frac{4}{\pi^2}\int_0^{\pi/2}\int_0^{\pi/2}\tilde{a}_i(\theta,\phi)d\theta d\phi, \\ \hat{B}_{ij} &= \frac{4}{\pi^2}\int_0^{\pi/2}\int_0^{\pi/2}\tilde{b}_{ij}(\theta,\phi)d\theta d\phi. \end{aligned} \tag{5.13}$$

The overall sensitivities are illustrated in Figure 5.10. One can see that $\hat{A}_1 > \hat{A}_2 > \hat{A}_3$ and $\hat{B}_{11} > \hat{B}_{22} > \hat{B}_{33}$. The inequalities for the first-order $\hat{A}_i$ and quadratic $\hat{B}_{ii}$ coefficients are controlled by the semi-axes for elliptical background model. For this parameterization (Case H), we have $1/V_0^2 > 1/V_{h1}^2 > 1/V_{h2}^2$, and this inequality explains the behavior of sensitivity coefficients. Similar analysis can be performed for other background models used in our tests.

In order to see the difference in the overall sensitivities between different parameterizations, Figures 5.11 and 5.12 show second order coefficients $\hat{B}_{ij}$ computed from all parameterizations listed in Table 5.1. One can see that the tendency is $\hat{B}_{11} > \hat{B}_{22} > \hat{B}_{33}$ for all the Cases except for Cases E and F. This behavior can also be explained by the corresponding slownesses, $1/V_{23}^2 > 1/V_{13}^2 > 1/V_{12}^2$. Note that the magnitude of $\hat{B}_{ij}$ computed for parameterization Case H is the smallest among all parameterizations. Note that using term group velocity inverse ($1/V_{group}$) instead of traveltime for the sensitivity analysis is because the traveltime can be converted from it and since there is no asymptotic behavior for traveltime at infinite offset, taking the integral along the offset up to infinite for traveltime is impossible to get the overall sensitivity in anellipticity parameters.

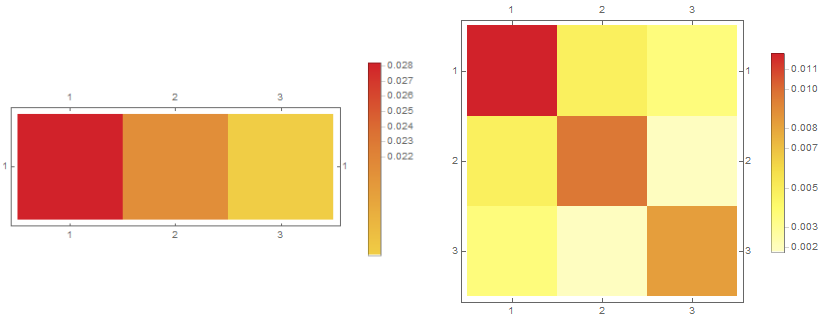

Figure 5.10. The overall sensitivity coefficients: first order (left) and second order (right) using parameterization Case H. The coefficients $\hat{A}_1$, $\hat{A}_2$ and $\hat{A}_3$ are shown from left to right. The second order coefficients are composed in matrix form with indices $1 \equiv \eta_{xy}, 2 \equiv \eta_{xz}, 3 \equiv \eta_{yz}$.

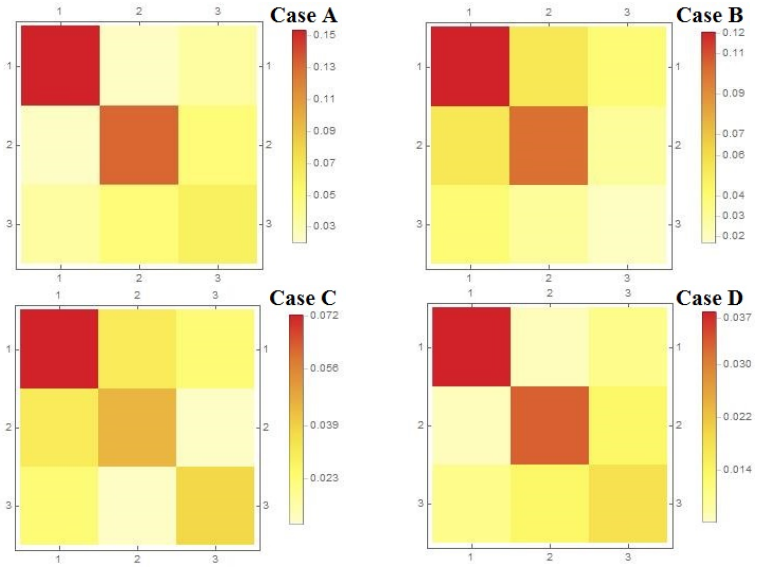

Figure 5.11. The second order overall sensitivity coefficients $\hat{B}_{ij}$ using non-symmetric parameterizations Cases A-D. The second order coefficients are composed in matrix form with indices $1 \equiv \eta_1, 2 \equiv \eta_2, 3 \equiv \eta_3$ for Case A, $1 \equiv \eta_1, 2 \equiv \eta_2, 3 \equiv \eta_{xy}$ for Cases B and D, $1 \equiv \eta_{xy}, 2 \equiv \eta_{xz}, 3 \equiv \eta_{yz}$ for Case C.

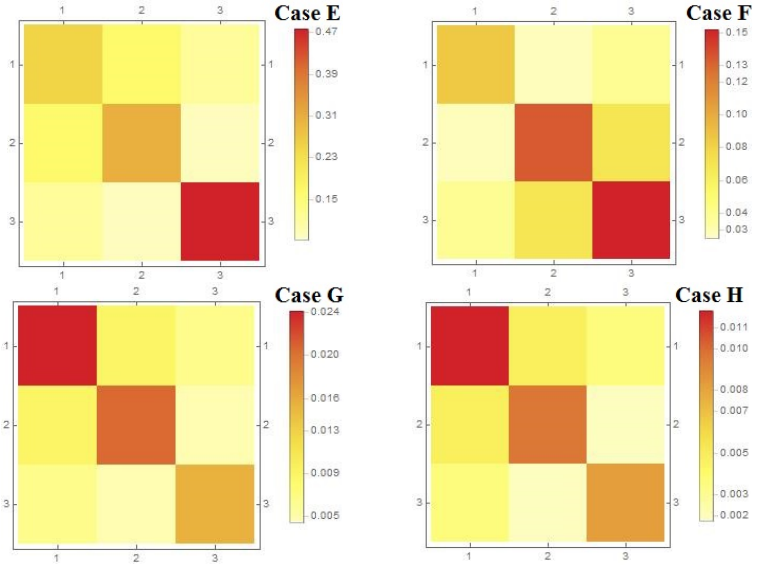

Figure 5.12. The second order overall sensitivity coefficients $\hat{B}_{ij}$ using symmetric parameterizations Cases E-H. The second order coefficients are composed in matrix form with indices $1 \equiv \eta_1, 2 \equiv \eta_2, 3 \equiv \eta_3$ for Cases E and G, $1 \equiv \eta_{xy}, 2 \equiv \eta_{xz}, 3 \equiv \eta_{yz}$ for Cases F and H.

5.5 Numerical examples

Using the ORT model from Table 5.2, the relative error in traveltime using the parameterization Case H computed from perturbation series in equation 5.6 and the Shanks transform in equation 5.9 are shown in Figure 5.13 (left and right, respectively). One can see that the Shanks transform significantly improves the accuracy of approximation.

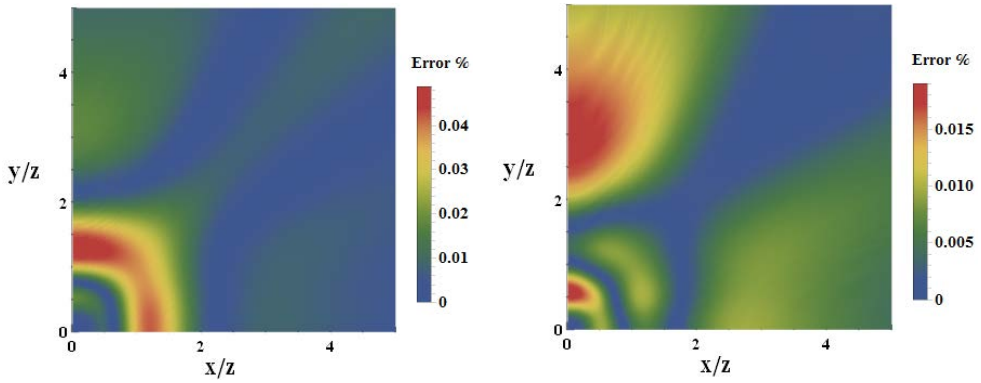

Figure 5.13. The relative error of perturbation series (left) and the Shanks transform (right) for traveltime with parameterization Case H.

Our set of parameterization is based on three types of background model and three types of anellipticity coefficients. In order to compare the accuracy of the Shanks transform using different parameterizations from Table 5.1 and analyze their impact, the relative error in traveltime using three different elliptical background models: (V_0, V_{n1}, V_{n2}), (V_0, V_{h1}, V_{h2}) and (V_{12}, V_{13}, V_{23}) is shown in Figure 5.14. One can see that the elliptical background model using vertical and two horizontal velocities is the most accurate one, while the one using the cross-term NMO velocities results in the worst accuracy even for short offset.

The relative error in traveltime from Shanks transform in equation 5.9 using the ORT model (Table 5.2) for all non-symmetric and symmetric parameterizations (Table 5.1) is shown in Figure 5.15 and 5.16, respectively. Note that all the accuracy plots are computed from the same ORT model but using different parameterizations. For parameterization Cases A, B, D

and G, the perturbation series coefficients for traveltime approximation are discussed in Xu et al (2016). The perturbation series coefficients a_i and b_{ij} for Cases C, E and F are given in Appendices B, C and D, respectively. From comparison of plots in Figure 5.15 and 5.16, one can see that the accuracy is mostly driven by selection of background model. The parameterization with the vertical and two horizontal velocities is generally more accurate, while the parameterization with the cross-term NMO velocity is generally less accurate. The selection of the set of anellipticity coefficients as the perturbation coefficients also affects the accuracy. For the parameterizations using vertical and two horizontal velocities as the background (Cases D, G and H), the one using three cross-term anellipticity parameters (Case H) is the most accurate one while the parameterization specified as Case G is the worst. One can say, the more cross-term anellipticity parameters we use, the more accurate result we obtain. From the overall sensitivity plots (Figure 5.11 and 5.12) and the accuracy plots (Figure 5.15 and 5.16), one can see the less magnitude of coefficient $\hat{B}_{ij}$ the more accurate result we obtain for traveltime approximation based on the Shanks transform. Above all, the approximation with symmetric parameterization (Case H) using vertical and two horizontal velocities as the background model, and three cross-term anellipticity parameters as the perturbation parameters results in the most accurate traveltime function.

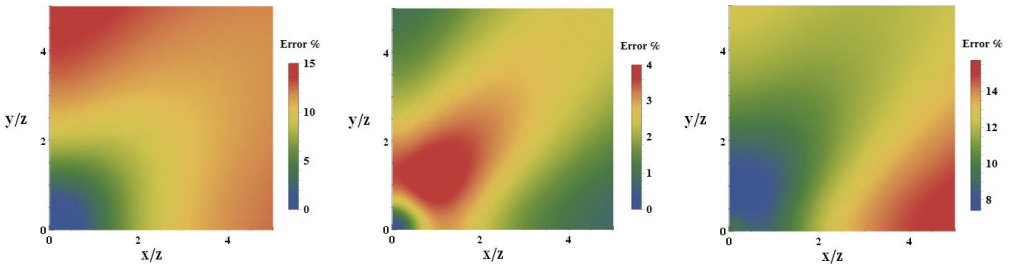

Figure 5.14. The relative error in traveltime using the hyperboloid approximation with vertical and two NMO velocities (left), vertical and two horizontal velocities (middle) and three cross-term NMO velocities (right).

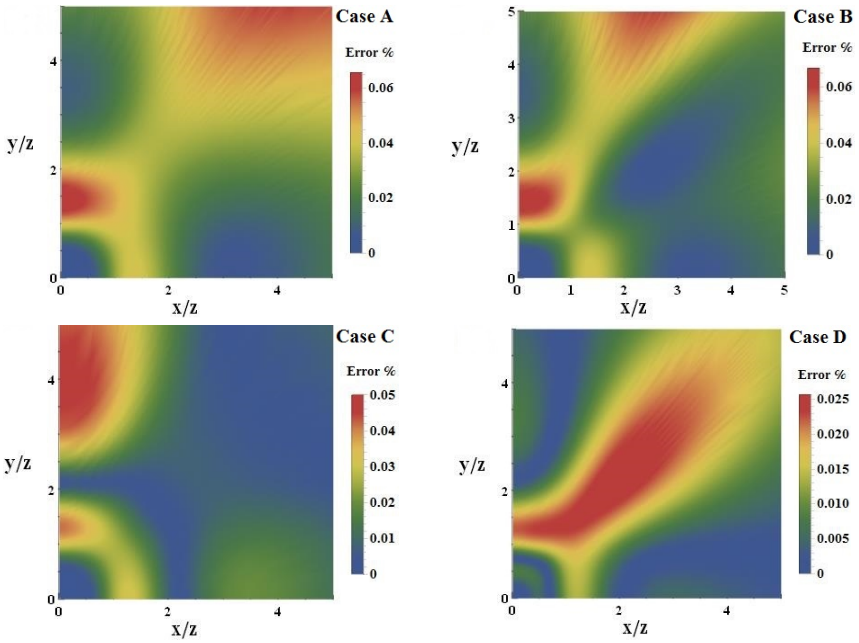

Figure 5.15. The relative error in traveltime of the Shanks transform for parameterizations from Cases A-D.

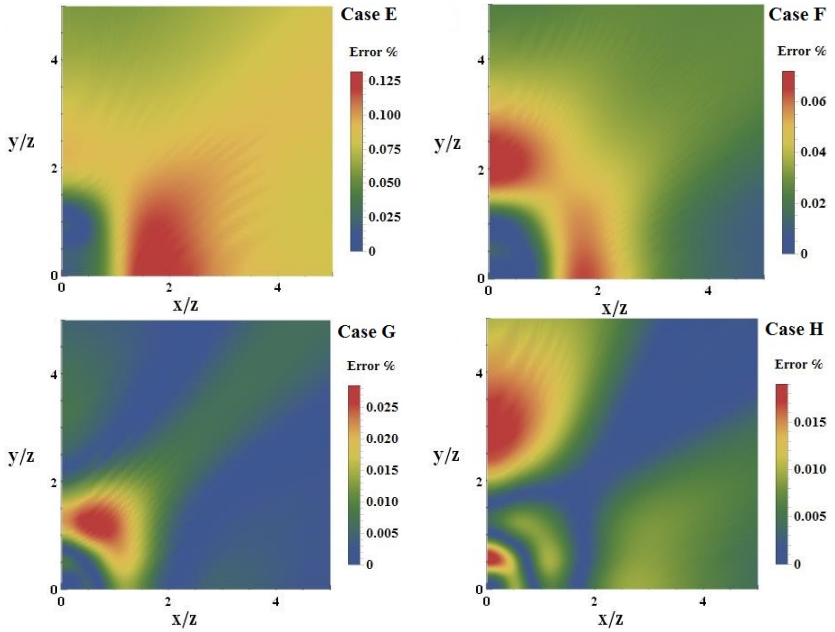

Figure 5.16. The relative error in traveltime of the Shanks transform for parameterizations from Cases E-H.

Velocities (km/s)	V_0	V_{h1}	V_{h2}	V_{n1}	V_{n2}	V_{12}	V_{13}	V_{23}
	2	2.4	2.6	2.1	2.23	2.17	2.04	1.94
Anellipticity parameters	η_1	η_2	η_3	η_{xy}	η_{xz}	η_{yz}		
	0.15	0.18	0.1	0.214	0.07	0.12		

Table 5.2. The ORT model parameters.

5.6 Discussions

In our proposed perturbation method for traveltime approximation, different parameterization selection impacts the accuracy of the traveltime approximation due to the selection of the elliptical background and different proportion in perturbation parameters (anellipticity parameters) from the selected parameterization. This difference in traveltime error is caused by the perturbation method that is fixing the elliptical (ellipsoidal) background and fitting with the perturbation coefficients (anellipticity parameters). For the parameterization using the NMO velocities as the background model, the better accuracy is obtained at short offset. Note that we using offset-depth ratio up to 5 (long offset) in the numerical examples that explains the more accurate result for those using the horizontal velocities as the background. Different parameterization causes the sensitivity difference in anellipticity parameters. More accurate result is obtained from the less sensitivity in perturbation parameters. While, the background model selection contributes most for the accuracy of the traveltime approximation using the perturbation method.

The NMO velocity might not be preserved for traveltime approximation given by the Shanks transform (equation 5.9) with arbitrary parameterization. Obviously, if NMO velocities are explicitly stay in the parameterization list (Cases A-C), they are preserved regardless to approximation. If NMO velocities are not in the parameterization list, they might be preserved

(Cases D and G) or might not be preserved (Cases E, F and H). For example, in Case H, the exact expressions for NMO velocities are

$$\begin{aligned} V_{n1} &= \frac{V_{h1}}{\sqrt{(1+\eta_{xy})(1+\eta_{xz})}} \approx V_{h1}\left(1-\frac{\eta_{xy}+\eta_{xz}}{2}+\frac{3\left(\eta_{xy}^2+\eta_{xz}^2\right)}{8}+\frac{\eta_{xy}\eta_{xz}}{4}\right), \\ V_{n2} &= \frac{V_{h2}}{\sqrt{(1+\eta_{xy})(1+\eta_{yz})}} \approx V_{h2}\left(1-\frac{\eta_{xy}+\eta_{yz}}{2}+\frac{3\left(\eta_{xy}^2+\eta_{yz}^2\right)}{8}+\frac{\eta_{xy}\eta_{yz}}{4}\right), \end{aligned} \tag{5.14}$$

However, the Shanks transform approximation gives inaccurate NMO velocities,

$$\begin{aligned} V_{n1} &= V_{h1}\sqrt{\frac{\eta_{xy}(\eta_{xz}-1)+\eta_{xz}}{\eta_{xy}+\eta_{xy}^2+\eta_{xz}+\eta_{xy}\eta_{xz}+\eta_{xz}^2}} \approx V_{h1}\left(1-\frac{\eta_{xy}+\eta_{xz}}{2}+\frac{3\left(\eta_{xy}^2+\eta_{xz}^2\right)}{8}+\frac{\eta_{xy}\eta_{xz}}{4}\right), \\ V_{n2} &= V_{h2}\sqrt{\frac{\eta_{xy}(\eta_{yz}-1)+\eta_{yz}}{\eta_{xy}+\eta_{xy}^2+\eta_{yz}+\eta_{xy}\eta_{yz}+\eta_{yz}^2}} \approx V_{h2}\left(1-\frac{\eta_{xy}+\eta_{yz}}{2}+\frac{3\left(\eta_{xy}^2+\eta_{yz}^2\right)}{8}+\frac{\eta_{xy}\eta_{yz}}{4}\right). \end{aligned} \tag{5.15}$$

The expressions in equations 5.14 and 5.15 are equivalent in case of weak-anellipticity.

The proposed approximation can be extended to the multilayered by using the effective model parameters from the Dix-type equations (Stovas, 2015). When there is the azimuthal variation between the multilayered ORT model, the effective parameters with different azimuthal orientation of the layers is listed in Ravve and Koren (2017) and Koren and Ravve (2017).

However, some parameterizations defined by the horizontal velocities might not that accurate as they are in the homogeneous case since the form of the approximation is derived from the homogeneous case, while the ray-tracing for horizontal velocities (infinite offset) is impossible for multilayered ORT model.

5.7 Conclusions

We defined a group of new parameterizations by using three cross-term anellipticity parameters (η_{xy}, η_{xz} and η_{yz}) and three cross-term NMO velocities (V_{12}, V_{13} and V_{23}) for a homogeneous ORT model. The perturbation-based traveltime approximations are proposed in

ORT media using the corresponding new parameterizations. Based on the symmetric behavior, we divide eight parameterizations into two groups and test their accuracy in traveltime in the numerical examples. The sensitivity analysis performed for perturbation coefficients at near-, mid- and far-offset range illustrates different effect for a selected set of anellipticity parameters. The overall sensitivity performed for the full range of offset shows that the corresponding coefficients are proportional to the slowness squared from given background velocity model. By comparison of eight different parameterizations, we show that the one with V_0, V_{h1}, V_{h2}, η_{xy}, η_{xz} and η_{yz} (Case H) results in the most accurate traveltime approximation based on the Shanks transform.

5.8 Acknowledgments

We would like to acknowledge China Scholarship Council (CSC) and ROSE project for financial support.

5.9 Appendix A

The perturbation series for traveltime in ORT model using the parameterization Case H (V_0, V_{h1}, V_{h2}, η_{xy}, η_{xz} and η_{yz})

The perturbation series for traveltime in ORT model is defined by (Stovas et al, 2016)

$$\tau = \tau_0 + \sum_i a_i \eta_i + \sum_{i,j} b_{ij} \eta_i \eta_j, \left(i, j = 1,2,3 \right). \tag{5.A.1}$$

For parameterization Case H with: V_0, V_{h1}, V_{h2}, η_{xy}, η_{xz} and η_{yz}, the index $1 \equiv xy$, $2 \equiv xz$ and $3 \equiv yz$ for the perturbation series in equation 5.A.1. The elliptical background model is given by

$$\tau_0 = \sqrt{t_0^2 + \frac{x^2}{V_{h1}^2} + \frac{y^2}{V_{h2}^2}}, \tag{5.A.2}$$

The perturbation coefficients in equation 5.A.1 are computed by solving the corresponding eikonal equation in equation 5.6 shown by

$$\begin{aligned}
a_1 &= \frac{t_0^2\left(\tau_{hx}^2 + \tau_{hy}^2\right)}{2\tau_0^3}, a_2 = \frac{\tau_{hx}^2\left(t_0^2 + \tau_{hy}^2\right)}{2\tau_0^3}, a_3 = \frac{\tau_{hy}^2\left(t_0^2 + \tau_{hx}^2\right)}{2\tau_0^3}, \\
b_{11} &= -\frac{9t_0^4\left(\tau_{hx}^2 + \tau_{hy}^2\right)^2}{8\tau_0^7}, \\
b_{22} &= -\frac{9\tau_{hx}^4\left(t_0^2 + \tau_{hy}^2\right)^2}{8\tau_0^7}, \\
b_{33} &= -\frac{9\tau_{hy}^4\left(t_0^2 + \tau_{hx}^2\right)^2}{8\tau_0^7}, \\
b_{12} &= \frac{t_0^2\tau_{hx}^2\left(2t_0^4 + 2\tau_{hx}^4 + \tau_{hx}^2\tau_{hy}^2 - \tau_{hy}^4 + t_0^2\left(-5\tau_{hx}^2 + \tau_{hy}^2\right)\right)}{4\tau_0^7}, \\
b_{13} &= \frac{t_0^2\tau_{hy}^2\left(2t_0^4 + 2\tau_{hy}^4 + \tau_{hx}^2\tau_{hy}^2 - \tau_{hx}^4 + t_0^2\left(-5\tau_{hy}^2 + \tau_{hx}^2\right)\right)}{4\tau_0^7}, \\
b_{23} &= \frac{\tau_{hx}^2\tau_{hy}^2\left(2\tau_{hx}^4 + 2\tau_{hy}^4 + t_0^2\tau_{hx}^2 - t_0^4 + \tau_{hy}^2\left(-5\tau_{hx}^2 + t_0^2\right)\right)}{4\tau_0^7}.
\end{aligned} \tag{5.A.3}$$

where $\tau_{hx} = x/V_{h1}$ and $\tau_{hy} = y/V_{h2}$.

5.10 Appendix B

The perturbation series for traveltime in ORT model using the parameterization Case C (V_0, V_{n1}, V_{n2}, η_{xy}, η_{xz} and η_{yz})

For parameterization Case C with: V_0, V_{n1}, V_{n2}, η_{xy}, η_{xz} and η_{yz}, the index $1 \equiv xy$, $2 \equiv xz$ and $3 \equiv yz$ for the perturbation series in equation 5.A.1. The elliptical background model is given by

$$\tau_0 = \sqrt{t_0^2 + \frac{x^2}{V_{n1}^2} + \frac{y^2}{V_{n2}^2}}, \tag{5.B.1}$$

Solving the corresponding eikonal equation with the perturbation series in 5.A.1, we obtain the series coefficients a_i and b_{ij}, $(i, j = 1,2,3)$ given by

$$\begin{aligned}
&a_1 = -\frac{\left(\tau_{nx}^2 + \tau_{ny}^2\right)^2}{2\tau_0^3}, a_2 = -\frac{\tau_{nx}^4}{2\tau_0^3}, a_3 = -\frac{\tau_{ny}^4}{2\tau_0^3}, \\
&b_{11} = \frac{3\left(\tau_{nx}^2 + \tau_{ny}^2\right)^3\left(4t_0^2 + \tau_{nx}^2 + \tau_{ny}^2\right)}{8\tau_0^7}, \\
&b_{22} = \frac{3\tau_x^6\left(4t_0^2 + \tau_{nx}^2 + 4\tau_{ny}^2\right)}{8\tau_0^7}, \\
&b_{33} = \frac{3\tau_y^6\left(4t_0^2 + 4\tau_{nx}^2 + \tau_{ny}^2\right)}{8\tau_0^7}, \\
&b_{12} = \frac{\tau_{nx}^4\left(\left(\tau_{nx}^2 + \tau_{ny}^2\right)^2 + 8t_0^2\left(\tau_{nx}^2 + \tau_{ny}^2\right) - 2t_0^4\right)}{4\tau_0^7}, \\
&b_{13} = \frac{\tau_{ny}^4\left(\left(\tau_{nx}^2 + \tau_{ny}^2\right)^2 + 8t_0^2\left(\tau_{nx}^2 + \tau_{ny}^2\right) - 2t_0^4\right)}{4\tau_0^7}, \\
&b_{23} = -\frac{9\tau_{nx}^4\tau_{ny}^4}{4\tau_0^7}.
\end{aligned} \tag{5.B.2}$$

where $\tau_{nx} = x/V_{n1}$ and $\tau_{ny} = y/V_{n2}$.

5.11 Appendix C

The perturbation series for traveltime in ORT model using the parameterization Case E (V_{12}, V_{13}, V_{23}, η_1, η_2 and η_3)

For parameterization Case E with: V_{12}, V_{13}, V_{23}, η_1, η_2 and η_3, the elliptical background model is given by

$$\tau_0 = \sqrt{\frac{x^2}{V_{k1}^2} + \frac{y^2}{V_{k2}^2} + \frac{z^2}{V_{k0}^2}}, \tag{5.C.1}$$

where $V_{k0} = V_{13}V_{23}/V_{12}$, $V_{k1} = V_{12}V_{23}/V_{13}$ and $V_{k2} = V_{12}V_{13}/V_{23}$, where V_{ij} are defined in equations 5.4.

Solving the corresponding eikonal equation with the perturbation series in 5.A.1, we obtain the series coefficients a_i and b_{ij} given by

$$\begin{aligned}
a_1 &= \frac{\tau_{kx}^2\left(-\tau_{ky}^2+\tau_{kz}^2\right)-\tau_{ky}^2\left(\tau_{ky}^2+\tau_{kz}^2\right)}{2\tau_0^3},\\
a_2 &= \frac{\tau_{ky}^2\left(-\tau_{kx}^2+\tau_{kz}^2\right)-\tau_{kx}^2\left(\tau_{kx}^2+\tau_{kz}^2\right)}{2\tau_0^3},\\
a_3 &= \frac{\tau_{kx}^2\left(-\tau_{kz}^2+\tau_{ky}^2\right)-\tau_{kz}^2\left(\tau_{ky}^2+\tau_{kz}^2\right)}{2\tau_0^3},\\
b_{11} &= \frac{1}{2\tau_0^7}\Big(4\tau_{kx}^6\tau_{ky}^2+\tau_{kx}^4\left(11\tau_{ky}^4+15\tau_{ky}^2\tau_{kz}^2-9\tau_{kz}^4\right)+5\tau_{kx}^2\tau_{ky}^2\left(\tau_{ky}^2+\tau_{kz}^2\right)\left(2\tau_{ky}^2+3\tau_{kz}^2\right)\\
&\quad+\tau_{ky}^2\left(\tau_{ky}^2+\tau_{kz}^2\right)^2\left(3\tau_{ky}^2+4\tau_{kz}^2\right)\Big),\\
b_{22} &= \frac{1}{2\tau_0^7}\Big(4\tau_{ky}^6\tau_{kx}^2+\tau_{ky}^4\left(11\tau_{kx}^4+15\tau_{kx}^2\tau_{kz}^2-9\tau_{kz}^4\right)+5\tau_{kx}^2\tau_{ky}^2\left(\tau_{kx}^2+\tau_{kz}^2\right)\left(2\tau_{kx}^2+3\tau_{kz}^2\right)\\
&\quad+\tau_{kx}^2\left(\tau_{kx}^2+\tau_{kz}^2\right)^2\left(3\tau_{kx}^2+4\tau_{kz}^2\right)\Big),\\
b_{33} &= \frac{1}{2\tau_0^7}\Big(4\tau_{kx}^6\tau_{kz}^2+\tau_{kx}^4\left(11\tau_{kz}^4+15\tau_{ky}^2\tau_{kz}^2-9\tau_{ky}^4\right)+5\tau_{kx}^2\tau_{kz}^2\left(\tau_{ky}^2+\tau_{kz}^2\right)\left(2\tau_{kz}^2+3\tau_{ky}^2\right)\\
&\quad+\tau_{kz}^2\left(\tau_{ky}^2+\tau_{kz}^2\right)^2\left(3\tau_{kz}^2+4\tau_{ky}^2\right)\Big),\\
b_{12} &= \frac{1}{\tau_0^7}\Big(\tau_{kx}^6\left(-\tau_{ky}^2+\tau_{kz}^2\right)-\tau_{kx}^4\left(2\tau_{ky}^4+2\tau_{ky}^2\tau_{kz}^2+\tau_{kz}^4\right)-\tau_{kx}^2\left(\tau_{ky}^6+2\tau_{ky}^4\tau_{kz}^2+15\tau_{ky}^2\tau_{kz}^4+2\tau_{kz}^6\right)\\
&\quad+\tau_{ky}^2\tau_{kz}^2\left(\tau_{ky}^4-\tau_{ky}^2\tau_{kz}^2-2\tau_{kz}^4\right)\Big),\\
b_{13} &= \frac{1}{\tau_0^7}\Big(\tau_{ky}^6\left(-\tau_{kz}^2+\tau_{kx}^2\right)-\tau_{ky}^4\left(2\tau_{kz}^4+2\tau_{kx}^2\tau_{kz}^2+\tau_{kx}^4\right)-\tau_{ky}^2\left(\tau_{kz}^6+2\tau_{kz}^4\tau_{kx}^2+15\tau_{kz}^2\tau_{kx}^4+2\tau_{kx}^6\right)\\
&\quad+\tau_{kx}^2\tau_{kz}^2\left(\tau_{kz}^4-\tau_{kx}^2\tau_{kz}^2-2\tau_{kx}^4\right)\Big),\\
b_{23} &= \frac{1}{\tau_0^7}\Big(\tau_{kz}^6\left(-\tau_{kx}^2+\tau_{ky}^2\right)-\tau_{kz}^4\left(2\tau_{kx}^4+2\tau_{kx}^2\tau_{ky}^2+\tau_{ky}^4\right)-\tau_{kz}^2\left(\tau_{kx}^6+2\tau_{kx}^4\tau_{ky}^2+15\tau_{kx}^2\tau_{ky}^4+2\tau_{ky}^6\right)\\
&\quad+\tau_{kx}^2\tau_{ky}^2\left(\tau_{kx}^4-\tau_{kx}^2\tau_{ky}^2-2\tau_{ky}^4\right)\Big),
\end{aligned} \tag{5.C.2}$$

where $\tau_{kx} = x/V_{k1}$, $\tau_{ky} = y/V_{k2}$ and $\tau_{kz} = z/V_{k0}$.

5.12 Appendix D

The perturbation series for traveltime in ORT model using the parameterization Case F (V_{12}, V_{13}, V_{23}, η_{xy}, η_{xz} and η_{yz})

For parameterization Case F with: V_{12}, V_{13}, V_{23}, η_{xy}, η_{xz} and η_{yz}, the index $1 \equiv xy$, $2 \equiv xz$ and $3 \equiv yz$ for the perturbation series in equation 5.A.1. The elliptical background model is given by

$$\tau_0 = \sqrt{\frac{x^2}{V_{k1}^2} + \frac{y^2}{V_{k2}^2} + \frac{z^2}{V_{k0}^2}}, \tag{5.D.1}$$

where $V_{k0} = V_{13}V_{23}/V_{12}$, $V_{k1} = V_{12}V_{23}/V_{13}$ and $V_{k2} = V_{12}V_{13}/V_{23}$, where V_{ij} are defined in equations 5.4.

Solving the corresponding eikonal equation with the perturbation series in 5.A.1, we obtain the series coefficients a_i and b_{ij} given by

$$
\begin{aligned}
&a_1 = -\frac{\left(\tau_{kx}^2+\tau_{ky}^2\right)^2}{2\tau_0^3}, a_2 = -\frac{\left(\tau_{ky}^2+\tau_{kz}^2\right)^2}{2\tau_0^3}, a_3 = -\frac{\left(\tau_{kx}^2+\tau_{kz}^2\right)^2}{2\tau_0^3},\\
&b_{11} = \frac{3\left(\tau_{kx}^2+\tau_{ky}^2\right)^3\left(4\tau_{kz}^2+\tau_{kx}^2+\tau_{ky}^2\right)}{8\tau_0^7},\\
&b_{22} = \frac{3\left(\tau_{ky}^2+\tau_{kz}^2\right)^3\left(\tau_{kz}^2+4\tau_{kx}^2+\tau_{ky}^2\right)}{8\tau_0^7},\\
&b_{33} = \frac{3\left(\tau_{kx}^2+\tau_{kz}^2\right)^3\left(\tau_{kz}^2+\tau_{kx}^2+4\tau_{ky}^2\right)}{8\tau_0^7},\\
&b_{12} = \frac{\tau_{kx}^4\left(\tau_{ky}^4-6\tau_{ky}^2\tau_{kz}^2-9\tau_{kz}^4\right)+\tau_{kx}^2\left(2\tau_{ky}^6-4\tau_{ky}^4\tau_{kz}^2-6\tau_{ky}^2\tau_{kz}^4\right)+\tau_{ky}^4\left(\tau_{ky}^2+\tau_{kz}^2\right)^2}{4\tau_0^7},\\
&b_{13} = \frac{\tau_{ky}^4\left(\tau_{kx}^4-6\tau_{kx}^2\tau_{kz}^2-9\tau_{kz}^4\right)+\tau_{ky}^2\left(2\tau_{kx}^6-4\tau_{kx}^4\tau_{kz}^2-6\tau_{kx}^2\tau_{kz}^4\right)+\tau_{kx}^4\left(\tau_{kx}^2+\tau_{kz}^2\right)^2}{4\tau_0^7},\\
&b_{23} = \frac{\tau_{kx}^4\left(\tau_{kz}^4-6\tau_{ky}^2\tau_{kz}^2-9\tau_{ky}^4\right)+\tau_{kx}^2\left(2\tau_{kz}^6-4\tau_{ky}^4\tau_{kz}^2-6\tau_{ky}^2\tau_{kz}^4\right)+\tau_{kz}^4\left(\tau_{ky}^2+\tau_{kz}^2\right)^2}{4\tau_0^7}.
\end{aligned}
\tag{5.D.2}
$$

where $\tau_{kx} = x/V_{k1}$, $\tau_{ky} = y/V_{k2}$ and $\tau_{kz} = z/V_{k0}$.

Chapter 6 An anelliptic approximation for geometrical spreading in transversely isotropic and orthorhombic media

Shibo Xu[1], Alexey Stovas[1] and Yanadet Sripanich[2]

[1]Norwegian University of Science and Technology, Trondheim, Norway,

[2]University of Texas at Austin, Austin, USA

Abstract The relative geometrical spreading along the ray-path contributes to the amplitude decay of the seismic wave propagation that needs to be considered for amplitude versus offset (AVO) or other seismic data processing methods that require the true amplitude processing. Expressing the P-wave geometrical spreading factor in terms of the offset-traveltime based parameters is a more practical and convenient way since these parameters can be estimated from the nonhyperbolic velocity analysis. We propose an anelliptic approximation for the relative geometrical spreading of P-wave in a homogeneous transversely isotropic medium with vertical symmetry axis (VTI) and an orthorhombic medium (ORT) under the acoustic anisotropy assumption. The coefficients in the proposed approximation are only defined within the symmetry planes and computed from fitting with the exact parametric expression. For ORT model, due to the symmetric behavior in different symmetry planes, the other coefficients in the approximation can be easily obtained by corresponding changes in indices from the computed the coefficients in one symmetry plane. From the numerical examples, we show that for a homogeneous VTI model, the anelliptic approximation is more accurate than the generalized nonhyperbolic moveout approximation (GMA) form for larger offset. For a homogeneous ORT model, the proposed anelliptic approximation is more accurate than the traveltime-based counterparts. Using the Dix-type equations for the effective parameters, the

proposal anelliptic form approximation is extended to a multilayered VTI and ORT models and show its highly accurate results in both models.

Presented at the 87th SEG Conference and Exhibition, September, 2017, Houston, USA; Published in Geophysics in November 2017.

6.1 Introduction

Geometrical spreading describes the amplitude decay of propagating waves and is one of the most fundamental subjects in seismic data processing. It is important for prestack Kirchhoff migration, amplitude versus offset (AVO) analysis and other seismic data processing methods that require the true amplitude processing. The amplitude distribution along the wavefront of the reflected wave is changed greatly if the velocity model is anisotropic. Seismic data must be compensated for geometrical spreading before AVO or amplitude versus angle (AVA) analysis in order to study reflection coefficients as a function of offset or incidence angle. Although geometrical spreading is a dynamic quantity, it is governed by the kinematic parameters of seismic waves. When the velocity model is available, the relative geometrical spreading can be computed by performing dynamic ray tracing. However, accurate information about the anisotropic velocity model for the whole overburden is seldom available for practice. To avoid the use of numerical ray tracing, expressing the geometrical spreading through traveltime of the reflection events recorded at the surface using ray theory (Červený 2001) is a more practical method for seismic time processing. Therefore, it is convenient to express the geometrical spreading in terms of the offset-traveltime parameters that can be estimated from the nonhyperbolic velocity analysis.

Ursin (1990) proposed a geometrical spreading approximation represented by traveltime parameters for a layered isotropic medium. One of the practical contributions from the paraxial ray theory is an expression for geometrical spreading in terms of the traveltime functions at the source and receivers locations (Červený, 2001). Zhou and McMechan (2000) derived an analytical formula for the geometrical spreading of P-waves in a layered transversely isotropic medium with vertical symmetry axis (VTI) with the source and receivers in the same layer. Ursin and Hokstad (2003) extended the method of Ursin (1990) for multiple reflected and converted P- and SV-waves in a layered VTI medium with the

source and receivers in different layers. For pure reflection modes (P or SV) in layered anisotropic media, the geometrical spreading as a function of traveltime derivatives was obtained by Xu *et al.* (2005). The geometrical spreading correction for an azimuthally anisotropic medium was later derived by Xu and Tsvankin (2006), and was extended for converted waves in a VTI medium (Xu and Tsvankin, 2008). A practical application of anisotropic geometrical spreading for AVO analysis was made by Xu and Tsvakin (2007) with the wide-azimuthal data acquired at the Rulison field, Colorado. The traveltime-based geometrical spreading approximation in TTI media was derived by Golikov and Stovas (2013). All these approximations are approximating the traveltime and use it and its derivatives for the computation of the geometrical spreading approximation, we refer it as the traveltime-based approximation or indirect approximation. Different nonhyperbolic moveout approximations for a homogeneous VTI model are listed in Fowler (2003) and Golikov and Stovas (2012). Although the geometrical spreading factor is controlled by first- and second-order traveltime derivatives, there is no guarantee that the most accurate traveltime approximation being used in equations for geometrical spreading results in the most accurate geometrical spreading equation. Different from the indirect type approximation, which is approximating the traveltime for geometrical spreading approximation, the direct type approximation is computed by approximating the geometrical spreading term directly from the exact parametric equations obtained from the dynamic ray-tracing. The first example of this comparison between indirect and direct type approximation is done by Stovas and Ursin (2009) who developed the rational type of approximation in direct form. They showed that the direct rational approximation is simpler and more accurate than the indirect counterpart for a homogeneous and multilayered VTI model. Xu and Stovas (2017) proposed a direct type approximation with the generalized nonhyperbolic form for the relative geometrical spreading for a VTI medium and compared them with the indirect ones.

The orthorhombic (ORT) model is introduced by Schoenberg and Helbig (1997) and has gained more attention due to the need to characterize the fractured earth. They have become a new standard to define model parameters to cover the azimuthal dependence of the traveltime surface. Tsvankin (1997, 2012) defined nine elastic model parameters for ORT model that can be reduced to six parameters in an acoustic approximation (Alkhalifah, 2003). In the group domain, we refer to the first order curvature as the normal moveout (NMO) velocity ellipses (Grechka and Tsvankin, 1999a, 1999b) and the second order curvature as the anellipticities because they represent the anelliptic behaviour for slowness and traveltime surface. Stovas (2015) derived azimuthally dependent kinematic properties of the orthorhombic media and defined the effective ORT parameters in the Dix-type in layered ORT media that derived from the Dix inversion (Dix, 1955). Sripanich and Fomel (2015) modified the anelliptic functional form of Fomel (2004) and extended it to ORT model to approximate P-wave phase and group velocities.

In this paper, we propose an anelliptic approximation in reminiscent of the functional form studied by Sripanich and Fomel (2015) for direct type relative geometrical spreading in VTI and ORT media. The coefficients in the approximation are defined within the symmetry plane and obtained from fitting with the exact relative geometrical spreading in the symmetry planes. Due to the symmetric behavior in different symmetry planes by using the acoustic anisotropy assumption (Alkhalifah, 1998), the computation for the coefficients in ORT model becomes easier by applying corresponding changes in the forms of the coefficients that obtained in one symmetry plane. Subsequently, we extend our method for layered VTI and ORT models by using the effective model parameters computed from the Dix-type equation (Stovas, 2015). Using numerical examples, we show that the results from the proposed approximation are highly accurate for both homogeneous and layered VTI and ORT cases.

6.2 Relative geometrical spreading in a VTI model

The relative geometrical spreading is given in Červený (2001) as

$$\mathcal{L} = \sqrt{\frac{\cos\theta_S \cos\theta_R}{|\det \mathbf{M}|}}, \tag{6.1}$$

where θ_S and θ_R are the angles between the ray and the normal to the surface measured at the source and receiver, respectively. Measured from the dynamic ray-tracing, θ_S and θ_R are all group angle. **M** is the second order derivatives matrix given by

$$\mathbf{M} = \begin{pmatrix} \dfrac{\partial^2 T}{\partial x_S \partial x_R} & \dfrac{\partial^2 T}{\partial x_S \partial y_R} \\ \dfrac{\partial^2 T}{\partial y_S \partial x_R} & \dfrac{\partial^2 T}{\partial y_S \partial y_R} \end{pmatrix}, \tag{6.2}$$

where (x_S, y_S) and (x_R, y_R) are the lateral coordinates of source and receiver, respectively. The relative geometrical spreading in a VTI model is given by (Ursin and Hokstad, 2003)

$$\mathcal{L} = \Omega \left(\frac{1}{x}\frac{dt}{dx}\right)^{-1/2} \left(\frac{d^2 t}{dx^2}\right)^{-1/2}, \tag{6.3}$$

where Ω is the radiation pattern given by $\Omega = \sqrt{\cos\theta_S \cos\theta_R}$. In our paper, we neglect the radiation pattern and focus only on the term $\mathcal{L}_N$ that is given as

$$\mathcal{L}_N = \left(\frac{1}{x}\frac{dt}{dx}\frac{d^2 t}{dx^2}\right)^{-1/2}. \tag{6.4}$$

The relative geometrical spreading term $\mathcal{L}_N$ given in equation 6.4 can also be written as a function of horizontal slowness p in the case of flat layer as follows (Stovas and Ursin, 2009)

$$\mathcal{L}_N = \left(\frac{x}{p}\frac{dx}{dp}\right)^{1/2}. \tag{6.5}$$

For a homogeneous VTI model, the offset under an acoustic approximation can be given in terms of horizontal slowness Alkhalifah (1998),

$$x(p) = \frac{p t_0 V_n^2}{\left(1 - 2\eta p^2 V_n^2\right)^{3/2} \sqrt{1 - (1+2\eta) p^2 V_n^2}}, \tag{6.6}$$

where t_0 is the vertical one way traveltime, V_n is the normal moveout (NMO) velocity and η is the anellipticity parameter (Alkhalifah, 1998).

Substituting equation 6.6 into equation 6.5 gives (Stovas and Ursin, 2009)

$$\mathcal{L}_N = \frac{t_0 V_n^2 \sqrt{1 + 4\eta p^2 V_n^2 - 6\eta(1+2\eta) p^4 V_n^4}}{\left(1 - 2\eta p^2 V_n^2\right)^2 \left(1 - (1+2\eta) p^2 V_n^2\right)}. \tag{6.7}$$

Equations 6.6 and 6.7 give an exact parametric equation for relative geometrical spreading $\mathcal{L}_N$ in terms of the horizontal slowness that can be measured from dynamic ray-tracing.

6.3 Anelliptic form approximation for the relative geometrical spreading in a VTI model

In VTI medium, we define the approximation for the relative geometrical spreading in an anelliptic resembling that of Sripanich and Fomel (2015) by

$$\mathcal{L}_N = h(1 - \hat{s}) + \hat{s} \sqrt{h^2 + \frac{2(\hat{q} - 1) w_1 w_3 x^2}{\hat{s}}}, \tag{6.8}$$

where the hyperbolic term $h = h(x)$ denotes the elliptic part of the relative geometrical spreading given by

$$h = w_1 x^2 + w_3, \tag{6.9}$$

with

$$w_1 = \lim_{x\to\infty} \frac{\mathcal{L}_N}{x^2} = \frac{1}{t_0\sqrt{1+2\eta}},$$
$$w_3 = \lim_{x\to 0} \mathcal{L}_N = t_0 V_n^2. \tag{6.10}$$

The functions $\hat{q} = \hat{q}(x)$ and $\hat{s} = \hat{s}(x)$ are defined by

$$\hat{q} = \frac{q_1 w_1 x^2 + q_3 w_3}{h},$$
$$\hat{s} = \frac{s_1 w_1 x^2 + s_3 w_3}{h}, \tag{6.11}$$

where q_1, q_3, s_1 and s_3 are the coefficients computed from the fitting process with the exact geometrical spreading form. Note that w_1 and w_3 in equation 6.9 have different units. If we define the hyperbolic term by $h = w_1 x^2 + w_3 t_0^2 V_0^2$, where V_0 is the vertical velocity, they will have the same units. The reason why we don't use this form is that we do not have vertical velocity in our list of parameters.

The offset and the depth is shown by the relation $x = z\tan(\theta)$, where z is the depth and θ is the dip group angle from the vertical axis. We define a function $r = r(\theta)$ that relates to the relative geometrical spreading as

$$r = \frac{\cos(\theta)^2 \mathcal{L}_N\left(x = z\tan(\theta)\right)}{z^2}. \tag{6.12}$$

The coefficients q_1, q_3, s_1 and s_3 in equation 6.8 can be computed by fitting with the exact equation for $\mathcal{L}_N$ (see equation A-3) through the second ($\partial^2 r/\partial\theta^2$) and forth order derivatives $\partial^4 r/\partial\theta^4$ at $\theta = 0^\circ$ and 90° as noted by the index 1 and 3 for the horizontal and vertical axes, respectively (Figure 6.1). The equations for q_1, q_3, s_1 and s_3 are given in Appendix A.

The coefficients q_1, q_3, s_1 and s_3 are plotted versus anellipticity parameter η in Figure 6.2. The coefficients q_1 and q_3 are gradually increasing with η, while s_1 and s_3 are almost

independent on η. When setting $\eta = 0$ corresponding to elliptical anisotropy, they become equivalent to each other with $q_1 = q_3 = 1$ and $s_1 = s_3 = 9/13$.

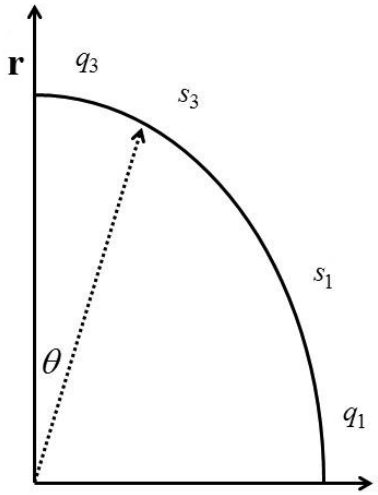

Figure 6.1. The location of fitting indices q_1, q_3, s_1 and s_3 in a homogeneous VTI model.

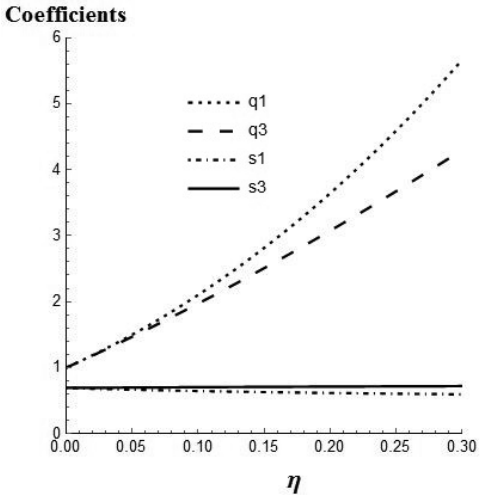

Figure 6.2. The sensitivity of coefficients q_1, q_3, s_1 and s_3 versus anellipticity η.

In order to test the accuracy of the anelliptic approximation, we use a homogeneous VTI model with parameters: $t_0 = 1\,s$, $V_n = 2km/s$ and $\eta = 0.2$. We show the relative error in relative geometrical spreading versus normalized offset computed from our proposed method and the approximation in GMA form approximation computed from infinite offset limit (Xu and Stovas, 2016) in Figure 6.3. Note that the approximations are compared with the exact parametric expression shown in equations 6.6 and 6.7 that are computed from dynamic ray-tracing. One can see that comparing with GMA form approximation in a homogeneous VTI model, the anelliptic approximation is less accurate at short offset while when approaching to a larger offset it becomes more accurate as the fixing elliptical background it used. Subsequently, we introduce a multi-layered VTI model using the parameters in Table 6.1 and show the relative error versus offset-depth ratio in Figure 6.4. The effective model parameters are computed from Dix-type equations shown in Appendix B. One can see that the errors are all increasing with η and the error from the anelliptic approximation is always smaller than the GMA form approximation.

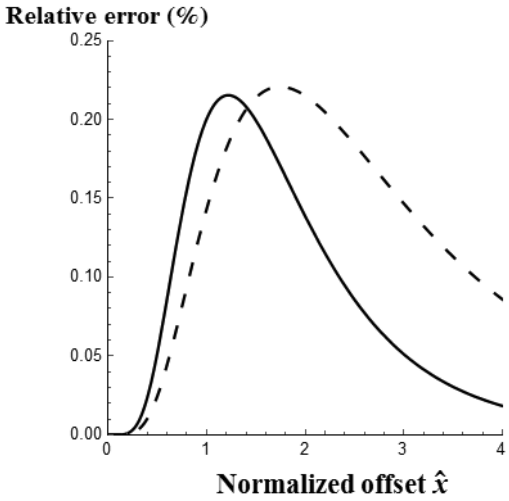

Figure 6.3. The relative error for anelliptic (solid) and GMA form (dashed) approximation for the relative geometrical spreading in a homogeneous VTI medium.

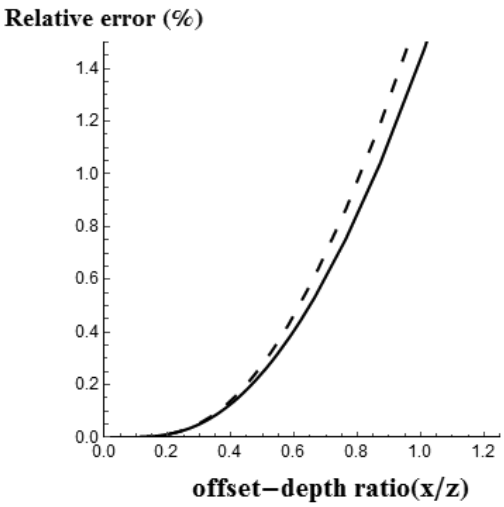

Figure 6.4. The relative error for anelliptic (solid) and GMA form (dashed) approximation for the relative geometrical spreading in a multi-layered VTI medium.

Layer	Layer thickness (km)	Vertical velocity (km/s)	NMO velocity (km/s)	Anellipicity parameter
1	0.3	1.5	1.8	0.1
2	0.7	1.8	2	0.15
3	1	2	2.2	0.18

Table 6.1. The model parameters in a multilayered VTI model.

6.4 Relative geometrical spreading in a homogeneous ORT model

For a homogeneous ORT model, we introduce two lateral offset projections

$$\begin{aligned} x &= x_R - x_S, \\ y &= y_R - y_S. \end{aligned} \tag{6.13}$$

The matrix **M** in equation 6.2 takes the form

$$\mathbf{M} = \begin{pmatrix} \dfrac{\partial^2 T}{\partial x^2} & \dfrac{\partial^2 T}{\partial x \partial y} \\ \dfrac{\partial^2 T}{\partial y \partial x} & \dfrac{\partial^2 T}{\partial y^2} \end{pmatrix}, \tag{6.14}$$

In phase domain, the relative geometrical spreading $\mathcal{L}_N$ can be given by Stovas (2017)

$$\mathcal{L}_N = \left(\frac{\partial x}{\partial p_x}\frac{\partial y}{\partial p_y} - \frac{\partial y}{\partial p_x}\frac{\partial x}{\partial p_y} \right)^{1/2}. \tag{6.15}$$

To compute the geometrical spreading for a homogeneous ORT model, we use exact parametric offset equations (Stovas, 2015):

$$\begin{aligned} x(p_x, p_y) &= p_x F_2^2 \frac{V_{n1}^2 t_0}{f_1^{1/2} f_2^{3/2}}, \\ y(p_x, p_y) &= p_y F_1^2 \frac{V_{n2}^2 t_0}{f_1^{1/2} f_2^{3/2}}, \end{aligned} \tag{6.16}$$

$x(p_x, p_y)$ and $y(p_x, p_y)$ are corresponding offset projections, and

$$\begin{aligned} F_1 &= 1 - p_x^2 V_{n1}^2 (2\eta_1 - \eta_{xy}), \\ F_2 &= 1 - p_y^2 V_{n2}^2 (2\eta_2 - \eta_{xy}), \\ f_1 &= 1 - (1+2\eta_1) p_x^2 V_{n1}^2 - (1+2\eta_2) p_y^2 V_{n2}^2 + \left((1+2\eta_1)(1+2\eta_2) - (1+\eta_{xy})^2 \right) p_x^2 p_y^2 V_{n1}^2 V_{n2}^2, \\ f_2 &= 1 - 2\eta_1 p_x^2 V_{n1}^2 - 2\eta_2 p_y^2 V_{n2}^2 + (4\eta_1\eta_2 - \eta_{xy}^2) p_x^2 p_y^2 V_{n1}^2 V_{n2}^2, \end{aligned} \tag{6.17}$$

where V_{n1} and V_{n2} are corresponding NMO velocities defined in $[X, Z]$ and $[Y, Z]$ planes, respectively. Anellipticity parameters η_1 and η_2 are defined in corresponding two vertical symmetry $[X, Z]$ and $[Y, Z]$ planes, respectively. Note that the definition of indices is different with the one defined in standard Tsvankin (1997) indices. The cross-term anellipticity parameter η_{xy} is defined as (Stovas, 2015)

$$\eta_{xy} = \sqrt{\frac{(1+2\eta_1)(1+2\eta_2)}{1+2\eta_3}} - 1, \tag{6.18}$$

where anellipticity parameter η_3 is defined in $[X, Y]$ plane (Vasconcelos and Tsvankin, 2006).

The relative geometrical spreading for ORT medium is given by Stovas (2017)

$$\mathcal{L}_N = t_0 V_{n1} V_{n2} \frac{F_1 F_2}{f_2^2 f_1} \sqrt{f_m}, \tag{6.19}$$

where

$$\begin{aligned} f_m = {} & 1 + 4\eta_1 p_x^2 V_{n1}^2 + 4\eta_2 p_y^2 V_{n2}^2 - 6\eta_1 (1+2\eta_1) p_x^4 V_{n1}^4 - 6\eta_2 (1+2\eta_2) p_y^4 V_{n2}^4 \\ & + 2\left(8\eta_1\eta_2 - \eta_{xy}\left(3 + 5\eta_{xy}\right)\right) p_x^2 p_y^2 V_{n1}^2 V_{n2}^2 \\ & - 6(1+2\eta_1)\left(4\eta_1\eta_2 - \eta_{xy}^2\right) p_x^4 p_y^2 V_{n1}^4 V_{n2}^2 - 6(1+2\eta_2)\left(4\eta_1\eta_2 - \eta_{xy}^2\right) p_x^2 p_y^4 V_{n1}^2 V_{n2}^4 \\ & + 9\left((1+2\eta_1)(1+2\eta_2) - (1+\eta_{xy})^2\right)\left(4\eta_1\eta_2 - \eta_{xy}^2\right) p_x^4 p_y^4 V_{n1}^4 V_{n2}^4. \end{aligned} \tag{6.20}$$

6.5 Anelliptic approximation for the relative geometrical spreading in an ORT model

In ORT medium, we define the approximation for relative geometrical spreading in an anelliptic form similar to Sripanich and Fomel (2015)

$$\mathcal{L}_{N(ORT)} = H(1-\hat{S}) + \hat{S}\sqrt{H^2 + F}, \tag{6.21}$$

with

$$F = F(x,y) = \frac{2\left(\left(\hat{Q}_1 - 1\right)W_2 W_3 y^2 + \left(\hat{Q}_2 - 1\right)W_1 W_3 x^2 + \left(\hat{Q}_3 - 1\right)W_1 W_2\right)}{\hat{S}}, \tag{6.22}$$

where the hyperbolic term $H = H(x,y)$ denotes the elliptic part of the relative geometrical spreading given by

$$H = W_1 x^2 + W_2 y^2 + W_3, \tag{6.23}$$

with

$$
\begin{aligned}
W_1 &= \lim_{x\to\infty, y\to 0} \frac{\mathcal{L}_{N(ORT)}}{x^2} = \frac{\left(1+\eta_{xy}\right)V_{n2}}{t_0\left(1+2\eta_1\right)^{3/2}V_{n1}}, \\
W_2 &= \lim_{x\to 0, y\to\infty} \frac{\mathcal{L}_{N(ORT)}}{y^2} = \frac{\left(1+\eta_{xy}\right)V_{n1}}{t_0\left(1+2\eta_2\right)^{3/2}V_{n2}}, \\
W_3 &= \lim_{x\to 0, y\to 0} \mathcal{L}_N(ORT) = t_0 V_{n1} V_{n2}.
\end{aligned}
\tag{6.24}
$$

The functions $\hat{Q}_i = \hat{Q}_i(x,y), (i=1,2,3)$ are defined as

$$
\begin{aligned}
\hat{Q}_1(x,y) &= \frac{Q_{21}W_2y^2 + Q_{31}W_3}{W_2y^2 + W_3}, \\
\hat{Q}_2(x,y) &= \frac{Q_{12}W_1x^2 + Q_{32}W_3}{W_1x^2 + W_3}, \\
\hat{Q}_3(x,y) &= \frac{Q_{13}W_1x^2 + Q_{23}W_2y^2}{W_1x^2 + W_2y^2}.
\end{aligned}
\tag{6.25}
$$

The functions $\hat{S} = \hat{S}(x,y)$ is given by

$$
\hat{S}(x,y) = \frac{\hat{S}_1(x,y)W_1x^2 + \hat{S}_2(x,y)W_2y^2 + \hat{S}_3(x,y)W_3}{H},
\tag{6.26}
$$

where

$$
\begin{aligned}
\hat{S}_1(x,y) &= \frac{S_{13}W_2y^2 + S_{12}W_3}{W_2y^2 + W_3}, \\
\hat{S}_2(x,y) &= \frac{S_{23}W_1x^2 + S_{21}W_3}{W_1x^2 + W_3}, \\
\hat{S}_3(x,y) &= \frac{S_{32}W_1x^2 + S_{31}W_2y^2}{W_1x^2 + W_2y^2}.
\end{aligned}
\tag{6.27}
$$

Similar to VTI case, we define a relative geometrical spreading related function by

$$
R = \frac{\cos(\theta)^2 \mathcal{L}_N\left(x = z\tan(\theta)\cos(\phi), y = z\tan(\theta)\sin(\phi)\right)}{z^2},
\tag{6.28}
$$

and define the dip angle θ and the azimuth ϕ in Figure 6.5, with the relations

$$\theta = \arctan\left(\frac{\sqrt{x^2+y^2}}{z}\right),$$
$$\phi = \arctan\left(\frac{y}{x}\right). \tag{6.29}$$

Twelve coefficients $Q_{ij},(i \neq j = 1,2,3)$ and $S_{ij},(i \neq j = 1,2,3)$ in equations 6.25 and 6.27, respectively, are computed by fitting with the exact relative geometrical spreading (see equation 6.C.2) through the second and forth order derivatives with respect to the dip and azimuth angles by

$$\begin{aligned}
&\frac{\partial^2 R(\phi=0^\circ)}{\partial\theta^2}\Big|(\theta=0^\circ,90^\circ)\Rightarrow(Q_{32},Q_{12}); \quad \frac{\partial^4 R(\phi=0^\circ)}{\partial\theta^4}\Big|(\theta=0^\circ,90^\circ)\Rightarrow(S_{32},S_{12}),\\
&\frac{\partial^2 R(\phi=90^\circ)}{\partial\theta^2}\Big|(\theta=0^\circ,90^\circ)\Rightarrow(Q_{31},Q_{21}); \quad \frac{\partial^4 R(\phi=90^\circ)}{\partial\theta^4}\Big|(\theta=0^\circ,90^\circ)\Rightarrow(S_{31},S_{21}),\\
&\frac{\partial^2 R(\theta=90^\circ)}{\partial\phi^2}\Big|(\phi=0^\circ,90^\circ)\Rightarrow(Q_{13},Q_{23}); \quad \frac{\partial^4 R(\theta=90^\circ)}{\partial\phi^4}\Big|(\phi=0^\circ,90^\circ)\Rightarrow(S_{13},S_{23}).
\end{aligned} \tag{6.30}$$

6.6 The symmetry of the anelliptic approximation

In order to calculate twelve coefficients $Q_{ij},(i \neq j = 1,2,3)$ and $S_{ij},(i \neq j = 1,2,3)$ required for $\hat{Q}_k(x,y)$ and $\hat{S}_k(x,y)$ given in equations 6.25 and 6.27, respectively, we focus on each individual symmetry plane separately. When we compute the coefficients in one symmetry plane, the similar coefficients for other two symmetry planes can be easily computed by corresponding changes in indices.

In $[X,Z]$ symmetry plane, when setting $y=0$, the anelliptic approximation in equation 6.21 is similar to the one computed for VTI model. In this symmetry plane, we need to define four coefficients: Q_{32}, Q_{12}, S_{32} and S_{12}. By taking the second and forth order derivatives of $R(\phi=0^\circ)$ with respect to the dip angle θ at 0° and 90°, the coefficients Q_{32}, Q_{12}, S_{32} and S_{12} are computed as it is shown in Appendix C.

The advantage of anelliptic approximation is its symmetric behavior in different symmetry planes. All required coefficients are computed within one plane and simple lead to corresponding expressions in the others. The notations for indices in coefficients Q_{ij} and S_{ij} are shown in Figure 6.5, and changing of indices can be obtained by clockwise rotation of the symmetry frame as shown in Figure 6.6.

When we have calculated the coefficients in $[X,Z]$ symmetry plane, the coefficients in $[Y,Z]$ and $[X,Y]$ symmetry planes can be easily computed using the transformation rule shown in Table 6.2. Note that the cross-term anellipticity parameter $\eta_{xy}^{(2,1)}$ defined in $[Y,Z]$ symmetry plane is the same as $\eta_{xy}^{(1,2)}$ defined in $[X,Z]$ symmetry plane.

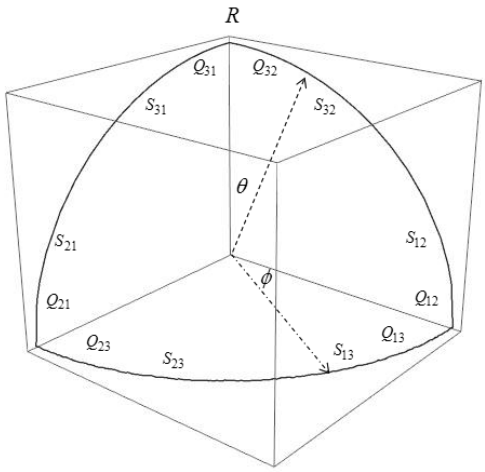

Figure 6.5. The location of fitting indices $Q_{ij},(i \neq j = 1,2,3)$ and $S_{ij},(i \neq j = 1,2,3)$ in a homogeneous ORT model.

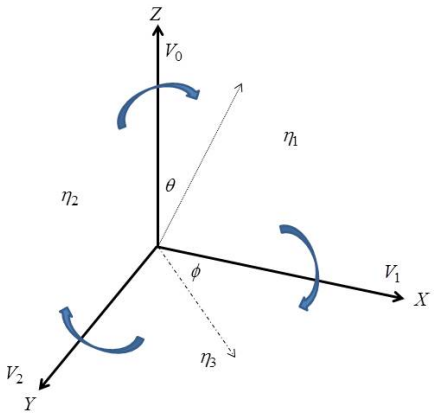

Figure 6.6. Rotation from $[X,Z]$ symmetry plane to $[X,Y]$ symmetry plane.

Plane	Vertical velocity	NMO velocity	Anellipticity parameter	Cross-term anellipticity parameter
$[X,Z]$	V_0	V_{n1}	η_1	$\eta_{xy}^{(1,2)} = \left(\sqrt{\frac{(1+2\eta_1)(1+2\eta_2)}{1+2\eta_3}} - 1 \right)$
$[Y,Z]$	V_0	V_{n2}	η_2	$\eta_{xy}^{(2,3)} = \left(\sqrt{\frac{(1+2\eta_2)(1+2\eta_1)}{1+2\eta_3}} - 1 \right)$
$[X,Y]$	$V_{n1}\sqrt{1+2\eta_1}$	$\frac{V_{n2}\sqrt{1+2\eta_2}}{\sqrt{1+2\eta_3}}$	η_3	$\eta_{xy}^{(1,3)} = \left(\sqrt{\frac{(1+2\eta_1)(1+2\eta_3)}{1+2\eta_2}} - 1 \right)$

Table 6.2. The corresponding transformation for the model parameters. The anellipticity parameter η_3 can be computed from η_1, η_2 and η_{xy} as $\eta_3 = \frac{1}{2}\left(\frac{(1+2\eta_1)(1+2\eta_2)}{(1+\eta_{xy})^2} - 1 \right)$.

6.7 Numerical examples

In order to illustrate the accuracy of proposed anelliptic approximation, we select an homogeneous ORT model with the parameters: $t_0 = 1s$, $V_{n1} = 2km/s$, $V_{n2} = 2.2km/s$, $\eta_1 = 0.1$, $\eta_2 = 0.12$ and $\eta_{xy} = 0.2$. We show the relative error from the approximation in Xu *et al.* (2005) (Figure 6.7, top), indirect rational type approximation (Appendix D) (Figure 6.7,

middle) and our proposed anellipic approximation (Figure 6.7, bottom). The form used in Xu *et al* (2005) is from the traveltime derivation based on the rational form moveout approximation (Tsvankin and Thomsen, 1994). One can tell from the comparison that our proposed approximation performs better accuracy, especially along x and y axes, and reaches the maximal error of 0.7% around 45° azimuth at the normalized offset $\hat{x} = \hat{y} \approx 1$.

We define a multi-layered ORT model with the parameters shown in Table 6.3 and show the relative error from the approximation in Xu *et al.* (2005) (Figure 6.8, top), indirect rational type approximation (Appendix D) (Figure 6.8, middle) and our proposed anellipic approximation (Figure 6.8, bottom). The effective model properties for the multilayered ORT model are computed form Dix-type equations shown in Appendix C. The error surface of the approximation from Xu *et al.* (2005) and the indirect rational form approximation are more complicated and their maximal error is larger than our proposed anelliptic approximation. Note that the value of anisotropy parameters in our paper is much larger the ones obtained from the field data in order to make the error from the approximation more visible. In practice, the result from our approximation is more accurate as the anisotropy in practical applicability is weaker.

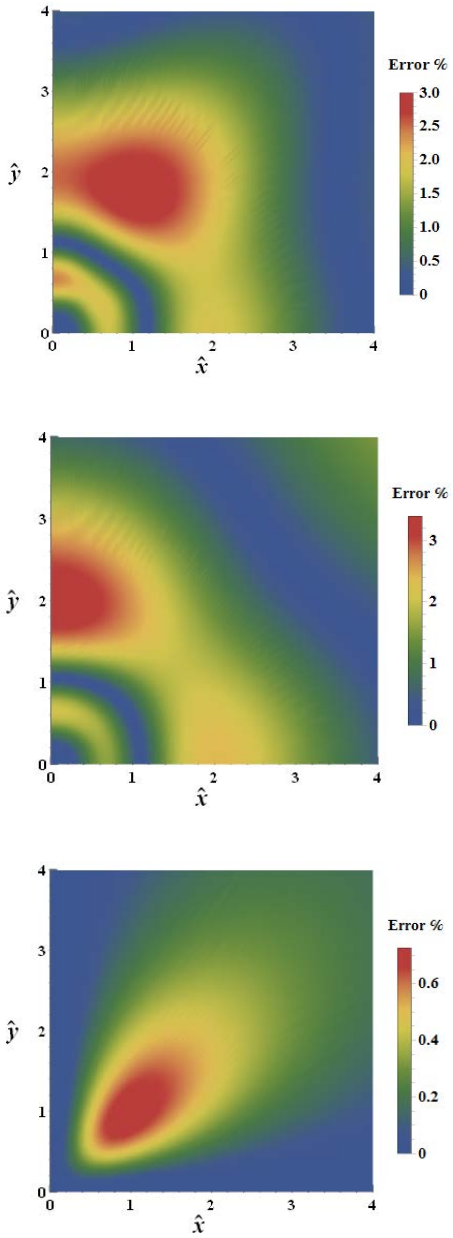

Figutre 6.7. The relative error of the relative geometrical spreading for a homegeneous ORT model by using the traveltime based approximation Xu *et al* (2005) (top), indierct rational approximaiton (middle) and anelliptic approximation (bottom).

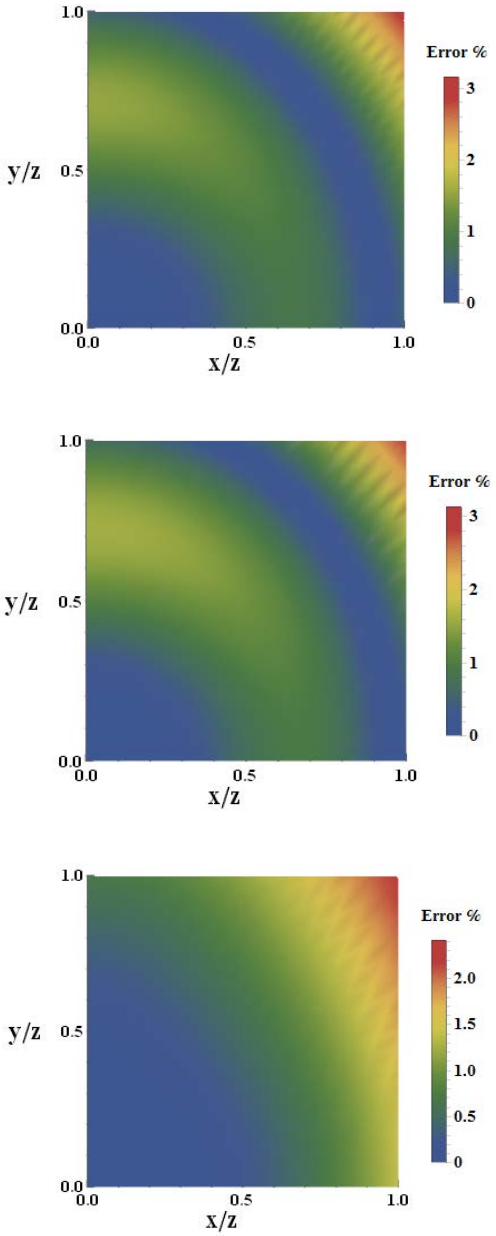

Figutre 6.8. The relative error of the relative geometrical spreading for a multi-layered ORT model by using the traveltime based approximation Xu *et al* (2005) (top), indierct rational approximaiton (middle) and anelliptic approximation (bottom).

Layer	$z(km)$	$V_0(km/s)$	$V_{n1}(km/s)$	$V_{n2}(km/s)$	η_1	η_2	η_{xy}
1	0.25	1.5	1.65	1.8	0.05	0.08	0.2
2	0.75	1.8	2	2.2	0.1	0.1	0.18
3	1	2	2.2	2.15	0.08	0.12	0.22

Table 6.3. The model parameters in a multilayered ORT model.

6.8 Discussions

For multilayered case, the expressions for relative geometrical spreading approximation we use are computed from the homogeneous model with the effective model parameters computed from Dix-type equations (Stovas, 2015). Selecting horizontal ray for calculation is impossible for ray-tracing, which means the assumption for infinite offset limit is not availed anymore, while we still using the expression computed from the homogeneous derived from the infinite offset assumption that explains the less accuracy compared with homogeneous case. When there is the azimuthal variation between the multilayered ORT model, the effective parameters with different azimuthal orientation of the layers is listed in Ravve and Koren (2017) and Koren and Ravve (2017).

Our anelliptic form resembling equations in (Sripanich and Fomel, 2015) are defined for the group velocity inverse for VTI and ORT model. The difference is that they define the anelliptic form for group velocity inverse first, computing the coefficients from fitting, then convert it to the traveltime approximation, while our proposed anelliptic form approximation is defined for relative geometrical spreading, then using the converted relation to obtain the coefficients. The converted relation is needed for both the anelliptic form traveltime and geometrical spreading approximation since there is no asymptotic behavior for traveltime or geometrical spreading at infinite offset that can be used for fitting.

The tricky part of our approximation is that we use the relative geometrical spreading related functions r (VTI) and R (ORT) to derive the coefficients used in approximation. This function has no physical meaning but used for a fitting technique. There is a simple relation between the function r (or R) and corresponding term $\mathcal{L}_N$. The form of this function is similar to the group velocity inverse in VTI and ORT models.

For example, in VTI case, function r is very similar to $1/V(\theta)^2$, where V is the group velocity and θ is the group angle. The traveltime and offset are given as

$$\begin{aligned} t &= \frac{z}{V(\theta)\cos(\theta)}, \\ x &= z\tan(\theta), \end{aligned} \tag{6.31}$$

The converted relation applied for traveltime and relative geometrical spreading are shown by

$$\begin{aligned} \frac{1}{V_{group}^2} &= \frac{\cos(\theta)^2}{z^2} t^2\left(x = z\tan(\theta)\right) \\ r &= \frac{\cos(\theta)^2}{z^2}\mathcal{L}_N\left(x = z\tan(\theta)\right), \end{aligned} \tag{6.32}$$

where z represents the depth. We do not have the value for depth as the offset x in the geometrical spreading approximation $\mathcal{L}_N$ is represent by $x = z\tan(\theta)$, which cancels the depth factor z in the denominator, keeping only the variable θ used for fitting.

The relative geometrical spreading $\mathcal{L}_N$ is shown by the form of traveltime derivative with respect to the offset in equation 6.4. Substituting the traveltime from in equation 6.31 and take the derivative with respect to the offset x gives

$$\mathcal{L}_N = \frac{V^2 z}{\cos(\theta)^2}\sqrt{\frac{V}{\left(V - V'\cot(\theta)\right)\left(2V'^2 + V\left(V - V''\right)\right)}}. \tag{6.33}$$

The function r can be represented in the group velocity and its derivatives with respect to the group angle

$$r = \frac{\mathcal{L}_N \cos(\theta)^2}{z^2} = \frac{V^2}{z}\sqrt{\frac{V}{(V - V'\cot(\theta))(2V'^2 + V(V - V''))}}. \tag{6.34}$$

For anelliptic form traveltime approximation (Sripanich and Fomel, 2015), $1/V^2(\theta)$ is the one used for fitting process at $\theta = 0^\circ$ and $\theta = 90^\circ$. However, for our proposed anellipitc form geometrical spreading, the function r (combination of group velocity and its derivatives) given in equation 6.34 is the one using for fitting process, which is much more completed compared with the traveltime case ($1/V^2(\theta)$).

The beauty of the anelliptic approximation is that we use the properties only on the three symmetry planes, therefore, the behavior in three planes are all symmetric. It is convenient to get the coefficients in other planes by properly rotation on the index after obtaining the coefficients in one symmetry plane.

For anelliptic traveltime approximation for ORT model (Sripanich and Fomel, 2015), when we focus on one symmetry plane, the approximation converges to the one defined for VTI model. For anelliptic relative geometrical spreading approximation, the situation is different, and approximation does not converge to the VTI counterpart (Appendix A) or any of symmetry planes due to different number of parameters. This happens due to the mixed derivatives entering the equation for geometrical spreading (equation 6.4). Both NMO velocities V_{n1}, V_{n2} and cross-term anellipticity parameters are presented in all equations defined either in $[X, Z]$ or $[Y, Z]$ symmetry planes.

To reduce the relative geometrical spreading from ORT to VTI cases, the following reduction in parameters is required.

$$
\begin{aligned}
&V_{n2} = V_{n1} = V_n, \\
&\eta_2 = \eta_1 = \eta, \\
&\eta_{xy} = 2\eta, \\
&\eta_3 = 0.
\end{aligned}
\tag{6.35}
$$

6.9 Conclusions

We propose an anelliptic form approximation for the relative geometrical spreading in a homogeneous VTI and ORT media under the acoustic anisotropy assumption. All the coefficients in the approximation are calculated by fitting with the exact parametric solution within the symmetry planes. Compared with the GMA form approximation, our proposed anelliptic approximation is more accurate for larger offset in a homogeneous VTI model. Due to symmetric behavior, the coefficients of the approximation in ORT model can be easily obtained after computing the coefficients in one symmetry plane and applying the required rotation for the other. The form of the anelliptic approximation is simpler while the traveltime-based counterparts are algebraically complicated. In the numerical examples, one can see that compared with the traveltime-based approximations, our anelliptic form approximation is more accurate for both homogeneous and multi-layered ORT models.

6.10 Acknowledgments

We would like to thank China Scholarship Council (CSC) and Rose Project for the financial support. Y. Sripanich thanks the sponsors of the Texas consortium for computational seismology for financial support. Y. Sripanich was also additionally supported by the Statoil fellows program at the university of Texas at Austin.

6.11 Appendix A

The coefficients q_1, q_3, s_1 and s_3 of the anelliptic approximation for a transversely isotropic medium with a vertical symmetry axis

The function r in VTI model is defined in equation 6.12, the derivatives of r with respect to the group angle θ at zero offset are

$$\begin{aligned}\frac{\partial^2 r}{\partial\theta^2}_{(\theta=0)} &= \frac{q_3}{t_0\sqrt{1+2\eta}} - \frac{t_0 V_n^2}{z^2},\\ \frac{\partial^4 r}{\partial\theta^4}_{(\theta=0)} &= \frac{2s_3\left((1+2\eta)t_0^4 V_n^4 - \sqrt{1+2\eta}\,q_3 t_0^2 V_n^2 z^2 + 3\sqrt{1+2\eta}(1-q_1-2q_3)z^4\right) - 3(q_3-1)^2 z^4}{6(1+2\eta)s_3 t_0^3 V_n^2 z^2}.\end{aligned} \tag{6.A.1}$$

The derivatives of r with respect to the group angle θ at infinite offset are

$$\begin{aligned}\frac{\partial^2 r}{\partial\theta^2}_{(\theta=\pi/2)} &= -\frac{1}{t_0\sqrt{1+2\eta}} + \frac{t_0 V_n^2 q_1}{z^2},\\ \frac{\partial^4 r}{\partial\theta^4}_{(\theta=\pi/2)} &= \frac{-3(1+2\eta)^{3/2} t_0^4 V_n^4\left(1+q_1^2-2(1+q_3)s_1-2q_1(1-2s_1)\right) - 2(1+2\eta)q_1 s_1 t_0^2 V_n^2 z^2 + 2\sqrt{1+2\eta}\,s_1 z^4}{6(1+2\eta)s_1 t_0 z^4}.\end{aligned} \tag{6.A.2}$$

By fitting with the exact form the coefficients q_1, q_3, s_1 and s_3 are given by

$$\begin{aligned} q_1 &= \sqrt{1+2\eta}\left(1+8\eta+12\eta^2\right),\\ q_3 &= \sqrt{1+2\eta}\,(1+8\eta),\\ s_1 &= \frac{\left(1+\eta\left(9+4\eta\left(15+2\eta\left(23+3\eta(11+6)\right)\right)\right)\right) - \sqrt{1+2\eta}\,(1+2\eta)(1+6\eta)}{\left(1+9\eta(1+2\eta)^3(1+4\eta)\right) - \sqrt{1+2\eta}\,(1+8\eta(1+3\eta))},\\ s_3 &= \frac{\left(1+9\eta+48\eta^2+64\eta^3\right) - \sqrt{1+2\eta}\,(1+8\eta)}{\left(1+9\eta+54\eta^2+72\eta^3\right) - \sqrt{1+2\eta}\left(1+8\eta-12\eta^2\right)}.\end{aligned} \tag{6.A.3}$$

In elliptical case ($\eta = 0$, $q_1 = q_3 = 1$ and $s_1 = s_3 = 9/13$), the function r becomes

$$r = \frac{\cos(\theta)^2 t_0 V_n^2}{z^2} + \frac{\sin(\theta)^2}{t_0} \tag{6.A.4}$$

6. 12 Appendix B

The effective model parameters for the multilayered transversely isotropic and orthorhombic media

The effective model parameters from the multilayered model are computed from traveltime parameters (high-frequency) and from upscaling (low-frequency). The computation in our

paper is computed from dynamic ray-tracing, so the traveltime parameters are used. The Dix type equation is derived from the Dix inversion (Dix, 1955) that is estimating the individual layer parameters from the recorded reflections on seismic seismogram for the horizontally layered medium.

In order to apply approximation in equation 6.8 computed from the homogeneous model for a multilayered VTI medium, the effective parameters by using the Dix-type equations are shown by:

$$\begin{aligned}
&\tilde{t}_0 = \sum_{j=1}^{m} t_{0j}, \\
&\tilde{V}_n = \sqrt{\frac{\sum_{j=1}^{m} V_{nj}^2 t_{0j}}{\tilde{t}_0}}, \\
&\tilde{\eta} = \frac{1}{8}\left(\frac{\sum_{j=1}^{m} \left(1+8\eta_j\right) V_{nj}^4 t_{0j}}{\tilde{V}_n^4 \tilde{t}_0} - 1 \right), m = 1,..,3.
\end{aligned} \tag{6.B.1}$$

The exact form of relative geometrical spreading in multilayered VTI case is computed from the summation as shown below

$$\begin{aligned}
&x(p) = \sum_{j=1}^{m} \frac{p t_{0j} V_{nj}^2}{\left(1-2\eta_j p^2 V_{nj}^2\right)^{3/2} \sqrt{1-\left(1+2\eta_j\right) p^2 V_{nj}^2}}, \\
&\mathcal{L}_N = \sum_{j=1}^{m} \frac{t_{0j} V_{nj}^2 \sqrt{1+4\eta_j p^2 V_{nj}^2 - 6\eta_j \left(1+2\eta_j\right) p^4 V_{nj}^4}}{\left(1-2\eta_j p^2 V_{nj}^2\right)^2 \left(1-\left(1+2\eta_j\right) p^2 V_{nj}^2\right)}, m = 1,..,3.
\end{aligned} \tag{6.B.2}$$

It is computed by summing for each individual layers (equation 6.B.2) that explains why the relative error doesn't go to zero for large offset-depth ratio.

Similar to the multilayered VTI case, the effective properties used in multilayered orthorhombic (ORT) model are computed from Dix-type equations (Stovas, 2015):

$$
\begin{aligned}
\tilde{t}_0 &= \sum_{j=1}^{m} t_{0j}, \\
\tilde{V}_{n1} &= \sqrt{\frac{\sum_{j=1}^{m} V_{n1j}^2 t_{0j}}{\tilde{t}_0}}, \\
\tilde{V}_{n2} &= \sqrt{\frac{\sum_{j=1}^{m} V_{n2j}^2 t_{0j}}{\tilde{t}_0}}, \\
\tilde{\eta}_1 &= \frac{1}{8}\left(\frac{\sum_{j=1}^{m} (1+8\eta_{1j}) V_{n1j}^4 t_{0j}}{\tilde{V}_{n1}^4 \tilde{t}_0} - 1 \right), \\
\tilde{\eta}_2 &= \frac{1}{8}\left(\frac{\sum_{j=1}^{m} (1+8\eta_{2j}) V_{n2j}^4 t_{0j}}{\tilde{V}_{n2}^4 \tilde{t}_0} - 1 \right), \\
\tilde{\eta}_{xy} &= \frac{1}{4}\left(\frac{\sum_{j=1}^{m} (1+4\eta_{xyj}) V_{n1j}^2 V_{n2j}^2 t_{0j}}{\tilde{V}_{n1}^2 \tilde{V}_{n2}^2 \tilde{t}_0} - 1 \right), m = 1,..,3.
\end{aligned}
\tag{6.B.3}
$$

The exact relative geometrical spreading in multilayered ORT is computed by summation for individual layers by parametric equations 6.15 and 6.17 as shown below

$$
\begin{aligned}
x(p_x, p_y) &== \sum_{j=1}^{m} p_x F_2'^2 \frac{V_{n1j}^2 t_{0j}}{f_1'^{1/2} f_2'^{3/2}}, \\
y(p_x, p_y) &= \sum_{j=1}^{m} p_y F_1'^2 \frac{V_{n2j}^2 t_{0j}}{f_1'^{1/2} f_2'^{3/2}}, \\
\mathcal{L}_N &= \sum_{j=1}^{m} t_{0j} V_{n1j} V_{n2j} \frac{F_1' F_2'}{f_2'^2 f_1'} \sqrt{f_m'}, m = 1,...,3,
\end{aligned}
\tag{6.B.4}
$$

where

$$
\begin{aligned}
F_1' &= 1 - p_x^2 V_{n1j}^2 \left(2\eta_{1j} - \eta_{xyj}\right), \\
F_2' &= 1 - p_y^2 V_{n2j}^2 \left(2\eta_{2j} - \eta_{xyj}\right), \\
f_1' &= 1 - \left(1+2\eta_{1j}\right) p_x^2 V_{n1j}^2 - \left(1+2\eta_{2j}\right) p_y^2 V_{n2j}^2 + \left(\left(1+2\eta_{1j}\right)\left(1+2\eta_{2j}\right) - \left(1+\eta_{xyj}\right)^2\right) p_x^2 p_y^2 V_{n1j}^2 V_{n2j}^2, \\
f_2' &= 1 - 2\eta_{1j} p_x^2 V_{n1j}^2 - 2\eta_{2j} p_y^2 V_{n2j}^2 + \left(4\eta_{1j}\eta_{2j} - \eta_{xyj}^2\right) p_x^2 p_y^2 V_{n1j}^2 V_{n2j}^2, \\
f_m' &= 1 + 4\eta_{1j} p_x^2 V_{n1j}^2 + 4\eta_{2j} p_y^2 V_{n2j}^2 - 6\eta_{1j}\left(1+2\eta_{1j}\right) p_x^4 V_{n1j}^4 - 6\eta_{2j}\left(1+2\eta_{2j}\right) p_y^4 V_{n2j}^4 \\
&\quad + 2\left(8\eta_{1j}\eta_{2j} - \eta_{xyj}\left(3+5\eta_{xyj}\right)\right) p_x^2 p_y^2 V_{n1j}^2 V_{n2j}^2 \\
&\quad - 6\left(1+2\eta_{1j}\right)\left(4\eta_{1j}\eta_{2j} - \eta_{xyj}^2\right) p_x^4 p_y^2 V_{n1j}^4 V_{n2j}^2 - 6\left(1+2\eta_{2j}\right)\left(4\eta_{1j}\eta_{2j} - \eta_{xyj}^2\right) p_x^2 p_y^4 V_{n1j}^2 V_{n2j}^4 \\
&\quad + 9\left(\left(1+2\eta_{1j}\right)\left(1+2\eta_{2j}\right) - \left(1+\eta_{xyj}\right)^2\right)\left(4\eta_{1j}\eta_{2j} - \eta_{xyj}^2\right) p_x^4 p_y^4 V_{n1j}^4 V_{n2j}^4 .
\end{aligned}
\tag{6.B.5}
$$

6.13 Appendix C

The coefficients of the anelliptic approximation for orthorhombic model in $[X,Z]$ plane

The coefficients of the anelliptic approximation defined in on symmetry plane of the orthorhombic model are not the same as those computed for the VTI case (Appendix A). Due to presence of mixed derivatives in equation 6.14 or equation 6.15, all ORT model parameters are entering the equations defined in any of symmetry planes. However, with the use of corss-term anelliptic parameter η_{xy}, the number of parameters can be reduced to five. For $[X,Z]$ symmetry plane, these parameters are V_0, V_{n1}, V_{n2}, η_1 and η_{xy}.

In order to calculate the coefficients in anelliptic form approximation in $[X,Z]$ plane, we set $y=0$ in approximation given in equation 6.21. Only the $[X,Z]$ plane coefficients: Q_{32}, Q_{12}, S_{32} and S_{12} remains in the approximation.

We introduce the relative geometrical spreading related function R ($R = \cos(\theta)^2 \mathcal{L}_N / z^2$), where θ is the dip group angle to the vertical axis and z is the depth, we get the second and forth order derivatives of R with respect to θ as following

$$
\begin{aligned}
\frac{\partial^2 R}{\partial\theta^2}_{(\theta=0)} &= \frac{V_{n2}}{V_{n1}t_0}\left(\frac{(1+\eta_{xy})Q_{32}}{(1+2\eta_1)^{3/2}} - \frac{V_{n1}^2 t_0^2}{z^2}\right),\\
\frac{\partial^4 R}{\partial\theta^4}_{(\theta=0)} &= \frac{V_{n2}}{6(1+2\eta_1)^{7/2}S_{32}t_0^3 V_{n1}^3 z^2}\Big(-3\sqrt{1+2\eta_1}(1+\eta_{xy})^2(Q_{32}-1)^2 z^4 + 2S_{32}\Big((1+2\eta_1)^{7/2}t_0^4 V_{n1}^4\\
&\quad -(1+2\eta_1)^2(1+\eta_{xy})Q_{32}t_0^2 V_{n1}^2 z^2 + 3\sqrt{1+2\eta_1}(1+\eta_{xy})^2(1+Q_{12}-2Q_{32})z^4\Big)\Big),\\
\frac{\partial^2 R}{\partial\theta^2}_{(\theta=\pi/2)} &= \frac{V_{n2}}{V_{n1}t_0}\left(\frac{V_{n1}^2 t_0^2 Q_{12}}{z^2} - \frac{1+\eta_{xy}}{(1+2\eta_1)^{3/2}}\right),\\
\frac{\partial^4 R}{\partial\theta^4}_{(\theta=\pi/2)} &= \frac{V_{n2}}{6(1+2\eta_1)^{7/2}S_{12}t_0 V_{n1} z^4}\Big(-3(1+2\eta_1)^3\big(1+Q_{12}^2-2(1+Q_{32})S_{12}+2Q_{12}(2S_{12}-1)\big)t_0^4 V_{n1}^4\\
&\quad -2(1+2\eta_1)^{3/2}(1+\eta_{xy})Q_{12}S_{12}t_0^2 V_{n1}^2 z^2 + 2(1+\eta_{xy})^2 S_{12} z^4\Big)\Big)
\end{aligned}
\tag{6.C.1}
$$

.

By fitting with the exact form, the coefficients: Q_{12}, Q_{32}, S_{32} and S_{12} are given as

$$
\begin{aligned}
Q_{12} &= \sqrt{1+2\eta_1}\,(1+8\eta_1+6\eta_1\eta_{xy}),\\
Q_{32} &= \frac{(1+2\eta_1)^{3/2}(1+6\eta_1+\eta_{xy})}{1+\eta_{xy}},\\
S_{12} &= \frac{e_1+\sqrt{1+2\eta_1}\,e_2}{e_3+\sqrt{1+2\eta_1}\,e_4},\\
S_{32} &= \frac{f_1+\sqrt{1+2\eta_1}\,f_2}{f_3+\sqrt{1+2\eta_1}\,f_4}.
\end{aligned}
\tag{6.C.2}
$$

where

$$
\begin{aligned}
e_1 &= (1+\eta_{xy})(1+\eta_1(9+6\eta_{xy}+2\eta_1(4+3\eta_{xy})(6+8\eta_1+3\eta_{xy}+6\eta_1\eta_{xy}))),\\
e_2 &= -(1+\eta_{xy})(1+\eta_1(8+6\eta_{xy})),\\
e_3 &= (1+\eta_{xy})(1+9\eta_1(1+6\eta_1+8\eta_1^2)(1+\eta_{xy})^2),\\
e_4 &= -1-\eta_{xy}+2\eta_1(-4+6\eta_1-\eta_{xy}(13+6\eta_{xy})),\\
f_1 &= 144\eta_1^5 + (1+\eta_{xy})^2 + 3\eta_1(1+\eta_{xy})(3+\eta_{xy}) + 24\eta_1^4(11+2\eta_{xy})\\
&\quad + 6\eta_1^2(10+\eta_{xy}(8+\eta_{xy})) + 4\eta_1^3(46+\eta_{xy}(20+\eta_{xy})),\\
f_2 &= -(1+2\eta_1)(1+\eta_{xy})(1+6\eta_1+\eta_{xy}),\\
f_3 &= 9\eta_1(1+2\eta_1)^3(1+4\eta_1)+(1+\eta_{xy})^2,\\
f_4 &= -(1+\eta_{xy})(1+\eta_{xy}+2\eta_1(4+12\eta_1-\eta_{xy}(5+3\eta_{xy})))
\end{aligned}
\tag{6.C.3}
$$

By setting $\eta_1 = \eta$ and $\eta_{xy} = 2\eta$, the coefficients defined in equations 6.C.2 become equivalent to those defined in equations 6.A.3 for VTI model, $Q_{12} = q_1$, $Q_{32} = q_3$, $S_{12} = s_1$ and $S_{32} = s_3$.

Due to the symmetric behavior in the symmetry plane in ORT model, the other coefficients in the approximation can be easily obtained by corresponding changes in indices from the computed the coefficients in one symmetry plane (see transformation form in Table 6.2). The coefficients (Q_{21}, Q_{31}, S_{21} and S_{31}) defined in $[Y,Z]$ plane and the coefficients (Q_{23}, Q_{13}, S_{23} and S_{13}) defined in $[X,Y]$ plane are obtained from $[X,Z]$ plane coefficients (Q_{32}, Q_{12}, S_{32} and S_{12}) by setting ($\eta_1 \to \eta_2$) and ($\eta_1 \to \eta_3, \eta_{xy} \to \eta_{xy}^{13}$), respectively. Note that $\eta_{xy} \equiv \eta_{xy}^{12} = \eta_{xy}^{21}$.

6.14 Appendix D

The indirect rational form approximation for relative geometrical spreading in an ORT model.

A rational form similar to (Vasconcelos and Tsvankin, 2006) approximation for the traveltime in ORT model is defined by

$$T_{RA}^2 = A_{00} + A_{20}x^2 + A_{02}y^2 + \frac{A_{40}x^4 + A_{22}x^2y^2 + A_{04}y^4}{1 + \left(B_{20}x^2 + B_{02}y^2\right)} \qquad (6.D.1)$$

where the coefficients A_{00}, A_{20}, A_{02}, A_{40}, A_{22} and A_{04} are computed from the Taylor series at zero offset are given by

$$
\begin{aligned}
A_0 &= t_0^2, \\
A_{20} &= \frac{1}{V_{n1}^2}, \\
A_{02} &= \frac{1}{V_{n2}^2}, \\
A_{40} &= -\frac{2\eta_1}{t_0^2 V_{n1}^4}, \\
A_{04} &= -\frac{2\eta_2}{t_0^2 V_{n2}^4}, \\
A_{22} &= -\frac{2\eta_{xy}}{t_0^2 V_{n1}^2 V_{n2}^2}.
\end{aligned}
\tag{6.D.2}
$$

The remaining coefficients B_{20} and B_{02} are computed by the infinite offset limit shown as

$$
\begin{aligned}
B_{20} &= \frac{1+2\eta_1}{t_0^2 V_{n1}^2}, \\
B_{02} &= \frac{1+2\eta_2}{t_0^2 V_{n2}^2}.
\end{aligned}
\tag{6.D.3}
$$

The indirect (traveltime-based) rational form approximation for relative geometrical spreading is given by the derivatives of traveltime approximation in equation 6.D.1 with respect to the offsets given by

$$
\mathcal{L}_N = \left(\left(\frac{\partial^2 T_{RA}}{\partial x^2} \frac{\partial^2 T_{RA}}{\partial y^2} \right) - \left(\frac{\partial^2 T_{RA}}{\partial x \partial y} \frac{\partial^2 T_{RA}}{\partial y \partial x} \right) \right)^{-1/2}. \tag{6.D.4}
$$

Note that the indirect rational form approximation in equation 6.D.4 is algebraically complicated due to the second order derivatives.

Chapter 7 Fresnel zone in vertical transversely isotropic and orthorhombic media

Shibo Xu and Alexey Stovas

Norwegian University of Science and Technology, Trondheim, Norway

Abstract. The reflecting zone in the subsurface insonified by the first quarter of a wavelength and the portion of the reflecting surface involved in these reflections is called the Fresnel zone or first Fresnel zone. The horizontal resolution is controlled by acquisition factors and the size of the Fresnel zone. We derive an analytic expression for the radius of the Fresnel zone in time domain in transversely isotropic medium with a vertical symmetry axis (VTI) using the perturbation method from the parametric offset-traveltime equation. The acoustic assumption is used for simplification. The Shanks transform is applied to stabilize the convergence of approximation and to improve the accuracy. The similar strategy is applied for the azimuth-dependent radius of the Fresnel zone in orthorhombic (ORT) model for a horizontal layer. Different with the VTI case, the Fresnel zone in ORT model has a quasi-elliptic shape. We show that the size of the Fresnel zone is proportional to the corresponding traveltime, depth and the frequency. From the numerical examples, we can see that the Shanks transform approximations for Fresnel zone are very accurate for both VTI and ORT media.

Presented at the 80th EAGE Conference and Exhibition, June, 2018, Copenhagen, Denmark; Published in Geophysical Journal International in December 2017.

7.1 Introduction

The most common question in the reflection seismology is the resolution of the seismic image. We can consider both vertical and horizontal resolution. The horizontal resolution is controlled by acquisition factors and the size of the Fresnel zone. The Fresnel zone is, named for physicist Augustin-Jean Fresnel, used to compute the radio waves propagating between a transmitter and a receiver in antenna system (Hristov, 2000). The Fresnel zone or first Fresnel zone in geophysics indicates the portion of a reflector from which the energy of a reflection can reach a detector where the wave propagates within a ¼ wavelength. The second Fresnel zone is defined from the energy that arrives delayed one-half to one cycle, adding destructively to the energy from the first zone. Similarly, there is a third zone and so on. The adjective “first” is often dropped away because when the contributions of all zones are added together, only the first Fresnel zone remains while the effects of all subsequent zones cancel each other. Borrowed from classical physical optics, Seismic interpreters often use the Fresnel-zone concept to estimate the lateral resolution of unmigrated, stacked P-wave data. (Sheriff, 1996, Lindsey, 1989).

The Fresnel zone can be defined as the region of constructive interference enclosing the ray-theoretical reflection or mode-conversion point (Sheriff, 1980). Fresnel zones and volumes can be computed very efficiently by forwarding dynamic ray tracing in a known velocity model (Červený and Soares, 1992). Eaton et al (1991) extended the Fresnel-zone concept to include mode-converted (P-SV) reflections for both surface and VSP geometries. The equation that describes the size of a Fresnel zone in a constant-velocity medium for a zero offset can be found in (Sheriff, 1996). How actual Fresnel zones are computed for 3-D zero-offset reflections by forwarding modeling in a known medium is described in Hubral et al. (1993).

The projected Fresnel zone of a zero-offset reflection onto the subsurface reflector using a standard 3D CMP traveltime analysis, without knowing the overburden was developed in (Hubral et al, 1993; Schleicher et al, 1997). The calculation for the Fresnel zone radius was done in the time domain by Trorey (1970).

Since the Fresnel zone width is a measure of lateral resolution, usually, seismic waves cannot detect the subsurface features smaller than the size of Fresnel zone. More attention has been made to the awareness of three-dimensional effect within the frame of seismic resolution. Aspects of the seismic resolution which can be achieved in a seismic survey and the physical factors that limit this resolution have been treated by Sheriff (1980) and Lindsey (1989). The Fresnel zone determines the spatial resolving power for unmigrated seismic data with which important lithological changes along a seismic profile direction may be observed (Sheriff 1980). Additionally, it also largely contributes to the reflected and transmitted wavefields, and more specifically to their amplitudes (Spetzler and Snieder, 2004; Favretto-Cristini et al, 2007a, 2007b). Hagedoorn (1954) pointed out that the reflections area of the interface, and therefore vertical resolution can also be thought of as a Fresnel-zone problem. While the vertical resolution is mostly linked to the seismic wavelength (see, for instance, Widess, 1982), the lateral resolution depends on Fresnel zone considerations (Lindsey, 1989) and its difference in pre- and post-migrated data. Červený (2001) suggests two methods to include the Fresnel zone parameter calculations into the ray tracing procedure in complex 2D and 3D structures. Using a derivation that is based on mostly geometric considerations, Monk (2010) examined the shape of the Fresnel zone for the nonzero offset for a model with constant velocity gradient. The implications for seismic acquisition for adequate imaging were made by Monk (2009) when the Fresnel zone is properly sampled.

Few papers have been devoted to anisotropic media. For instance, Okoye and Uren (2000) calculate the Fresnel zone radius for zero-offset configurations for P- and SH-waves in TI

media and isotropic media and for dipping plane reflectors. They conclude that the Fresnel zone radius is predominantly dependent on the curvatures and wavelength of the wavefront as well as the dip angle of the reflector. The Thomsen anisotropy parameters δ, ε and γ (Thomsen, 1986) also affect the Fresnel zone radius. Moser and Červený (2007) show how the Fresnel region can be calculated by conventional dynamic ray tracing in Cartesian coordinates, for isotropic and anisotropic inhomogeneous layered media. Fresnel volume and interface Fresnel zone for reflected and transmitted waves from a curved interface in anisotropic media were analyzed by Ursin et al (2014).

In this paper, an analytic expression for the Fresnel zone radius is derived using the traveltime for VTI model by using the perturbation method. In order to do that, the parametric offset-traveltime equations under the acoustic approximation are used. We apply the Shanks transform to stabilize the approximation and improve the accuracy. The similar perturbation strategy is applied for the analytic expression of Fresnel zone radius in orthorhombic (ORT) model. The accuracy of proposed approximation for Fresnel zone is illustrated for both VTI and ORT models.

7.2 Fresnel zone using the traveltime

The seismic wave sent out from the source propagates in space and spread out over a larger area. The horizontal resolution is controlled by the Fresnel zone, the part of a reflector covered by the seismic signal at a certain depth where the wave propagates within ¼ wavelength after it first touches the reflector. The Fresnel zone (or first Fresnel zone) radius for a homogeneous horizontal layer is defined in Figure 7.1 (top). It is convenient to express the Fresnel zone using the traveltime parameters. The Fresnel zone radius X_F can be treated as the wave propagates in lateral direction with certain traveltime t_F and the Fresnel zone

radius using the traveltime is calculated by using the Pythagorean theorem (Figure 7.1, bottom),

$$X_F^2 + Z^2 = \left(V_\varphi t_F\right)^2, \tag{7.1}$$

where t_F is the corresponding traveltime when the wave propagates by ¼ wavelength after arriving the reflector with $t_F = t_0 + \Delta t$, where $\Delta t = \frac{1}{4f}$, f is the frequency, t_0 is the vertical traveltime with $t_0 = \frac{Z}{V_0}$, Z is the reflector depth, V_0 is the P-wave vertical velocity, V_φ is the corresponding group velocity computed for group angle φ defined from the vertical axis.

For a horizontal layer in a homogeneous isotropic (ISO) medium ($V_\varphi = V_0 = V$), the Fresnel radius using the traveltime is computed as following

$$X_F = V\sqrt{t_F^2 - t_0^2}. \tag{7.2}$$

By using $t_F = t_0 + \frac{1}{4f}$, the radius of Fresnel zone X_F can be computed from simple geometrical considerations (Figure 7.1, top),

$$X_F^2 + Z^2 = \left(t_0 V + \frac{\lambda}{4}\right)^2, \tag{7.3}$$

where λ is the wavelength with $\lambda = \frac{V}{f}$, V is the constant velocity. Solving equation (7.3) for X_F gives

$$X_F = \sqrt{\left(Z + \frac{V}{4f}\right)^2 - Z^2}. \tag{7.4}$$

As the wave propagates in three dimensions, the Fresnel zone for the isotropic model above is a circle with the radius computed from equation (7.4) shown in Figure 7.2.

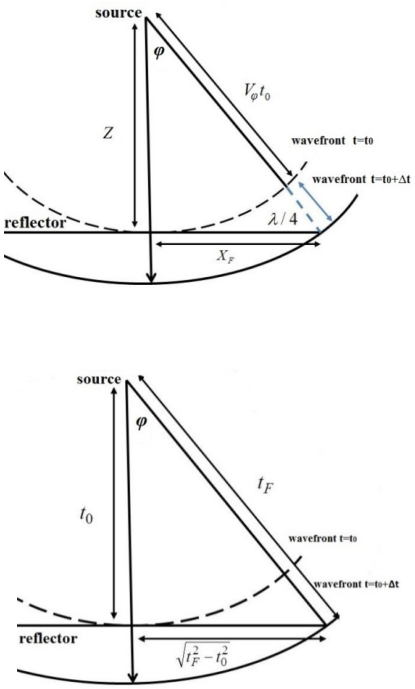

Figure 7.1. The first Fresnel zone diagram in represented by the depth (top) and traveltime (bottom).

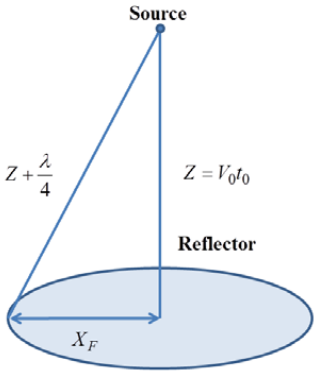

Figure 7.2. The diagram showing the Fresnel zone in an isotropic medium.

7.3 The Fresnel zone in a VTI medium

In an anisotropic medium, the velocity of the seismic wave varies with the propagation angle. For a homogeneous VTI model, there are two additional anisotropic parameters δ and ε (Thomsen, 1986). The shape of the P-wave wavefront in VTI model is a quasi-ellipse instead of a circle as it is shown in Figure 3.

Based on the concept of the Fresnel zone, which indicates the area in the vicinity of a ray that can be expressed in terms of the traveltime (t_F) (Figure 7.1, bottom) and the change in this traveltime with one-fourth of the wavelength (Δt). Computed from the dynamic ray tracing, the parametric equations for traveltime and offset are given by (Alkahlifah, 1998)

$$\begin{aligned} x(p) &= \frac{p t_0 V_n^2}{\left(1-2\eta p^2 V_n^2\right)^{3/2}\sqrt{1-(1+2\eta)p^2V_n^2}}, \\ t(p) &= \frac{t_0\left(2\eta p^4 V_n^4+\left(1-2\eta p^2V_n^2\right)^2\right)}{\left(1-2\eta p^2 V_n^2\right)^{3/2}\sqrt{1-(1+2\eta)p^2V_n^2}}, \end{aligned} \tag{7.5}$$

where V_n is the NMO velocity with $V_n = V_0\sqrt{1+2\delta}$, $\eta = \dfrac{\varepsilon-\delta}{1+2\delta}$ is the anellipticity parameter (Alkhalifah and Tsvankin, 1995), and p is the ray parameter (horizontal slowness). For the Fresnel zone in VTI model, the radius is computed from the corresponding offset when the ray travels from the source to the edge of the Fresnel zone with certain traveltime t_F. The geometry for calculating the radius of Fresnel zone in a homogeneous ISO and VTI model is shown in Figure 7.3.

In order to obtain an analytic expression in VTI model, we define the perturbation series for Fresnel radius squared up to third order by

$$X_F^2 = M_0 + M_1\eta + M_2\eta^2 + M_3\eta^3, \tag{7.6}$$

For the elliptical case ($\eta = 0$), the traveltime and offset squared are shown by

$$X^2(p)_{\eta=0} = \frac{p_F^2 t_0^2 V_n^4}{1 - p_F^2 V_n^2},$$
$$T^2(p)_{\eta=0} = \frac{t_0^2}{1 - p_F^2 V_n^2}, \tag{7.7}$$

where the slowness for the elliptical assumption is given by

$$p_F = \frac{\sqrt{t_F^2 - t_0^2}}{t_F V_n} \tag{7.8}$$

The zero order coefficient M_0 is computed by

$$M_0 = X^2(p)_{\eta=0} = \frac{p_F^2 t_0^2 V_n^4}{1 - p_F^2 V_n^2} = \left(t_F^2 - t_0^2\right) V_n^2. \tag{7.9}$$

The other coefficients (see Appendix A) in equation (7.6) are given by

$$M_1 = \frac{2\left(t_F^2 - t_0^2\right)^2 V_n^2}{t_F^2},$$
$$M_2 = \frac{4t_0^2\left(t_F^2 - t_0^2\right)^3 V_n^2}{t_F^6}, \tag{7.10}$$
$$M_3 = \frac{24t_0^4\left(t_F^2 - t_0^2\right)^4 V_n^2}{t_F^{10}}.$$

In order to stabilize the approximation and improve the accuracy, two types of Shanks transform (Bender and Orszag, 1978) are defined on the perturbation series in equation (7.6) given by

$$X_{S1}^2 = \frac{X_0 X_2 - X_1^2}{X_0 + X_2 - 2X_1},$$
$$X_{S2}^2 = \frac{X_1 X_3 - X_2^2}{X_1 + X_3 - 2X_2}, \tag{7.11}$$

where $X_k^2 = \sum_{j=0}^{k} M_j \eta^j,\ k = 0,1,2,3.$ The perturbation coefficients M_j ($j = 0,1,2,3$) are given in equations (7.9) and (7.10).

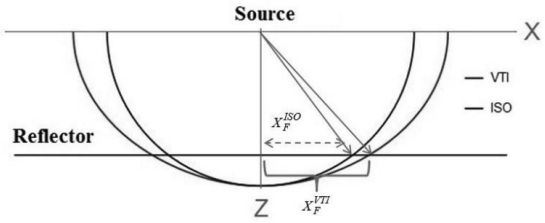

Figure 7.3. The radius of Fresnel zone for P-wave in a homogeneous ISO and VTI medium.

In order to test the accuracy of the approximations above, we introduce a VTI model with the parameters: $V_0 = 2km/s$, $V_n = 2.2km/s$ and $\eta = 0.2$, and plot the relative error in Fresnel radius versus corresponding traveltime (t_F), depth and frequency by using the approximations from second and third perturbation series and the Shanks transforms in Figure 7.4. Note that the Fresnel zone varies with depth at frequency $f = 30Hz$ and the Fresnel zone varies with frequency at depth $z = 2km$. One can see that the accuracy from third order perturbation series is higher than second order and the Shanks transform improves the accuracy greatly for both second and third order series. The second order Shanks transform approximation X_{S2} results in the most accurate result and even as accurate as the exact one. We plot the Fresnel zone radius approximation X_{S2} versus anisotropic parameters δ (with $\eta = 0.2$) and η (with $\delta = 0.1$) in Figure 7.5. One can see that the Fresnel radius is increasing both with δ and η, and it is more sensitive with δ. The radius of Fresnel zone using the approximation X_{S2} in ISO and VTI models versus traveltime t_F, depth and frequency are shown in Figure 7.6. The tendency for the Fresnel zone radius with respect to traveltime, depth and frequency for ISO and VTI model is very similar. We plot the shape of Fresnel zone for ISO ($V = 2km/s$, $f = 30Hz$ and $z = 2km$) and VTI ($V_0 = 2km/s$, $V_n = 2.2km/s$, $\eta = 0.2$, $f = 30Hz$ and $z = 2km$) models in Figure 7.7. One can see that, similar to ISO case, the Fresnel zone in VTI model is also a circle but with a larger radius as the velocity in VTI model is independent with

the azimuth. Note that the exact numerical results or the reference results are obtained from performing the dynamic ray tracing on the parametric offset-traveltime on equations (7.5). Similar to the moveout approximation $t(x)$, the Fresnel zone radius using the traveltime parameters can be treated as $x(t)$. The exact results can be computed from the parametric offset-traveltime equation shown in equations (7.5).

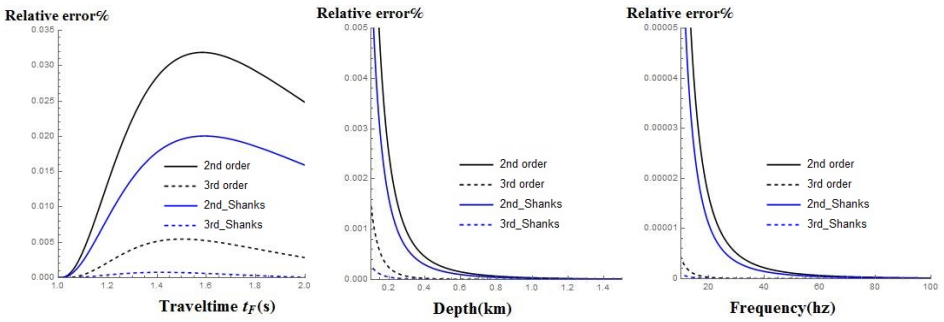

Figure 7.4. The relative error in Fresnel radius versus the corresponding traveltime (left), depth (middle) and frequency (right) using four types of approximation in VTI model. (Note that the Fresnel zone varies with depth at frequency $f = 30Hz$ and the Fresnel zone varies with frequency at depth $z = 2km$).

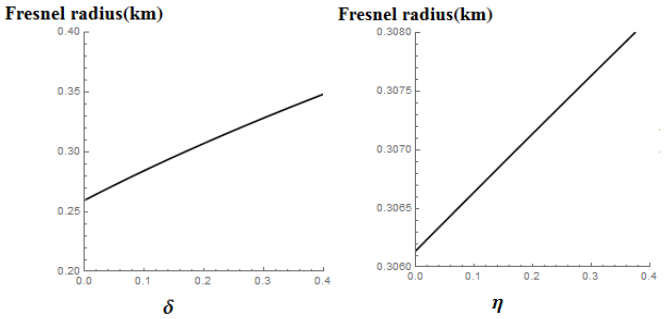

Figure 7.5. The Fresnel radius using second order Shanks transform approximation X_{S2} versus anisotropy parameters δ (with $\eta = 0.2$) and η (with $\delta = 0.1$).

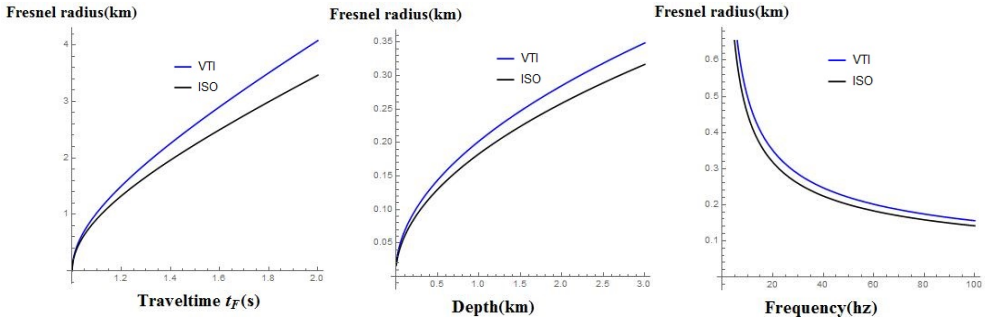

Figure 7.6. The radius of Fresnel zone in ISO and VTI models versus traveltime (left), depth (middle) and Frequency (right). The Fresnel radius computed from ISO and VTI model is shown by black and blue colors, respectively. (Note that the Fresnel zone varies with depth at frequency $f = 30Hz$; The Fresnel zone varies with frequency at depth $z = 2km$).

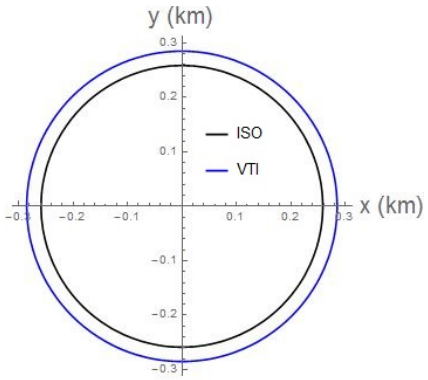

Figure 7.7. The Fresnel zone in ISO and VTI model. The Fresnel zone computed from ISO and VTI model is shown by black and blue colors, respectively.

7.4 The Fresnel zone in an ORT medium

To compute the azimuth-dependent radius of the Fresnel zone for a homogeneous ORT model, we use exact parametric offset and traveltime equations (Stovas, 2015):

$$\begin{aligned} x(p_x, p_y) &= p_x F_2^2 \frac{V_{n1}^2 t_0}{f_1^{1/2} f_2^{3/2}}, \\ y(p_x, p_y) &= p_y F_1^2 \frac{V_{n2}^2 t_0}{f_1^{1/2} f_2^{3/2}}, \\ t(p_x, p_y) &= \frac{t_0\left(F_1^2 p_y^2 V_{n2}^2 + F_2^2 p_x^2 V_{n1}^2 + f_1 f_2\right)}{f_1^{1/2} f_2^{3/2}}, \end{aligned} \tag{7,12}$$

where x and y are the corresponding offset projections, and

$$\begin{aligned} F_1 &= 1 - p_x^2 V_{n1}^2 (2\eta_1 - \eta_{xy}), \\ F_2 &= 1 - p_y^2 V_{n2}^2 (2\eta_2 - \eta_{xy}), \\ f_1 &= 1 - (1+2\eta_1) p_x^2 V_{n1}^2 - (1+2\eta_2) p_y^2 V_{n2}^2 + \left((1+2\eta_1)(1+2\eta_2) - (1+\eta_{xy})^2\right) p_x^2 p_y^2 V_{n1}^2 V_{n2}^2, \\ f_2 &= 1 - 2\eta_1 p_x^2 V_{n1}^2 - 2\eta_2 p_y^2 V_{n2}^2 + \left(4\eta_1\eta_2 - \eta_{xy}^2\right) p_x^2 p_y^2 V_{n1}^2 V_{n2}^2, \end{aligned} \tag{7,13}$$

with V_0, V_{n1}, V_{n2} being the vertical and NMO velocities. NMO velocities V_{n1} and V_{n2} are defined in $[X,Z]$ and $[Y,Z]$ planes, respectively. Anellipticity parameters η_1 and η_2 are defined in corresponding two vertical symmetry $[X,Z]$ and $[Y,Z]$ planes. The cross-term anellipticity parameter η_{xy} is defined as (Stovas, 2015)

$$\eta_{xy} = \sqrt{\frac{(1+2\eta_1)(1+2\eta_2)}{1+2\eta_3}} - 1, \tag{7.14}$$

where anellipticity parameter η_3 is defined in the $[X,Y]$ plane (Vasconcelos and Tsvankin, 2006).

Similar to VTI case, by setting the traveltime t equal to t_F, we relate the Fresnel zone $R(X_F, Y_F)$ with the depth of reflector. We introduce a homogeneous ORT model with

parameters: $V_0 = 2km/s$, $V_{n1} = 2.2km/s$, $V_{n2} = 2.4km/s$, $\eta_1 = 0.2$, $\eta_2 = 0.15$, $\eta_{xy} = 0.2$, $f = 30Hz$ and the depth of the horizontal reflector is $z = 2km$ and show the exact Fresnel zone $R(X_F, Y_F)$ for ORT model with a quasi-elliptic shape in Figure 7.8. Note that similar to the VTI case, the exact solution is computed from performing the dynamic ray tracing in the parametric offsets-traveltime equaiton through the ray parameters (two horizontal slownesses) shown in equations (7.12).

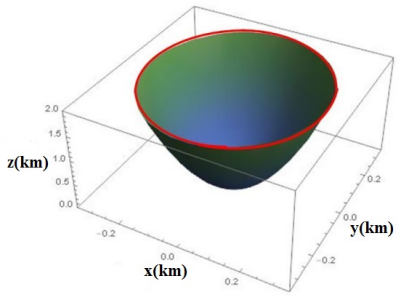

Figure 7.8. The Fresnel zone computed for a homogeneous ORT model. The model parameters are: $V_0 = 2km/s$, $V_{n1} = 2.2km/s$, $V_{n2} = 2.4km/s$, $\eta_1 = 0.2$, $\eta_2 = 0.15$, $\eta_{xy} = 0.2$ and $f = 30Hz$. The depth of the horizontal reflector is $z = 2km$. The Fresnel zone in ORT model has a quasi-elliptical shape.

In order to get the analytic expression of the azimuth-dependent radius for the Fresnel zone in ORT model, we define the perturbation series up to the second order by

$$R_F^2 = x_F^2 + y_F^2 = N_0 + \sum_{j=1,2,3} N_j \eta_j + \sum_{i,j=1,2,3} N_{ij} \eta_i \eta_j, \tag{7.15}$$

where $3 \equiv xy$, the perturbation coefficients N_j and N_{ij} are given by the model parameters: V_0, V_{n1}, V_{n2}, η_1, η_2, η_{xy}, the frequency f and the group azimuth Φ. To compute the perturbation coefficients, we format the parametric offset and traveltime squared from two projections into the radial offset and the azimuth given by Koren and Ravve (2014)

$$R^2(p_r,\phi) = x^2(p_r,\phi) + y^2(p_r,\phi),$$
$$T^2(p_r,\phi) = t^2(p_r,\phi), \tag{7.16}$$

with the relations

$$p_x = p_r \cos(\phi),$$
$$p_y = p_r \sin(\phi). \tag{7.17}$$

Angle ϕ in equations (7.16) is the phase azimuth. The group azimuth Φ can be computed from the following transform in the ellipsoidal assumption (Stovas, 2015),

$$\tan(\Phi) = \frac{V_{n2}^2}{V_{n1}^2}\tan(\phi). \tag{7.18}$$

Note that this equation is correct not only for the ellipsoidal assumption, but also as zero-order approximation for any non-elliptic VTI media with arbitrarily large intrinsic anellipticity η, but for infinitesimal (actually, close to zero) offset or horizontal slowness. Otherwise, the transform between the acquisition azimuth and the phase azimuth will include, in addition to this zero-order term, also other terms with (even) powers of offset or horizontal slowness.

The analytic expression for Fresnel zone in ORT model in equation (7.15) is derived by equating the exact equations (7.12) by setting the traveltime into t_F with the perturbation series defined in equation (7.15).

The coefficient N_0 is computed by setting all anellipticity parameters into zero given by

$$N_0 = \left(t_F^2 - t_0^2\right)V_n^2(\Phi), \tag{7.19}$$

where $V_n(\Phi)$ is the NMO ellipse (Grechka and Tsvankin, 1999) with

$$\frac{1}{V_n^2(\Phi)} = \frac{\cos(\Phi)^2}{V_{n1}^2} + \frac{\sin(\Phi)^2}{V_{n2}^2}. \tag{7.20}$$

The coefficient N_0 provides the radius squared of Fresnel zone in the ellipsoidal isotropic medium. The other perturbation coefficients N_j and N_{ij} are computed by equating the exact expressions with the perturbation series shown in Appendix B.

Using the ORT model above, we show the polar plots of sensitivity computed from first order (left), quadratic (middle) and cross-term (right) coefficients in the perturbation series versus the group azimuth in Figure 7.9, respectively. One can see from the plots that for first and quadratic order coefficients, the sensitivity in anellipticity parameters η_1 and η_2 have the similar shapes and reach the maximal values for 0 and $\pi/2$ azimuth angle, respectively. The sensitivity in cross-term anellipticity parameter η_{xy} reaches its maximal value at $\pi/4$ azimuth angle for first order coefficient. For quadratic order coefficient, the sensitivity to cross-term anellipticity parameter is very small. For cross-term coefficients, the sensitivity to anellipticity parameters $\eta_1\eta_2$ reaches the maximal value at $\pi/4$ azimuth angle. For the sensitivity to anellipticity parameters $\eta_1\eta_{xy}$ and $\eta_2\eta_{xy}$, they obtain their maximal values at around $\pi/6$ and $\pi/3$ azimuth angle, respectively.

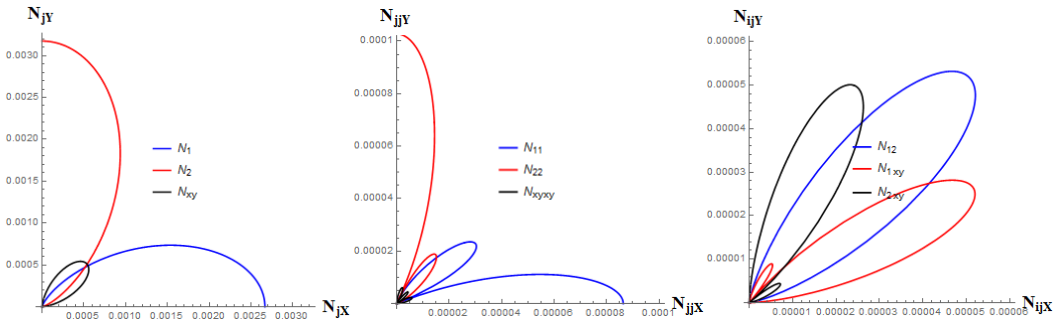

Figure 7.9. The sensitivity computed from first order (left), quadratic (middle) and cross-term coefficients in equation (7.15) in the perturbation series for Fresnel zone versus the group azimuth. The depth of the horizontal reflector is $z = 2km$.

Similar to the approximations in VTI case, the Shanks transform can also be applied to the perturbation series in ORT model (equation (7.15)) and results in

$$R_S = N_0 + \frac{R_1^2}{R_1 - R_2}, \tag{7.21}$$

where N_0 is defined in equation (7.19), $R_1 = \sum_i N_i \eta_i$ and $R_2 = \sum_{ij} N_{ij} \eta_i \eta_j, (i, j = 1,2, xy)$ are the first- and second- order term coefficients are given in Appendix B (equations (7.B10), (7.B12) and (7.B14)).

7.5 Numerical examples

In order to test the accuracy of the Fresnel zone approximation in ORT model, we use the ORT model introduced above with the parameters: $V_0 = 2km/s$, $V_{n1} = 2.2km/s$, $V_{n2} = 2.4km/s$, $\eta_1 = 0.2$, $\eta_2 = 0.15$ and $\eta_{xy} = 0.2$. Note that for the computation versus traveltime $t_0 = 1s$, the computation versus depth $f = 30Hz$ and the computation versus frequency $z = 2km$. The relative error in Fresnel zone with two approximations (perturbation series and the Shanks transform) using the ORT model above versus corresponding (travetime, group azimuth) and (depth, group azimuth) is shown in Figure 7.10, respectively. One can see that for the error plotted with traveltime t_F, the maximal error is obtained at about 40° azimuth for traveltime $t_F = 1.5s$, for the plots versus depth, the maximal error is obtained at zero depth around 35° azimuth for two approximations and the accuracy from these two approximations is almost the same. The Shanks transform does not help a lot in improving the accuracy on the perturbation series for the Fresnel zone radius approximation, the reason for this is that the sensitivity in perturbation coefficients is very small (shown in Figure 7.9), the effect by using the Shanks transform is not obvious. We show another numerical example with higher anellipticity parameters with $\eta_1 = 0.4$, $\eta_2 = 0.3$ and $\eta_{xy} = 0.4$, while keeping the

remaining model parameters the same in Figure 7.11. Compared with the plots in Figure 7.10, the error for the ORT model with higher anellipticity parameters is larger and the effect from the Shanks transform is more significate. One more numerical example, with all negative anellipticity parameters: $\eta_1 = -0.2$, $\eta_2 = -0.15$ and $\eta_{xy} = -0.2$, while keeping the same remaining model parameters, is shown in Figure 7.12. One can tell that comparing with the plots in Figure 7.10 the error from negative anellipticity parameters is larger. Similar to the plots in Figure 7.10, the effect from the Shanks transform is not obvious.

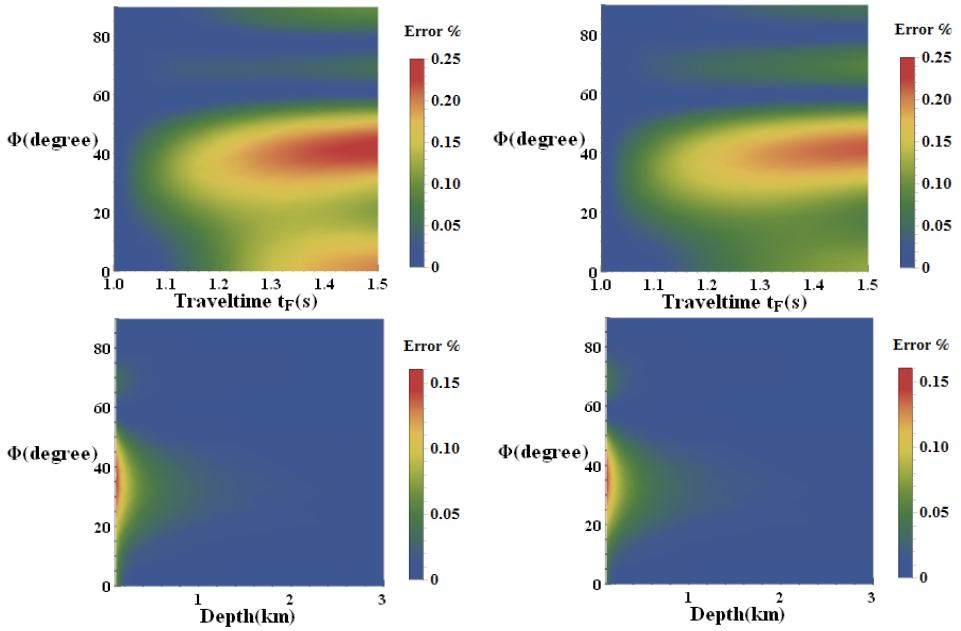

Figure 7.10. The contour plot of error in R_F from two approximations for ORT model plotted versus corresponding traveltime and the group azimuth (top) and depth and the group azimuth (bottom). The perturbation series approximation and Shanks transform are shown in left and right, respectively. The model parameters are given in caption for Figure 7.8.

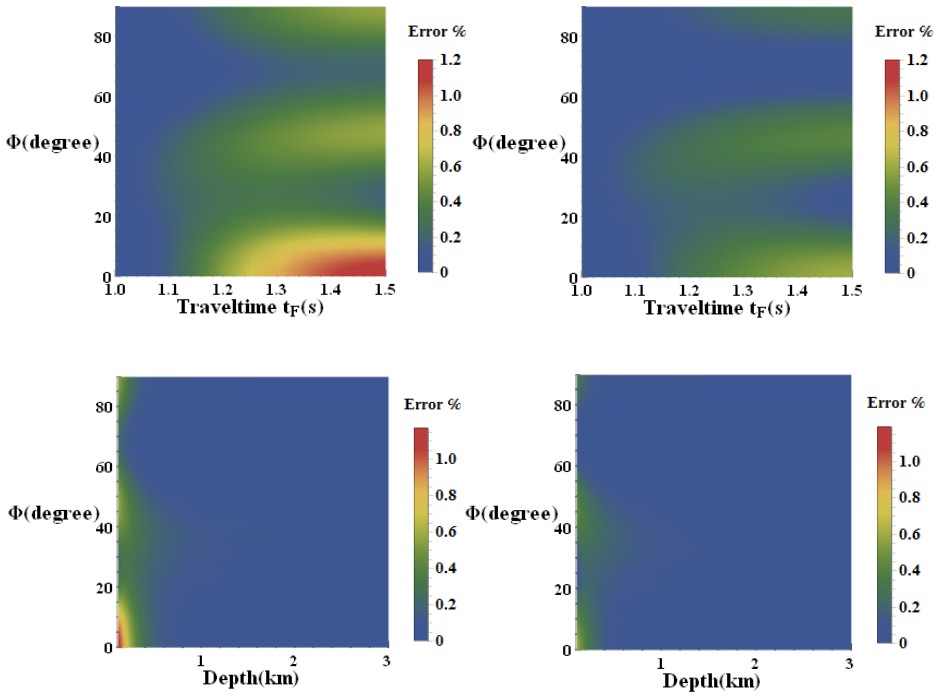

Figure 7.11. The contour plot of error in R_F from two approximations for ORT model plotted versus corresponding traveltime and the group azimuth (top) and depth and the group azimuth (bottom). The perturbation series approximation and Shanks transform are shown in left and right, respectively. The ORT model parameters are defined with the velocities specified in the caption for Figure 7.8 and the higher anellipticity parameters: $\eta_1 = 0.4$, $\eta_2 = 0.3$ and $\eta_{xy} = 0.4$.

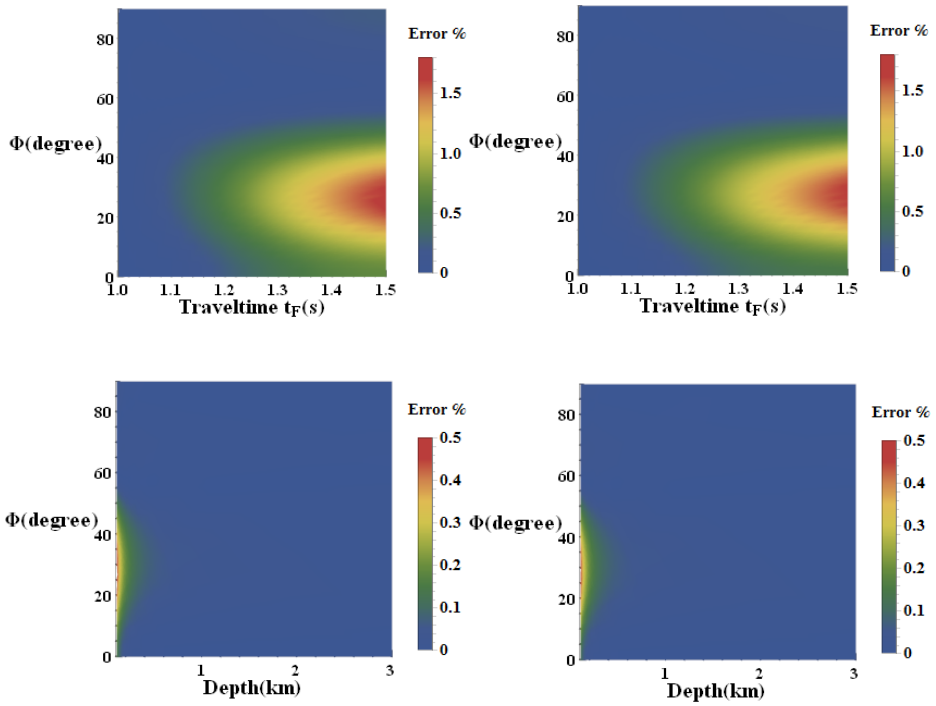

Figure 7.12. The contour plot of error in R_F from two approximations for ORT model plotted versus corresponding traveltime and the group azimuth (top) and depth and the group azimuth (bottom). The perturbation series approximation and Shanks transform are shown in left and right, respectively. The ORT model parameters are defined with the velocities specified in the caption for Figure 7.8 and the negative anellipticity parameters: $\eta_1 = -0.2$, $\eta_2 = -0.15$ and $\eta_{xy} = -0.2$.

Using the Shanks transform approximation in equation (7.21), we show the radius of the Fresnel zone versus different traveltime, depth and frequency in Figure 7.13. One can see from the plots that the radius increases with traveltime and depth while decreases with frequency.

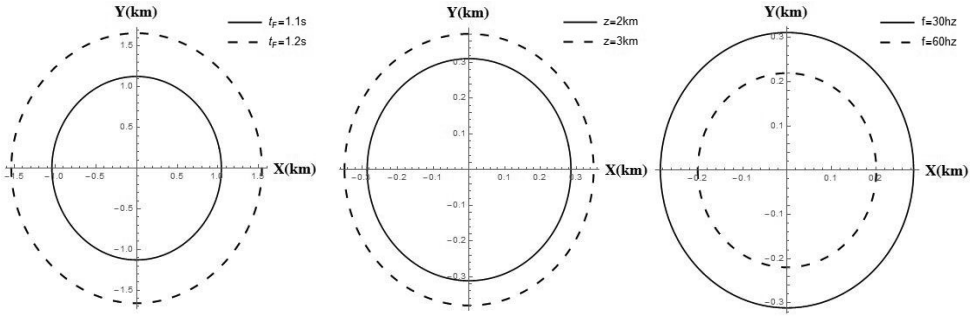

Figure 7.13. The Fresnel zone computed for ORT model for different traveltime (left), depth (middle) and frequency (right) using the ORT model with parameters given in the caption for Figure 7.8.

Selecting a horizontal reflector with the depth $z = 2km$, we show the shape of the Fresnel zone using the Shanks transform approximation (shown in equation (7.21)) for ORT, elliptical isotropic (EI), and ISO model in Figure 7.14, respectively. Note that for EI model, all anellipticity parameters are zero ($\eta_1 = \eta_2 = \eta_3 = 0$), for ISO model, there is one velocity with $V = V_0 = V_{n1} = V_{n2} = 2km/s$. One can see from the plots that the Fresnel zones for ORT and EI model almost coincide that indicates that less sensitivity of the Fresnel zone in anellipticity parameters, which is also explained by the polar plots in Figure 7.9. For ISO case, the Fresnel zone is just a circle with the radius smaller than the ones in ORT and EI model.

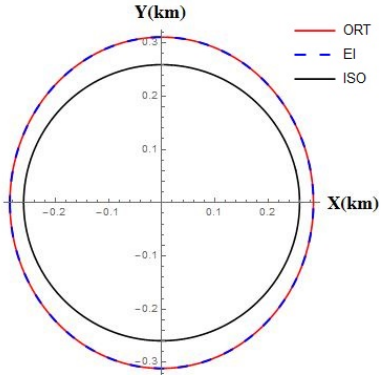

Figure 7.14. The shape of the Fresnel zone computed for ISO, EI and ORT model. The depth of the horizontal reflector is $z = 2km$.

Note that the advantage of this paper is an attempt of a direct offset-traveltime approximation, perturbing the anellipticity of VTI, or the three anellipticities of ORT medium. The Fresnel zone calculation is a particular case for this method, when the time is the Fresnel zone traveltime, and the offset is its radius. Similarly, the moveout approximation can also be derived from the same strategy.

7.6 Discussions

The reason why we derive the approximation for the Fresnel zone using the traveltime is to avoid the complexity in dealing with the phase domain velocities. By the definition, the Fresnel zone radius is defined by the lateral projection when the seismic wave propagates for ¼ wavelength after arriving the reflector with $\lambda = \frac{V_\theta}{f}$, V_θ is the wavefront velocity (phase velocity) with the phase angle θ. Shown in Figure 7.15, if the model is isotropic, the phase angle θ_1 measured at wavefront ($t = t_0$) is equal to θ_2 measured at wavefront ($t = t_0 + \Delta t$). However, for the anisotropic model, two wavefronts are not parallel ($\theta_1 \neq \theta_2$), to compute the Fresnel zone radius X_F, the change in the phase angle needs to be taken into consideration, which makes the computation much more complicated. Using the traveltime parameters, what

we are interested in is the ray traveling from the source to the reflector with the certain traveltime $t_F = t_0 + \Delta t$ (Figure 7.1, bottom) that makes the derivation much simpler for anisotropic media.

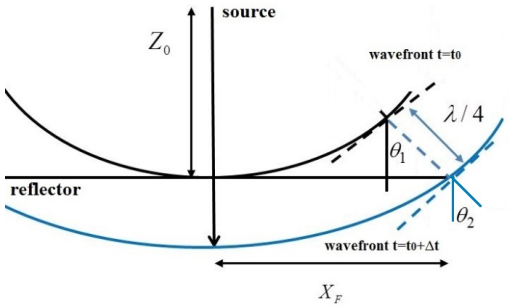

Figure 7.15. The diagram showing the Fresnel zone in an anisotropic medium. Angle θ_1 and θ_2 are phase angles measured in corresponding points at wave-fronts $t = t_0$ and $t = t_0 + \Delta t$, respectively.

In order to singularize the anomaly of error plot in ORT model, we apply one more numerical example from the perturbation series (equation (7.15)) and the Shanks transform approximation (equation (7.21)) in Figure 7.16, (left and right, respectively) with a smaller t_0 ($t_0 = 0.6s$) and frequency ($f = 10Hz$). One can see that for the error plot versus traveltime and group azimuth, the shape of the anomaly is more obvious and maximal error is obtained at the center of the anomaly. For the error plot versus depth and group azimuth, the maximal error is obtained at about 40° azimuth when the depth is zero.

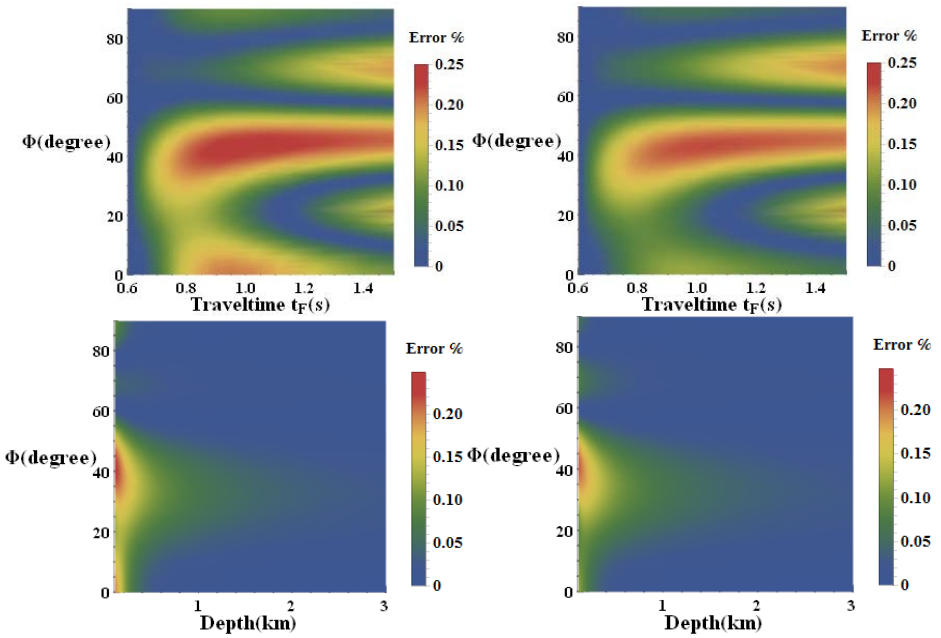

Figure 7.16. The contour plot of error in R_F from two approximations for ORT model plotted versus corresponding traveltime and the group azimuth (top) and depth and the group azimuth (bottom). The perturbation series approximation and Shanks transform are shown in left and right, respectively. The ORT model parameters are: (Top) $t_0 = 0.6s$, $V_{n1} = 2.2km/s$, $V_{n2} = 2.4km/s$, $\eta_1 = 0.2$, $\eta_2 = 0.15$ and $\eta_{xy} = 0.2$; (Bottom): $V_0 = 2km/s$, $V_{n1} = 2.2km/s$, $V_{n2} = 2.4km/s$, $\eta_1 = 0.2$, $\eta_2 = 0.15$, $\eta_{xy} = 0.2$ and $f = 10Hz$.

This perturbation based method for the Fresnel zone in the anisotropic model can be extended for the model with a dip reflector. Shown in Figure 7.17, the Fresnel zone for a dip reflector with the dip angle α in a homogenous VTI model is consist of two parts (r_1 and r_2), which is the corresponding distance in two directions along the dip reflector when the seismic wave propagates within ¼ wavelength after it first touches the dip reflector. We assume the value of the dip angle α and the depth of the first touching point z_0' are known. The Fresnel zones (r_1 and r_2) are calculated by

$$r_1 = \frac{x_0' - x_1'}{\cos\alpha}, r_2 = \frac{x_2' - x_0'}{\cos\alpha}, \tag{7.22}$$

where x_0' is the offset for the first touching point, x_1' and x_2' are the corresponding offsets for the Fresnel zone boundary point with the corresponding depth z_1' and z_2'. The corresponding offsets x_1' and x_2' are computed by the Shanks transform approximation shown in equations 7.10 with the certain traveltime $t_F = t_0 + \Delta t$

$$\begin{aligned} x_1' &= \{z_1', t_F, V_0, V_n, \eta, \alpha\}, \\ x_2' &= \{z_2', t_F, V_0, V_n, \eta, \alpha\}, \end{aligned} \tag{7.23}$$

where the two corresponding depth z_1' and z_2' are obtained from the Pythagorean theorem

$$\begin{aligned} \frac{z_0'}{\tan\alpha} + \left(x_0' - x_1'[z_1']\right) &= z_1' \tan\alpha \Rightarrow z_1', \\ \frac{z_0'}{\tan\alpha} - \left(x_2'[z_2'] - x_0'\right) &= z_2' \tan\alpha \Rightarrow z_2'. \end{aligned} \tag{7.24}$$

Note that on contrary to the horizontal reflector case, the Fresnel zone is not symmetric for dip reflector case ($r_1 \neq r_2$).

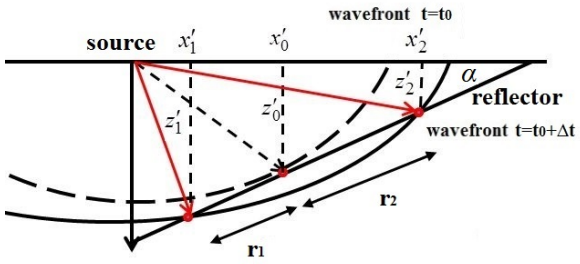

Figure 7.17. The sketch showing the Fresnel zone for a dip reflector in a homogeneous VTI model.

7.7 Conclusions

We derive the form of Fresnel zone radius using the traveltime parameter and use it to obtain the analytic expressions in an acoustic VTI and ORT models from the exact offset-traveltime

parametric equation using the perturbation method. The analysis of the Fresnel zone radius is applied versus corresponding traveltime, depth and the frequency. One can tell that the Fresnel zone radius in anisotropic media (VTI and ORT) increases with traveltime and depth, while decreases with frequency. The Shanks transform is applied to stabilize the approximation and improve the accuracy for both two models. Shown from the numerical examples that for VTI model, the second order Shanks transform is the most accurate approximation that is almost as accurate as the exact one. For ORT model, the quasi-elliptical shape is obtained for the Fresnel zone. The perturbation series and the Shanks transform approximation are all very accurate and almost the same accuracy for the Fresnel zone calculation due to the small sensitivity in perturbation coefficients.

7.8 Acknowledgments

We would like to acknowledge China Scholarship Council (CSC) and ROSE project for financial support. We also acknowledge I. Ravve and an anonymous reviewer for their valuable comments.

7.9 Appendix A

The analytic expression for Fresnel zone in a homogeneous VTI model using the perturbation method

In order to obtain an analytic expression for Fresnel radius squared in VTI model, we define the perturbation series up to third order by

$$X_F^2 = M_0 + M_1\eta + M_2\eta^2 + M_3\eta^3, \tag{7.A1}$$

For elliptical case ($\eta = 0$), the traveltime and offset squared are obtained from the parametric equations (7.5) by

$$X^2(p)_{\eta=0} = \frac{p_F^2 t_0^2 V_n^4}{1 - p_F^2 V_n^2},$$
$$T^2(p)_{\eta=0} = \frac{t_0^2}{1 - p_F^2 V_n^2}, \tag{7.A2}$$

where $p_F = \frac{\sqrt{t_F^2 - t_0^2}}{t_F V_n}$ for the elliptical assumption. The zero order coefficient M_0 is computed by

$$M_0 = X^2(p)_{\eta=0} = \frac{p_F^2 t_0^2 V_n^4}{1 - p_F^2 V_n^2} = \left(t_F^2 - t_0^2\right) V_n^2 \tag{7.A3}$$

The first order coefficient is obtained by

$$M_1 = \left[\frac{\partial X^2(p)}{\partial \eta} - \frac{\partial M_0\left(t_F^2 \to t^2\right)}{\partial \eta}\right] = \frac{2\left(t_F^2 - t_0^2\right)^2 V_n^2}{t_F^2} \tag{7.A4}$$

Subsequently, we compute the second and third order coefficients given by

$$M_2 = \left[\frac{\partial^2 X^2(p)}{\partial \eta^2} - \frac{\partial M_1\left(t_F^2 \to t^2\right)}{\partial \eta} - \frac{\partial^2 M_0\left(t_F^2 \to t^2\right)}{\partial \eta^2}\right] = \frac{4t_0^2\left(t_F^2 - t_0^2\right)^3 V_n^2}{t_F^6},$$
$$M_3 = \left[\frac{\partial^3 X^2(p)}{\partial \eta^3} - \frac{\partial M_2\left(t_F^2 \to t^2\right)}{\partial \eta} - \frac{\partial^2 M_1\left(t_F^2 \to t^2\right)}{\partial \eta^2} - \frac{\partial^3 M_0\left(t_F^2 \to t^2\right)}{\partial \eta^3}\right] \tag{7.A5}$$
$$= \frac{24t_0^4\left(t_F^2 - t_0^2\right)^4 V_n^2}{t_F^{10}}.$$

Note that these perturbations coefficients $M_i, (i = 0,...,3)$ are all η independent since t_F is an argument in the approximation. The parameters for the approximation in VTI model are: t_F, t_0 and V_n. The effect for the anellipticity is hidden in parameter t_F. $t_F^2 \to t^2$ means t_F here should use the function form shown in the parametric equation (equations (7.5)) for derivation after that the elliptical assumption is applied to get the expression for the coefficients (M_1, M_2 and M_3).

7.10 Appendix B

The analytic expression for Fresnel zone in a homogeneous ORT model using the perturbation method

To compute the perturbation coefficients in equation (7.15), we format the parametric offset and traveltime squared from two projections into the radius offset and the phase azimuth given by

$$\begin{aligned} R^2(p_r,\phi) &= x^2(p_r,\phi) + y^2(p_r,\phi), \\ T^2(p_r,\phi) &= t^2(p_r,\phi). \end{aligned} \tag{7.B1}$$

with the relations as below

$$\begin{aligned} p_x &= p_r \cos(\phi), \\ p_y &= p_r \sin(\phi). \end{aligned} \tag{7.B2}$$

We represent the parametric equations in terms of slowness p_r and the phase azimuth ϕ for the elliptical assumption

$$\begin{aligned} R^2(p_r,\phi)_{\eta=0} &= \frac{p_r^2 t_0^2 \left(V_{n1}^4 \cos(\phi)^2 + V_{n2}^4 \sin(\phi)^2\right)}{1 - p_r^2 \left(V_{n1}^2 \cos(\phi)^2 + V_{n2}^2 \sin(\phi)^2\right)}, \\ T^2(p_r,\phi)_{\eta=0} &= \frac{t_0^2}{1 - p_r^2 \left(V_{n1}^2 \cos(\phi)^2 + V_{n2}^2 \sin(\phi)^2\right)}. \end{aligned} \tag{7.B3}$$

That gives

$$p_r = \frac{\sqrt{t_F^2 - t_0^2}}{t_F \sqrt{V_{n1}^2 \cos(\phi)^2 + V_{n2}^2 \sin(\phi)^2}}. \tag{7.B4}$$

First the coefficient N_0 for the ellipsoidal case is computed by setting all anellipticity parameters into zero given by

$$N_0 = \frac{\left(t_F^2 - t_0^2\right)\left(V_{n1}^4 \cos(\phi)^2 + V_{n2}^4 \sin(\phi)^2\right)}{V_{n1}^2 \sin(\phi)^2 + V_{n2}^2 \cos(\phi)^2}. \tag{7.B5}$$

Note that the azimuth ϕ in equations above is the phase azimuth. We need to convert the azimuth from phase to group domain by the relation in the elliptic assumption

$$\tan(\Phi) = \frac{V_{n2}^2}{V_{n1}^2} \tan(\phi). \tag{7.B6}$$

The coefficient N_0 for the ellipsoidal case is term of group azimuth is given by

$$N_0 = \left(t_F^2 - t_0^2\right) V_n^2(\Phi). \tag{7.B7}$$

where $V_n(\Phi)$ is the NMO ellipse (Grechka and Tsvankin, 1999) with

$$\frac{1}{V_n^2(\Phi)} = \frac{\cos(\Phi)^2}{V_{n1}^2} + \frac{\sin(\Phi)^2}{V_{n2}^2}. \tag{7.B8}$$

Similar to VTI case, using the perturbation method, we compute the first order coefficients as following

$$\begin{aligned} N_1 &= \left[\frac{\partial R_F^2}{\partial \eta_1} - \frac{\partial N_0}{\partial \eta_1}\right]_{\eta_2 = \eta_{xy} = 0}, \\ N_2 &= \left[\frac{\partial R_F^2}{\partial \eta_2} - \frac{\partial N_0}{\partial \eta_2}\right]_{\eta_1 = \eta_{xy} = 0}, \\ N_{xy} &= \left[\frac{\partial R_F^2}{\partial \eta_{xy}} - \frac{\partial N_0}{\partial \eta_{xy}}\right]_{\eta_1 = \eta_2 = 0}. \end{aligned} \tag{7.B9}$$

The first order coefficients N_1, N_2 and N_{xy} in term of group azimuth are given by

$$
\begin{aligned}
N_1 &= \frac{2\cos(\Phi)^4\left(t_F^2-t_0^2\right)^2 V_{n1}^2 V_{n2}^4\left(V_{n2}^2\cos(\Phi)^2+\left(4V_{n1}^2-3V_{n2}^2\right)\sin(\Phi)^2\right)}{t_F^2\left(V_{n1}^2\sin(\Phi)^2+V_{n2}^2\cos(\Phi)^2\right)^3},\\
N_2 &= \frac{2\sin(\Phi)^4\left(t_F^2-t_0^2\right)^2 V_{n1}^4 V_{n2}^2\left(V_{n1}^2\sin(\Phi)^2+\left(4V_{n2}^2-3V_{n1}^2\right)\cos(\Phi)^2\right)}{t_F^2\left(V_{n1}^2\sin(\Phi)^2+V_{n2}^2\cos(\Phi)^2\right)^3},\\
N_{xy} &= \frac{2\sin(\Phi)^2\cos(\Phi)^2\left(t_F^2-t_0^2\right)^2 V_{n1}^2 V_{n2}^2\left(2V_{n1}^4\sin(\Phi)^2-V_{n1}^2V_{n2}^2+2V_{n2}^4\cos(\Phi)^2\right)}{t_F^2\left(V_{n1}^2\sin(\Phi)^2+V_{n2}^2\cos(\Phi)^2\right)^3}.
\end{aligned}
\tag{7.B10}
$$

Subsequently, the quadratic coefficients N_{11}, N_{22} and N_{xyxy} are computed as following

$$
\begin{aligned}
N_{11} &= \left[\frac{1}{2}\left(\frac{\partial^2 R_F^2}{\partial\eta_1^2}\right)-\left(\frac{\partial^2 N_0}{\partial\eta_1^2}+\frac{\partial N_1}{\partial\eta_1}\right)\right]_{\eta_2=\eta_{xy}=0},\\
N_{22} &= \left[\frac{1}{2}\left(\frac{\partial^2 R_F^2}{\partial\eta_2^2}\right)-\left(\frac{\partial^2 N_0}{\partial\eta_2^2}+\frac{\partial N_2}{\partial\eta_2}\right)\right]_{\eta_1=\eta_{xy}=0},\\
N_{xyxy} &= \left[\frac{1}{2}\left(\frac{\partial^2 R_F^2}{\partial\eta_{xy}^2}\right)-\left(\frac{\partial^2 N_0}{\partial\eta_{xy}^2}+\frac{\partial N_{xy}}{\partial\eta_{xy}}\right)\right]_{\eta_1=\eta_2=0},
\end{aligned}
\tag{7.B11}
$$

and shown in terms of group azimuth by

$$
\begin{aligned}
N_{11} &= -\frac{4\cos(\Phi)^6\left(t_F^2-t_0^2\right)^3 V_{n1}^2 V_{n2}^6}{t_F^6\left(V_{n1}^2\sin(\Phi)^2+V_{n2}^2\cos(\Phi)^2\right)^5}\left(t_0^2 V_{n2}^4\cos(\Phi)^4+\left(\left(8t_0^2+t_F^2\right)V_{n1}^2-\left(\left(7t_0^2+6t_F^2\right)\right)V_{n2}^2\right)V_{n2}^2\sin(\Phi)^2\cos(\Phi)^2\right.\\
&\quad\left.+5t_F^2 V_{n1}^2\sin(\Phi)^4\left(V_{n2}^2-2V_{n1}^2\right)\right),\\
N_{22} &= -\frac{4\sin(\Phi)^6\left(t_F^2-t_0^2\right)^3 V_{n1}^6 V_{n2}^2}{t_F^6\left(V_{n1}^2\sin(\Phi)^2+V_{n2}^2\cos(\Phi)^2\right)^5}\left(t_0^2 V_{n1}^4\sin(\Phi)^4+\left(\left(8t_0^2+t_F^2\right)V_{n2}^2-\left(\left(7t_0^2+6t_F^2\right)\right)V_{n1}^2\right)V_{n1}^2\sin(\Phi)^2\cos(\Phi)^2\right.\\
&\quad\left.+5t_F^2 V_{n2}^2\cos(\Phi)^4\left(V_{n1}^2-2V_{n2}^2\right)\right),\\
N_{xyxy} &= \frac{\sin(\Phi)^2\cos(\Phi)^2\left(t_F^2-t_0^2\right)^3 V_{n1}^2 V_{n2}^2}{t_F^6\left(V_{n1}^2\sin(\Phi)^2+V_{n2}^2\cos(\Phi)^2\right)^5}\left(6t_F^2 V_{n1}^8\sin(\Phi)^6-V_{n1}^6V_{n2}^2\left(t_F^2\sin(\Phi)^2+\left(16t_0^2+21t_F^2\right)\cos(\Phi)^2\right)\sin(\Phi)^4\right.,\\
&\quad\left.+4V_{n1}^4V_{n2}^4\left(3t_0^2+4t_F^2\right)\sin(\Phi)^2\cos(\Phi)^2-\left(t_F^2\cos(\Phi)^2+\left(16t_0^2+21t_F^2\right)\right)V_{n1}^2V_{n2}^6\cos(\Phi)^4+6t_F^2V_{n2}^8\cos(\Phi)^6\right).
\end{aligned}
\tag{7.B12}
$$

The remaining cross-term coefficients N_{12}, N_{1xy} and N_{2xy} are computed as following

$$
\begin{aligned}
N_{12} &= \left[\frac{\partial^2 R_F^2}{\partial \eta_1 \partial \eta_2} - \left(\frac{\partial N_0}{\partial \eta_1}\frac{\partial N_0}{\partial \eta_2} + \frac{\partial N_1}{\partial \eta_2} + \frac{\partial N_2}{\partial \eta_1} \right) \right]_{\eta_{xy}=0}, \\
N_{1xy} &= \left[\frac{\partial^2 R_F^2}{\partial \eta_1 \partial \eta_{xy}} - \left(\frac{\partial N_0}{\partial \eta_1}\frac{\partial N_0}{\partial \eta_{xy}} + \frac{\partial N_1}{\partial \eta_{xy}} + \frac{\partial N_{xy}}{\partial \eta_1} \right) \right]_{\eta_2=0}, \\
N_{2xy} &= \left[\frac{\partial^2 R_F^2}{\partial \eta_2 \partial \eta_{xy}} - \left(\frac{\partial N_0}{\partial \eta_2}\frac{\partial N_0}{\partial \eta_{xy}} + \frac{\partial N_2}{\partial \eta_{xy}} + \frac{\partial N_{xy}}{\partial \eta_2} \right) \right]_{\eta_1=0},
\end{aligned}
\tag{7.B13}
$$

and shown in terms of group azimuth by

$$
\begin{aligned}
N_{12} &= -\frac{8\sin(\Phi)^4\cos(\Phi)^4\left(t_F^2-t_0^2\right)^3 V_{n1}^4 V_{n2}^4}{t_F^6\left(V_{n1}^2\sin(\Phi)^2+V_{n2}^2\cos(\Phi)^2\right)^5}\left(4\left(t_0^2+2t_F^2\right)V_{n1}^4\sin(\Phi)^2-3\left(t_0^2+t_F^2\right)V_{n1}^2V_{n2}^2+4\left(t_0^2+2t_F^2\right)V_{n2}^4\cos(\Phi)^2\right), \\
N_{1xy} &= -\frac{4\sin(\Phi)^2\cos(\Phi)^4\left(t_F^2-t_0^2\right)^3 V_{n1}^2 V_{n2}^4}{t_F^6\left(V_{n1}^2\sin(\Phi)^2+V_{n2}^2\cos(\Phi)^2\right)^5}\left(-8t_F^2V_{n1}^6\sin(\Phi)^4+V_{n1}^4V_{n2}^2\sin(\Phi)^2\left(3t_F^2\sin(\Phi)^2+\left(12t_0^2+13t_F^2\right)\cos(\Phi)^2\right)\right. \\
&\quad \left. -V_{n1}^2V_{n2}^4\cos(\Phi)^2\left(\left(10t_0^2+13t_F^2\right)\sin(\Phi)^2+\left(2t_0^2+t_F^2\right)\cos(\Phi)^2\right)+2V_{n2}^6\left(2t_0^2+3t_F^2\right)\cos(\Phi)^4\right), \\
N_{2xy} &= -\frac{4\sin(\Phi)^4\cos(\Phi)^2\left(t_F^2-t_0^2\right)^3 V_{n1}^4 V_{n2}^2}{t_F^6\left(V_{n1}^2\sin(\Phi)^2+V_{n2}^2\cos(\Phi)^2\right)^5}\left(-8t_F^2V_{n2}^6\cos(\Phi)^4+V_{n1}^2V_{n2}^4\cos(\Phi)^2\left(3t_F^2\cos(\Phi)^2+\left(12t_0^2+13t_F^2\right)\sin(\Phi)^2\right)\right. \\
&\quad \left. -V_{n1}^4V_{n2}^2\sin(\Phi)^2\left(\left(10t_0^2+13t_F^2\right)\cos(\Phi)^2+\left(2t_0^2+t_F^2\right)\sin(\Phi)^2\right)+2V_{n1}^6\left(2t_0^2+3t_F^2\right)\sin(\Phi)^4\right),
\end{aligned}
\tag{7.B14}
$$

Note that when taking the derivatives for the coefficients N_j and N_{ij}, we need to set the t_F in the coefficients into T shown in equations (7.B1) for computation.

Chapter 8 Conclusions

In this research work, we derive the P-wave traveltime approximations, relative geometrical spreading and the radius of Fresnel zone in a homogeneous VTI and ORT medium from the parametric traveltime-offset equations through the fitting process and the perturbation-based approach. The acoustic assumption is used to reduce the model parameters for simplification. The Shanks transform is applied to stabilize the convergence of approximation and to improve the accuracy. The accuracy of these approximations is tested in the numerical examples where the exact (standard) solutions are computed from the parametric equations measured through the dynamic ray tracing. In order to apply these approximations to the multilayered case, the Dix-type equation is utilized to compute the effective model parameters. For multilayered ORT model, in case of azimuthal variations in the symmetry axis between the layers, the least-squares approximation is adopted to estimate the effective anellipticity parameters from this layered medium.

For the moveout approximation in anisotropic media, we define a group of parameterization for acoustic ORT model and test the accuracy in traveltime by using a different parameterization of the perturbation-based approximation. Shown in the numerical examples, we conclude that the accuracy of the traveltime approximation is mostly driven by the selection of the elliptical background model and the parameterization with vertical and horizontal velocities is generally more accurate. The selection of the anellipticity parameters also affects the perturbation-based traveltime approximation. A more accurate result is obtained from less sensitivity in the anellipticity perturbation parameters.

The relative geometrical spreading term can be written as a function of the horizontal slowness, which allows us to derive the approximation directly from the parametric equation. We derive the analytic expressions for the relative geometrical spreading in the GMA and

anelliptic forms for a homogeneous VTI and ORT model and extend the approximations to the multilayered cases. Using the numerical examples, we show that our approximations are highly accurate than the conventional traveltime based traveltime-based counterparts in for homogeneous and multi-layered VTI and ORT models.

For anisotropy estimation, we develop an analytical formula for the residual moveout of diving waves in a factorized velocity model and estimate the anisotropy parameters from the semblance analysis on residual moveout in the RTM image gathers. These inverted models, which are based on diving waves, can provide an initial velocity model that is sufficiently close to the true model within the FWI requirements. We also propose a new method to evaluate the anisotropy parameters and the circular reflector parameters from the behavior of estimates with the midpoint position for a circular reflector based on the anisotropic CRS approximation.

Seismic anisotropy impacts the data processing methods like smoothing and resolution studies. For the studies of the horizontal resolution, we derive the approximation for the radius of the Fresnel zone in the time domain in VTI model using the perturbation method and apply this strategy for the azimuth-dependent radius of the Fresnel zone in ORT model for a horizontal layer. From the numerical examples, we can see that the Shanks transform approximations for Fresnel zone are very accurate for both VTI and ORT media. A certain degree of smoothness of velocity models is required for most ray-based migration and tomography. We extend the PTS method to ORT model with and without the azimuthal variation between the layers and show that the smoothing driven errors in traveltime are very small for the practical application.

Appendix A Perturbation-based moveout approximations in anisotropic media

Shibo Xu, Alexey Stovas and Qi Hao

Norwegian University of Science and Technology, Trondheim, Norway

Abstract. The moveout approximations play an important role in seismic data processing. The standard hyperbolic moveout approximation is based on an elliptical background model with two velocities, vertical and normal moveout ones. We propose a new set of moveout approximations based on the perturbation series in anellipticity parameter using the alternative elliptical background model defined by vertical and horizontal velocities. We start with transversely isotropic medium with a vertical symmetry axis (VTI). Then, we extend this approach to a homogeneous orthorhombic (ORT) medium. To define the perturbation coefficients for a new background, we solve the eikonal equation with horizontal velocities in VTI and ORT media. In order to stabilize the perturbation series and improve the accuracy, the Shanks transform is applied for all the cases. We select different parameterizations for both velocities and anellipticity parameters for ORT model. From the comparison in traveltime error, the new moveout approximations result in better accuracy comparing with the standard perturbation based methods and other approximations.

Presented at the 86th SEG Conference and Exhibition, October, 2016, Dallas, USA; Published in Geophysical Prospecting in December 2016.

A.1 Introduction

The moveout approximations are commonly used in seismic data processing such as velocity analysis, modeling and time migration. In isotropic or elliptical isotropic media, the moveout function has a hyperbolic form. We need to take non-hyperbolicity (driven by anellipticity) into consideration, as it is commonly exists and plays an important role in seismic data processing and interpretation, especially for large offsets. The moveout function has a non-hyperbolic form in anisotropic media. Different nonhyperbolic moveout approximations for a homogeneous transversely isotropic medium with vertical symmetry axis (VTI) are listed and discussed in Fowler (2003), Fomel (2004) and Golikov and Stovas (2012). Fomel and Stovas (2010) proposed the generalized nonhyperbolic moveout approximation (GMA) based on parameters computed from the zero-offset ray and one additional nonzero-offset ray. This approximation is very accurate and can be converted into other well-known approximations by the appropriate choice of the parameters. Alkhalifah (2011) proposed the traveltime expression with series in terms of anelliptic parameter η by solving the eikonal equation for acoustic VTI medium and by applying the Shanks transform to obtain the higher accuracy.

The orthorhombic (ORT) model is introduced by Schoenberg and Helbig (1997) to describe fractured reservoirs and explains well the azimuthal dependency in surface seismic data Tsvankin (1997, 2012) defined nine elastic model parameters for ORT model that can be reduced to six parameters in an acoustic approximation (Alkhalifah, 2003). In group domain, we call the first order curvatures the normal moveout (NMO) velocity ellipses (Grechka and Tsvankin, 1999a, 1999b) and the second order curvatures the anellipticities as they represent the anelliptic behaviour for slowness or traveltime surface. Stovas (2015) derived the azimuthally dependent kinematic properties of the orthorhombic media and defined the effective ORT parameters in the Dix-type when there are azimuth variations between the multilayers. Recently, Sripanich and Fomel (2015) proposed an anelliptic approximation for

qP velocities in ORT media. A very accurate GMA approximation in ORT media for phase and group velocities is developed by Hao and Stovas (2016). The perturbation based moveout approximation with a traditional elliptic background for ORT media is discussed by Stovas, Masmoudi and Alkhalifah (2016). The traveltime approximation for orthorhombic model using perturbation theory by other anellipticity parameters in inhomogeneous background media is developed by Masmoudi and Alkhalifah (2016).

We develop a new perturbation based moveout approximation based on an alternative background model in VTI and ORT models, and apply the Shanks transform (Bender and Orszag, 1978) to improve the accuracy. For a homogeneous ORT model, we select different parameterizations for both velocity background and anelliptic parameters.

A.2 New moveout approximation in a VTI model

In order to define the nonhyperbolic traveltime approximation for a VTI model, we select the hyperbolic traveltime background and anellipticity parameter η (Alkhalifah, 1998), where $\eta = (\varepsilon - \delta)/(1+2\delta)$ with parameters δ and ε being the Thomsen anisotropy parameters (Thomsen, 1986). In the standard case, one can use the Taylor series in offset for traveltime squared to obtain the moveout approximation. Alternatively, we can have more options to represent the traveltime function when using the perturbation series in terms of small model parameters. Alkhalifah (2011) proposed a moveout approximation based on the perturbation series in anellipticity parameter η, which is more accurate than the standard Taylor series in offset. In our approach, we follow the same idea. For a VTI model, compared with the orthorhombic model, there is only one parameter that can be considered as the small one, namely, anellipticity parameter η.

To define the standard background model, we use two velocities: vertical velocity (or zero offset traveltime) and normal moveout velocity. The classic moveout is given by hyperbolic equation,

$$t^2 \approx t_0^2 + \frac{x^2}{V_n^2}, \tag{A.1}$$

where t and t_0 are the traveltime and vertical traveltime, respectively, x is the offset and V_n is the normal moveout (NMO) velocity. For a VTI model, $V_n = V_0\sqrt{1+2\delta}$, V_0 is the vertical velocity.

Alkhalifah (2011) proposed to expand the traveltime expression into series in anelliptic parameter η by solving the eikonal equation (Alkhalifah, 2000)

$$V_n^2(1+2\eta)\left(\frac{\partial\tau}{\partial x}\right)^2 + V_0^2\left(\frac{\partial\tau}{\partial z}\right)^2 - 2\eta V_n^2 V_0^2\left(\frac{\partial\tau}{\partial x}\right)^2\left(\frac{\partial\tau}{\partial z}\right)^2 = 1. \tag{A.2}$$

The perturbation series is defined by

$$\tau = a_0 + a_1\eta + a_2\eta^2, \tag{A.3}$$

where the series coefficients $a_j(x)$ can be found in Appendix A. The Shanks transform (Bender and Orszag, 1978) is applied to the approximation presented in equation (A.3) to obtain a higher accuracy.

In this paper, we propose an alternative hyperbolic background model,

$$t^2 \approx t_0^2 + \frac{x^2}{V_h^2}, \tag{A.4}$$

where V_h is the horizontal velocity with $V_h = V_0\sqrt{1+2\varepsilon} = V_n\sqrt{1+2\eta}$. Using the alternative background model means instead of the vertical velocity V_0 and NMO velocity V_n (the curvature of slowness surface at zero horizontal slowness) we are using the vertical velocity

V_0 (or the vertical slowness) and the horizontal velocity V_h (or the horizontal slowness) to represent the model as shown in Figure A.1.

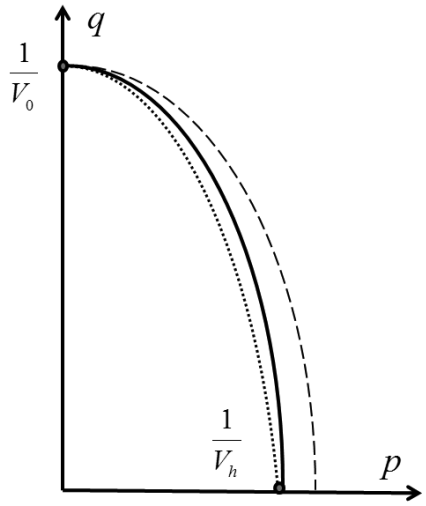

Figure A.1. The slowness curve for VTI model. p and q are the horizontal and vertical slowness, respectively. The exact one, the approximations by vertical velocity and NMO velocity, and by vertical velocity and horizontal velocity are shown by solid, dashed and dotted lines, respectively.

The comparison between the hyperbolic moveout approximations (A.1) and (A.4) is illustrated in Figure A.2 for a VTI model with parameters: $V_0 = 2km/s$, $t_0 = 0.5s$, $\delta = 0.1$ and $\eta = 0.1$. One can see that the new approximation is slightly worse for intermediate offset but much better for large offsets.

To define the perturbation coefficients for a new background, we solve the VTI eikonal equation (Alkhalifah, 2000) defined with horizontal velocity,

$$V_h^2\left(\frac{\partial \tau}{\partial x}\right)^2 + V_0^2\left(\frac{\partial \tau}{\partial z}\right)^2 - \frac{2\eta}{1+2\eta} V_h^2 V_0^2 \left(\frac{\partial \tau}{\partial x}\right)^2 \left(\frac{\partial \tau}{\partial z}\right)^2 = 1. \qquad \text{(A.5)}$$

Similar to equation (A.3), the new perturbation series up to the third order in η is defined as

$$\tau = \tau_0 + b_1\eta + b_2\eta^2 + b_3\eta^3. \tag{A.6}$$

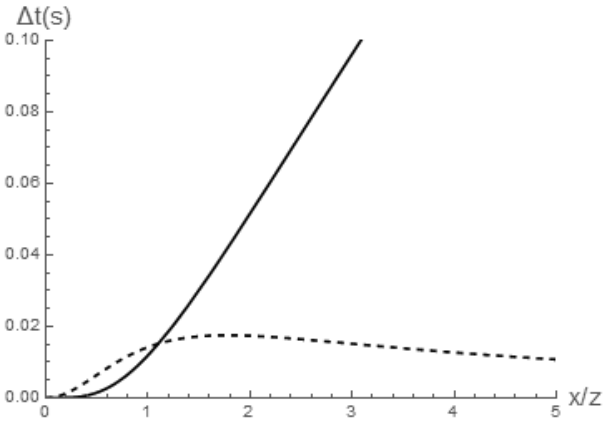

Figure A.2. The traveltime error from hyperbolic moveout approximations using two background models in VTI media. The results using NMO and horizontal velocities are shown by solid and dashed lines, respectively.

Solving eikonal equation (A.5) for a homogeneous VTI medium results in the following coefficients (Appendix B),

$$\begin{aligned}
\tau_0 &= \sqrt{t_0^2 + \frac{x^2}{V_h^2}}, \\
b_1 &= \frac{t_0^2 x^2}{\tau_0^3 V_h^2}, \\
b_2 &= -\frac{9t_0^4 x^4}{2\tau_0^7 V_h^4}, \\
b_3 &= \frac{-8t_0^8 V_h^4 x^4 + 65t_0^6 V_h^2 x^6 - 8t_0^4 x^8}{2\tau_0^{11} V_h^8}.
\end{aligned} \tag{A.7}$$

To improve the accuracy of perturbation series in equation (A.6), we can use the first- and second-order Shanks transform (Bender and Orszag, 1978) that give

$$\begin{aligned}
\tau_{S1} &= \frac{\tau_0\tau_2 - \tau_1^2}{\tau_0 + \tau_2 - 2\tau_1}, \\
\tau_{S2} &= \frac{\tau_1\tau_3 - \tau_2^2}{\tau_1 + \tau_3 - 2\tau_2},
\end{aligned} \tag{A.8}$$

where $\tau_k = \tau_0 + \sum_{j=1}^{k} b_j \eta^j,\ k = 1,2,3.$

Using the VTI model parameters introduced above, we compare the accuracy of the proposed approximations in equations (A.8) with other well-known approximations: GMA and Alkhalifah (2011) (Appendix A). The results are shown in Figure A.3 with different values for anellipticity parameter η. The relative error in traveltime is plotted versus normalized offset, $\hat{x} = x/(t_0 V_n)$. One can see that, regardless of the chosen values for η, the second-order Shanks transform from equations (A.8) gives the best accuracy, while the Alkhalifah (2011)'s method is the worst one. The sensitivity analysis from the second-order Shanks transform τ_{S2} with anellipticity parameter η is shown in Figure A.4. The error is very small with a small value of η.

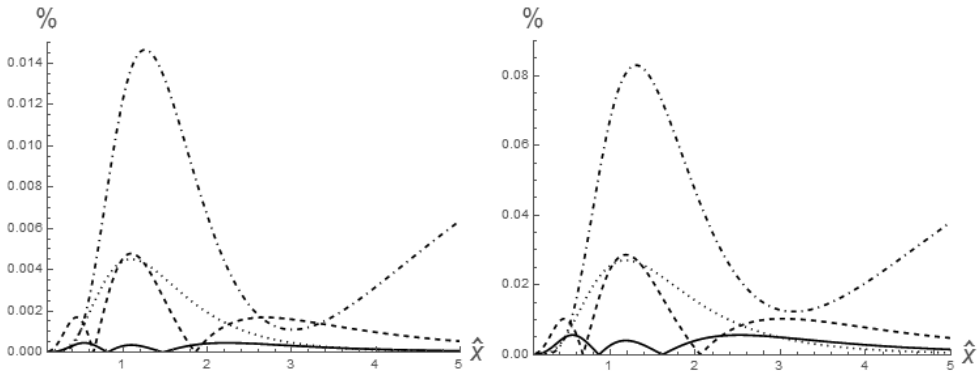

Figure A.3. The relative traveltime error from non-hyperblic approximations in VTI media with $\eta = 0.1$ (left) and $\eta = 0.2$ (right). The results from the GMA, Alkhalifah (2011) approximation, the first- and second-order Shanks transform (equations (A.8)) are shown by dotted, dotdashed, dashed and solid lines, respectively. $\hat{x}$ is the normalized offset.

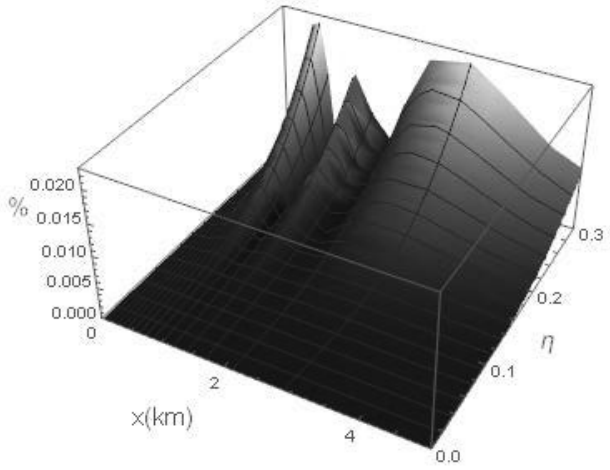

Figure A.4. The relative traveltime error with offset and anellipticity parameter η using the second-order Shanks transform τ_{S2}.

A.3 New moveout approximation in an ORT model

We can also select the perturbation series in anellipticity parameters for ORT case. Compared with VTI model, different from the anellipticity parameters in Masmoudi and Alkhalifah (2016), three anellipticity parameters in ORT model are η_1 and η_2 defined in two vertical symmetry planes $[X,Z]$ and $[Y,Z]$, and η_3 in horizontal plane $[X,Y]$ (Vasconcelos and Tsvankin, 2006) or anellipticity parameters η_1 and η_2 defined in two vertical symmetry planes $[X,Z]$ and $[Y,Z]$, and one cross-term anelliptic parameter η_{xy} (Stovas, 2015). With these parameterizations, we define different forms of the moveout approximation based on selection of anellipticity parameters and elliptical background models shown in Table A.1.

The perturbation series in terms of anellipticity parameters is defined up to the second order (Stovas *et al*. 2016),

$$\tau = \tau_0 + \sum_i a_i^k \eta_i + \sum_{i,j} b_{ij}^k \eta_i \eta_j, \ k = A,B,C,D. \tag{A.9}$$

First, we define case A for ORT medium by selecting the elliptical background model by V_0, V_{n1} and V_{n2} and the perturbation parameters η_1, η_2 and η_3.

Parameterization	Background	Perturbation parameters
Case A	V_0, V_{n1}, V_{n2}	η_1, η_2, η_3
Case B	V_0, V_{n1}, V_{n2}	$\eta_1, \eta_2, \eta_{xy}$
Case C	V_0, V_{h1}, V_{h2}	η_1, η_2, η_3
Case D	V_0, V_{h1}, V_{h2}	$\eta_1, \eta_2, \eta_{xy}$

Table A.1. Four types of parameterizations based on different background models and the perturbation parameters.

We solve the ORT eikonal equation (Alkhalifah, 2003) with NMO velocities,

$$\begin{aligned} &V_0^2\left(\frac{\partial\tau}{\partial z}\right)^2+(1+2\eta_1)V_{n1}^2\left(\frac{\partial\tau}{\partial x}\right)^2+(1+2\eta_2)V_{n2}^2\left(\frac{\partial\tau}{\partial y}\right)^2-2\eta_1V_{n1}^2V_0^2\left(\frac{\partial\tau}{\partial x}\right)^2\left(\frac{\partial\tau}{\partial z}\right)^2 \\ &-2\eta_2V_{n2}^2V_0^2\left(\frac{\partial\tau}{\partial y}\right)^2\left(\frac{\partial\tau}{\partial z}\right)^2-\left(\frac{(1+2\eta_1)(1+2\eta_2)2\eta_3}{1+2\eta_3}\right)V_{n1}^2V_{n2}^2\left(\frac{\partial\tau}{\partial x}\right)^2\left(\frac{\partial\tau}{\partial y}\right)^2 \\ &+\left(4\eta_1\eta_2-\left(\sqrt{\frac{(1+2\eta_1)(1+2\eta_2)}{1+2\eta_3}}-1\right)^2\right)V_{n1}^2V_{n2}^2V_0^2\left(\frac{\partial\tau}{\partial x}\right)^2\left(\frac{\partial\tau}{\partial y}\right)^2\left(\frac{\partial\tau}{\partial z}\right)^2=1, \end{aligned} \tag{A.10}$$

where V_0, V_{n1}, V_{n2} are the vertical and the corresponding NMO velocities, respectively. Anellipticity parameters η_1, η_2 and η_3 are defined in corresponding two vertical symmetry planes and horizontal plane, respectively. For homogeneous ORT model, the series coefficients a_i^A and b_{ij}^A, $(i, j = 1,2,3)$ are given in Appendix C.

We also define case B by selecting the elliptical background model by V_0, V_{n1} and V_{n2} and the cross-term anelliptic parameter η_{xy} defined by Stovas (2015)

$$\eta_{xy}=\sqrt{\frac{(1+2\eta_1)(1+2\eta_2)}{1+2\eta_3}}-1. \tag{A.11}$$

The eikonal equation in this case takes the form of

$$
\begin{aligned}
&V_0^2\left(\frac{\partial\tau}{\partial z}\right)^2+(1+2\eta_1)V_{n1}^2\left(\frac{\partial\tau}{\partial x}\right)^2+(1+2\eta_2)V_{n2}^2\left(\frac{\partial\tau}{\partial y}\right)^2-2\eta_1V_{n1}^2V_0^2\left(\frac{\partial\tau}{\partial x}\right)^2\left(\frac{\partial\tau}{\partial z}\right)^2\\
&-2\eta_2V_{n2}^2V_0^2\left(\frac{\partial\tau}{\partial y}\right)^2\left(\frac{\partial\tau}{\partial z}\right)^2-\left((1+2\eta_1)(1+2\eta_2)-(1+\eta_{xy})^2\right)V_{n1}^2V_{n2}^2\left(\frac{\partial\tau}{\partial x}\right)^2\left(\frac{\partial\tau}{\partial y}\right)^2\\
&+\left(4\eta_1\eta_2-\eta_{xy}^2\right)V_{n1}^2V_{n2}^2V_0^2\left(\frac{\partial\tau}{\partial x}\right)^2\left(\frac{\partial\tau}{\partial y}\right)^2\left(\frac{\partial\tau}{\partial z}\right)^2=1.
\end{aligned}
\tag{A.12}
$$

Solving the eikonal equation (A.12) with the corresponding perturbation series, we obtain the series coefficients a_i^B and b_{ij}^B, $(i,\ j=1,2,xy)$ shown in Appendix C.

Similarly, we select another hyperbolic background model case with the horizontal velocities and reparameterize the ORT eikonal equation and solve it by using the corresponding perturbation series. The relation between horizontal and NMO velocities is given by $V_{hj}=V_{nj}\sqrt{1+2\eta_j}$, $j=1,2$, and the relation between η_3 and η_{xy} is given in equation (A.11).

We define the case C by using V_0, V_{h1} and V_{h2} as elliptical background model and the perturbation parameters by η_1, η_2 and η_3. The eikonal equation is given by

$$
\begin{aligned}
&V_0^2\left(\frac{\partial\tau}{\partial z}\right)^2+V_{h1}^2\left(\frac{\partial\tau}{\partial x}\right)^2+V_{h2}^2\left(\frac{\partial\tau}{\partial y}\right)^2-\frac{2\eta_1}{1+2\eta_1}V_{h1}^2V_0^2\left(\frac{\partial\tau}{\partial x}\right)^2\left(\frac{\partial\tau}{\partial z}\right)^2\\
&-\frac{2\eta_2}{1+2\eta_2}V_{h2}^2V_0^2\left(\frac{\partial\tau}{\partial y}\right)^2\left(\frac{\partial\tau}{\partial z}\right)^2-\frac{2\eta_3}{1+2\eta_3}V_{h1}^2V_{h2}^2\left(\frac{\partial\tau}{\partial x}\right)^2\left(\frac{\partial\tau}{\partial y}\right)^2\\
&+\frac{4\eta_1\eta_2-\left(\sqrt{\frac{(1+2\eta_1)(1+2\eta_2)}{1+2\eta_3}}-1\right)^2}{(1+2\eta_1)(1+2\eta_2)}V_{h1}^2V_{h2}^2V_0^2\left(\frac{\partial\tau}{\partial x}\right)^2\left(\frac{\partial\tau}{\partial y}\right)^2\left(\frac{\partial\tau}{\partial z}\right)^2=1,
\end{aligned}
\tag{A.13}
$$

and the corresponding series coefficients a_i^C and b_{ij}^C, $(i,\ j=1,2,3)$ are shown in Appendix C.

For case D, we solve the ORT eikonal equation with horizontal velocities V_{h1} and V_{h2} and the perturbation parameters η_1, η_2 and η_{xy},

$$
\begin{aligned}
&V_0^2\left(\frac{\partial\tau}{\partial z}\right)^2+V_{h1}^2\left(\frac{\partial\tau}{\partial x}\right)^2+V_{h2}^2\left(\frac{\partial\tau}{\partial y}\right)^2-\frac{2\eta_1}{1+2\eta_1}V_{h1}^2V_0^2\left(\frac{\partial\tau}{\partial x}\right)^2\left(\frac{\partial\tau}{\partial z}\right)^2\\
&-\frac{2\eta_2}{1+2\eta_2}V_{h2}^2V_0^2\left(\frac{\partial\tau}{\partial y}\right)^2\left(\frac{\partial\tau}{\partial z}\right)^2-\frac{(1+2\eta_1)(1+2\eta_2)-(1+\eta_{xy})^2}{(1+2\eta_1)(1+2\eta_2)}V_{h1}^2V_{h2}^2\left(\frac{\partial\tau}{\partial x}\right)^2\left(\frac{\partial\tau}{\partial y}\right)^2 \qquad \text{(A.14)}\\
&+\frac{4\eta_1\eta_2-\eta_{xy}^2}{(1+2\eta_1)(1+2\eta_2)}V_{h1}^2V_{h2}^2V_0^2\left(\frac{\partial\tau}{\partial x}\right)^2\left(\frac{\partial\tau}{\partial y}\right)^2\left(\frac{\partial\tau}{\partial z}\right)^2=1.
\end{aligned}
$$

The corresponding series coefficients a_i^D and b_{ij}^D, $(i, j = 1,2, xy)$ are shown in Appendix C.

To test the proposed method, we select case D as an example for ORT model with the parameters: $t_0 = 0.5s$, $V_0 = 2km/s$, $V_{h1} = 2.4km/s$ $(V_{n1} = 2.191km/s)$, $V_{h2} = 2.6km/s$ $(V_{n2} = 2.28km/s)$, $\eta_1 = 0.1$, $\eta_2 = 0.15$ and $\eta_3 = 0.2$ $(\eta_{xy} = 0.0556)$. The coefficients $a_i^D, b_{ij}^D (i,k = 1,2, xy)$ from equation (A.C8) are plotted in Figures A.5, A.6 and A.7. One can see that the first order coefficients a_i^D (Figure A.5) are of the same magnitude, while the second order diagonal coefficients b_{11}^D and b_{22}^D (Figure A.6) are slightly higher in magnitude comparing with coefficient b_{xyxy}^D. The cross-term coefficients b_{12}^D, b_{1xy}^D and b_{2xy}^D are smaller comparing with b_{11}^D, b_{22}^D and b_{xyxy}^D. Relatively large values of b_{1xy}^D and b_{2xy}^D at azimuth of $\pm\pi/4$ indicate the cross-talk between anelliptic parameters η_1 and η_{xy}, η_2 and η_{xy}, respectively.

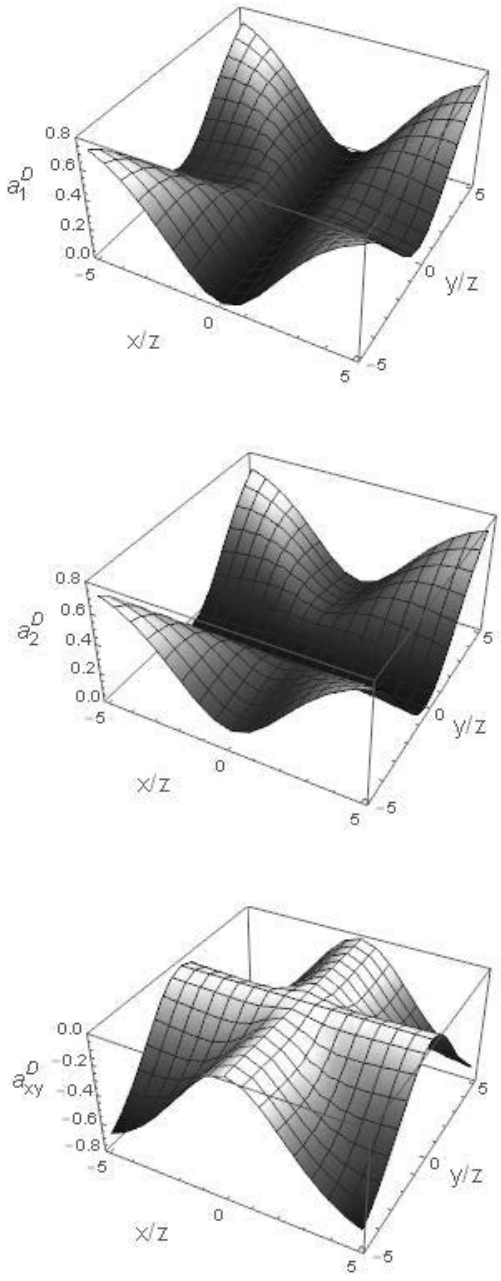

Figure A.5. The first order coefficients a_1^D (Top), a_2^D (Middle) and a_{xy}^D (Bottom) computed from equations (A.C8) in ORT model.

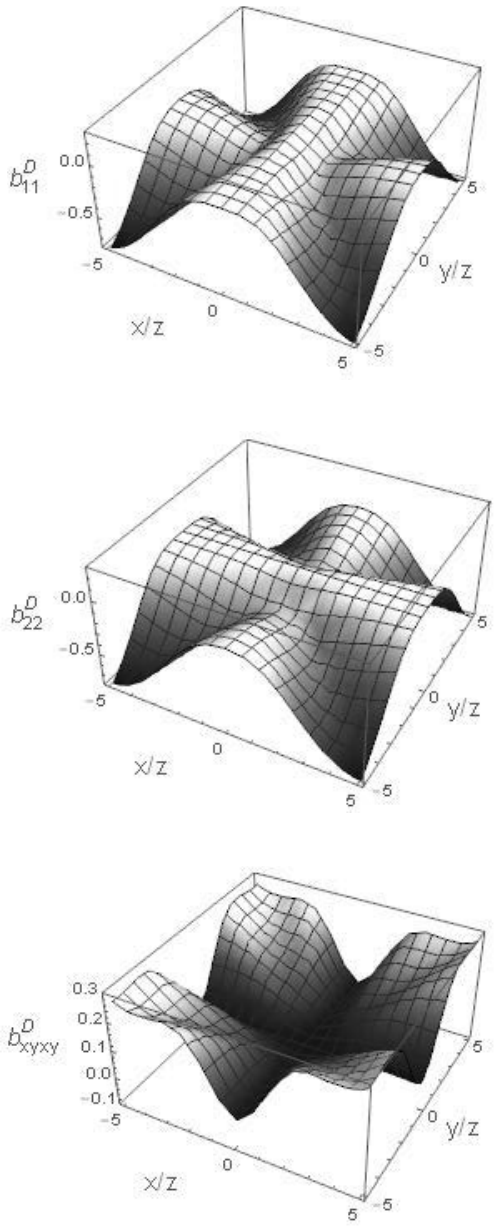

Figure A.6. The second order coefficients b_{11}^D (Top), b_{22}^D (Middle) and b_{xyxy}^D (Bottom) computed from equations (A.C8) in ORT model.

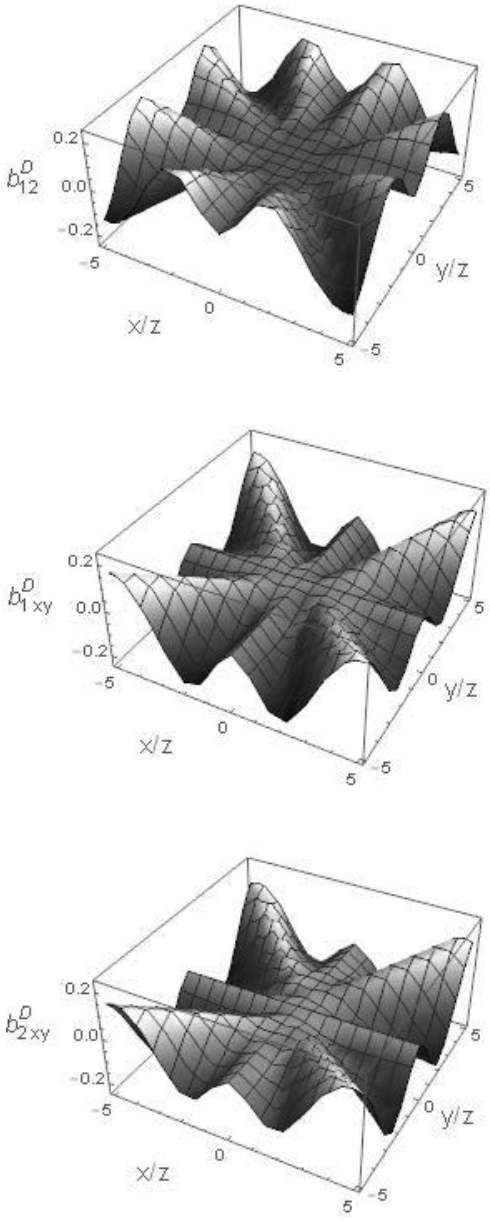

Figure A.7. The cross term coefficients b_{12}^D (Top), b_{1xy}^D (Middle) and b_{2xy}^D (Bottom) computed from equations (A.C8) in ORT model.

The anellipticity in terms of azimuth is given by Stovas (2015),

$$\eta_r(\Phi) = \frac{\dfrac{\eta_1 \cos^4\Phi}{V_{n1}^4} + \dfrac{\eta_2 \sin^4\Phi}{V_{n2}^4} + \dfrac{\eta_{xy} \sin^2\Phi \cos^2\Phi}{V_{n1}^2 V_{n2}^2}}{\left(\dfrac{\cos^2\Phi}{V_{n1}^2} + \dfrac{\sin^2\Phi}{V_{n2}^2}\right)^2}, \tag{A.15}$$

where the group azimuth is defined by

$$\tan\Phi = \frac{y}{x}, \tag{A.16}$$

with x and y being the corresponding projections of radial offset.

The azimuth dependent anellipticity from equation (A.15) defined for ORT model described above is shown in Figure A.8. We see that the anellipticity is very weak at the azimuth around $\pm\pi/4$ because the cross-term η_{xy} in this model is very small, which can be observed from coefficients b_{1xy}^D and b_{2xy}^D shown in Figure A.7.

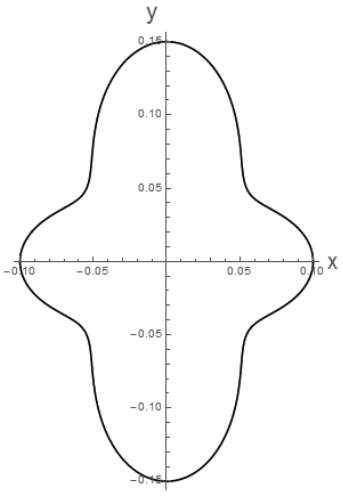

Figure A.8. The azimuth-dependent anellipticity from equation (A.15) in ORT model.

In order to obtain a higher accuracy, the Shanks transform (Bender and Orszag, 1978) is applied for all these four cases defined in Table A.1 by the form given by

$$\tau_3 = \frac{\tau_0\tau_2 - \tau_1^2}{\tau_0 + \tau_2 - 2\tau_1}, \tag{A.17}$$

where τ_0 is defined in equation (A.C1) and $\tau_1 = \tau_0 + \sum_i a_i^k \eta_i$ and $\tau_2 = \tau_1 + b_{ij}^k \eta_i \eta_j$,

$k = A, B, C, D$.

To demonstrate equation (A.17), we select case D and use the ORT model with parameters mentioned above. In Figure A.9 (Top), one can see the relative error in the estimation of traveltime curves from the perturbation series approximation given in equation (A.C7). The relative error in the estimation of traveltime from approximation with Shanks transform given by equation (A.17) is shown in Figure A.9 (Bottom). One can see that the Shanks transform results in one order improvement in traveltime accuracy.

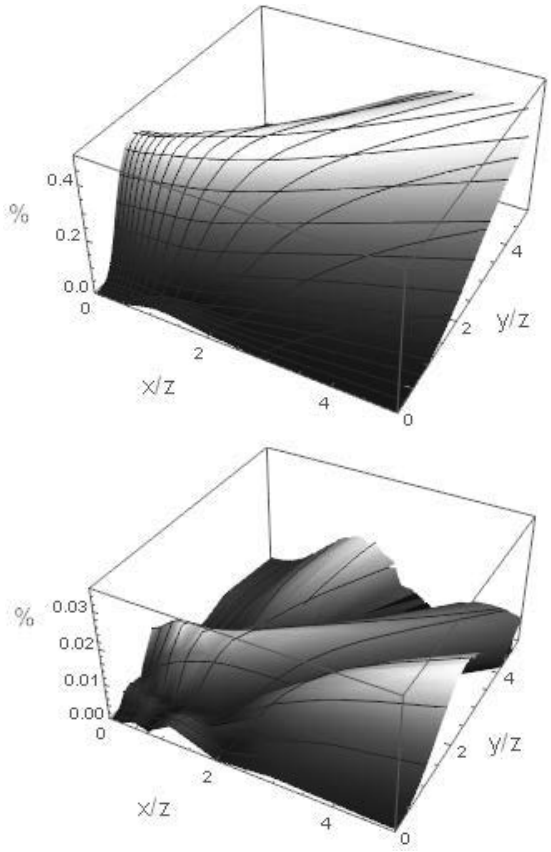

Figure A.9. The relative traveltime error for ORT model by using the perturbation series approximation in equation (A.C7) (Top) and the one after Shanks transform in equation (A.17) (Bottom).

A.4 Numerical examples

To compute the traveltime for ORT model, we use exact parametric offset-traveltime equations (Stovas 2015):

$$\begin{aligned} x(p_x, p_y) &= p_x F_2 \frac{V_{n1}^2 t_0}{f_1^{1/2} f_2^{3/2}}, \\ y(p_x, p_y) &= p_y F_1 \frac{V_{n2}^2 t_0}{f_1^{1/2} f_2^{3/2}}, \\ t(p_x, p_y) &= \frac{t_0\left(F_1 p_y^2 V_{n2}^2 + F_2 p_x^2 V_{n1}^2 + f_1 f_2\right)}{f_1^{1/2} f_2^{3/2}}, \end{aligned} \tag{A.18}$$

where x and y are the corresponding offset projections, p_x and p_y are the horizontal slowness defined in two vertical symmetry planes, and

$$\begin{aligned} F_1 &= \left(p_x^2 V_{n1}^2 \left(2\eta_1 - \eta_{xy}\right) - 1\right)^2, \\ F_2 &= \left(p_y^2 V_{n2}^2 \left(2\eta_2 - \eta_{xy}\right) - 1\right)^2, \\ f_1 &= 1 - \left(1 + 2\eta_1\right) p_x^2 V_{n1}^2 - \left(1 + 2\eta_2\right) p_y^2 V_{n2}^2 + \left(\left(1 + 2\eta_1\right)\left(1 + 2\eta_2\right) - \left(1 + \eta_{xy}\right)^2\right) p_x^2 p_y^2 V_{n1}^2 V_{n2}^2, \\ f_2 &= 1 - 2\eta_1 p_x^2 V_{n1}^2 - 2\eta_2 p_y^2 V_{n2}^2 + \left(4\eta_1\eta_2 - \eta_{xy}^2\right) p_x^2 p_y^2 V_{n1}^2 V_{n2}^2. \end{aligned} \tag{A.19}$$

Using the ORT model introduced above, the results of the Shanks transform applied for perturbation series using these parameterizations are illustrated in Figure A.10. One can see that the results obtained with the Shanks transform in case A are very similar with the results obtained with the Shanks transform in case B, while the best results are obtained with the Shanks transform in cases C and D (with horizontal velocities parameterization). The detailed analysis indicates that the case D results in slightly better accuracy comparing with the case C.

In order to compare our results with other well-known moveout approximations, we select the most accurate ones: from Sripanich and Fomel (2015) and Hao and Stovas (2016). The results from these approximations are shown in Figure A.11. One can see that the Sripanich-Fomel approximation is one order less accurate comparing with our best approximation, and the Hao-Stovas approximation is slightly worse in accuracy.

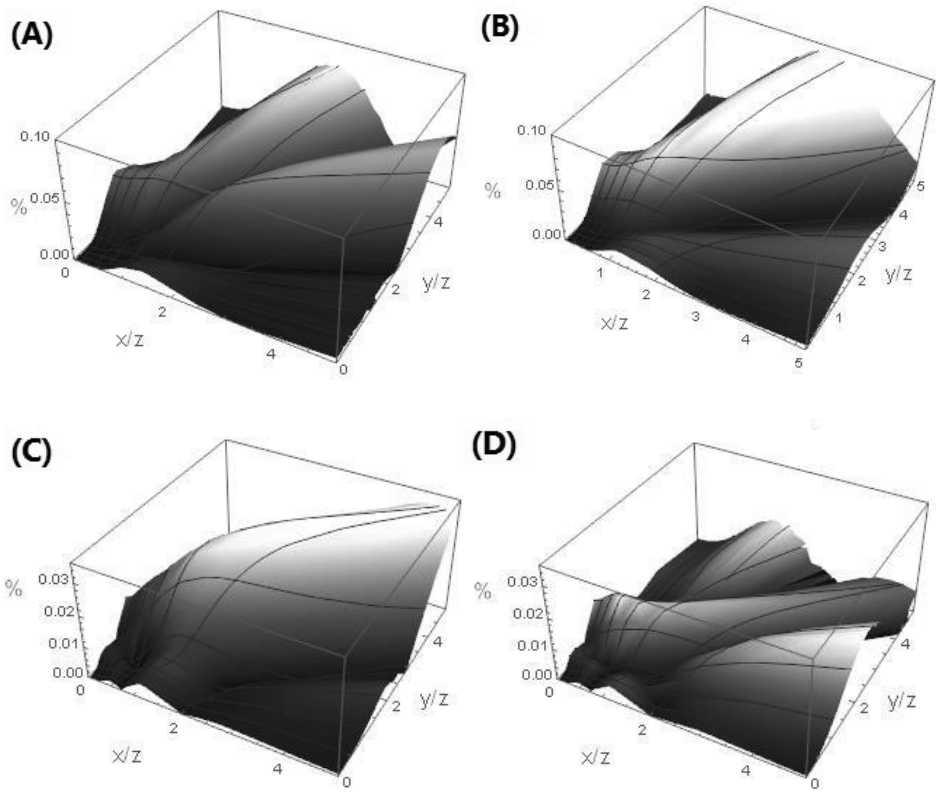

Figure A.10. The relative traveltime error for ORT model by using Shanks transform based on different parameterizations (cases A, B, C and D correspond to the ones specified in the main text).

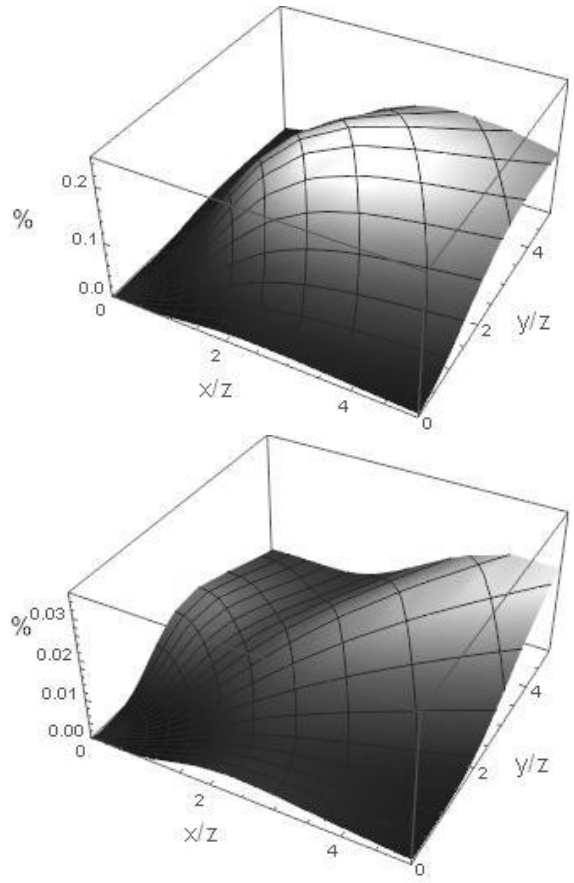

Figure A.11. The relative traveltime error for ORT model by using the approximations from Sripanich and Fomel (2015) (Top) and Hao and Stovas (2016) (Bottom).

A.5 Conclusions

We developed a new moveout approximation based on the perturbation method with alternative background model. We applied this approach for homogeneous VTI and ORT media. We test our approach with different parameterizations both for velocities and anelliptic parameters in ORT model. The comparison between the results from the standard moveout approximations based on NMO velocities and two well-known moveout approximations shows that the application of our proposed approach with horizontal velocities as a background model results in a better traveltime accuracy. The parameterization with anelliptic

parameters $\eta_1, \eta_2, \eta_{xy}$ results in the best accuracy for traveltime estimation in ORT model. The Shanks transform improves almost one order in trraveltime accuracy. This method is applied for a homogeneous model but can be extended for a multi-layered medium.

A.6 Acknowledgments

We would like to acknowledge China Scholarship Council (CSC) and ROSE project for financial support.

A.7 Appendix A

Fomel and Stovas (2010) proposed the generalized nonhyperbolic moveout approximation (GMA) from the zero-offset ray and one additional nonzero-offset ray given by

$$\begin{aligned} t^2 &= t_0^2\left(1+\hat{x}^2-\frac{4\eta\hat{x}^4}{1+B\hat{x}^2+\sqrt{1+2B\hat{x}^2+C\hat{x}^4}}\right), \\ B &= \frac{1+8\eta+8\eta^2}{1+2\eta}, \\ C &= \frac{1}{(1+2\eta)^2}, \end{aligned} \tag{A.A1}$$

where the parameters B and C are set for acoustic VTI medium, $\hat{x}$ is the normalized offset defined by $\hat{x} = x/(t_0 V_n)$.

Alkhalifah (2011) proposed to expand the traveltime expression into series by anelliptic parameter η (Alkhalifah, 1998) by solving the eikonal equation (Alkhalifah, 2000), where $\eta = (\varepsilon - \delta)/(1+2\delta)$ with parameters δ and ε being the Thomsen anisotropy parameters (Thomsen, 1986).

$$V_n^2(1+2\eta)\left(\frac{\partial\tau}{\partial x}\right)^2 + V_0^2\left(\frac{\partial\tau}{\partial z}\right)^2 - 2\eta V_n^2 V_0^2\left(\frac{\partial\tau}{\partial x}\right)^2\left(\frac{\partial\tau}{\partial z}\right)^2 = 1. \tag{A.A2}$$

The perturbation series is defined by

$$\tau = a_0 + a_1\eta + a_2\eta^2, \tag{A.A3}$$

where the series coefficients are

$$\begin{aligned} a_0 &= \tau_0\sqrt{1+\hat{x}^2} \\ a_1 &= -\tau_0\sqrt{1+\hat{x}^2}\,\frac{\hat{x}^4}{\left(1+\hat{x}^2\right)^2}, \\ a_2 &= \tau_0\sqrt{1+\hat{x}^2}\,\frac{3\hat{x}^6\left(4+\hat{x}^2\right)}{2\left(1+\hat{x}^2\right)^4}. \end{aligned} \tag{A.A4}$$

Shanks transform is applied to the approximation presented in equation (A.A3) to obtain a higher accuracy with the following form,

$$\begin{aligned} \tau &= \frac{A_0A_2 - A_1^2}{A_0 + A_2 - 2A_1}, \\ A_0 &= a_0, \\ A_1 &= a_0 + a_1\eta, \\ A_2 &= a_0 + a_1\eta + a_2\eta^2. \end{aligned} \tag{A.A5}$$

A.8 Appendix B

In order to derive the perturbation series for traveltime, we solve the eikonal equation for VTI media (Alkhalifah, 2000) with horizontal velocity,

$$V_h^2\left(\frac{\partial\tau}{\partial x}\right)^2 + V_0^2\left(\frac{\partial\tau}{\partial z}\right)^2 - \frac{2\eta}{1+2\eta}V_h^2V_0^2\left(\frac{\partial\tau}{\partial x}\right)^2\left(\frac{\partial\tau}{\partial z}\right)^2 = 1. \tag{A.B1}$$

A trial solution can be represented as a series expansion in parameter η from solving equation (A.B1) by the perturbation method,

$$\tau = \tau_0 + b_1\eta + b_2\eta^2 + b_3\eta^3. \tag{A.B2}$$

where b_j, $j = 1,3$ are the coefficients of the expansion.

The zero order term τ_0 can be obtained by solving equation (A.B1) with $\eta = 0$,

$$\left(\frac{\partial \tau_0}{\partial z}\right)^2 V_0^2 + \left(\frac{\partial \tau_0}{\partial x}\right)^2 V_h^2 = 1. \tag{A.B3}$$

In succession, the first order coefficient b_1 can be obtained by solving the following equation

$$\frac{\partial \tau_0}{\partial z}\frac{\partial b_1}{\partial z} V_0^2 + \frac{\partial \tau_0}{\partial x}\frac{\partial b_1}{\partial x} V_h^2 = \left(\frac{\partial \tau_0}{\partial x}\frac{\partial \tau_0}{\partial z}\right)^2 V_h^2 V_0^2, \tag{A.B4}$$

The second order coefficient b_2 can be computed from the following equation,

$$\begin{aligned} &2\left(\left(\frac{\partial \tau_0}{\partial x}\frac{\partial b_2}{\partial x}\right)V_h^2 + \left(\frac{\partial \tau_0}{\partial z}\frac{\partial b_2}{\partial z}\right)V_0^2\right) = 4V_0^2 V_h^2 \left(\frac{\partial \tau_0}{\partial x}\right)\left(\frac{\partial \tau_0}{\partial z}\right) \\ &\left(\frac{\partial \tau_0}{\partial z}\frac{\partial b_1}{\partial x} + \frac{\partial \tau_0}{\partial x}\left(\frac{\partial b_1}{\partial z} - \frac{\partial \tau_0}{\partial z}\right)\right) - \left(\left(\frac{\partial b_1}{\partial x}\right)^2 V_h^2 + \left(\frac{\partial b_1}{\partial z}\right)^2 V_0^2\right) \end{aligned} \tag{A.B5}$$

The third order coefficient b_3 is computed from,

$$\begin{aligned} &V_h^2\left(\frac{\partial \tau_0}{\partial x}\frac{\partial b_3}{\partial x}\right) + V_0^2\left(\frac{\partial \tau_0}{\partial z}\frac{\partial b_3}{\partial z}\right) = V_0^2 V_h^2\left(\left(\frac{\partial \tau_0}{\partial z}\right)^2\left(\frac{\partial b_1}{\partial x}\right)^2 + 2\frac{\partial \tau_0}{\partial x}\frac{\partial \tau_0}{\partial z}\left(2\frac{\partial b_1}{\partial x}\frac{\partial b_1}{\partial z} + \frac{\partial \tau_0}{\partial z}\left(\frac{\partial b_2}{\partial x} - 2\frac{\partial b_1}{\partial x}\right)\right)\right. \\ &\left. + \left(\frac{\partial \tau_0}{\partial x}\right)^2\left(2\frac{\partial \tau_0}{\partial z}\frac{\partial b_2}{\partial z} + \left(\frac{\partial b_1}{\partial z} - 2\frac{\partial \tau_0}{\partial z}\right)^2\right) - \left(\left(\frac{\partial b_1}{\partial z}\frac{\partial b_2}{\partial z}\right)V_0^2 + \left(\frac{\partial b_1}{\partial x}\frac{\partial b_2}{\partial x}\right)V_h^2\right) \end{aligned} \tag{A.B6}$$

For a homogeneous VTI medium, these coefficients can be explicitly computed as

$$\begin{aligned} \tau_0 &= \sqrt{t_0^2 + \frac{x^2}{V_h^2}}, \\ b_1 &= \frac{t_0^2 x^2}{\tau_0^3 V_h^2}, \\ b_2 &= -\frac{9 t_0^4 x^4}{2\tau_0^7 V_h^4}, \\ b_3 &= \frac{-t_0^4 x^4 \left(8 t_0^4 V_h^4 - 65 t_0^2 V_h^2 x^2 + 8 x^4\right)}{2\tau_0^{11} V_h^8}. \end{aligned} \tag{A.B7}$$

A.9 Appendix C

We can select different parameterizations for both velocities and anellipticity parameters. We use the following parameterization cases shown in Table A.1: $(V_0, V_{n1}, V_{n2}, \eta_1, \eta_2, \eta_3$, case A), $(V_0, V_{n1}, V_{n2}, \eta_1, \eta_2, \eta_{xy}$, case B); $(V_0, V_{h1}, V_{h2}, \eta_1, \eta_2, \eta_3$, case C) and $(V_0, V_{h1}, V_{h2}, \eta_1, \eta_2, \eta_{xy}$, case D). In order to compute the perturbation coefficients, we have to reparameterize the ORT eikonal equation and solve it by using the corresponding perturbation series shown in equation (A.9).

Using the standard elliptical background model with vertical and NMO velocities and anellipcitity parameters η_1, η_2, η_3, the perturbation series for ORT model (Case A) is defined by

$$\tau = \tau_0 + \sum_i a_i^A \eta_i + \sum_{i,j} b_{ij}^A \eta_i \eta_j, \; i, j = 1,2,3. \tag{A.C1}$$

For a homogeneous ORT model, the coefficients a_i^A and b_{ij}^A are computed from equation (A.10) and given by

$$
\begin{aligned}
\tau_0 &= \sqrt{t_0^2 + \tau_{nx}^2 + \tau_{ny}^2}, \\
a_1^A &= -\frac{\tau_{nx}^2\left(\tau_{nx}^2 + \tau_{ny}^2\right)}{\tau_0^3}, \\
a_2^A &= -\frac{\tau_{ny}^2\left(\tau_{nx}^2 + \tau_{ny}^2\right)}{\tau_0^3}, \\
a_3^A &= \frac{\tau_{nx}^2\tau_{ny}^2}{\tau_0^3}, \\
b_{11}^A &= \frac{\tau_{nx}^2\left(t_0^4\tau_{ny}^2 + \left(\tau_{nx}^2 + \tau_{ny}^2\right)^2\left(3\tau_{nx}^2 + 4\tau_{ny}^2\right) + t_0^2\left(12\tau_{nx}^4 + 17\tau_{nx}^2\tau_{ny}^2 + 5\tau_{ny}^4\right)\right)}{2\tau_0^7}, \\
b_{22}^A &= \frac{\tau_{ny}^2\left(t_0^4\tau_{nx}^2 + \left(\tau_{nx}^2 + \tau_{ny}^2\right)^2\left(3\tau_{ny}^2 + 4\tau_{nx}^2\right) + t_0^2\left(12\tau_{ny}^4 + 17\tau_{nx}^2\tau_{ny}^2 + 5\tau_{nx}^4\right)\right)}{2\tau_0^7}, \\
b_{33}^A &= -\frac{3\tau_{nx}^2\tau_{ny}^2\left(t_0^4 + 3\tau_{nx}^2\tau_{ny}^2 + t_0^2\left(\tau_{nx}^2 + \tau_{ny}^2\right)\right)}{2\tau_0^7}, \\
b_{12}^A &= -\frac{\tau_{nx}^2\tau_{ny}^2\left(t_0^4 + \left(\tau_{nx}^2 + \tau_{ny}^2\right)^2 - 7t_0^2\left(\tau_{nx}^2 + \tau_{ny}^2\right)\right)}{\tau_0^7}, \\
b_{13}^A &= \frac{\tau_{nx}^2\tau_{ny}^2\left(t_0^4 + \tau_{nx}^4 - \tau_{nx}^2\tau_{ny}^2 - 2\tau_{ny}^4 - t_0^2\left(7\tau_{nx}^2 + \tau_{ny}^2\right)\right)}{\tau_0^7}, \\
b_{23}^A &= \frac{\tau_{nx}^2\tau_{ny}^2\left(t_0^4 + \tau_{ny}^4 - \tau_{nx}^2\tau_{ny}^2 - 2\tau_x^4 - t_0^2\left(7\tau_{ny}^2 + \tau_{nx}^2\right)\right)}{\tau_0^7},
\end{aligned}
\tag{A.C2}
$$

where $\tau_{nx} = x/V_{n1}$ and $\tau_{ny} = y/V_{n2}$.

Using the standard elliptical background model with vertical and NMO velocities and anellipcitity parameters $\eta_1, \eta_2\ \eta_{xy}$, the perturbation series for ORT model (Case B) is defined by

$$
\tau = \tau_0 + \sum_i a_i^B \eta_i + \sum_{i,j} b_{ij}^B \eta_i \eta_j,\ i, j = 1,2, xy. \tag{A.C3}
$$

For a homogeneous ORT model, the coefficients a_i^B and b_{ij}^B are computed from equation (A.12) and given by

$$
\begin{aligned}
&\tau_0 = \sqrt{t_0^2 + \tau_{nx}^2 + \tau_{ny}^2}, \\
&a_1^B = -\frac{\tau_{nx}^4}{\tau_0^3}, \\
&a_2^B = -\frac{\tau_{ny}^4}{\tau_0^3}, \\
&a_{xy}^B = -\frac{\tau_{nx}^2 \tau_{ny}^2}{\tau_0^3}, \\
&b_{11}^B = \frac{3\tau_{nx}^6 \left(4t_0^2 + 4\tau_{ny}^2 + \tau_{nx}^2\right)}{2\tau_0^7}, \\
&b_{22}^B = \frac{3\tau_{ny}^6 \left(4t_0^2 + 4\tau_{nx}^2 + \tau_{ny}^2\right)}{2\tau_0^7}, \\
&b_{xyxy}^B = \frac{3\tau_{nx}^2 \tau_{ny}^2 \left(\tau_{nx}^4 - \tau_{nx}^2 \tau_{ny}^2 + \tau_{ny}^4 + t_0^2 \left(\tau_{nx}^2 + \tau_{ny}^2\right)\right)}{2\tau_0^7}, \\
&b_{12}^B = -\frac{9\tau_{nx}^4 \tau_{ny}^4}{\tau_0^7}, \\
&b_{1xy}^B = \frac{3\tau_{nx}^4 \tau_{ny}^2 \left(2t_0^2 - \tau_{nx}^2 + 2\tau_{ny}^2\right)}{\tau_0^7}, \\
&b_{2xy}^B = \frac{3\tau_{ny}^4 \tau_{nx}^2 \left(2t_0^2 - \tau_{ny}^2 + 2\tau_{nx}^2\right)}{\tau_0^7}.
\end{aligned}
\tag{A.C4}
$$

Using the elliptical background model with vertical and horizontal velocities and anellipcitity parameters η_1, η_2, η_3, the perturbation series for ORT model (Case C) is defined by

$$
\tau = \tau_0 + \sum_i a_i^C \eta_i + \sum_{i,j} b_{ij}^C \eta_i \eta_j, \; i, j = 1,2,3. \tag{A.C5}
$$

For a homogeneous ORT model, the coefficients a_i^C and b_{ij}^C are computed from equation (A.13) and given by

$$
\begin{aligned}
\tau_0 &= \sqrt{t_0^2 + \tau_{hx}^2 + \tau_{hy}^2}, \\
a_1^C &= \frac{t_0^2 \tau_{hx}^2}{\tau_0^3}, \\
a_2^C &= \frac{t_0^2 \tau_{hy}^2}{\tau_0^3}, \\
a_3^C &= \frac{\tau_{hx}^2 \tau_{hy}^2}{\tau_0^3}, \\
b_{11}^C &= -\frac{3t_0^2 \tau_{hx}^2 \left(\tau_{hy}^2 \left(\tau_{hx}^2 + \tau_{hy}^2\right) + t_0^2 \left(3\tau_{hx}^2 + \tau_{hy}^2\right)\right)}{2\tau_0^7}, \\
b_{22}^C &= -\frac{3t_0^2 \tau_{hy}^2 \left(\tau_{hx}^2 \left(\tau_{hx}^2 + \tau_{hy}^2\right) + t_0^2 \left(3\tau_{hy}^2 + \tau_{hx}^2\right)\right)}{2\tau_0^7}, \\
b_{33}^C &= -\frac{3\tau_{hx}^2 \tau_{hy}^2 \left(t_0^4 + 3\tau_{hx}^2 \tau_{hy}^2 + t_0^2 \left(\tau_{hx}^2 + \tau_{hy}^2\right)\right)}{2\tau_0^7}, \\
b_{12}^C &= \frac{3t_0^2 \tau_{hx}^2 \tau_{hy}^2 \left(\tau_{hx}^2 + \tau_{hy}^2 - 2t_0^2\right)}{\tau_0^7}, \\
b_{13}^C &= \frac{3t_0^2 \tau_{hx}^2 \tau_{hy}^2 \left(\tau_{hy}^2 - 2\tau_{hx}^2 + t_0^2\right)}{\tau_0^7}, \\
b_{23}^C &= \frac{3t_0^2 \tau_{hx}^2 \tau_{hy}^2 \left(\tau_{hx}^2 - 2\tau_{hy}^2 + t_0^2\right)}{\tau_0^7},
\end{aligned}
\tag{A.C6}
$$

where $\tau_{hx} = x/V_{h1}$ and $\tau_{hy} = y/V_{h2}$.

Using the elliptical background model with vertical and horizontal velocities and anellipcitity parameters η_1, η_2 η_{xy} the perturbation series for ORT model (Case D) is defined by

$$
\tau = \tau_0 + \sum_i a_i^D \eta_i + \sum_{i,j} b_{ij}^D \eta_i \eta_j, \; i, j = 1,2, xy. \tag{A.C7}
$$

For a homogeneous ORT model, the coefficients a_i^D and b_{ij}^D are computed from equation (A.14) and given by

$$
\begin{aligned}
&\tau_0 = \sqrt{t_0^2 + \tau_{hx}^2 + \tau_{hy}^2}, \\
&a_1^D = \frac{\tau_{hx}^2\left(t_0^2 + \tau_{hy}^2\right)}{\tau_0^3}, \\
&a_2^D = \frac{\tau_{hy}^2\left(t_0^2 + \tau_{hx}^2\right)}{\tau_0^3}, \\
&a_{xy}^D = -\frac{\tau_{hx}^2\tau_{hy}^2}{\tau_0^3}, \\
&b_{11}^D = -\frac{9\tau_{hx}^4\left(t_0^2 + \tau_{hy}^2\right)^2}{2\tau_0^7}, \\
&b_{22}^D = -\frac{9\tau_{hy}^4\left(t_0^2 + \tau_{hx}^2\right)^2}{2\tau_0^7}, \\
&b_{xyxy}^D = \frac{3\tau_{hx}^2\tau_{hy}^2}{2\tau_0^7}\left(\tau_{hx}^4 + \tau_{hy}^4 - \tau_{hx}^2\tau_{hy}^2 + t_0^2\left(\tau_{hx}^2 + \tau_{hy}^2\right)\right), \\
&b_{12}^D = \frac{\tau_{hx}^2\tau_{hy}^2}{\tau_0^7}\left(2\tau_{hx}^4 + 2\tau_{hy}^4 - t_0^4 - 5\tau_{hx}^2\tau_{hy}^2 + t_0^2\left(\tau_{hx}^2 + \tau_{hy}^2\right)\right), \\
&b_{1xy}^D = -\frac{\tau_{hx}^2\tau_{hy}^2}{\tau_0^7}\left(2\tau_{hx}^4 + 2\tau_{hy}^4 + 2t_0^4 - 5\tau_{hx}^2\tau_{hy}^2 + t_0^2\left(4\tau_{hy}^2 - 5\tau_{hx}^2\right)\right), \\
&b_{2xy}^D = -\frac{\tau_{hx}^2\tau_{hy}^2}{\tau_0^7}\left(2\tau_{hx}^4 + 2\tau_{hy}^4 + 2t_0^4 - 5\tau_{hx}^2\tau_{hy}^2 + t_0^2\left(4\tau_{hx}^2 - 5\tau_{hy}^2\right)\right).
\end{aligned}
\tag{A.C8}
$$

Appendix B Three-dimensional generalized non-hyperbolic approximation for relative geometrical spreading

Shibo Xu and Alexey Stovas

Norwegian University of Science and Technology, Trondheim, Norway

Compensation for geometrical spreading along the ray-path is important in AVO (amplitude versus offset) analysis since it contributes to the seismic amplitude preservation. The P-wave geometrical spreading factor is expressed by the reflection traveltime described by a nonhyperbolic moveout approximation using the traveltime parameters that can be estimated in velocity analysis. The generalized nonhyperbolic moveout approximation (GMA) for traveltime was proposed by Fomel and Stovas (2010) by using two reference rays. We develop a 3D GMA type approximation for the relative geometrical spreading in a homogeneous orthorhombic (ORT) medium using the same strategy. Two type of GMA form approximations are defined by different selection of reference rays: two reference rays with finite offsets and two horizontal reference rays in two corresponding vertical symmetry planes. One horizontal ray in between the vertical symmetry planes is selected to compute the cross-term coefficient in the approximation. In the numerical examples, we compare our proposed GMA form approximations with other type of approximations in a homogeneous transversely isotropic medium with a vertical symmetry axis (VTI), transversely isotropic medium with a horizontal symmetry axis (HTI), ORT and multilayered ORT models and show that our GMA type approximations are superior among all approximations.

Published in Geophysical Journal International in August 2017.

B.1 Introduction

Geometrical spreading describes the amplitude decay of propagating waves and is one of the most fundamental subjects in seismic data processing. It is important to prestack Kirchhoff migration, amplitude versus offset (AVO) analysis and other seismic data processing methods that require the true amplitude processing. If the velocity model is anisotropic, the amplitude distribution along the wavefront of the reflected wave is changed significantly. Without an accurate geometrical spreading correction, estimation of the reflection coefficient for targets beneath anisotropic layers may be strongly distorted. In order to study reflection coefficients as a function of offset or incidence angle, seismic date must be compensated for geometrical spreading before AVO or amplitude versus angle (AVA) analysis. Although geometrical spreading is a dynamic quantity, it is governed by the kinematic parameters of seismic waves. The relative geometrical spreading can be computed by performing dynamic ray tracing when the velocity model is available. Accurate information about the anisotropic velocity model for the whole overburden is seldom available for practice. To avoid the use of numerical ray tracing, expressing the geometrical spreading through traveltime of the reflection events recorded at the surface using ray theory (Červený, 2001) is a more practical method for seismic time processing. Therefore, it is convenient to express the geometrical spreading in terms of the processing parameters that can be estimated from the nonhyperbolic velocity analysis.

Ursin (1990) proposed a geometrical spreading approximation represented by traveltime parameters for a layered isotropic medium. Červený (2001) developed an expression for geometrical spreading in terms of the traveltime functions at the source and receivers locations that is one of the practical contributions from the paraxial ray theory. Zhou and McMechan (2000) derived an analytical formula for the geometrical spreading of P-waves in a layered transversely isotropic medium with vertical symmetry axis (VTI) with the source

and receivers in the same layer. Ursin and Hokstad (2003) extended the method of Ursin (1990) for multiple reflected and converted P- and SV-waves in a layered VTI medium with the source and receivers in different layers. The geometrical spreading of SV-waves in TI media was discussed by Tsvankin (1995, 2005). For azimuthally anisotropic media, the geometrical spreading as a function of traveltime derivatives was derived by Xu et al. (2005) who used the traveltime approximation from Tsvankin and Thomsen (1994).The geometrical spreading correction for an azimuthally anisotropic medium was later derived by Xu and Tsvankin (2006), and was extended for converted waves in a VTI medium (Xu and Tsvankin, 2008). The traveltime-based geometrical spreading approximation (based on the traveltime approximation) in TTI media was derived by Golikov and Stovas (2013). The approximations we mentioned above are using the traveltime approximation to compute the geometrical spreading approximation, we refer these methods as the indirect type (traveltime-based) approximations.

As the name indicates, the indirect type (traveltime-based) approximation for geometrical spreading is defined from the traveltime approximation since the relative geometrical spreading is expressed by traveltime and its derivatives. Instead of approximating the geometrical spreading directly, these types of approximation are obtained by substituting the traveltime approximation and its derivatives into the form of relative geometrical spreading. Although the geometrical spreading factor is controlled by first- and second-order traveltime derivatives, there is no guarantee that the most accurate traveltime approximation being used in equations for geometrical spreading results in the most accurate geometrical spreading approximation.

Different with the indirect type approximation, the direct type approximation is obtained by approximating the geometrical spreading term directly. Using the horizontal slowness instead of traveltime, the explicit form for relative geometrical spreading is derived from the exact

parametric equation that obtained from dynamic ray tracing. In direct type approximation, the accuracy of the approximation is decided directly by properly define the form of the approximation. The first example of the direct type approximation for relative geometrical spreading is done by Stovas and Ursin (2009) who developed the rational form approximation directly. They showed that the direct rational approximation is simpler and more accurate than the indirect counterpart for a homogeneous and multilayered VTI model. Xu and Stovas (2017) proposed a direct approximation in GMA type for the relative geometrical spreading for a VTI medium and compared them with the traveltime-based ones.

The orthorhombic (ORT) model is introduced by Schoenborg and Helbig (1997) and has gained more attention due to the need to characterize the fractured earth and has become a new standard to define model parameters to cover the azimuthal dependence of the traveltime surface. Tsvankin (1997, 2012) defined nine elastic model parameters for ORT model that can be reduced to six parameters in an acoustic approximation (Alkhalifah, 2003). The first order curvatures are defined by the normal moveout (NMO) velocity ellipse (Grechka and Tsvankin, 1999a, 1999b), and the second order curvatures are defined by the azimuth-dependent anellipticity. Stovas (2015) derived azimuthally dependent kinematic properties of the orthorhombic media and defined the effective ORT parameters in the Dix-type formula in layered ORT media. The VTI and HTI model can be considered as the special cases from the ORT model by proper operating the ORT model parameters (Tsvankin, 1997; Stovas, 2015). Sripanich and Fomel (2015) modified the anelliptic functional form of Fomel (2004) and extended it to ORT model to approximate P-wave phase and group velocities. Xu et al (2017) derived the perturbation-based traveltime approximations using the alternative elliptical background model. Xu et al. (2017) developed an anelliptic approximation for the relative geometrical spreading in a homogeneous ORT model with the coefficients defined within the symmetry planes and showed its superior accuracy compared with the traveltime-based one.

Fomel and Stovas (2010) derived a generalized nonhyperbolic moveout approximation (GMA) for the traveltime approximation defined from zero-offset and one nonzero-offset ray computation, which is very accurate even as good as exact for many practical implement such as the model parameters estimation in velocity analysis. Sripanich et al. (2016) extend it to the 3D multi-azimuth case using zero-offset attributes and four additional far-offset rays.

In this paper, we revisit the direct type GMA form approximation for the relative geometrical spreading in a VTI model and propose a direct rational form approximation in a homogeneous ORT model. We subsequently extend the 2D GMA approximation to 3D case in the homogeneous ORT model by using different selected rays: two reference rays with finite offsets and two horizontal reference rays in two vertical symmetry planes and one horizontal reference ray in between the vertical symmetry planes. The acoustic approximation is used to reduce the number of parameters that makes the forms of direct GMA relative geometrical spreading approximation similar to the GMA traveltime approximation (Fomel and Stovas, 2010). Using the numerical tests in different models, we show that the proposed 3D GMA type approximations perform several orders of magnitude more accurate than other form of approximations in all tested models.

B.2 Relative geometrical spreading in a VTI model

The geometrical spreading is given in Červený (2001) as

$$\mathcal{L} = \sqrt{\frac{\cos\theta_S \cos\theta_R}{|\det \mathbf{M}|}}, \tag{B.1}$$

where θ_S and θ_R are the angles between the ray and the normal to the surface measured at the source and receiver, respectively, and **M** is the second order derivatives matrix given by

$$\mathbf{M} = \begin{pmatrix} \dfrac{\partial^2 T}{\partial x_S \partial x_R} & \dfrac{\partial^2 T}{\partial x_S \partial y_R} \\ \dfrac{\partial^2 T}{\partial y_S \partial x_R} & \dfrac{\partial^2 T}{\partial y_S \partial y_R} \end{pmatrix}, \tag{B.2}$$

where T is the traveltime, (x_S, y_S) and (x_R, y_R) are the lateral coordinates of source and receiver, respectively. Note that equation (B.1) gives a general form for geometrical spreading. The relative geometrical spreading in a VTI model is given by (Ursin and Hokstad, 2003)

$$\mathcal{L} = \Omega \left(\frac{1}{x} \frac{dt}{dx} \right)^{-1/2} \left(\frac{d^2 t}{dx^2} \right)^{-1/2}, \tag{B.3}$$

where Ω is the radiation pattern given by $\Omega = \sqrt{\cos\theta_S \cos\theta_R}$, t is the traveltime in VTI model. In our paper, we focus only on the term $\mathcal{L}_N$, we call it the relative geometrical spreading factor that is given as

$$\mathcal{L}_N = \left(\frac{1}{x} \frac{dt}{dx} \frac{d^2 t}{dx^2} \right)^{-1/2}. \tag{B.4}$$

Note that $\mathcal{L} = \Omega \mathcal{L}_N$. The relative geometrical spreading factor $\mathcal{L}_N$ given in equation (B.4) can also be written as a function of horizontal slowness p with $p = \partial t / \partial x$ as follows (Stovas and Ursin, 2009)

$$\mathcal{L}_N = \left(\frac{x}{p} \frac{dx}{dp} \right)^{1/2}. \tag{B.5}$$

For a homogeneous VTI model, the offset can also be given in terms of horizontal slowness,

$$x(p) = \frac{p t_0 V_n^2}{\left(1 - 2\eta p^2 V_n^2\right)^{3/2} \sqrt{1 - (1 + 2\eta) p^2 V_n^2}}. \tag{B.6}$$

where t_0 is the vertical travel time, V_n is the normal moveout (NMO) velocity and η is the anellipticity parameter (Alkhalifah, 1998). Substituting equation (B.6) into equation (B.5) gives (Stovas and Ursin, 2009)

$$\mathcal{L}_N = \frac{t_0 V_n^2 \sqrt{1+4\eta p^2 V_n^2 - 6\eta(1+2\eta)p^4 V_n^4}}{\left(1-2\eta p^2 V_n^2\right)^2 \left(1-(1+2\eta)p^2 V_n^2\right)}. \tag{B.7}$$

Instead of using the traveltime derivative form approximation in equation (B.4), equations (B.6) and (B.7) give a parametric equation for relative geometrical spreading $\mathcal{L}_N$ in terms of horizontal slowness.

B.3 GMA-type geometrical spreading approximations

The generalized nonhyperbolic moveout (GMA) approximation proposed by Fomel and Stovas (2010) is based on parameters computed from the zero-offset ray and the reference ray. The direct GMA type approximation of the relative geometrical spreading in VTI model is given by the similar form (Xu and Stovas, 2017),

$$\mathcal{L}_{N(GMA)} = \mathcal{L}_0 \left(1 + A_2 \hat{x}^2 + \frac{2A_4 \hat{x}^4}{1 + C_2 \hat{x}^2 + \sqrt{1 + 2C_2 \hat{x}^2 + C_4 \hat{x}^4}}\right), \tag{B.8}$$

where $\hat{x}$ is the normalized offset defined by $\hat{x} = x/(t_0 V_n)$, $\mathcal{L}_0 = t_0 V_n^2$, A_2 and A_4 are the Taylor series coefficients computed in zero offset ray given as

$$A_2 = 1 + 8\eta, A_4 = -9\eta(1+4\eta). \tag{B.9}$$

To compute coefficients C_2 and C_4, we use similar approach as for GMA traveltime approximation (Fomel and Stovas, 2010). For a given reference ray, we define $\mathcal{L}_N$ and $d\mathcal{L}_N / dx$. Being converted for normalized offset $\hat{X}$, they result in two equations: $W_1 = \mathcal{L}_N\left(\hat{x} = \hat{X}\right)$ and $W_2 = d\mathcal{L}_N / d\hat{x}\left(\hat{x} = \hat{X}\right)$. The coefficients C_2 and C_4 take the following form

$$C_2 = \frac{2\mathcal{L}_0 A_2 \hat{X} - W_2}{2\mathcal{L}_0 \hat{X} - 2W_1 \hat{X} + W_2 \hat{X}^2} - \frac{2\mathcal{L}_0 A_4 \hat{X}^2}{\mathcal{L}_0 - W_1 + \mathcal{L}_0 A_2 \hat{X}^2},$$
$$C_4 = \frac{\left(2\mathcal{L}_0 A_2 \hat{X} - W_2\right)^2}{\hat{X}^2 \left(2\mathcal{L}_0 - 2W_1 + W_2 \hat{X}\right)^2} + \frac{4\mathcal{L}_0 A_4}{\mathcal{L}_0 - W_1 + \mathcal{L}_0 A_2 \hat{X}^2}. \quad \text{(B.10)}$$

For a horizontal reference ray, the coefficients C_2 and C_4 take the form,

$$C_2 = \frac{18\eta\sqrt{1+2\eta}(1+4\eta)}{\sqrt{1+2\eta}(1+8\eta)-1},$$
$$C_4 = \left(\frac{\sqrt{1+2\eta}(1+8\eta)-1}{\sqrt{1+2\eta}-(1+2\eta)^2(1+6\eta)}\right)^2. \quad \text{(B.11)}$$

Two types of the GMA form approximation are defined with reference limited offset GMA_X at $\hat{X} = 2.5$ and the infinite offset limit GMA_∞. The form of two GMA type approximations is the same shown in equation (B.8). The difference is the computation for coefficients C_2 and C_4. Using the horizontal ray, the coefficients C_2 and C_4 are offset independent and represent only in anellipticity parameter η explicitly. Using the reference ray, the information about the geometrical spreading at certain normalized offset $\hat{X}$ are involved in the approximation for relative geometrical spreading.

We show their relative error in a homogeneous VTI model (Figure B.1, left) with parameters $t_0 = 1s$, $V_n = 2km/s$ and $\eta = 0.2$ and a five-layer VTI model (Figure B.1, right) with the parameters in Table B.1. One can tell that the GMA_X approximation results in better accuracy comparing with GMA_∞ in both homogeneous and multi-layered VTI models.

Layer	Z (km)	V_0 (km/s)	V_n (km/s)	η
1	0.3	1.5	1.7	0.1
2	0.7	1.8	2	0.12
3	1	2	2.3	0.18
4	1.5	2.2	2.5	0.2
5	0.5	2.5	2.8	0.22

Table B.1. The model parameters in a multilayered VTI model.

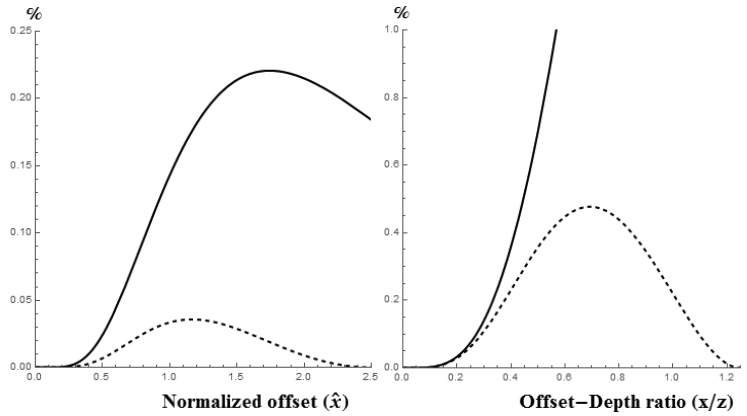

Figure B.1. The relative error in relative geometrical spreading of two type of GMA approximation in homogeneous (left) and multi-layered (right) VTI models. The result from GMA_∞ and GMA_X are computed from infinite and reference offset limit and shown by solid and dashed lines, respectively. Note that normalized offset $\hat{x} = x/(t_0 V_n)$.

B.4 Direct relative geometrical spreading in a homogeneous ORT model

For a homogeneous ORT model, we introduce two lateral offset projections

$$\begin{aligned} x &= x_R - x_S, \\ y &= y_R - y_S. \end{aligned} \tag{B.12}$$

The matrix **M** in equation (B.2) takes the form

$$\mathbf{M} = \begin{pmatrix} \dfrac{\partial^2 T}{\partial x^2} & \dfrac{\partial^2 T}{\partial x \partial y} \\ \dfrac{\partial^2 T}{\partial y \partial x} & \dfrac{\partial^2 T}{\partial y^2} \end{pmatrix}. \tag{B.13}$$

In phase domain, the relative geometrical spreading $\mathcal{L}_N$ can be given by

$$\mathcal{L}_N = \left(\frac{\partial x}{\partial p_x}\frac{\partial y}{\partial p_y} - \frac{\partial y}{\partial p_x}\frac{\partial x}{\partial p_y} \right)^{1/2}. \tag{B.14}$$

To compute the geometrical spreading for a homogeneous ORT model, we use exact parametric offset equations (Stovas, 2015):

$$\begin{aligned} x(p_x, p_y) &= p_x F_2^2 \frac{V_{n1}^2 t_0}{f_1^{1/2} f_2^{3/2}}, \\ y(p_x, p_y) &= p_y F_1^2 \frac{V_{n2}^2 t_0}{f_1^{1/2} f_2^{3/2}}, \end{aligned} \tag{B.15}$$

x and y are corresponding offset projections, and

$$\begin{aligned} F_1 &= 1 - p_x^2 V_{n1}^2 (2\eta_1 - \eta_{xy}), \\ F_2 &= 1 - p_y^2 V_{n2}^2 (2\eta_2 - \eta_{xy}), \\ f_1 &= 1 - (1+2\eta_1) p_x^2 V_{n1}^2 - (1+2\eta_2) p_y^2 V_{n2}^2 + \left((1+2\eta_1)(1+2\eta_2) - (1+\eta_{xy})^2 \right) p_x^2 p_y^2 V_{n1}^2 V_{n2}^2, \\ f_2 &= 1 - 2\eta_1 p_x^2 V_{n1}^2 - 2\eta_2 p_y^2 V_{n2}^2 + \left(4\eta_1\eta_2 - \eta_{xy}^2 \right) p_x^2 p_y^2 V_{n1}^2 V_{n2}^2, \end{aligned} \tag{B.16}$$

where V_0, V_{n1}, V_{n2} are vertical and corresponding NMO velocities defined in $[XOZ]$ and $[YOZ]$ planes. Anellipticity parameters η_1 and η_2 are defined in symmetry planes $[XOZ]$ and $[YOZ]$, respectively. The cross-term anellipticity parameter η_{xy} is defined as (Stovas, 2015)

$$\eta_{xy} = \sqrt{\frac{(1+2\eta_1)(1+2\eta_2)}{1+2\eta_3}} - 1, \tag{B.17}$$

where anellipticity parameter η_3 is defined in $[XOY]$ plane (Vasconcelos and Tsvankin, 2006).

The relative geometrical spreading for ORT medium is given by Stovas (2017)

$$\mathcal{L}_N = t_0 V_{n1} V_{n2} \frac{F_1 F_2}{f_2^2 f_1} \sqrt{f_m}, \tag{B.18}$$

where

$$\begin{aligned} f_m = {} & 1 + 4\eta_1 p_x^2 V_{n1}^2 + 4\eta_2 p_y^2 V_{n2}^2 - 6\eta_1 (1 + 2\eta_1) p_x^4 V_{n1}^4 - 6\eta_2 (1 + 2\eta_2) p_y^4 V_{n2}^4 \\ & + 2\left(8\eta_1\eta_2 - \eta_{xy}\left(3 + 5\eta_{xy}\right)\right) p_x^2 p_y^2 V_{n1}^2 V_{n2}^2 \\ & - 6(1 + 2\eta_1)\left(4\eta_1\eta_2 - \eta_{xy}^2\right) p_x^4 p_y^2 V_{n1}^4 V_{n2}^2 - 6(1 + 2\eta_2)\left(4\eta_1\eta_2 - \eta_{xy}^2\right) p_x^2 p_y^4 V_{n1}^2 V_{n2}^4 \\ & + 9\left((1 + 2\eta_1)(1 + 2\eta_2) - (1 + \eta_{xy})^2\right)\left(4\eta_1\eta_2 - \eta_{xy}^2\right) p_x^4 p_y^4 V_{n1}^4 V_{n2}^4. \end{aligned} \tag{B.19}$$

B.5 Direct type approximations for relative geometrical spreading in ORT model

In ORT model, the limited Taylor series for relative geometrical spreading up to the forth order in terms of two offset projections x and y is shown as

$$\mathcal{L}_N = a_{00} + a_{20} x^2 + a_{02} y^2 + a_{40} x^4 + a_{04} y^4 + a_{22} x^2 y^2, \tag{B.20}$$

where the series coefficients computed in zero offsets are given by

$$\begin{aligned} a_{00} &= t_0 V_{n1} V_{n2}, \\ a_{20} &= \frac{V_{n2}(1 + 6\eta_1 + \eta_{xy})}{t_0 V_{n1}}, \\ a_{02} &= \frac{V_{n1}(1 + 6\eta_2 + \eta_{xy})}{t_0 V_{n2}}, \\ a_{40} &= -\frac{9\eta_1 V_{n2}(1 + 4\eta_1)}{t_0^3 V_{n1}^3}, \\ a_{04} &= -\frac{9\eta_2 V_{n1}(1 + 4\eta_2)}{t_0^3 V_{n2}^3}, \\ a_{22} &= -\frac{9\left(-4\eta_1\eta_2 + \eta_{xy} + 2\eta_1\eta_{xy} + 2\eta_2\eta_{xy} + \eta_{xy}^2\right)}{t_0^3 V_{n1} V_{n2}}. \end{aligned} \tag{B.21}$$

We first define the direct rational form approximation similar to (Vasconcelos and Tsvankin, 2006) for the relative geometrical spreading by

$$\mathcal{L}_N = a_{00} + a_{20}x^2 + a_{02}y^2 + \frac{a_{40}x^4 + a_{04}y^4 + a_{22}x^2y^2}{1 + b_{20}x^2 + b_{02}y^2}, \tag{B.22}$$

where the coefficients a_{00}, a_{20}, a_{02}, a_{40}, a_{22} and a_{04} are given in equations (B.21), the coefficients b_{20} and b_{02} are computed separately from asymptotic behavior of $\mathcal{L}_N$ in $[XOZ]$ and $[YOZ]$ symmetry planes, respectively (Appendix B).

We also develop the GMA form approximation for the relative geometrical spreading:

$$\mathcal{L}_N = a_{00} + \tilde{A}_2(x,y) + \frac{2\tilde{A}_4(x,y)}{1 + \tilde{C}_2(x,y) + \sqrt{1 + 2\tilde{C}_2(x,y) + \tilde{C}_4(x,y)}}, \tag{B.23}$$

where

$$\begin{aligned} \tilde{A}_2 &= a_{20}x^2 + a_{02}y^2, \\ \tilde{A}_4 &= a_{40}x^4 + a_{22}x^2y^2 + a_{04}y^4, \\ \tilde{C}_2 &= c_{20}x^2 + c_{02}y^2, \\ \tilde{C}_4 &= c_{40}x^4 + c_{22}x^2y^2 + c_{04}y^4. \end{aligned} \tag{B.24}$$

The coefficients a_{00}, a_{20}, a_{02}, a_{40}, a_{22} and a_{04} are given in equations (B.21). The coefficients c_{20}, c_{40} and c_{02}, c_{04} are computed from two reference rays separately in $[XOZ]$ and $[YOZ]$ symmetry planes, respectively (Appendix C). Note that the rational type approximation can be easily converted from GMA type approximation by setting $c_{40} = c_{20}^2, c_{04} = c_{02}^2, c_{22} = 2c_{20}c_{02}$.

Similarly to the VTI case, we define two types of GMA form approximation for ORT model from two groups of reference rays: $\mathcal{L}_{N(GMA_X)}$ and $\mathcal{L}_{N(GMA_\infty)}$. For reference offsets case ($\mathcal{L}_{N(GMA_X)}$), we use two rays 1 and 2 with offsets $(d,0)$ and $(0,d)$ in two vertical symmetry planes and ray 3 with offset (d,d). The coefficients c_{20}, c_{40} and c_{02}, c_{04} are computed from the reference rays 1 and 2, respectively. The cross-term coefficient c_{22} is computed from ray

3. Another infinite offsets case ($\mathcal{L}_{N(GMA_\infty)}$) can be obtained by sending d to infinity for rays 1 and 2 (they become horizontal rays) and keeping finite d for ray 3. In order to see difference of selecting different d along ray 3, we introduce a homogeneous ORT model with the parameters: ($T_0 = 1s$, $V_{n1} = 2km/s$, $V_{n2} = 2.5km/s$, $\eta_1 = 0.2$,. $\eta_2 = 0.1$ and $\eta_{xy} = 0.15$) and show the relative error of $\mathcal{L}_{N(GMA_\infty)}$ selecting different d by $d = 2$ (top), $d = 4$ (middle) and $d = 10$ (bottom) in Figure B.2. The error is small for short offsets for the case $d = 2$, but increasing greatly along the offsets especially for the diagonal direction. The maximal error is increasing when we increase the value of d from the comparison between the cases $d = 4$ and $d = 10$.

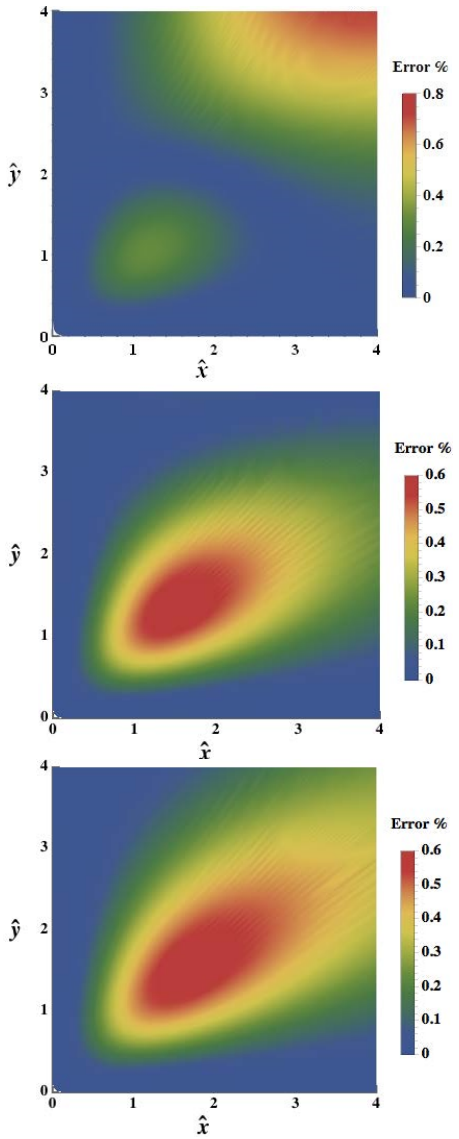

Figure B.2. The relative error in relative geometrical spreading $\mathcal{L}_{N(GMA_\infty)}$ using the constrain point at $d = 2$ (top), 4 (middle) and 10 (bottom).

For GMA type approximation computed from the finite-offset rays ($\mathcal{L}_{N(GMA_X)}$), the selection of the reference offsets depends on the acquisition part. When fixing the computation area, the certain reference offsets (X and Y) and the information at these offset are involved in the computation of the relative geometrical spreading. Since the information about the certain

offsets is obtained in advance from the acquisition process, the approximation $\mathcal{L}_{N(GMA_X)}$ using the certain reference offsets is more accurate and preferable.

B.6 Numerical examples

To test the accuracy of the proposed approximations, we compare our GMA type approximations ($\mathcal{L}_{N(GMA_X)}$ and $\mathcal{L}_{N(GMA_\infty)}$) with other approximations: traveltime based approximation (TBA) (Xu *et al.* 2005), indirect rational approximation (IRA) (Appendix D), direct rational form approximation (DRA) in equation (B.22) and anelliptic form approximation (AFA) (Xu *et al.* 2017) shown in Table B.2 in a homogeneous VTI, HTI, ORT and multilayered ORT models. Note that approximations TBA and IRA are all traveltime based approximation, the difference between them is the form of the traveltime approximation. We use the constrain point $d = 4$ in ray 3 for both two GMA type approximations: $\mathcal{L}_{N(GMA_X)}$ and $\mathcal{L}_{N(GMA_\infty)}$ for the following numerical examples in homogeneous VTI, HTI and ORT models. The exact results for relative geometrical spreading used in the numerical examples are obtained by dynamic ray tracing shown in parametric equations (B.14) and (B.15).

Homogeneous VTI model

We first consider a homogeneous VTI model which can be treated as a special case from ORT model with the parameters setting by: ($T_0 = 1s$, $V_{n1} = V_{n2} = V_n = 2km/s$, $\eta_1 = \eta_1 = \eta = 0.1$ and $\eta_{xy} = 2\eta = 0.2$). The relative error from the approximations TBA, IRA, DRA and AFA and two GMA type approximations $\mathcal{L}_{N(GMA_X)}$ and $\mathcal{L}_{N(GMA_\infty)}$ are shown in Figure B.3. One can see from the comparison that GMA type approximations are more accurate than other approximations while the approximation from the direct rational form is the worst. Among two GMA approximations, the one with reference offset $\mathcal{L}_{N(GMA_X)}$ is more accurate.

Homogeneous HTI model

The HTI model is obtained by using the model parameters: ($V_0 = 1.8\,km/s$, $z = 1.8\,km$, $V_{n1} = 2.2\,km/s$, $V_{n2} = V_0 = 1.8\,km/s$, $\eta_1 = 0.1$, $\eta_2 = 0$ and $\eta_{xy} = 0$), where V_0 is the vertical velocity and z is the depth associated with the vertical traveltime by $T_0 = z/V_0$. The relative error from TBA, IRA, DRA, AFA and two types of GMA form approximations are shown in Figure B.4. The GMA type approximations show several orders of magnitude more accurate than other approximations while the traveltime-based approximation TBA (Xu *et al*. 2005) is the worst.

Homogeneous ORT model

We use the homogeneous ORT model introduced above and show the relative error of geometrical spreading from TBA, IRA, DRA and AFA approximations and our proposed two GMA type approximations $\mathcal{L}_{N(GMA_X)}$ and $\mathcal{L}_{N(GMA_\infty)}$ in Figure B.5. One can tell from the comparison that the GMA type approximations are the most accurate ones, while the rational form approximation (DRA) is the worst. Compared with accuracy in GMA type approximation, anelliptic form approximation (AFA) is slightly less accurate. The approximations $\mathcal{L}_{N(GMA_X)}$ and $\mathcal{L}_{N(GMA_\infty)}$ result in almost the same accuracy.

Multi-layered ORT model

For the multilayered ORT model, we use a 3-layer ORT model with the parameters shown in Table B.3. We apply all mentioned approximations from the homogeneous ORT case to multilayered ORT model with the effective parameters computed from the Dix-type equations (Stovas, 2015):

$$
\begin{aligned}
\tilde{t}_0 &= \sum_{j=1}^{m} t_{0j}, \\
\tilde{V}_{n1} &= \sqrt{\frac{\sum_{j=1}^{m} V_{n1j}^2 t_{0j}}{\tilde{t}_0}}, \\
\tilde{V}_{n2} &= \sqrt{\frac{\sum_{j=1}^{m} V_{n2j}^2 t_{0j}}{\tilde{t}_0}}, \\
\tilde{\eta}_1 &= \frac{1}{8}\left(\frac{\sum_{j=1}^{m} (1+8\eta_{1j}) V_{n1j}^4 t_{0j}}{\tilde{V}_{n1}^4 \tilde{t}_0} - 1 \right), \\
\tilde{\eta}_2 &= \frac{1}{8}\left(\frac{\sum_{j=1}^{m} (1+8\eta_{2j}) V_{n2j}^4 t_{0j}}{\tilde{V}_{n2}^4 \tilde{t}_0} - 1 \right), \\
\tilde{\eta}_{xy} &= \frac{1}{4}\left(\frac{\sum_{j=1}^{m} (1+4\eta_{xyj}) V_{n1j}^2 V_{n2j}^2 t_{0j}}{\tilde{V}_{n1}^2 \tilde{V}_{n2}^2 \tilde{t}_0} - 1 \right),
\end{aligned}
\tag{B.25}
$$

where the symbols with index j denote the individual layer parameters, the symbols with tilde denote the effective parameters, m is the number of layers the wave passing through. Note that the expressions for geometrical spreading approximation we use are computed from homogeneous model with the effective model parameters computed from Dix-type equations. To compute the error for multi-layered case, the model parameters in exact expression (t_0, V_{n1}, V_{n2}, η_1, η_2 and η_{xy}) become depth dependent ($t_0[j]$, $V_{n1}[j]$, $V_{n2}[j]$, $\eta_1[j]$, $\eta_2[j]$ and $\eta_{xy}[j]$), and the exact geometrical spreading is computed from the integral for equations (B.18) along the depth.

We show the relative error of these corresponding approximations above versus offset-depth ratio in Figure B.6. One can see from the comparison that the GMA type approximations perform better accuracy than the others while the direct rational form approximation (DRA) is

the worst. The GMA type approximation computed from the reference normalized offset ($\mathcal{L}_{N(GMA_X)}$) performs the most accurate result among all approximations.

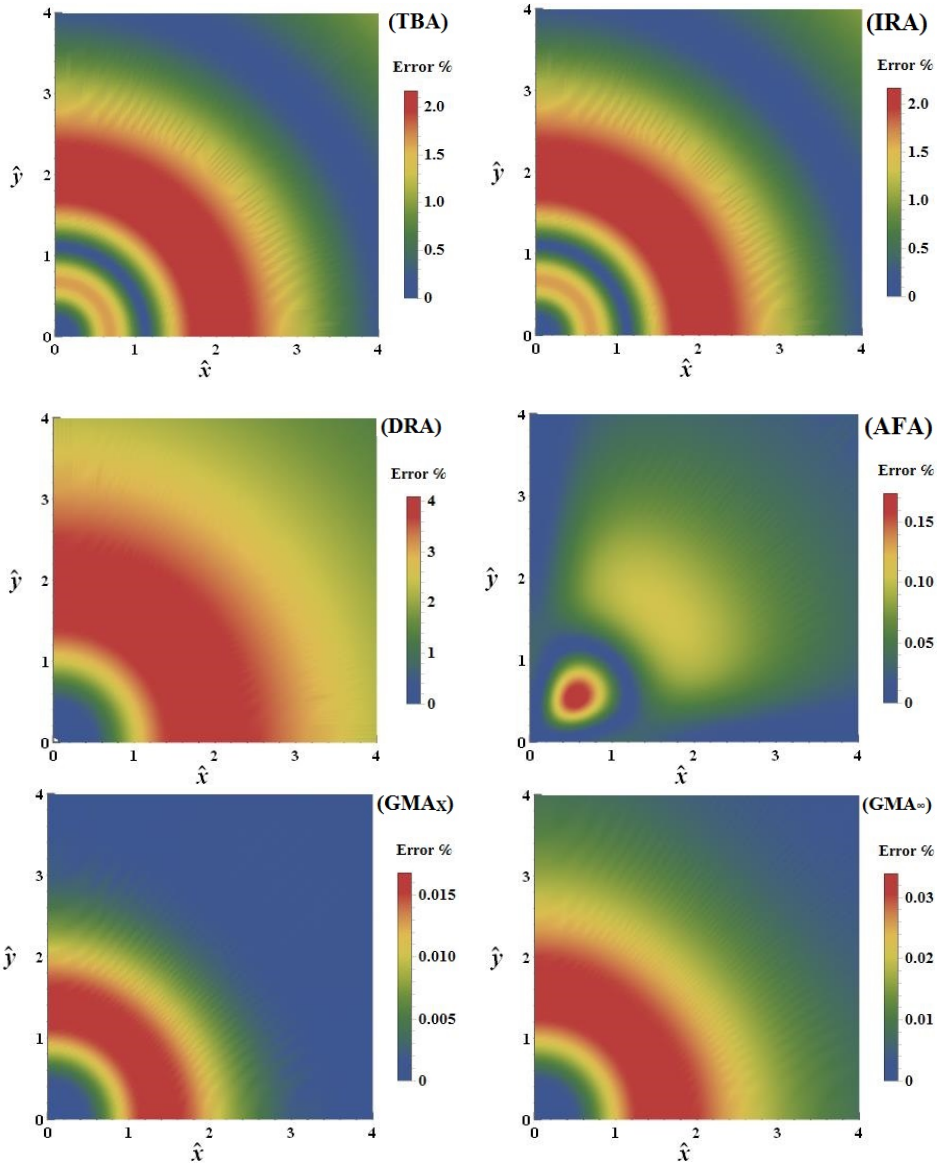

Figure B.3. The relative error in relative geometrical spreading from the traveltime based approximation (TBA) (Xu *et al*. 2005) (top, left), indirect rational approximation (IRA) (top, right), direct rational form approximation (DRA) (middle, left), anelliptic form approximation (AFA) (Xu *et al*. 2017) (middle, right), GMA form approximation GMA_X (bottom, left) and GMA_∞ (bottom, right) computed for a homogeneous VTI model.

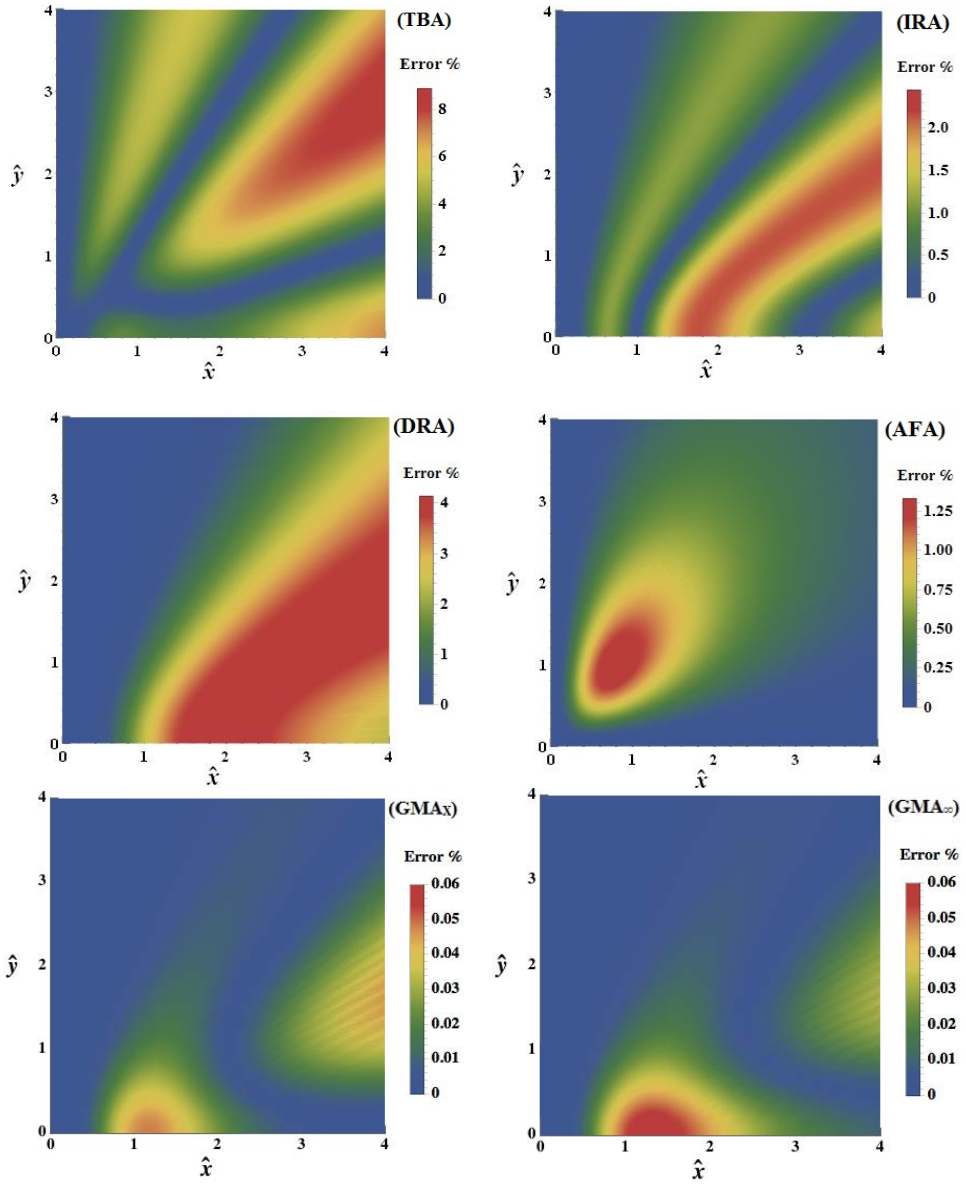

Figure B.4. The relative error in relative geometrical spreading from the traveltime based approximation (TBA) (Xu *et al*. 2005) (top, left), indirect rational approximation (IRA) (top, right), direct rational form approximation (DRA) (middle, left), anelliptic form approximation (AFA) (Xu *et al*. 2017) (middle, right), GMA form approximation GMA_X (bottom, left) and GMA_∞ (bottom, right) computed for a homogeneous HTI model.

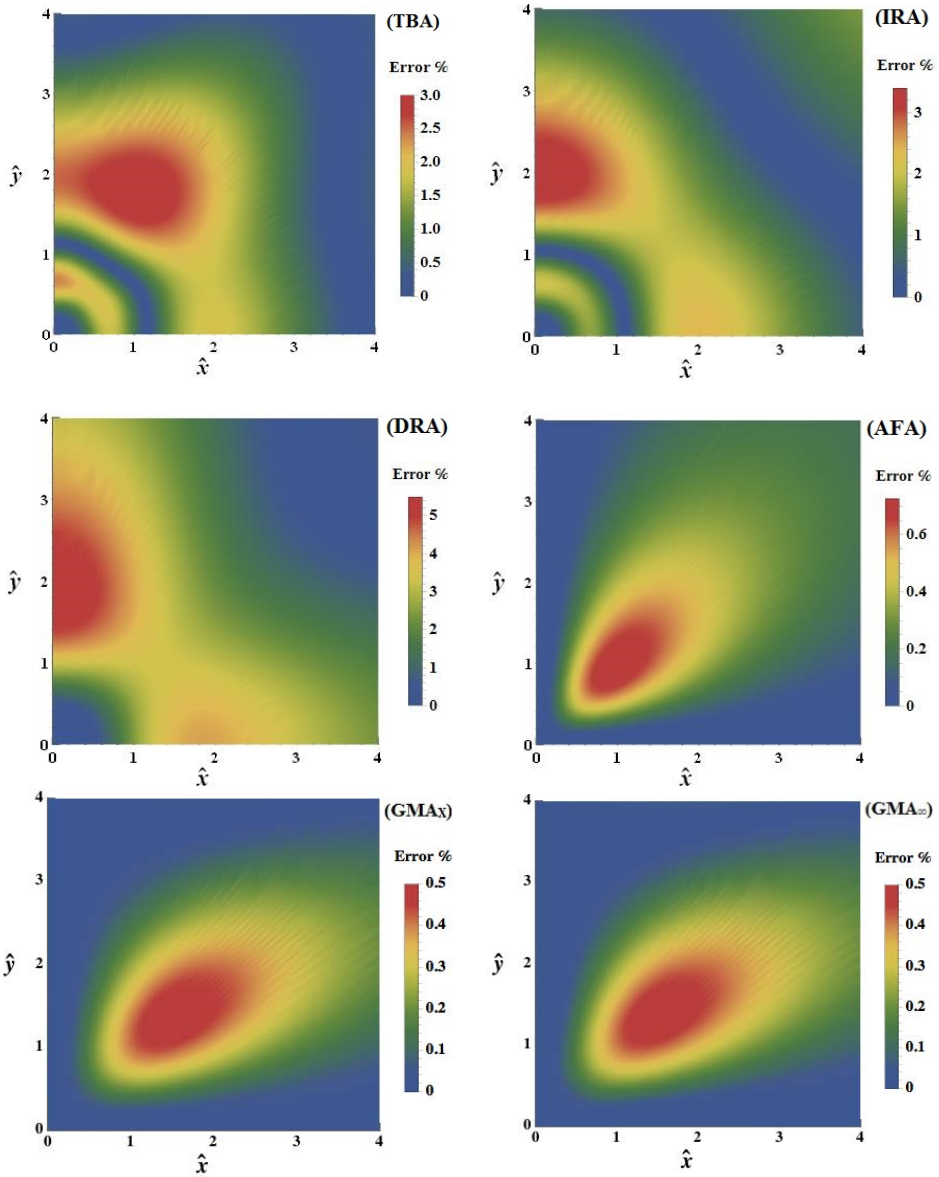

Figure B.5. The relative error in relative geometrical spreading from the traveltime based approximation (TBA) (Xu *et al*. 2005) (top, left), indirect rational approximation (IRA) (top, right), direct rational form approximation (DRA) (middle, left), anelliptic form approximation (AFA) (Xu *et al*. 2017) (middle, right), GMA form approximation GMA_X (bottom, left) and GMA_∞ (bottom, right) computed for a homogeneous ORT model.

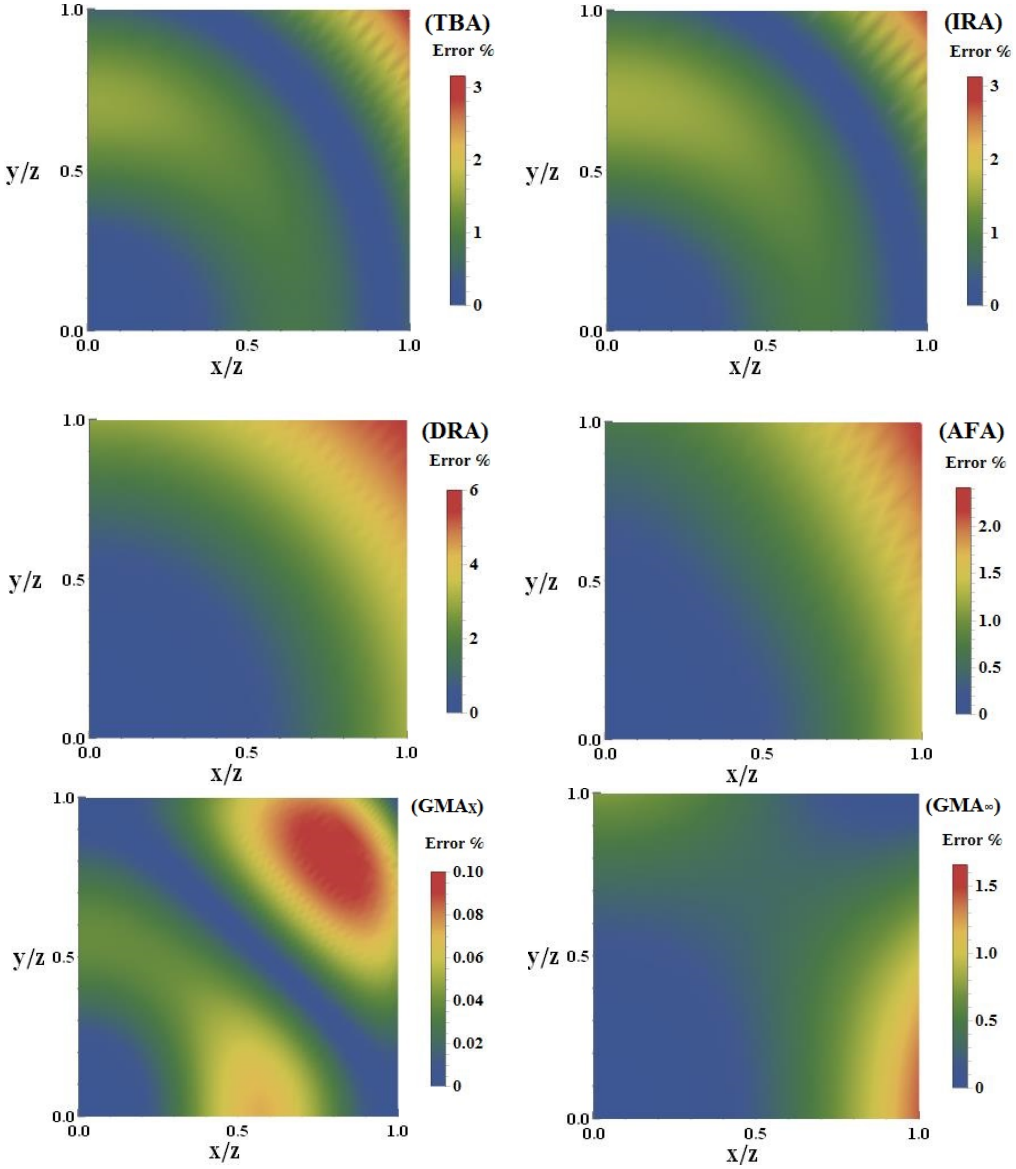

Figure B.6. The relative error in relative geometrical spreading from the traveltime based approximation (TBA) (Xu *et al*. 2005) (top, left), indirect rational approximation (IRA) (top, right), direct rational form approximation (DRA) (middle, left), anelliptic form approximation (AFA) (Xu *et al*. 2017) (middle, right), GMA form approximation GMA_X (bottom, left) and GMA_∞ (bottom, right) computed for a multilayered ORT model.

Geometrical spreading approximation	**Type**	**Form**
Traveltime based approximation (**TBA**)	Indirect	$\mathcal{L}_N = \left(\left(\frac{\partial^2 T}{\partial x^2} \frac{\partial^2 T}{\partial y^2} \right) - \left(\frac{\partial^2 T}{\partial x \partial y} \frac{\partial^2 T}{\partial y \partial x} \right) \right)^{-1/2}$ The traveltime approximation T is shown in Tsvankin and Thomsen (1994)
Indirect rational approximation (**IRA**)	Indirect	$\mathcal{L}_N = \left(\left(\frac{\partial^2 T}{\partial x^2} \frac{\partial^2 T}{\partial y^2} \right) - \left(\frac{\partial^2 T}{\partial x \partial y} \frac{\partial^2 T}{\partial y \partial x} \right) \right)^{-1/2}$ The rational traveltime approximation T is shown in Appendix D.
Direct rational approximation (**DRA**)	Direct	$\mathcal{L}_N = a_{00} + a_{20} x^2 + a_{02} y^2 + \frac{a_{40} x^4 + a_{04} y^4 + a_{22} x^2 y^2}{1 + b_{20} x^2 + b_{02} y^2}$, The coefficients are shown in equations (21) and (B4).
Anelliptic form approximation (**AFA**)	Direct	$\mathcal{L}_N = H(1 - \hat{S}) + \hat{S} \sqrt{H^2 + F}$, The anelliptic form geometrical spreading approximation is shown in Xu *et al* (2017).
GMA approximation with reference offset (**GMA$_X$**)	Direct	$\mathcal{L}_N = a_{00} + \tilde{A}_2(x,y) + \frac{2\tilde{A}_4(x,y)}{1 + \tilde{C}_2(x,y) + \sqrt{1 + 2\tilde{C}_2(x,y) + \tilde{C}_4(x,y)}}$ The coefficients are shown in equations (21) and (C2).
GMA approximation with infinite offset (**GMA$_\infty$**)	Direct	$\mathcal{L}_N = a_{00} + \tilde{A}_2(x,y) + \frac{2\tilde{A}_4(x,y)}{1 + \tilde{C}_2(x,y) + \sqrt{1 + 2\tilde{C}_2(x,y) + \tilde{C}_4(x,y)}}$, The coefficients are shown in equations (21) and (C3).

Table B.2. Six approximations for the relative geometrical spreading computed in the numerical examples.

Layer	$z(km)$	$V_0(km/s)$	$V_{n1}(km/s)$	$V_{n2}(km/s)$	η_1	η_2	η_{xy}
1	0.25	1.5	1.65	1.8	0.05	0.08	0.2
2	0.75	1.8	2	2.2	0.1	0.1	0.18
3	1	2	2.2	2.15	0.08	0.12	0.22

Table B.3. The model parameters in a multilayered ORT model.

B.7 Discussions

For multilayered case, the expressions for geometrical spreading approximation we use are computed from homogeneous model with the effective model parameters computed from Dix-type equations. Compared with the other cases, the GMA type approximation computed from infinite offset limit ($\mathcal{L}_{N(GMA_\infty)}$) and the anelliptic form approximation (AFA) are less accurate for multilayered case. That is because the coefficients in the approximations are computed from the horizontal ray (infinite offset), while, it is impossible to trace the horizontal rays for multilayered ORT case, which means that the assumption for infinite offset limit is not availed anymore. After using the Dix-type equations for effective model parameters, the approximations used for multi-layered ORT case are become effective homogeneous, while for the computation of the exact form, we still need to take the properties of each individual layer ($t_0[j]$, $V_{n1}[j]$, $V_{n2}[j]$, $\eta_1[j]$, $\eta_2[j]$ and $\eta_{xy}[j]$) into considersion that is different with the exact form calcualtion in homogeneous ORT case, which explains the difference in the error plot in Figure B.5 and Figure B.6.

For GMA type approximation computed from reference offset ($\mathcal{L}_{N(GMA_X)}$), the expression computed from homogeneous ORT model is still applicable since the information at certain reference offsets X and Y are needed for computation regardless the model is homogenous

or not that explains the more accurate result from $\mathcal{L}_{N(GMA_X)}$ compared with the horizontal rays case $\mathcal{L}_{N(GMA_\infty)}$ in multilayered ORT model in Figure B.6.

The application of GMA type approximation with the reference rays is not straight forward because the coefficients W_{X1}, W_{X2} and W_{Y1}, W_{Y2} are not available in the practical use. In order to compute them, the information about the traveltime function and its derivatives are required. For example, the coefficients W_{X1} and W_{X2} in $[XOZ]$ symmetry plane can be computed as follows. For W_{X1} can be obtained from corresponding value of $\mathcal{L}_N(X,0)$,

$$W_{X1} = \left(\frac{\partial^2 T}{\partial x^2}\frac{\partial^2 T}{\partial y^2} - \frac{\partial^2 T}{\partial x \partial y}\frac{\partial^2 T}{\partial y \partial x} \right)^{-1/2} \Bigg|_{x=X,y=0} . \tag{B.26}$$

The coefficient W_{X2} can be obtained by taking corresponding derivative $\partial \mathcal{L}_N(X,0)/\partial x$,

$$W_{X2} = \frac{\left(\frac{\partial^3 T}{\partial x^2 \partial y}\frac{\partial^2 T}{\partial y \partial x} + \frac{\partial^3 T}{\partial y \partial x^2}\frac{\partial^2 T}{\partial x \partial y} - \frac{\partial^3 T}{\partial x^3}\frac{\partial^2 T}{\partial y^2} - \frac{\partial^3 T}{\partial y^2 \partial x}\frac{\partial^2 T}{\partial x^2} \right)}{\left(\frac{\partial^2 T}{\partial x^2}\frac{\partial^2 T}{\partial y^2} - \frac{\partial^2 T}{\partial x \partial y}\frac{\partial^2 T}{\partial y \partial x} \right)^{3/2}} \Bigg|_{x=X,y=0} . \tag{B.27}$$

Note that computation in equations (B.26) and (B.27) requires information about traveltime derivatives up to the third order taken at the reference offset.

The VTI and HTI model can be considered as the special cases from the ORT model by resetting the model parameters: for VTI ($V_{n1} = V_{n2} = V_n$, $\eta_1 = \eta_1 = \eta$ and $\eta_{xy} = 2\eta$); for HTI ($V_{n2} = V_0$, $\eta_2 = 0$ and $\eta_{xy} = 0$). For GMA type approximation with reference rays $\mathcal{L}_{N(GMA_X)}$, the contribution is equivalent for the reference rays at $(d,0)$ and $(0,d)$ in VTI case and $(0,0)$ and $(0,d)$ in HTI case due to their equivalent properties, respectively.

B.8 Conclusions

We develop the direct rational and GMA type approximations for the relative geometrical spreading in a homogeneous ORT medium. The acoustic approximation is used to reduce the number of medium parameters that makes the GMA form of direct relative geometrical spreading approximation similar to the GMA traveltime approximation. Two types of GMA form approximations are defined from the reference offsets and the infinite offsets assumption, respectively. One horizontal ray in between the vertical symmetry planes is selected to compute the cross-term coefficients in the approximation. We also apply our approximations for a multilayered ORT model with the effective parameters computed from the Dix-type equations. In the numerical examples, we test our proposed approximations with other direct and indirect type (traveltime-based) approximations in a homogeneous VTI, HTI, ORT and multilayered ORT models. We show from the comparison in the numerical examples that our GMA type approximations perform the best regardless to the model.

B.9 Acknowledgments

We would like to acknowledge China Scholarship Council (CSC) and ROSE project for financial support. We also acknowledge Y. Sripanich and an anonymous reviewer for their valuable comments.

B.10 Appendix A

The GMA type approximations of the direct geometrical spreading in a VTI model.

The generalized nonhyperbolic moveout (GMA) approximation proposed by Fomel and Stovas (2010) is based on parameters computed from the zero-offset ray and the reference ray. The direct GMA type approximation of the relative geometrical spreading is defined by Xu and Stovas (2017)

$$\mathcal{L}_N = \mathcal{L}_0\left(1 + A_2\hat{x}^2 + \frac{2A_4\hat{x}^4}{1 + C_2\hat{x}^2 + \sqrt{1 + 2C_2\hat{x}^2 + C_4\hat{x}^4}}\right), \tag{B.A1}$$

where $\mathcal{L}_0 = t_0 V_n^2$, A_2 and A_4 are the Taylor series coefficients computed from zero offset limit given by

$$A_2 = 1 + 8\eta, A_4 = -9\eta(1 + 4\eta). \tag{B.A2}$$

For a horizontal reference ray, we define two asymptotic terms of geometrical spreading in GMA form at infinite offset,

$$\begin{aligned} &\lim_{\hat{x}\to\infty} \frac{\mathcal{L}_N}{\hat{x}^2} = m_2, \\ &\lim_{\hat{x}\to\infty} \left(\mathcal{L}_N - m_2\hat{x}^2\right) = m_0, \end{aligned} \tag{B.A3}$$

where m_0 and m_2 corresponds to the asymptotic intercept and asymptotic slope, respectively. Computing these limits gives

$$\begin{aligned} m_2 &= \frac{\mathcal{L}_0}{\sqrt{1 + 2\eta}}, \\ m_0 &= \mathcal{L}_0(1 + 6\eta)(1 + 2\eta)^{3/2}. \end{aligned} \tag{B.A4}$$

To compute these asymptotic parameters from proposed approximation (B.A1), we take the corresponding limits,

$$\begin{aligned} M_2 &= \lim_{\hat{x}\to\infty}\left(\frac{\mathcal{L}_N}{\hat{x}^2}\right) = \frac{\mathcal{L}_0\left(2A_4 + A_2(C_2 + \sqrt{C_4})\right)}{C_2 + \sqrt{C_4}}, \\ M_0 &= \lim_{\hat{x}\to\infty}\left(\mathcal{L}_N - M_2\hat{x}^2\right) = \mathcal{L}_0 + \frac{\mathcal{L}_0 A_2 - M_2}{\sqrt{C_4}}. \end{aligned} \tag{B.A5}$$

By fitting m_2 with M_2 and m_0 with M_0, respectively, we obtain the coefficients C_2 and C_4

$$C_2 = \frac{\mathcal{L}_0 A_2 - m_2}{\mathcal{L}_0 - m_0} - \frac{2\mathcal{L}_0 A_4}{\mathcal{L}_0 A_2 - m_2},$$
$$C_4 = \left(\frac{\mathcal{L}_0 A_2 - m_2}{\mathcal{L}_0 - m_0} \right)^2, \tag{B.A6}$$

substitute m_0 and m_2 from equations (A4) results in

$$C_2 = \frac{18\eta\sqrt{1+2\eta}(1+4\eta)}{\sqrt{1+2\eta}(1+8\eta)-1},$$
$$C_4 = \left(\frac{\sqrt{1+2\eta}(1+8\eta)-1}{\sqrt{1+2\eta}-(1+2\eta)^2(1+6\eta)} \right)^2. \tag{B.A7}$$

B.11 Appendix B

The direct rational form approximation for relative geometrical spreading in ORT model.

The rational approximation for geometrical spreading in a homogeneous ORT media is defined by

$$\mathcal{L}_N = a_{00} + a_{20}x^2 + a_{02}y^2 + \frac{a_{40}x^4 + a_{04}y^4 + a_{22}x^2y^2}{1 + b_{20}x^2 + b_{02}y^2}, \tag{B.B1}$$

where the series coefficients a_{00}, a_{20}, a_{02}, a_{40}, a_{22} and a_{04} are obtained from the

zero-offset expansion given in equations (B.25). Similar to the rational approximation in VTI case, we calculate the coefficients b_{20} and b_{02} separately from two VTI cases in two symmetry $[XOZ]$ and $[YOZ]$ planes, respectively.

In $[XOZ]$ plane, we calculate the asymptotic term at infinite offset limit by setting the slowness p_y into zero gives

$$m_x = \frac{(1+\eta_{xy})V_{n2}}{(1+2\eta_1)^{3/2}V_{n1}T_0}, \tag{B.B2}$$

and the term in $[YOZ]$ plane

$$m_y = \frac{(1+\eta_{xy})V_{n1}}{(1+2\eta_2)^{3/2}V_{n2}T_0}. \tag{B.B3}$$

The coefficients b_{20} and b_{02} are represented by the zero-offset coefficients and the infinite terms given by

$$b_{20} = \frac{a_{40}}{m_x - a_{20}},\ b_{02} = \frac{a_{04}}{m_y - a_{02}}. \tag{B.B4}$$

B.12 Appendix C

The direct GMA form approximation for relative geometrical spreading in an ORT model.

The GMA form approximation for the geometrical spreading given by

$$\begin{aligned}\mathcal{L}_N &= a_{00} + a_{20}x^2 + a_{02}y^2 \\ &+ \frac{2\left(a_{40}x^4 + a_{22}x^2y^2 + a_{04}y^4\right)}{1 + c_{20}x^2 + c_{02}y^2 + \sqrt{1 + 2\left(c_{20}x^2 + c_{02}y^2\right) + c_{40}x^4 + c_{22}x^2y^2 + c_{04}y^4}},\end{aligned} \tag{B.C1}$$

Similar to the rational form approximation, the coefficients a_{00}, a_{20}, a_{02}, a_{40}, a_{22} and a_{04} are obtained from the zero-offset expansion given in equations (B.21), the coefficients c_{20}, c_{02}, c_{40} and c_{04} are computed separately from two VTI cases in two symmetry $[XOZ]$ and $[YOZ]$ planes, respectively.

To compute the coefficients c_{20} and c_{40}, we use the similar approach as in the VTI case. For the given reference rays in $[XOZ]$ symmetry plane, we define $\mathcal{L}_N(\hat{x}, 0)$ and $d\mathcal{L}_N / d\hat{x}(\hat{x}, 0)$ by equations: $W_{X1} = \mathcal{L}_N(\hat{X}, 0)$ and $W_{X2} = d\mathcal{L}_N / d\hat{x}(\hat{X}, 0)$. The coefficients c_{20} and c_{40}, take the following form

$$
\begin{aligned}
c_{20} &= \frac{2\mathcal{L}_0 a_{20}\hat{X} - W_{X2}}{2\mathcal{L}_0\hat{X} - 2W_{X1}\hat{X} + W_{X2}\hat{X}^2} - \frac{2\mathcal{L}_0 a_{40}\hat{X}^2}{\mathcal{L}_0 - W_{X1} + \mathcal{L}_0 a_{20}\hat{X}^2}, \\
c_{40} &= \frac{\left(2\mathcal{L}_0 a_{20}\hat{X} - W_{X2}\right)^2}{\hat{X}^2\left(2\mathcal{L}_0 - 2W_{X1} + W_{X2}\hat{X}\right)^2} + \frac{4\mathcal{L}_0 a_{40}}{\mathcal{L}_0 - W_{X1} + \mathcal{L}_0 a_{20}\hat{X}^2}.
\end{aligned}
\tag{B.C2}
$$

For $[YOZ]$symmetry plane, for a normalized $\hat{Y}$, the coefficients c_{02} and c_{04} are computed from similar equations: $W_{Y1} = \mathcal{L}_N\left(0,\hat{Y}\right)$ and $W_{Y2} = d\mathcal{L}_N / d\hat{y}\left(0,\hat{Y}\right)$. They take the following form

$$
\begin{aligned}
c_{02} &= \frac{2\mathcal{L}_0 a_{02}\hat{Y} - W_{Y2}}{2\mathcal{L}_0\hat{Y} - 2W_{Y1}\hat{Y} + W_{Y2}\hat{Y}^2} - \frac{2\mathcal{L}_0 a_{04}\hat{Y}^2}{\mathcal{L}_0 - W_{Y1} + \mathcal{L}_0 a_{02}\hat{Y}^2}, \\
c_{04} &= \frac{\left(2\mathcal{L}_0 a_{02}\hat{Y} - W_{Y2}\right)^2}{\hat{Y}^2\left(2\mathcal{L}_0 - 2W_{Y1} + W_{Y2}\hat{Y}\right)^2} + \frac{4\mathcal{L}_0 a_{04}}{\mathcal{L}_0 - W_{Y1} + \mathcal{L}_0 a_{02}\hat{Y}^2}.
\end{aligned}
\tag{B.C3}
$$

For two horizontal reference rays, the coefficients c_{20}, c_{02}, c_{40} and c_{04} are computed from the asymptotic terms within two corresponding symmetry planes, respectively. In $[XOZ]$ symmetry plane, we calculate the asymptotic behavior at the infinite offsets limit, the asymptotic intercept and the slope are given by

$$
\begin{aligned}
S_{x2} &= \lim_{\hat{x}\to\infty}\left(\frac{\mathcal{L}_N(\hat{x},0)}{\hat{x}^2}\right) = -\frac{\left(1+\eta_{xy}\right)V_{n2}}{\left(1+2\eta_1\right)^{3/2}T_0 V_{n1}}. \\
S_{x0} &= \lim_{\hat{x}\to\infty}\left(\mathcal{L}_N(\hat{x},0) - S_{x2}\hat{x}^2\right) = -\sqrt{1+2\eta_1}\,T_0 V_{n1} V_{n2}\left(1+\eta_2\left(8+6\eta_{xy}\right)\right).
\end{aligned}
\tag{B.C4}
$$

The asymptotic intercept and the slope in $[YOZ]$ plane are given by

$$
\begin{aligned}
S_{y2} &= \lim_{\hat{y}\to\infty}\left(\frac{\mathcal{L}_N(0,\hat{y})}{\hat{y}^2}\right) = -\frac{\left(1+\eta_{xy}\right)V_{n1}}{\left(1+2\eta_2\right)^{3/2}T_0 V_{n2}}, \\
S_{y0} &= \lim_{\hat{y}\to\infty}\left(\mathcal{L}_N(0,\hat{y}) - S_{y2}\hat{y}^2\right) = -\sqrt{1+2\eta_2}\,T_0 V_{n1} V_{n2}\left(1+\eta_1\left(8+6\eta_{xy}\right)\right).
\end{aligned}
\tag{B.C5}
$$

The series coefficients c_{20}, c_{02}, c_{40} and c_{04} are subsequently given by the forms:

$$
\begin{aligned}
c_{20} &= \frac{a_{20}^2 - 2a_{00}a_{40} + 2a_{40}S_{x0} - 2a_{20}S_{x2} + S_{x2}^2}{\left(a_{00} - S_{x0}\right)\left(a_{20} - S_{x2}\right)}, \\
c_{20} &= \frac{a_{02}^2 - 2a_{00}a_{04} + 2a_{04}S_{y0} - 2a_{02}S_{y2} + S_{y2}^2}{\left(a_{00} - S_{y0}\right)\left(a_{02} - S_{y2}\right)}, \\
c_{40} &= \frac{\left(a_{20} - S_{x2}\right)^2}{\left(a_{00} - S_{x0}\right)^2}, \\
c_{40} &= \frac{\left(a_{02} - S_{y2}\right)^2}{\left(a_{00} - S_{y0}\right)^2},
\end{aligned}
\tag{B.C6}
$$

B.13 Appendix D

The indirect rational form approximation for relative geometrical spreading in an ORT model.

To compute the indirect rational form approximation for relative geometrical spreading in an ORT model, we first need to derive the traveltime approximation from the exact traveltime equation (Stovas, 2015):

$$
T(p_x, p_y) = \frac{T_0\left(F_1^2 p_y^2 V_{n2}^2 + F_2^2 p_x^2 V_{n1}^2 + f_1 f_2\right)}{f_1^{1/2} f_2^{3/2}},
\tag{B.D1}
$$

where the functions F_1, F_2, f_1 and f_2 are given in equations (B.16) in the main text.

A rational form similar to (Vasconcelos and Tsvankin, 2006) approximation for the traveltime in ORT model is defined by

$$
T_{RA}^2 = A_{00} + A_{20}x^2 + A_{02}y^2 + \frac{A_{40}x^4 + A_{22}x^2y^2 + A_{04}y^4}{1 + \left(B_{20}x^2 + B_{02}y^2\right)}
\tag{B.D2}
$$

where the coefficients A_{00}, A_{20}, A_{02}, A_{40}, A_{22} and A_{04} are computed from the Taylor series at zero offset are given by

$$A_0 = t_0^2, A_{20} = \frac{1}{V_{n1}^2}, A_{02} = \frac{1}{V_{n2}^2},$$
$$A_{40} = -\frac{2\eta_1}{t_0^2 V_{n1}^4}, A_{04} = -\frac{2\eta_2}{t_0^2 V_{n2}^4}, A_{22} = -\frac{2\eta_{xy}}{t_0^2 V_{n1}^2 V_{n2}^2}. \tag{B.D3}$$

Two asymptotic terms in $[XOZ]$ and $[YOZ]$ symmetry planes are computed respectively by infinite offsets limit given by

$$K_x = \lim_{x\to\infty} \frac{T^2(x,0)}{x^2} = \frac{1}{\left(1+2\eta_1 V_{n1}^2\right)},$$
$$K_y = \lim_{y\to\infty} \frac{T^2(0,y)}{y^2} = \frac{1}{\left(1+2\eta_2 V_{n2}^2\right)}. \tag{B.D4}$$

The remaining coefficients B_{20} and B_{02} are computed by

$$B_{20} = -\frac{A_{40}}{A_{20} - K_x}$$
$$B_{02} = -\frac{A_{04}}{A_{02} - K_y} \tag{B.D5}$$

We show the relative error from rational form approximation in equation (B.D2) and the one from Tsvankin and Thomsen (1994) using the homogeneous ORT model defined in the main text in Figure B.7. We can see that the proposed rational form approximation is more accurate than the one from Tsvankin and Thomsen (1994).

The indirect rational form approximation for relative geometrical spreading is given by the derivatives of traveltime approximation in equation (B.D2) with respect to the offsets given by

$$\mathcal{L}_N = \left(\left(\frac{\partial^2 T_{RA}}{\partial x^2}\frac{\partial^2 T_{RA}}{\partial y^2}\right) - \left(\frac{\partial^2 T_{RA}}{\partial x \partial y}\frac{\partial^2 T_{RA}}{\partial y \partial x}\right)\right)^{-1/2}. \tag{B.D6}$$

Note that the indirect rational form approximation in equation (B.D6) is algebraically complicated due to the second order derivatives.

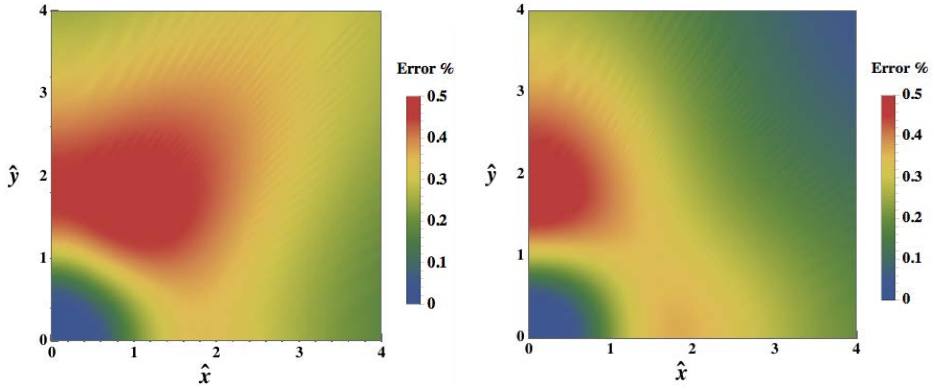

Figure B.7. The relative error in traveltime from rational form approximation shown in equation (B.D2) (left) and from Tsvankin and Thomsen (1994) (right) in a homogeneous ORT model.

List of Tables

List of Figures

Figure 2.10. The reflection from a circular reflector in a homogeneous anisotropic medium.

Figure 2.11. The difference between reflection and incidence group angle in EI model plotted versus ϕ_1 and α ($\delta = 0.1$ top, $\delta = 0.2$ bottom), $\phi_1 + \alpha \le \frac{\pi}{2}$.

Figure 2.12. The point diffractor in a homogeneous medium.

Figure 2.13. The CRS attributes for a point diffractor plotted versus m_0. The ISO, EI and VTI cases are shown by solid, dotted and dashed lines, respectively.

Figure 2.14. The estimated model parameters for a point diffractor plotted versus m_0. The ISO, EI and VTI cases are shown by solid, dotted and dashed lines, respectively.

Figure 2.15. The sensitivity coefficients for anisotropy parameters δ and η, shown by solid, dotted lines, respectively, and plotted versus m_0. The corresponding CRS attributes are $\hat{R}_{NIP}$ (top), $\hat{R}_N$ (middle) and $\sin\hat{\beta}$ (bottom).

Figure 2.16. The sensitivity coefficients for anisotropy parameters δ and η, shown by solid, dotted lines, respectively, and plotted versus m_0. The corresponding estimates for isotropic model parameters are $\hat{R}$ (top), $\hat{V}$ (middle) and $\hat{z}_0$ (bottom).

Figure 3.1. Ray trajectory of diving wave in a factorized VTI medium.

Figure 3.2. Change in ray trajectory due to perturbations in V_0, G, ε and η, respectively. The model parameters are $V_0 = 2\,km/s$, $G = 0.5\,s^{-1}$, $\varepsilon = 0.2$ and $\eta = 0.2$ with perturbations of $\Delta V_0 = \pm 0.2\,km/s$, $\Delta G = \pm 0.1\,s^{-1}$, $\Delta\varepsilon = \pm 0.1$ and $\Delta\eta = \pm 0.1$.

Figure 3.3. Diving-wave imaging moveout. (imaging point shift from the turning point). The ray trajectories in factorized VTI and isotropic media are shown by solid and dashed lines, respectively.

Figure 3.4. Exact imaging moveout with the perturbations in V_0 and G and anisotropy parameters ε and η. The parameters are $V_0 = 2\,km/s$, $G = 0.5\,s^{-1}$, $\varepsilon = 0.3$ and $\eta = 0.15$, and with the perturbations are $\Delta V_0 = \pm 0.5\,km/s$, $\Delta G = \pm 0.2\,s^{-1}$, $\Delta\varepsilon = \pm 0.1$ and $\Delta\eta = \pm 0.1$.

Figure 3.5. The limited Taylor series approximations from equation (3.11) (left) and their errors (right). The one-, two-, three- and four-term approximations are shown by large dashed, tiny dashed, dotted and dash-dotted lines, respectively. The exact imaging moveout curve is

shown by solid line. The parameters are $V_0 = 2\ km/s$, $G = 1.5\ s^{-1}$, $\varepsilon = 0.22$ and $\eta = 0.1$. The error in imaging moveout is $S = \Delta x_{\mathbf{exact}}(z_p) - \Delta x_{\mathbf{app}}(z_p)$.

Figure 3.6. The imaging moveout of three types of Padé approximation $P[2,2]$, $P[2,3]$, $P[3,3]$ (left) and their errors (right) are shown by dashed, dotted and dash-dotted lines, respectively. The exact imaging moveout curve is shown by solid line.

Figure 3.7. The imaging moveout of two rational approximations in equations (3.15) and (3.16) and their errors are shown in dashed and dotted lines, respectively. The exact imaging moveout curve is shown by solid line.

Figure 3.8. (a) The common shot gather for the diving wave from the synthetic data with the parameters $V_0 = 2\ km/s$, $G_1 = 1.5\ s^{-1}$, $\varepsilon = 0.22$ and $\eta = 0.1$. (b) The common shot gather for the diving wave from the synthetic data with the parameters $V_0 = 2\ km/s$, $G_2 = 2\ s^{-1}$, $\varepsilon = 0.22$ and $\eta = 0.1$.

Figure 3.9. The common image gather for the diving wave when applying the anisotropic RTM with the accurate parameters.

Figure 3.10. (a) The common image gather when using the isotropic RTM with parameters $V_0 = 2\ km/s$, $G_1 = 1.5\ s^{-1}$, $\varepsilon = 0.22$ and $\eta = 0.1$. (b) The common image gather when using the isotropic RTM with parameters $V_0 = 2\ km/s$, $G_2 = 2\ s^{-1}$, $\varepsilon = 0.22$ and $\eta = 0.1$. We overlay the residual curve predicted by the imaging moveout from rational approximation R_2 in equation (3.16).

Figure 3.11. The semblance plots for different parameterizations computed for factorized model with $G_1 = 1.5 s^{-1}$ (a) V_N-fixed, ε, η; (b) V_N-fixed, ε, δ; (c) V_0-fixed, δ, V_H; (d) V_N-fixed, ε, V_H. The anisotropy parameters can be evaluated from the coordinates of the maximal value of the semblance plot.

Figure 3.12. The semblance plots for different parameterizations computed for factorized model with $G_1 = 2 s^{-1}$ (a) V_N-fixed, ε, η; (b) V_N-fixed, ε, δ; (c) V_0-fixed, δ, V_H; (d) V_N-fixed, ε, V_H. The anisotropy parameters can be evaluated from the coordinates of the maximal value of the semblance plot.

Figure 3.13. The ray trajectory of the diving waves.

Figure 3.14. Subsurface image gathers in offset pulled from left (a) (4400m) and right (b) (4600m) of the model migrated with the correct velocity.

Figure 4.1. The unsmoothed and smoothed composite parameters (left). The same composite parameter with compensation functions (right). The unsmoothed and smoothed parameters are shown by solid and dashed lines, respectively.

Figure 4.2. The composite parameters m_1 (top), m_2 (middle) and m_3 (bottom) before and after smoothing for VTI model. The unsmoothed and smoothed parameters are shown by solid and dashed lines, respectively.

Figure 4.3. The model parameters V_0 (top), V_{nmo} (middle) and η (bottom) before and after smoothing for VTI model. The unsmoothed and smoothed parameters are shown by solid and dashed lines, respectively.

Figure 4.4. The kinematic parameters V_{nmo} (top) and η (bottom) computed for isotropic model.

Figure 4.5. The smoothing induced anisotropy parameters δ (top) and ε (bottom) computed for isotropic model.

Figure 4.6. The induced anellipticity from EI (solid line) and ISO (dashed line) models.

Figure 4.7. The traveltime error between two models-smoothed and unsmoothed for VTI, elliptical isotropic (EI) and the isotropic (ISO) cases shown by solid, dashed and dotted lines, respectively.

Figure 4.8. The composite parameters before and after smoothing for ORT model. The unsmoothed and smoothed parameters are shown by solid and dashed lines, respectively.

Figure 4.9. The model parameters V_0 (top), V_{nmo1} (middle) and V_{nmo2} (bottom) before and after smoothing for ORT model. The unsmoothed and smoothed parameters are shown by solid and dashed lines, respectively.

Figure 4.10. Four anellipticity parameters before and after smoothing for ORT model. The unsmoothed and smoothed parameters are shown by solid and dashed lines, respectively.

Figure 4.11. The composite parameters before and after smoothing for ORT_ϕ model. The unsmoothed and smoothed parameters are shown by solid and dashed lines, respectively.

Figure 4.12. The effective velocities and effective azimuth before and after smoothing for ORT_ϕ model. The unsmoothed and smoothed parameters are shown by solid and dashed lines, respectively.

Figure 4. 13. Four anellipticity parameters before and after smoothing for ORT_ϕ model. The unsmoothed and smoothed parameters are shown by solid and dashed lines, respectively.

Figure 4.14. The PTS results in smoothing induced anellipticity, η_1 (top), η_2 (middle) and η_{xy} (bottom). The anellipticity from the ORT model and ORT_ϕ model are shown in dashed and dotted lines, respectively.

Figure 4.15. The traveltime error surface for ORT model (left) and EI model (right).

Figure 4.16. The traveltime error surface for ORT_ϕ model (top) and EI_ϕ model (bottom).

Figure 4.17. The traveltime error surface using conventional smoothing for ORT model (top) and EI model (bottom).

Figure 4.18. The traveltime error surface using conventional smoothing for ORT_ϕ model (top) and EI_ϕ model (bottom).

Figure 5.1. Sketch for cross-term anellipticity parameters: η_{xy}, η_{xz} and η_{yz} (left) and cross-term NMO velocities: V_{12}, V_{13} and V_{23} (right) in ORT model.

Figure 5.2. Sketch for non-symmetric parameterizations for acoustic ORT model defined by Cases A-D.

Figure 5.3. Sketch for symmetric parameterizations for acoustic ORT model defined by Cases E-H.

Figure 5.4. The first order perturbation coefficients a_i (Case H). Coefficients a_1, a_2 and a_3 are shown in left, middle and right, respectively.

Figure 5.5. The quadratic perturbation coefficients b_{ii} (Case H). Coefficients b_{11}, b_{22} and b_{33} are shown in left, middle and right, respectively.

Figure 5.6. The cross-term perturbation coefficients $b_{ij},(i \neq j)$ (Case H). Coefficients b_{12}, b_{13} and b_{23} are shown in left, middle and right, respectively.

Figure 5.7. The first order sensitivity coefficients $\hat{a}_i$ in Case H for short offset (left) ($\theta \in (0,30^\circ)$), intermediate offset (middle) ($\theta \in (30^\circ,60^\circ)$), and far offset (right) ($\theta \in (60^\circ,90^\circ)$). The coefficients a_1, a_2 and a_3 are shown by blue, red and black colors, respectively.

Figure 5.8. The quadratic sensitivity coefficients $\hat{b}_{ii}$ in Case H for short offset (left) ($\theta \in (0,30^\circ)$), intermediate offset (middle) ($\theta \in (30^\circ,60^\circ)$), and far offset (right) ($\theta \in (60^\circ,90^\circ)$). The coefficients b_{11}, b_{22} and b_{33} are shown by blue, red and black colors, respectively.

Figure 5.9. The cross-term sensitivity coefficients $b_{ij},(i \neq j)$ in Case H for short offset (left) ($\theta \in (0,30^\circ)$), intermediate offset (middle) ($\theta \in (30^\circ,60^\circ)$), and far offset (right) ($\theta \in (60^\circ,90^\circ)$). The coefficients b_{12}, b_{13} and b_{23} are shown by blue, red and black colors, respectively.

Figure 5.10. The overall sensitivity coefficients: first order (left) and second order (right) using parameterization Case H. The coefficients $\hat{A}_1$, $\hat{A}_2$ and $\hat{A}_3$ are shown from left to right. The second order coefficients are composed in matrix form with indices $1 \equiv \eta_{xy}, 2 \equiv \eta_{xz}, 3 \equiv \eta_{yz}$.

Figure 5.11. The second order overall sensitivity coefficients $\hat{B}_{ij}$ using non-symmetric parameterizations Cases A-D. The second order coefficients are composed in matrix form with indices $1 \equiv \eta_1, 2 \equiv \eta_2, 3 \equiv \eta_3$ for Case A, $1 \equiv \eta_1, 2 \equiv \eta_2, 3 \equiv \eta_{xy}$ for Cases B and D, $1 \equiv \eta_{xy}, 2 \equiv \eta_{xz}, 3 \equiv \eta_{yz}$ for Case C.

Figure 5.12. The second order overall sensitivity coefficients $\hat{B}_{ij}$ using symmetric parameterizations Cases E-H. The second order coefficients are composed in matrix form with indices $1 \equiv \eta_1, 2 \equiv \eta_2, 3 \equiv \eta_3$ for Cases E and G, $1 \equiv \eta_{xy}, 2 \equiv \eta_{xz}, 3 \equiv \eta_{yz}$ for Cases F and H.

Figure 5.13. The relative error of perturbation series (left) and the Shanks transform (right) for traveltime with parameterization Case H.

Figure 5.14. The relative error in traveltime using the hyperboloid approximation with vertical and two NMO velocities (left), vertical and two horizontal velocities (middle) and three cross-term NMO velocities (right).

Figure 5.15. The relative error in traveltime of the Shanks transform for parameterizations from Cases A-D.

Figure 5.16. The relative error in traveltime of the Shanks transform for parameterizations from Cases E-H.

Figure 6.1. The location of fitting indices q_1, q_3, s_1 and s_3 in a homogeneous VTI model.

Figure 6.2. The sensitivity of coefficients q_1, q_3, s_1 and s_3 versus anellipticity η.

Figure 6.3. The relative error for anelliptic (solid) and GMA form (dashed) approximation for the relative geometrical spreading in a homogeneous VTI medium.

Figure 6.4. The relative error for anelliptic (solid) and GMA form (dashed) approximation for the relative geometrical spreading in a multi-layered VTI medium.

Figure 6.5. The location of fitting indices $Q_{ij}, (i \neq j = 1,2,3)$ and $S_{ij}, (i \neq j = 1,2,3)$ in a homogeneous ORT model.

Figure 6.6. Rotation from $[X, Z]$ symmetry plane to $[X, Y]$ symmetry plane.

Figutre 6.7. The relative error of the relative geometrical spreading for a homegeneous ORT model by using the traveltime based approximation Xu *et al* (2005) (top), indierct rational approximaiton (middle) and anelliptic approximation (bottom).

Figutre 6.8. The relative error of the relative geometrical spreading for a multi-layered ORT model by using the traveltime based approximation Xu *et al* (2005) (top), indierct rational approximaiton (middle) and anelliptic approximation (bottom).

Figure 7.1. The first Fresnel zone diagram in represented by the depth (top) and traveltime (bottom).

Figure 7.2. The diagram showing the Fresnel zone in an isotropic medium.

Figure 7.3. The radius of Fresnel zone for P-wave in a homogeneous ISO and VTI medium.

Figure 7.4. The relative error in Fresnel radius versus the corresponding traveltime (left), depth (middle) and frequency (right) using four types of approximation in VTI model. (Note that the Fresnel zone varies with depth at frequency $f = 30Hz$ and the Fresnel zone varies with frequency at depth $z = 2km$).

Figure 7.5. The Fresnel radius using second order Shanks transform approximation X_{S2} versus anisotropy parameters δ (with $\eta = 0.2$) and η (with $\delta = 0.1$).

Figure 7.6. The radius of Fresnel zone in ISO and VTI models versus traveltime (left), depth (middle) and Frequency (right). The Fresnel radius computed from ISO and VTI model is shown by black and blue colors, respectively. (Note that the Fresnel zone varies with depth at frequency $f = 30Hz$; The Fresnel zone varies with frequency at depth $z = 2km$).

Figure 7.7. The Fresnel zone in ISO and VTI model. The Fresnel zone computed from ISO and VTI model is shown by black and blue colors, respectively.

Figure 7.8. The Fresnel zone computed for a homogeneous ORT model. The model parameters are: $V_0 = 2km/s$, $V_{n1} = 2.2km/s$, $V_{n2} = 2.4km/s$, $\eta_1 = 0.2$, $\eta_2 = 0.15$, $\eta_{xy} = 0.2$ and $f = 30Hz$. The depth of the horizontal reflector is $z = 2km$. The Fresnel zone in ORT model has a quasi-elliptical shape.

Figure 7.9. The sensitivity computed from first order (left), quadratic (middle) and cross-term coefficients in equation (7.15) in the perturbation series for Fresnel zone versus the group azimuth. The depth of the horizontal reflector is $z = 2km$.

Figure 7.10. The contour plot of error in R_F from two approximations for ORT model plotted versus corresponding traveltime and the group azimuth (top) and depth and the group azimuth (bottom). The perturbation series approximation and Shanks transform are shown in left and right, respectively. The model parameters are given in caption for Figure 7.8.

Figure 7.11. The contour plot of error in R_F from two approximations for ORT model plotted versus corresponding traveltime and the group azimuth (top) and depth and the group azimuth (bottom). The perturbation series approximation and Shanks transform are shown in left and right, respectively. The ORT model parameters are defined with the velocities specified in the caption for Figure 7.8 and the higher anellipticity parameters: $\eta_1 = 0.4$, $\eta_2 = 0.3$ and $\eta_{xy} = 0.4$.

Figure 7.12. The contour plot of error in R_F from two approximations for ORT model plotted versus corresponding traveltime and the group azimuth (top) and depth and the group azimuth (bottom). The perturbation series approximation and Shanks transform are shown in left and right, respectively. The ORT model parameters are defined with the velocities specified in the caption for Figure 7.8 and the negative anellipticity parameters: $\eta_1 = -0.2$, $\eta_2 = -0.15$ and $\eta_{xy} = -0.2$.

Figure 7.13. The Fresnel zone computed for ORT model for different traveltime (left), depth (middle) and frequency (right) using the ORT model with parameters given in the caption for Figure 7.8.

Figure 7.14. The shape of the Fresnel zone computed for ISO, EI and ORT model. The depth of the horizontal reflector is $z = 2km$.

Figure 7.15. The diagram showing the Fresnel zone in an anisotropic medium. Angle θ_1 and θ_2 are phase angles measured in corresponding points at wave-fronts $t = t_0$ and $t = t_0 + \Delta t$, respectively.

Figure 7.16. The contour plot of error in R_F from two approximations for ORT model plotted versus corresponding traveltime and the group azimuth (top) and depth and the group azimuth (bottom). The perturbation series approximation and Shanks transform are shown in left and right, respectively. The ORT model parameters are: (Top) $t_0 = 0.6s$, $V_{n1} = 2.2km/s$, $V_{n2} = 2.4km/s$, $\eta_1 = 0.2$, $\eta_2 = 0.15$ and $\eta_{xy} = 0.2$; (Bottom): $V_0 = 2km/s$, $V_{n1} = 2.2km/s$, $V_{n2} = 2.4km/s$, $\eta_1 = 0.2$, $\eta_2 = 0.15$, $\eta_{xy} = 0.2$ and $f = 10Hz$.

Figure 7.17. The sketch showing the Fresnel zone for a dip reflector in a homogeneous VTI model.

Figure A.1. The slowness curve for VTI model. p and q are the horizontal and vertical slowness, respectively. The exact one, the approximations by vertical velocity and NMO velocity, and by vertical velocity and horizontal velocity are shown by solid, dashed and dotted lines, respectively.

Figure A.2. The traveltime error from hyperbolic moveout approximations using two background models in VTI media. The results using NMO and horizontal velocities are shown by solid and dashed lines, respectively.

Figure A.3. The relative traveltime error from non-hyperblic approximations in VTI media with $\eta = 0.1$ (left) and $\eta = 0.2$ (right). The results from the GMA, Alkhalifah (2011) approximation, the first- and second-order Shanks transform (equations (A.8)) are shown by dotted, dotdashed, dashed and solid lines, respectively. $\hat{x}$ is the normalized offset.

Figure A.4. The relative traveltime error with offset and anellipticity parameter η using the second-order Shanks transform τ_{S2}.

Figure A.5. The first order coefficients a_1^D (Top), a_2^D (Middle) and a_{xy}^D (Bottom) computed from equations (A.C8) in ORT model.

Figure A.6. The second order coefficients b_{11}^D (Top), b_{22}^D (Middle) and b_{xyxy}^D (Bottom) computed from equations (A.C8) in ORT model.

Figure A.7. The cross term coefficients b_{12}^D (Top), b_{1xy}^D (Middle) and b_{2xy}^D (Bottom) computed from equations (A.C8) in ORT model.

Figure A.8. The azimuth-dependent anellipticity from equation (A.15) in ORT model.

Figure A.9. The relative traveltime error for ORT model by using the perturbation series approximation in equation (A.C7) (Top) and the one after Shanks transform in equation (A.17) (Bottom).

Figure A.10. The relative traveltime error for ORT model by using Shanks transform based on different parameterizations (cases A, B, C and D correspond to the ones specified in the main text).

Figure A.11. The relative traveltime error for ORT model by using the approximations from Sripanich and Fomel (2015) (Top) and Hao and Stovas (2016) (Bottom).

Figure B.1. The relative error in relative geometrical spreading of two type of GMA approximation in homogeneous (left) and multi-layered (right) VTI models. The result from GMA_∞ and GMA_X are computed from infinite and reference offset limit and shown by solid and dashed lines, respectively. Note that normalized offset $\hat{x} = x/(t_0 V_n)$.

Figure B.2. The relative error in relative geometrical spreading $\mathcal{L}_{N(GMA_\infty)}$ using the constrain point at $d = 2$ (top), 4 (middle) and 10 (bottom).

Figure B.3. The relative error in relative geometrical spreading from the traveltime based approximation (TBA) (Xu *et al*. 2005) (top, left), indirect rational approximation (IRA) (top, right), direct rational form approximation (DRA) (middle, left), anelliptic form approximation (AFA) (Xu *et al*. 2017) (middle, right), GMA form approximation GMA_X (bottom, left) and GMA_∞ (bottom, right) computed for a homogeneous VTI model.

Figure B.4. The relative error in relative geometrical spreading from the traveltime based approximation (TBA) (Xu *et al*. 2005) (top, left), indirect rational approximation (IRA) (top, right), direct rational form approximation (DRA) (middle, left), anelliptic form approximation (AFA) (Xu *et al*. 2017) (middle, right), GMA form approximation GMA_X (bottom, left) and GMA_∞ (bottom, right) computed for a homogeneous HTI model.

Figure B.5. The relative error in relative geometrical spreading from the traveltime based approximation (TBA) (Xu *et al*. 2005) (top, left), indirect rational approximation (IRA) (top, right), direct rational form approximation (DRA) (middle, left), anelliptic form approximation (AFA) (Xu *et al*. 2017) (middle, right), GMA form approximation GMA_X (bottom, left) and GMA_∞ (bottom, right) computed for a homogeneous ORT model.

Figure B.6. The relative error in relative geometrical spreading from the traveltime based approximation (TBA) (Xu *et al*. 2005) (top, left), indirect rational approximation (IRA) (top, right), direct rational form approximation (DRA) (middle, left), anelliptic form approximation (AFA) (Xu *et al*. 2017) (middle, right), GMA form approximation GMA_X (bottom, left) and GMA_∞ (bottom, right) computed for a multilayered ORT model.

Figure B.7. The relative error in traveltime from rational form approximation shown in equation (B.D2) (left) and from Tsvankin and Thomsen (1994) (right) in a homogeneous ORT model.

References

Alkhalifah, T. 1995, Efficient synthetic-seismogram generation in transversely isotropic, inhomogeneous media. Geophysics **60**, 1139-1150.

Alkhalifah, T. and R.-É. Plessix, 2014, A recipe for practical full-waveform inversion in anisotropic media: An analytical parameter resolution study. Geophysics **79**, R91-R101.

Alkhalifah, T., 1998, Acoustic approximations for processing in transversely isotropic media: Geophysics, **63,** 623-631.

Alkhalifah, T., 2000, An acoustic wave equation for anisotropic media: Geophysics, **65**, 1239-1250.

Alkhalifah, T., 2003, An acoustic wave equation for orthorhombic anisotropy: Geophysics, **68**, 1169-1172.

Alkhalifah, T., 2011, Scanning anisotropy parameters in complex media: Geophysics, **76**, U13–U22.

Alkhalifah, T., 2013, Traveltime approximations for inhomogeneous transversely isotropic media with a horizontal symmetry axis: Geophysical Prospecting, 61, 495–503

Alkhalifah, T., and I. Tsvankin, 1995, Velocity analysis for transversely isotropic media: Geophysics, **60**, 1550–1566.

Alkhalifah, T., and R.-É. Plessix, 2014, A recipe for practical full-waveform inversion in anisotropic media: An analytical parameter resolution study: Geophysics, **79**, R91–R101

Baina, R., E. Zamboni, and G. Lambaré, 2006, How to cope with smoothing effect in ray based PSDM: 68th EAGE Conference and Exhibition, Extended Abstracts.

Baker, G. A., J. Gammel, and J. G. Wills, 1961, An investigation of the applicability of the Padé approximant method: Journal of Mathematical Analysis and Applications, **2**, 405–418.

Baykulov, M., and D. Gajewski, 2009, Prestack seismic data enhancement with partial common-reflection-surface (CRS) stack: Geophysics, **74**, V49-V58.

Bender, C. M., and S. A. Orszag, 1978, Advanced mathematical methods for scientists and engineers: McGraw-Hill. ISBN 978-0-387-98931-0.

Červený, V., 2001, Seismic Ray Theory: Cambridge Univ. Press, Cambridge.

Červený, V., and J. Soares, 1992, Fresnel volume ray-tracing: Geophysics, **57**, 902–915.

Crampin, S., 1984, An introduction to wave propagation in anisotropic media: Geophysical Journal International, 76, 17-28.

Crampin, S., 1987, The basis for earthquake prediction: Geophysical Journal International, 92, 331-347.

Dix, C. H., 1955, Seismic velocities from surface measurements: Geophysics, **20**, 68-86.

Duveneck, E., 2004, Velocity model estimation with data-derived wavefront attributes: Geophysics, **69**, 265-274.

Eaton, D., W., Stewart, and M. P. Harrison, 1991, The Fresnel zone for P-SV waves: Geophysics, **56**, 360-364.

Favretto-Cristini, N., P. Cristini, and E. deBazelaire, 2007a, Influence on the interface Fresnel zone on the reflected P-wave amplitude modelling: Geophysical Journal International, **171**, 841–846.

Favretto-Cristini, N., P. Cristini, and E. deBazelaire, 2007b, Some reflections on reflectors and wave amplitudes: Acta Acustica united with Acustica, **93**, 909–916.

Fomel, S., 2004, On anelliptic approximations for qP velocities in VTI media: Geophysical Prospecting, **52**, 247–259.

Fomel, S., and A. Stovas, 2010, Generalized nonhyperbolic moveout approximation: Geophysics, **75**, U9–U18.

Fomel, S., and R. Kazinnik, 2013, Non-hyperbolic common reflection surface: Geophysical Prospecting, **61,** 21-27.

Fowler, P. J., 2003, Practical VTI approximations: a systematic anatomy: Journal of Applied Geophysics, **54**, 347–367.

Gelchinsky, B., A. Berkovitch, and S. Keydar, 1999a, Multifocusing homeomorphic imaging - Part 1 Basic concepts and formulae: Journal of Applied Geophysics, **42,** 229-242.

Gelchinsky, B., A. Berkovitch, and S. Keydar, 1999b Multifocusing homeomorphic imaging - Part 2 Multifold data set and multifocusing: Journal of Applied Geophysics, **42**, 243-260.

Gholami, Y., Brossier, R., Operto, Stephane., Ribodetti, A., and Virieux. J., 2013, Which parameterization is suitable for acoustic vertical transverse isotropic full waveform inversion? Part 1: Sensitivity and trade-off analysis: Geophysics, **78**, R81-R105.

Golikov, P., and A. Stovas, 2012, Accuracy comparison of nonhyperbolic moveout approximations for qP-waves in VTI media: Journal of Geophysics and Engineering, **9**, 428-432.

Golikov, P., and A. Stovas, 2013, Moveout-based geometrical spreading approximation in TTI media: 75th EAGE Conference and Exhibition incorporating SPE EUROPEC.

Gonzalez, R., and R. Woods, 2008, Digital Image Processing: 3rd edition, Prentice Hall.

Grechka, V., and I. Tsvankin, 1999a, 3-D moveout velocity analysis and parameter estimation for orthorhombic media: Geophysics, **64**, 820–837.

Grechka, V., and I. Tsvankin, 1999b. 3-D moveout inversion in azimuthally anisotropic media with lateral velocity variation: Theory and a case study: Geophysics, **64**, 1202–1218.

Hagedoorn, J. G., 1954, A process of seismic reflection interpretation: Geophysical Prospecting, **2**, 85-127.

Hao, Q., and A. Stovas, 2016, Analyic calculation of phase and group velocities of P-waves in orthorhomic media: Geophysics, **81**, C79-C97.

Helbig, K., 1994, Foundations of anisotropy for exploration seismics: Handbook of geophysical exploration, I: Seismic exploration.

Höcht, G., E. de Bazelaire, P. Majer, and P. Hubral, 1999, Seismics and optics: Hyperbolae and curvatures: Journal of Applied Geophysics, **42,** 261-281.

Hristov, H. D., 2000, Fresnal Zones in Wireless Links, Zone Plate Lenses and Antennas: Artech House, Inc. ISBN: 0890068496

Hubral, P., 1983, Computing true amplitude reflections in a laterally inhomogeneous earth: Geophysics, **48,** 1051-1062.

Hubral, P., J. Schleicher, M. Tygel, and V. C. Hanitzch, 1993, Determination of Fresnel zones from traveltime measurements: Geophysics, **58**, 703–712.

Jäger, R., J. Mann, G. Höcht, and P. Hubral, 2001, Common-reflection-surfacestack: Image and attributes: Geophysics, **66,** 97-109.

Kazei, V., V. Troyan, B. Kashtan, and W. Mulder, 2013, On the role of reflections, refractions and diving waves in full-waveform inversion: Geophysical Prospecting, **61**, 1252–1263.

Koren, Z., and I. Ravve, 2014, Azimuthally varying anisotropic velocity model update: Geophysics, **79**, C27-C53.

Koren, Z., and I. Ravve, 2017, Fourth-order normal moveout velocity in elastic layered orthorhombic media — Part 2: Offset-azimuth domain: Geophysics, **82**, C113-C132.

Landa, E., S. Keydar, and T. J. Moser, 2010, Multifocusing revisited: Inhomogeneous media and curved interfaces: Geophysical Prospecting, **58,** 925-938.

Levin, F. K., 1996, Anatomy of diving waves: Geophysics, **61**, 1417–1424.

Lindsey, J. P., 1989, The Fresnel zone and its interpretive significance: The Leading Edge, **7**, 33-39.

Masmoudi, N., and T. Alkhalifah, 2014, Multi-parameters scanning in HTI media: 84th Annual International Meeting, SEG, Expanded Abstracts, 480–485.

Masmoudi, N., and T. Alkhalifah, 2016, Traveltime approximations and parameter estimation for orthorhombic media: Geophysics, **81,** C127-C137.

Monk, D., 2009, Fresnel zone binning: Application to 3D seismic fold and coverage assessments: The Leading Edge, **28,** 288–295

Monk, D., 2010, Fresnel-zone binning: Fresnel-zone shape with offset and velocity function: Geophysics, **75**, T9–T14.

Moser, T. J., and V. Červený, 2007, Paraxial ray methods for anisotropic inhomogeneous media: Geophysical Prospecting, **55**, 21–37.

Okoye, P., and N. Uren, 2000, Fresnel zones and spatial resolution for P- and SH-waves in transversely isotropic media: Geophysics, **65**, 1168–1178.

Ravve, I., and Z. Koren, 2017, Fourth-order normal moveout velocity in elastic layered orthorhombic media — Part 1: Slowness-azimuth domain: Geophysics, **82**, C91- C111.

Rogister, Y., and M. A. Slawinski, 2005, Analytic solution of ray-tracing equations for a linearly inhomogeneous and elliptically anisotropic velocity model: Geophysics, **70**, D37–D41.

Sarkar, D., and I. Tsvankin, 2003, Analysis of image gathers in factorized VTI media: Geophysics, **68**, 2016–2025.

Schleicher, J., P. Hubral, M. Jaya, and M. Tygel, 1997, Minimum apertures and Fresnel zones in migration and demigration: Geophysics, **62**, 183–194.

Schoenberg, M., and K. Helbig, 1997, Orthorhombic media: Modeling elastic wave behavior in a vertically fractured earth: Geophysics, **62**, 1954–1974.

Schwarz, B, C. Vanelle, D. Gajewski and B. Kashtan, 2014, Curvatures and inhomogeneities: An improved common reflection surface approach: Geophysics, **79,** S231-S240.

Shen, P., 2013, Subsurface focusing measurement of diving waves and its application to reflection tomography: 75th Annual International Conference and Exhibition, EAGE, Extended Abstracts, Th1005.

Sheriff, R. E., 1996, Understanding the Fresnel zone: AAPG Explorer, 18-19

Sheriff, R.E., 1980, Nomogram for Fresnel-zone calculation: Geophysics, **45**, 968-972.

Sirgue, L., and R. G. Pratt, 2004, Efficient waveform inversion and imaging: A strategy for selecting temporal frequencies: Geophysics, **69**, 231–248.

Spetzler, J., and R. Snieder, 2004, The Fresnel volume and transmitted waves -A tutorial: Geophysics, **69**, 653–663.

Sripanich, Y., and S. Fomel, 2015, On anelliptic approximations for qP velocities in transversely isotropic and orthorhombic media: Geophysics, **80,** C89-C105.

Sripanich, Y., S. Fomel, A. Stovas, and Q. Hao, 2016, 3D generalized nonhyperboloidal moveout approximation: Geophysics, **82**, C49–C59.

Stovas, A., 2008, Kinematically equivalent velocity distributions: Geophysics, **73**, VE369-VE375.

Stovas, A., 2010, Kinematical characteristics of the factorized velocity model: Geophysical Prospecting, **58**, 219-227.

Stovas, A., 2015, Azimuthally dependent kinematic properties of orthorhombic media: Geophysics, **80,** C107-C122.

Stovas, A., 2017, Geometrical spreading in orthorhombic media: Geophysics, **83**, C61-C73.

Stovas, A., and B. Ursin, 2009, Improved geometric-spreading approximation in layered transversely isotropic media: Geophysics, **74**, D85–D95.

Stovas, A., and T. Alkhalifah, 2014, Analytical approximations of diving wave imaging in constant-gradient medium: Geophysics, **79**, S131–S140.

Stovas, A., N. Masmoudi, and T. Alkhalifah, 2016, Application of perturbation theory for P-wave eikonal equation in orthorhombic media: Geophysics, **81,** C309-C317.

Tang, Y., S. Lee, A. Baumstein, and D. L. Hinkley, 2013, Tomographically enhanced full wavefield inversion: 83rd Annual International Meeting, SEG, Expanded Abstracts, 1037–1041.

Thomsen, L., 1986, Weak elastic anisotropy: Geophysics, **51,** 1954–66.

Thomsen, L., 2001, Seismic anisotropy: Geophysics, **66**, 40-41.

Trorey, A.W., 1970, A simple theory for seismic diffraction: Geophysics, **35**, 762-784.

Tsvankin, I., 1995, Body-wave radiation patterns and AVO in transversely isotropic media: Geophysics, **60**, 1409–1425.

Tsvankin, I., 1997, Anisotropic parameters and P-wave velocity for orthorhombic media: Geophysics, **62**, 1292–1309.

Tsvankin, I., 2005, Seismic Signatures and Analysis of Reflection Data in Anisotropic Media, 2nd edition.

Tsvankin, I., 2012, Seismic signatures and analysis of reflection data in anisotropic media, In: Geophysical References Series, Vol. 19. SEG. ISBN 9781560803003.

Tsvankin, I., and L. Thomsen, 1994, Nonhyperbolic reflection moveout in anisotropic media: Geophysics, **59**, 1290-1304.

Tygel, M., and L. T. Santos, 2007, Quadratic normal moveouts of symmetric reflections in elastic media: A quick tutorial: Studia Geophysica et Geodaetica, **51,** 185-206.

Ursin, B. and K. Hokstad, 2003, Geometrical spreading in a layered transversely isotropic medium with vertical symmetry axis: Geophysics, **68**, 2082–2091.

Ursin, B., 1990, Offset-dependent geometrical spreading in a layered medium: Geophysics, **55**, 492–496.
Ursin, B., and K. Hokstad, 2003, Geometrical spreading in a layered transversely isotropic medium with vertical symmetry axis: Geophysics, **68**, 2082–2091.

Ursin, B., N. Favretto-Cristini, and P. Cristini, 2014, Fresnel volume and interface Fresnel zone for reflected and transmitted waves from a curved interface in anisotropic media: Geophysics, **79**, C123-C134.

Vanelle, C., M. Bobsin, P. Schemmert, B. Kashtan and D. Gajewski, 2012, i-CRS: A new multiparameter stacking operator for an/isotropic media: 82nd Annual International Meeting SEG Expanded Abstracts.

Vasconcelos, I., and I. Tsvankin, 2006, Non-hyperbolic moveout inversion of wide-azimuth P-wave data for orthorhombic media: Geophysical Prospecting, **54**, 535-552.

Vinje, V., A. Stovas, and D. Reynaud, 2012, Preserved-traveltime smoothing: Geophysical Prospecting, **61**, 380-390.

Vinje, V., E. Iversen, K. Åstebøl, and H. Gjøystdal, 1996, Estimation of multivalued arrivals in 3D models using wavefront construction, Part I: Geophysical Prospecting, **44**, 819-842.

Virieux, J., and S. Operto, 2009, An overview of full-waveform inversion in exploration geophysics: Geophysics, **74**, WCC1–WCC26.

Widess, M. B., 1982, Quantifying resolving power of seismic systems: Geophysics, **47**, 1160-1173.

Xu, S., A. Stovas, and Q. Hao, 2017, Perturbation-based moveout approximations in anisotropic media: Geophysical Prospecting, **65**,1218-1230.

Xu, S., A. Stovas, and Y. Sripanich, 2017, An anelliptic approximation for geometrical spreading in transversely isotropic and orthorhombic media, Geophysics, **83**, C37-C47.

Xu, S., and A. Stovas, 2017, A new parameterization for acoustic orthorhombic media: Geophysics, **82**, C229-C240.

Xu, S., and A. Stovas, 2017. Direct Geometrical Spreading Approximations in Anisotropic Media: Technical Program of the 79th EAGE Conference and Exhibition, Tu P8 13.

Xu, X., and I. Tsvankin, 2006, Anisotropic geometrical-spreading correction for wide-azimuth P-wave reflection: Geophysics, **71**, D161–D170.

Xu, X., and I. Tsvankin, 2006, Anisotropic geometrical-spreading correction for wide-azimuth P-wave reflection: Geophysics, **71**, D161–D170.

Xu, X., and I. Tsvankin, 2007, A case study of azimuthal AVO analysis with anisotropic spreading correction: The leading edge, **26**, 1552-1561.

Xu, X., and I. Tsvankin, 2008, Moveout-based geometrical-spreading correction for PS-waves in layered anisotropic media: Journal of Geophysics and Engineering, **5**, 195-202.

Xu, X., I. Tsvankin, and A. Pech, 2005, Geometrical spreading of P-waves in horizontally layered, azimuthally anisotropic media: Geophysics, **70**, D43–D53.

Yilmaz, O., 2001, Seismic Data Analysis: Processing, Inversion, and Interpretation of Seismic Data: Investigations in Geophysics.

Zhou, H., and McMechan, G. A., 2000, Analytical study of the geometrical spreading of P-waves in a layered transversely isotropic medium with vertical symmetry axis: Geophysics, **65**, 1305–1315.